Carnegie-Mellon University
PITTSBURGH, PENNSYLVANIA 15213

DEPARTMENT OF
MECHANICAL ENGINEERING

ELASTO-PLASTIC FLOW IN CRACKED BODIES USING A NEW FINITE ELEMENT MODEL

MICHAEL E. KARABIN, JR.

Report SM 77-11 November 1977

Submitted in partial fulfillment of the
requirements for the degree of
Doctor of Philosophy at Carnegie-Mellon University

Department of Mechanical Engineering
Carnegie Institute of Technology
Carnegie-Mellon University
Pittsburgh, Pennsylvania

ELASTO-PLASTIC FLOW IN CRACKED BODIES USING A NEW FINITE ELEMENT MODEL

MICHAEL E. KARABIN, JR.

Report SM-77-11 November 1977

Submitted in partial fulfillment of the
requirements for the degree of
Doctor of Philosophy at Carnegie-Mellon University

Department of Mechanical Engineering
Carnegie Institute of Technology
Carnegie-Mellon University
Pittsburgh, Pennsylvania

Carnegie-Mellon University

CARNEGIE INSTITUTE OF TECHNOLOGY

THESIS

SUBMITTED IN PARTIAL FULFILLMENT OF THE REQUIREMENTS

FOR THE DEGREE OF Doctor of Philosophy

TITLE ELASTO-PLASTIC FLOW IN CRACKED BODIES USING A NEW FINITE ELEMENT MODEL

PRESENTED BY MICHAEL E. KARABIN, JR.

ACCEPTED BY THE DEPARTMENT OF Mechanical Engineering

MAJOR PROFESSOR — DATE 30 Nov 1977

DEPARTMENT HEAD — DATE

APPROVED BY THE COLLEGE COUNCIL

DEAN — DATE 30 Nov 77

ACKNOWLEDGEMENTS

The author takes great pleasure in recognizing the contributions of all those involved with this thesis. Foremost, the author is indebted to his advisor, Professor Jerold L. Swedlow, for his continual guidance and assistance. Also, sincere gratitude is expressed to Professor Swedlow for his gift of SPECEL which provided the basis for this work. The author appreciates the constant financial support of the National Aeronautics and Space Administration through NASA Research Grant NGR 39-087-053. Thanks are offered to Miss Gerry Bradley for her careful typing of this thesis and for her helpful suggestions. In addition, the author recognizes the efforts of his brother, Richard, in the preparation of the figures. Finally, the author is extremely grateful to his parents for their encouragement and understanding.

ABSTRACT

Cracked geometries are studied by finite element techniques with the aid of a new special element embedded at the crack tip. This model seeks to accurately represent the singular stresses and strains associated with the elasto-plastic flow process. Previous finite element schemes incorporating special elements represent either the linear elastic singularity or the singularity associated with materials possessing a power law stress-strain relationship and yielding according to the deformation theory of plasticity (commonly referred to as the HRR singularity). The present model is not restricted to a material type and does not predetermine a singularity. Rather the singularity is treated as an unknown. For each step of the incremental process the nodal degrees of freedom and the unknown singularity are found through minimization of an energy-like functional. The singularity and nodal degrees of freedom are determined by means of an iterative process.

Solutions to a set of elastic test cases and a series of four elasto-plastic problems constitute the bulk of this work. The elastic cases serve as a check of the method's ability to determine the singularity as a function of notch opening angle. The elasto-plastic problems study four specimens, each consisting of a different material, and incorporate some geometric changes. These problems offer opportunities to compare results with analytical theories, laboratory test results of a real material, and numerical data of other finite element analyses.

Elastic results from the model show excellent agreement with the theoretical prediction. As yielding progresses there is some convergence

to the HRR model although the process takes place slowly. Particular attention is given to the stress field surrounding the crack tip and the parameter J. The J analysis suggests that this quantity is not path independent in specimens with a large amount of plasticity. Two contributing factors are identified as causes for the path dependence: 1) the nonproportionality of the stresses near the crack tip which violates a basic premise of the deformation theory of plasticity; 2) a resharpening of the crack tip in center cracked specimens. An experiment is proposed to determine if these factors are real.

After evaluating all the results it is concluded that the model works. Information is provided nearer the crack tip with better resolution than previous numerical analyses. There is a large degree of agreement with existing theories and yet there are some original results. It is important to test these findings as outlined in the thesis to guarantee their validity.

TABLE OF CONTENTS

Page

CHAPTER I: Introduction ---------- 1

CHAPTER II: Method ---------- 4

A: Equations of Elasto-Plastic Flow ---------- 4
B. Singularities ---------- 8
C. Plastic Singular Elements ---------- 10
D. SPECEL ---------- 13
E. Accumulated Exponents ---------- 16

CHAPTER III: Types of Problems Solved ---------- 18

A. Preliminary Problems ---------- 18
B. Singularity as a Function of Notch Opening Angle -------- 21
C. Power Hardening Material (PH) ---------- 22
D. Bilinear Material (BIL) ---------- 24
E. A533B Steel (RS) ---------- 25
F. Task Group - Round Robin (Bend) ---------- 26

CHAPTER IV: Discussion of the Results ---------- 29

A. Notched Disks ---------- 29
B. Power Hardening Material (PH) ---------- 30
C. Bilinear Material (BIL) ---------- 40
D. A533B Steel (RS) ---------- 46
E. E-24 Task Group Problem - Round Robin (Bend) ---------- 50
F. J, COD, δ_M ---------- 56

CHAPTER V: Proposal for Experimentation ---------- 64

CHAPTER VI: Summary, Conclusions and Suggestions ---------- 69

FIGURES ---------- 74

REFERENCES ---------- 172

APPENDIX ---------- 174

LIST OF FIGURES

Figure		Page
1	Notch Tip Geometry	74
2	Sectors Comprising Special Element Surrounding Crack Tip	75
3	Flow Chart for SPECEL	76
4	Finite Element Map, Special Element Size a/16	77
5	Finite Element Map, Special Element Size a/32	78
6	Finite Element Map, Special Element Size a/64	79
7	Special Element Embedded in Regular Elements	80
8a	Finite Element Map for Notch Problems	81
8b	Insert for Fig. 8a	82
8c	Insert for Fig. 8b	82
9	Finite Element Map for Power Hardening and Bilinear Problems	83
10	Octahedral Stress-Strain Relationships for Power Hardening and Bilinear Materials	84
11	Small Strain Octahedral Stress-Strain Relationships for Power Hardening and Bilinear Materials	85
12	Finite Element Map for RS Problem	86
13	Finite Element Map for Bend Problem	87
14	Elastic Exponent (p) VS. Notch Enclosure Angle (2α)	88
15	Incremental Exponent VS. Applied Load for Every Fifth Load Step (PH)	89
16	Accumulated Exponent VS. Angular Position (PH)	90
17	Accumulated Exponent VS. Applied Load (PH)	91
18	Energy Exponent VS. Angular Position (PH)	92
19	$\sigma_r/\sigma_{e\ max}$ VS. r/a at $\theta = 3.75°$ (PH)	93
20	$\sigma_r/\sigma_{e\ max}$ VS. r/a at $\theta = 93.75°$ (PH)	94

Figure		Page
21	$\sigma_\theta/\sigma_{e\ max}$ VS. r/a at 3.75° and 93.75° (PH) ----------	95
22	$\sigma_e/\sigma_{e\ max}$ VS. r/a at 3.75° (PH) ----------	96
23	$\tau_{r\theta}/\sigma_{e\ max}$ VS. r/a at 93.75° (PH) ----------	96
24	$\sigma_e/\sigma_{e\ max}$ VS. θ for $\hat{r}$ = 0.001 (PH) ----------	97
25	$\sigma_r/\sigma_{e\ max}$ VS. θ for $\hat{r}$ = 0.001 (PH) ----------	98
26	$\sigma_\theta/\sigma_{e\ max}$ VS. θ for $\hat{r}$ = 0.001 (PH) ----------	99
27	$\tau_{r\theta}/\sigma_{e\ max}$ VS. θ for $\hat{r}$ = 0.001 (PH) ----------	100
28	Max Shear Direction (α) VS. θ (PH) ----------	101
29	Normalized J VS. Distance from the Crack Tip (PH) -----	102
30	Plastic Strain Intensity Factor VS. Applied Stress (PH) ----------	103
31	J* VS. $\bar{\sigma}/\sigma_y$ for J Paths Outside the Special Element (PH)	104
32	Y/Y_{el} VS. $\bar{\sigma}/\sigma_y$ for Near and Far Field Paths (PH) ----	105
33	$\sigma_r/\bar{\sigma}$ VS. θ for $\hat{r}$ = 0.001 (PH) ----------	106
34	$\sigma_\theta/\bar{\sigma}$ VS. θ for $\hat{r}$ = 0.001 (PH) ----------	107
35	$\tau_{r\theta}/\bar{\sigma}$ VS. θ for $\hat{r}$ = 0.001 (PH) ----------	108
36	$\sigma_r/\bar{\sigma}$ VS. θ for $\hat{r}$ = 0.977 (PH) ----------	109
37	$\sigma_\theta/\bar{\sigma}$ VS. θ for $\hat{r}$ = 0.977 (PH) ----------	110
38	$\tau_{r\theta}/\bar{\sigma}$ VS. θ for $\hat{r}$ = 0.977 (PH) ----------	110
39	s_{ij}/τ_0 VS. $\bar{\sigma}/\sigma_y$ Ahead of Crack Tip (PH) ----------	111
40	s_{ij}/τ_0 VS. $\bar{\sigma}/\sigma_y$ Above Crack Tip (PH) ----------	112
41	Crack Opening Profiles within the Special Element (PH)-	113
42	Crack Opening Profiles along Entire Crack Flank (PH) --	114
43	Crack Mouth Opening VS. Applied Load (PH) ----------	115
44	Incremental Exponent VS. Applied Load for Every Fifth Load Step (BIL) ----------	116

Figure		Page
45	Accumulated Exponent VS. Applied Load (BIL) ----------	117
46	Energy Exponent VS. Angular Position (BIL) ----------	118
47	$\sigma_r/\sigma_{e\ max}$ VS. r/a at θ = 3.75° (BIL) ----------	119
48	$\sigma_r/\sigma_{e\ max}$ VS. r/a at θ = 93.75° (BIL) ----------	120
49	$\sigma_\theta/\sigma_{e\ max}$ VS. r/a at θ = 3.75° and 93.75° (BIL) ----	121
50	$\sigma_e/\sigma_{e\ max}$ VS. r/a at θ = 3.75° (BIL) ----------	122
51	$\tau_{r\theta}/\sigma_{e\ max}$ VS. r/a at θ = 93.75° (BIL) ----------	122
52	$\sigma_e/\sigma_{e\ max}$ VS. θ for $\hat{r}$ = 0.001 (BIL) ----------	123
53	$\sigma_r/\sigma_{e\ max}$ VS. θ for $\hat{r}$ = 0.001 (BIL) ----------	124
54	$\sigma_\theta/\sigma_{e\ max}$ VS. θ for $\hat{r}$ = 0.001 (BIL) ----------	125
55	$\tau_{r\theta}/\sigma_{e\ max}$ VS. θ for $\hat{r}$ = 0.001 (BIL) ----------	126
56	Normalized J VS. Distance from the Crack Tip (BIL) --	127
57	Near and Far Field J Values VS. Applied Load (BIL) ----	128
58	$\sigma_r/\overline{\sigma}$ VS. θ for $\hat{r}$ = 0.001 (BIL) ----------	129
59	$\sigma_r/\overline{\sigma}$ VS. θ for $\hat{r}$ = 0.977 (BIL) ----------	130
60	Crack Opening Profiles within the Special Element (BIL)	131
61	Crack Opening Profiles along Entire Crack Flank (BIL) -	132
62	Octahedral Stress Comparison of Power Hardening and Bilinear Materials at $\hat{r}$ = 0.001 (BIL and PH) ----------	133
63	Octahedral Stress Comparison of Power Hardening and Bilinear Materials at $\hat{r}$ = 0.977 (BIL and PH) ----------	133
64	Comparison of Power Hardening and Bilinear Parameters (BIL and PH) ----------	134
65	Normalized J VS. Distance from the Crack Tip (RS) ---	135
66	Octahedral Stress-Strain Curves (RS) ----------	136
67	Near and Far Field J Values VS. Applied Load (RS) -----	137
68	Crack Opening Profiles within the Special Element (RS)-	138
69	Crack Opening Profile along Entire Crack Flank (RS) ---	139

Figure		Page
70	$(\delta^*/\delta^*_{el})^{1/2}$ VS. $\overline{\sigma}/\sigma_y$ (RS)	140
71	Load-Deflection Curve (Bend)	141
72	Hydrostatic Stress along Crack Ligament (Bend)	142
73	Hydrostatic Stress along Crack Ligament (PH)	143
74	Effective Stress along Crack Ligament (Bend)	144
75	J as a Function of Distance from the Tip for a Number of Load Levels (Bend)	145
76	$\overline{J}$ VS. Applied Displacement (Bend)	146
77	Incremental Exponent VS. Applied Displacement (Bend)	147
78	Accumulated Exponent VS. Applied Displacement (Bend)	148
79	Energy Exponent VS. Angular Position (Bend)	149
80	$\sigma_\theta/\sigma_{e\ max}$ VS. r/a at θ = 3.75° and 93.75° (Bend)	150
81	$\sigma_e/\sigma_{e\ max}$ VS. θ for $\hat{r}$ = 0.001 (Bend)	151
82	$\sigma_r/\sigma_{e\ max}$ VS. θ for $\hat{r}$ = 0.001 (Bend)	152
83	$\sigma_\theta/\sigma_{e\ max}$ VS. θ for $\hat{r}$ = 0.001 (Bend)	153
84	$\tau_{r\theta}/\sigma_{e\ max}$ VS. θ for $\hat{r}$ = 0.001 (Bend)	154
85	Normalized J VS. Distance from the Crack Tip (Bend)	155
86	Crack Opening Profiles near the Crack Tip (Bend)	156
87	Crack Opening Profiles along Remainder of Crack Flank (Bend)	157
88	J VS. Applied Displacement (RS)	158
89	J VS. Crack Mouth Opening (PH and BIL)	159
90	J VS. Crack Mouth Opening from the Point of Net Section Yield (PH and BIL)	160
91	J and Applied Displacement VS. Crack Mouth Opening (RS)	161
92	J VS. Crack Mouth Opening (Bend)	162
93	Crack Flank Opening (δ) VS. Crack Mouth Opening (δ_M) (Bend)	163

Figure		Page
94	J VS. COD (Bend)	164
95	Far Field J VS. Crack Tip Opening (PH)	165
96	J VS. Crack Flank Displacement at Respective Distances from the Crack Tip (PH)	166
97	Crack Flank Opening (δ) VS. Crack Mouth Opening (δ_M) (PH)	167
98	Crack Flank Opening (δ) VS. Crack Mouth Opening (δ_M) (BIL)	168
99	Crack Flank Opening (δ) VS. Crack Mouth Opening (δ_M) (RS)	169
100	Flow Chart for Proposed Experiment	170

CHAPTER I

INTRODUCTION

The study of cracks in solid bodies has been hampered by the complex behavior at the crack tip. Discontinuities in geometry give rise to singularities at the tip which make modelling very difficult. Some analytical solutions to the problem have been developed by assuming a particular material response. Hence, numerical procedures based on this analytical work are restricted to certain material types. Computational methods that do not build in such material characterization are limited by the fact that their credibility diminishes near the crack tip due to the singularity. A "zone of blindness" develops in this region.

Swedlow (1974)* has developed a new computer model for solving crack problems. It is not restricted by material behavior yet provides a much more detailed description of the response near the crack tip including singularities. The "zone of blindness" is shrunk considerably.

Of course, this representation entails a few limitations, but these are common to many other analyses. No history is given as to how the crack appeared. It is simply assumed to exist in a virgin material. The body itself is modelled as a two-dimensional continuum. Appropriate plane stress or plane strain designation is given to effect the third dimension. The crack is assumed to be sharp until a load is applied to the body. By sharp it is meant that the sides of the crack are straight and the tip has a zero radius of curvature. No growth of the crack takes place throughout the loading process.

Although it may not be possible to adhere to all these assumptions

*References are indicated by author and date.

in the laboratory it is still a reasonable representation. And in light of the simplifications they make for numerical computation these idealizations are justified. Now, using this model as a basis, a few material characteristics are incorporated into the model.

Each specimen that is studied in this work consists of only one material that is assumed to be homogeneous and isotropic. The tensile stress-strain curve has an initial linear elastic portion and a subsequent plastic portion with a positive slope at each point. Incremental elasto-plastic flow theory is used for which the plastic part of the stress-strain curve is discretized into a number of small straight line segments. Loading of the body can be produced with displacements and/or tractions. It is always applied in the plane of the two-dimensional body.

The program, SPECEL, solves problems through finite element techniques. This basic method has inherent assumptions which are elucidated elsewhere, for example Zienkiewicz (1967). Finite elements discretize the body into a number of sub-bodies and assume displacement forms for these regions. This particular finite element procedure, SPECEL, incorporates a displacement function in the region surrounding the crack tip (special element) that accounts for singular stresses and strains. This singularity is not predetermined but is treated as a degree of freedom. Surrounding this region are conventional finite elements which in themselves pose no problems but cause minor difficulties when used in conjunction with the special element. A novel approach and solution method will be discussed later in this work.

As stated earlier, the formulation and development of SPECEL has been carried out by Swedlow (1974). The emphasis in this effort is placed on the usage of SPECEL. First, it is necessary to show that

SPECEL does work within the framework of the model. This is accomplished by comparing SPECEL's results to those found by accepted analytical and numerical methods. Of course, the model places certain limitations on SPECEL and it is important to keep this in mind when evaluating results. Having checked out the program the next inquiry to make is what one can learn with this new tool. Answering this question is the central purpose of this thesis.

Following this introduction the remaining discussion is divided into five chapters. Chapter two begins by briefly reviewing the equations of elasto-plastic flow. Then the two analytical limit cases (elastic and plastic) plus some other numerical models of near tip crack analysis are discussed. All this provides the motivation for the development of SPECEL. An outline of SPECEL's formulation concludes chapter two.

Chapter three describes in detail the problems to be solved in this work. A series of notched disks for a linear elastic material are loaded to test the singularity response of SPECEL. Then three center cracked specimens and one three point bend specimen, each with different material properties, are excited for full elasto-plastic solutions. The results of these problems are discussed at length in chapter four. Out of this discussion emerges a proposal for experimentation which is outlined in chapter five. Conclusions and a summary are presented in the final chapter.

CHAPTER II

METHOD

A. Equations of Elasto-Plastic Flow

Primarily, SPECEL is geared to solve elasto-plastic stationary crack problems. Before discussing the difficulty caused by the introduction of a crack into the geometry first consider the incremental theory of plasticity and solution procedure that is employed in SPECEL. A detailed description may be found in Swedlow (1968) so only an outline of the pertinent material is presented here. Quantities used frequently are defined as follows:

$$\tau_0 = \sqrt{s_{ij} s_{ij}/3} \qquad \text{octahedral stress}$$

$$\sigma_e = \frac{3}{\sqrt{2}} \tau_0 \qquad \text{effective stress}$$

$$s_{ij} = \sigma_{ij} - \delta_{ij} \sigma_{kk}/3 \qquad \text{stress deviator}$$

$$\varepsilon_0^p = \int d\varepsilon_0^p = \int \dot{\varepsilon}_0^p \, dt \qquad \text{octahedral plastic strain}$$

$$\dot{\varepsilon}_0^p = \sqrt{\dot{\varepsilon}_{ij}^p \dot{\varepsilon}_{ij}^p/3} \qquad \text{octahedral plastic strain rate}$$

$$\dot{\varepsilon}_{ef}^p = \sqrt{2}\, \dot{\varepsilon}_0^p \qquad \text{effective plastic strain rate}$$

$$\varepsilon_{ef} = \int \dot{\varepsilon}_{ef}^p \, dt + \frac{\sigma_e}{E} \qquad \text{effective strain}$$

where σ_{ij}, ε_{ij} are the stress and strain tensors, δ_{ij} is the Kronecker delta, E is Young's modulus, t is the time variable, and the usual summation convention of indicial notation is used. The process is assumed to be quasi-static so that inertial and convective effects are neglected. Thus, the dot operator represents

$$\frac{\partial}{\partial t} = \frac{d}{dt}$$

For small strains the usual strain-displacement relation is translated into a rate equation as

$$\dot{\varepsilon}_{ij} = \frac{1}{2}(\dot{u}_{i,j} + \dot{u}_{j,i}) \tag{1}$$

where the comma denotes differentiation. The strain rates are separated into elastic and plastic components

$$\dot{\varepsilon}_{ij} = \dot{\varepsilon}^{e}_{ij} + \dot{\varepsilon}^{p}_{ij} \tag{2}$$

and the elastic portion obeys Hooke's law

$$\dot{\varepsilon}^{e}_{ij} = [(1+\nu)\dot{\sigma}_{ij} - \nu\dot{\sigma}_{kk}\,\delta_{ij}]/E \tag{3}$$

where ν is Poisson's ratio. The stress rates satisfy the analogous equilibrium rate equation in the absence of body forces

$$\dot{\sigma}_{ij,j} = 0 \qquad \text{with } \dot{\sigma}_{ij} = \dot{\sigma}_{ji} \tag{4}$$

Using the Von Mises yield criterion with Drucker's definition of work hardening the following flow rule is obtained:

$$2\mu^{p}_{0}\,\dot{\varepsilon}^{p}_{ij} = \frac{s_{ij}\,s_{k\ell}}{3\tau_0^{\,2}}\,\dot{\sigma}_{k\ell} \tag{5}$$

where $2\mu^{p}_{0} = d\tau_0/d\varepsilon^{p}_{0} = \dot{\tau}_0/\dot{\varepsilon}^{p}_{0}$ which is the local slope of the octahedral

stress-plastic strain curve. Boundary conditions are given in terms of displacement rates or traction rates

$$\dot{t}_i = \dot{\sigma}_{ij} n_j \tag{6}$$

where the n_j are the components of the outward unit normal to the boundary. All the problems in this exercise are of the plane strain type, although SPECEL may be rigged to solve problems in plane stress. Substituting the total strain rates for the stress rates (adding equations (3) and (5), then taking the inverse) in the equilibrium equations (4) and then replacing the strain rates with the displacement rates (1) yields a set of quasi-linear partial differential equations for the displacement rates. While the derivations are performed in terms of rates the numerical solution proceeds in terms of increments. A large number of increments is necessary so that the error in going from rates to increments is minimized. For a quantity q the relation

$$\int_{t_1}^{t_2} \dot{q}\, dt \doteq \int_{t_1}^{t_2} \frac{q(t_2)-q(t_1)}{t_2-t_1}\, dt = q(t_2) - q(t_1) = \delta q \tag{7}$$

is a good approximation provided t_2-t_1 is small.

Actual solutions to incremental plasticity problems are found usually through energy methods. The following energy-like term is written for a plane strain situation in terms of the cartesian components:

$$\Pi = (E/2) \int_A \Big\{ [(\lambda + 2G)/E - s_{xx}^2 / (1 + 1/\beta)]\ \delta\varepsilon_{xx}^2$$

$$- 4[s_{yy}\ s_{xy} / (1 + 1/\beta)]\ \delta\varepsilon_{yy}\ \delta\varepsilon_{xy}$$

$$+ [(\lambda + 2G)/E - s_{yy}^2 / (1 + 1/\beta)]\ \delta\varepsilon_{yy}^2$$

$$- 4[s_{xx}\ s_{xy} / (1 + 1/\beta)]\ \delta\varepsilon_{xx}\ \delta\varepsilon_{xy}$$

$$+ 4[G/E - s_{xy}^2 / (1 + 1/\beta)]\ \delta\varepsilon_{xy}^2$$

$$+ 2[\lambda/E - s_{xx}\ s_{yy} / (1 + 1/\beta)]\ \delta\varepsilon_{xx}\ \delta\varepsilon_{yy} \Big\}\ dA$$

$$- \int_{S_t} (\delta t_x\ \delta u + \delta t_y\ \delta v)\ dS \qquad (8)$$

where A represents the body, S_t is that portion of the boundary on which tractions are specified, $G = E/\big(2(1+\nu)\big)$, $\lambda = 2\nu G/(1-2\nu)$, and $\beta = G/\mu_0^p$. An analog to the theorem of minimum potential energy states that a stationary value of Π (actually a minimum) leads to the correct solution (Jones, 1972). SPECEL uses finite element techniques to find a minimum of Π. This method discretizes the body into a number of sub-bodies (elements) which have a specified displacement form

$$\{\delta u_i(x_i)\} = [f(x_i)]\ \{\delta \underline{u}_i\} \qquad (9)$$

where $\{\delta u_i(x_i)\}$ are the displacement increments at point (x_i) within an element, $[f(x_i)]$ represents the displacement functions, and $\{\delta \underline{u}_i\}$ are the incremental displacements at the element nodes. Taking the derivative

of $\{\delta u_i(x_i)\}$ to find the expressions for the strain increments, substituting these into the expression for Π, and then minimizing Π leads to the usual stiffness equations

$$[K]\ \{\delta \underline{u}_i\} = \{\delta T_i\} \tag{10}$$

where [K] represents the stiffness matrix (updated for each step of the incremental loading) and $\{\delta T_i\}$ represents the incremental nodal forces. The stiffness equations are solved for every load increment and the program tracks accumulated displacements, stresses, strains, and forces. A detailed description of the finite element solution procedure may be found in Swedlow (1973).

B. Singularities

Having considered the general solution method of elasto-plastic problems, the next step is to introduce the crack into the geometry. Williams (1952,1957) considered the case of a sharp notch in a two-dimensional, linear elastic, stress field. The geometry can be seen in Fig. (1). For planar elasticity the compatibility equation is

$$\nabla^4 \chi = 0 \tag{11}$$

where χ is the Airy stress function and the stresses are defined in terms of this function such that equilibrium is satisfied. A solution of the form

$$\chi = r^{p+1} f(\theta) \tag{12}$$

is assumed. $f(\theta)$ behaves like $\sin\left((p\pm1)\theta\right)$, $\cos\left((p\pm1)\theta\right)$. Imposing stress free boundary conditions on the faces of the notch leads to a set of four homogeneous equations. In order for these equations to yield a nontrivial solution the following eigenequation must be satisfied:

$$\sin[p2\alpha] = p \sin 2\alpha \tag{13}$$

Solutions are found by letting

$$z = p2\alpha = (x+iy)2\alpha \tag{14}$$

The real part of z must be greater than zero to insure finite displacements as r approaches zero. For a sharp crack, $2\alpha = 2\pi$, the minimum real z is 1/2. Williams (1952) gives the minimum real z for a wide range of α values. For $2\alpha > \pi$ the minimum real z is less than unity which leads to singular stresses and strains at the notch tip.

A similar analysis, called the HRR model, was carried out by Hutchinson (1968a,b), Rice and Rosengren (1968) for a sharp crack in a power hardening material behaving in accordance with the deformation theory of plasticity. The tensile stress-strain relation is of the form

$$\varepsilon = \sigma + \alpha\sigma^n \tag{15}$$

where stresses and strains are normalized on the yield stress and yield strain respectively, α is a constant, and n is the constant power hardening exponent. This transforms into the generalized stress-strain relation

$$\varepsilon_{ij} = (1+\nu)s_{ij} + \frac{(1-2\nu)}{3}\sigma_{pp}\delta_{ij} + \frac{3}{2}\alpha\sigma_e^{n-1}s_{ij} \tag{16}$$

In order to guarantee their validity solutions must be checked so that no unloading takes place and that the deformation history at every point is proportional; that is, the stress components remain in a fixed proportion to one another, or nearly so, as deformation proceeds. The analysis is analogous to the Williams solution to the elastic problem except for the material relationship. In terms of strains the compatibility equation may be written as

$$r^{-1}\,(r\varepsilon_\theta)'' + r^{-2}\,\ddot{\varepsilon}_r - r^{-1}\,\varepsilon_r' - 2r^{-2}\,(\dot{\varepsilon}_{r\theta} r)' = 0 \qquad (17)$$

where the superscripts $'$,$\cdot$ denote differentiation with respect to the radial and tangential coordinates respectively. Using (16) stresses are substituted for the strains in (17) and then stresses are replaced with their representations in terms of the Airy stress function. The elastic contribution is dropped from the compatibility equation because near the crack tip its influence is insignificant compared to the plastic contribution due to the strength of their respective singularities. Assuming a separation of variables solution for the stress function, $kr^s f(\theta)$, the problem is solved using numerical techniques. It is found that the characteristic singularity of the problem is dependent only on the power hardening exponent of the material

$$s = \frac{2n+1}{n+1} \qquad (18)$$

This leads to the following exponential r dependence for displacements, stresses, and strains

$$\frac{1}{n+1}\,, \quad \frac{-1}{n+1}\,, \quad \frac{-n}{n+1} \qquad (19)$$

Strain energy density is inversely proportional to r, the same as for the elastic problem. No corresponding plastic analysis has been done on the notch problem ($2\alpha < 2\pi$).

C. Plastic Singular Elements

A number of analysts have incorporated the HRR theory into finite element solution techniques. Hilton and Hutchinson (1971) and Goldman and Hutchinson (1975) use roughly the same method. A singular circular core element surrounds the crack tip. Displacements within this element are of the form

$$u = K r^{\frac{1}{n+1}} f(\theta) + C \qquad (20)$$

where K is an unknown amplitude, $\frac{1}{n+1}$ and $f(\theta)$ give the "correct" exponential and angular response from the HRR theory, and C accounts for rigid body motion. The size of the singular element is 2.5% of the crack length (half crack length in center cracked geometries). Outside the singular core region conventional constant strain triangular elements are employed. The solution is found by minimizing the potential energy with respect to the unknowns K, C, and the nodal displacements of the constant strain triangles that are not on the singular core. This leads to a nonlinear system of equations which is solved iteratively.

Tracey (1973) also imbeds the power law hardening singularity in sectors of core elements. But the angular variation in these elements consists of degrees of freedom rather than assuming the prescribed HRR field. Isoparametric quadrilateral elements surround these singular elements which enables compatibility but not traction continuity to exist between the two element types. The problems are solved in an incremental manner using a minimum potential energy variational principle and an iterative scheme which allows convergence to the best representative constituitive relation for the increment.

More recent attempts using the HRR theory by Atluri, et al. (1977a,b) use finite deformation techniques. Core elements contain the $r^{\frac{1}{n+1}}$ singularity but the θ variation is approximated in the usual sense of the finite element method. Surrounding the singular elements are regular eight-node isoparametric quadrilateral elements. Compatibility of displacements and continuity of tractions between singular and regular elements are enforced by means of Lagrangian multipliers. An incremental finite element analysis is employed where the stiffness matrix is updated

at each step to account for both material and geometric changes. The stiffness equations are obtained by a variational principle based on the most recent geometry.

All of these previous methods embed a singularity that remains constant throughout the loading process. The singularity is the one associated with a power hardening material as predicted by the HRR analysis. No attempts are made to explain how the material goes from an elastic response as characterized by Williams to the HRR behavior. SPECEL's formulation is such that it is not restricted to purely power hardening materials and it is able to describe the process in going from an elastic to a plastic material characterization.

A parameter frequently used in fracture mechanics is the J integral

$$J = \int_{\Gamma} W dy - t_k \frac{\partial u_k}{\partial x} ds \qquad (21)$$

where Γ is a counterclockwise path encircling the crack tip, W is the strain energy density, t_k and u_k represent the traction and displacement components, (x,y) are the usual cartesian coordinate directions with the origin at the crack tip (x is aligned with the crack, y perpendicular to it), and s is the variable of integration along the path Γ. J has been defined by Rice (1968) and Knowles and Sternberg (1973) based on infinitesimal and finite deformations respectively. Both definitions show J to be path independent for elastic materials and those with a power-law stress-strain curve and behaving according to the deformation theory of plasticity. Atluri's work compares the difference in these two J definitions numerically for three point bend specimens. He finds that J is virtually path independent when using the latter definition in his finite deformation program whereas the former definition of J

leads to substantial differences (16%) in the parameter depending on whether it is measured near or far from the tip. This fact should be kept in mind when the J results of SPECEL are discussed (Chapter IV).

D. SPECEL

A new approach to the singular problem at the crack tip is taken by Swedlow (1974). Rather than using an elastic or power hardening singularity the region near the crack tip is given a variable singularity. Its value is fixed at 1/2 for the elastic (first) step and then found by minimizing the energy-like functional, (8), for the remaining load steps. The initial formulation used two singularities, one each for the radial and tangential displacements. But due to a number of reasons, the most crucial being that the development is not coordinate system independent, only one singularity is now used.

The special element consists of a number of sectors centered at the crack tip; the optimal number is around 48 for a problem with no symmetry. This arrangement is shown in Fig. (2). Incremental displacements, radial and tangential respectively, have the following form:

$$\delta u_r = A_1(\theta) + A_2(\theta)r + A_3(\theta)r^p$$

$$\delta v_\theta = B_1(\theta) + B_2(\theta)r + B_3(\theta)r^p \qquad (22)$$

where the amplitudes of $A_1(\theta),\ldots,$ are to be determined;* A_1 and B_1 represent rigid translations; the remainder of the expressions admit constant strains as well as rigid rotations; p is a variable exponent. The special element is surrounded by constant strain triangular elements. So there is an incompatibility and discontinuity of tractions at the

*the complete form of $A_1(\theta),\ldots$ is given in the addendum (page 177).

interface of the special and regular elements. However, it will be shown that these irregularities are not critical.

Let Π represent the sum of the energy-like terms (8) from both element types, special and regular.

$$\Pi = \Pi_s + \Pi_r \tag{23}$$

Solving the problem requires the minimization of Π with respect to the degrees of freedom

$$d\Pi = (\partial\Pi/\partial\{\delta u\})d\{\delta u\} + (\partial\Pi/\partial p)dp = 0 \tag{24}$$

where $\{\delta u\}$ represents the vector array of all the nodal degrees of freedom (in all the elements). Attempting to solve this system of equations in a straightforward manner would be quite expensive due to the nonlinear nature of the equations caused by the variable exponent. A sufficient condition for the solution is

$$\begin{aligned} &\partial\Pi/\partial\{\delta u\} = [K]\{\delta u\} - \{\delta T\} = 0 \\ &\Pi_s = \text{minimum w.r.t. } p \end{aligned} \tag{25}$$

The first of these represents the usual stiffness equations and is a set of linear algebraic relations, whereas the second expression in (25) is a nonlinear equation. Both relations in (25) must be satisfied simultaneously.

Actually, SPECEL does not solve these equations simultaneously but uses an iterative procedure to find the minimum of Π. Its scheme for a particular increment, the kth, may be outlined as follows. First, p is set equal to the value of the previous increment, p_{k-1}, and while keeping this value fixed the stiffness equations are set up and solved. The value of Π is noted. Call it Π_1. Then Π_s is minimized with respect

to p. This is done by searching the range of p's in the vicinity of p_{k-1} until a minimum value of Π_s is found. The new p is p_k. Now the stiffness equations are reformulated and solved again using p_k. The new value of Π is denoted Π_2. If

$$\frac{|\Pi_1 - \Pi_2|}{\Pi_1} < \Delta$$

where Δ is some convergence criterion (set to 0.001 for elasto-plastic problems) then the increment is completed and a new increment of load may be applied. If the change in Π's is greater than the convergence criterion the process is repeated until a minimum of Π is found that meets the requirements. A flow chart for the procedure may be seen in Fig. (3).

SPECEL uses infinitesimal strain theory. Hence, the definition of J used is the one given by Rice (1968). Integration within the special element is carried out numerically by Gaussian techniques (seven radial and three tangential points in each of the twenty-four sectors). Although this method is not exact for singular functions the large number of points gives good results. It is not possible to use a one point, exact integration method for singularities proposed by Tracey and Cook (1977) because the exponent is not predetermined. Other procedures used by SPECEL follow conventional methods for solving incremental elasto-plactic flow problems as given by Swedlow (1973). More detailed information about SPECEL can be found in Swedlow (1974).

E. Accumulated Exponents

Although the incremental exponent, p, provides a sophisticated model near the crack tip it is not directly comparable to the singularity presented in the HRR model (18). One characterizes incremental quantities, the other describes total or accumulated values. For this reason a companion program to SPECEL has been developed to determine the exponent associated with accumulated displacements. The method fits the displacements within the special element at a fixed angular position into the following form

$$u = \sum_{i=1}^{N} \delta u_i = \sum_{i=1}^{N} \left(A_{1i} + A_{2i} r + A_{3i} r^{p_i} \right) = C_1 + C_2 r + C_3 r^{p^*} \qquad (26)$$

where N is the number of increments, $A_{1i},\ldots,C_1,\ldots$ are constants for fixed θ, p_i are the incremental exponents, and p^* is the accumulated exponent. There is no proof that the form of the accumulated displacements is correct but in view of the incremental form it looks intuitively correct. (This intuition is supported in the results, discussed in Chapter IV.)

For each angular position the seven Gauss points within the special element are used to determine the unknowns C_1, C_2, C_3 and p^*. In fact, C_1 is already known since it represents the rigid translation of the node at the crack tip. Therefore, for any one of the seven Gauss points the displacement u_j (j=1,7) is

$$\frac{u_j(r_j) - C_1}{r_j} = C_2 + C_3 r_j^{p^*-1} \qquad (27)$$

where all the information on the left side of the equation is known. Note u is a function of r only since θ is fixed. Let $y_j = r_j^{p^*-1}$, then

$$F(y_j) = C_2 + C_3 y_j \tag{28}$$

Assuming values for p* gives values of y_j and C_2, C_3 may be found through linear regression techniques. The closeness of the fit of SPECEL's displacements to the predicted curve is expressed by the coefficient of determination. This parameter ranges from zero to one, one being a perfect fit. Appropriate values of p* are chosen until the coefficient of determination is maximized, thus providing the best fit of the data. Hence, p* is the accumulated exponent and may be compared directly with HRR results.

This method may be used for finding exponential values for any parameter that can be expressed in the following form:

$$KV(r) = a + br^s$$

where KV represents known values of the parameter as a function of r, a and b are the regression coefficients to be determined, and s is the exponent to be found by maximization of the coefficient of determination. More details of the procedure for accumulated displacements are given in Appendix A.

The purpose of this chapter has been twofold: (1) to provide motivation for and (2) to describe SPECEL. In discussing the Williams and HRR analyses as well as the numerical models based on these theories, hopefully a need has been demonstrated for a more critical look at the problem. The description of SPECEL has been intentionally brief. Emphasis has been given only to the new aspects of the program. With this background information the reader is in a position to appreciate the problem selection and discussion presented in the next two chapters.

CHAPTER III

TYPES OF PROBLEMS SOLVED

A. Preliminary Problems

Before describing in detail the problems whose results constitute the bulk of this work a word about the early test problems of SPECEL is in order. The initial checks of the code were performed by Swedlow (1974). It was found that using twenty-four special element sectors gave the most reasonable results in terms of compatibility with surrounding regular elements and time required for solution.

For elastic problems, with the exponent preset to 1/2, center cracked panels subject to uniform tension and a pure K_I loading were studied. For the case of uniform tension a crack length/ligament length ratio of 1/2 gave an average J, which, when converted to K_I, was

$$K_I = 3.12 \bar{\sigma} \sqrt{a}$$

where $\bar{\sigma}$ is the applied stress and a is the half crack length. The coefficient of variation* of K_I over the seven J paths of the special element was 0.9%. This underpredicts the conventional stress intensity of

$$K_I = 3.17 \bar{\sigma} \sqrt{a}$$

given by Brown and Srawley (1966) by about 1.5%. For the case where pure K_I displacement loading was applied at the boundary nodes the numerical K_I result overpredicted the analytical result by 2.41%. The

*The coefficient of variation is the standard deviation divided by the mean.

amount of error was reasonable for both problems and the sign of the error was typical of finite element results. Namely, displacement loadings overpredict stresses and traction loadings underpredict stresses due to the fact that finite elements are stiffer than the continuum they represent. Further discussion and results are presented in Swedlow (1974).

A series of problems has been run to observe initial plastic response and determine the size of the special element to be used. The specimens are center cracked panels with a crack length/ligament length ratio of 1/2 and the loading is uniform extension. (A fuller description of this problem is given under the A533B STEEL problem headings.) The radius of the special element is either 1/16, 1/32 or 1/64 of the half crack length. Finite element maps for these problems can be seen in Figs. (4-6). Only one quarter of the specimen is modelled due to two degrees of symmetry along x=0, y=0. The special element and surrounding regular elements are shown in Fig. (7). Each near tip finite element map has the same shape but varies in size by successive factors of two.

All three problems are loaded for ten increments. The first is the elastic response and by step ten a small amount of plasticity has spread through the special element. The following results show the stiffness and J values (measured at the seventh and largest path in the special element) for the three cases:

	$P/E\delta$		
	a/16	a/32	a/64
Step 1	0.822	0.822	0.824
Step 10	0.822	0.824	0.824

	$Jh^2/E\delta^2a$		
	a/16	a/32	a/64
Step 1	2.64	2.51	2.39
Step 10	2.65	2.52	2.40

δ is the applied displacement, P is the resulting applied force, and h is the half specimen length. The maps with larger special elements exhibit slightly more compliance. Also, J values and, hence, stress and strain intensity factors are smaller for smaller special elements. This seems to indicate that both the overall and near tip maps are less stiff when larger special elements are used. This is due to the fact that maps using larger special elements have more of the continuum represented by a less stiff element than the regular constant strain triangles.

However, stiffness is not the primary reason for selecting a special element size. The dominant singularities of the Williams' and the HRR analyses are valid in regions near the crack tip. Taking too large a special element may force the singularity in SPECEL to accommodate more information than is intended.

Also, the results in the special element are somewhat suspect as the boundary of the yield zone moves through it to the regular elements. This is due to the fact that one exponent must handle both an elastic and plastic response. It has been argued in Brown and Srawley (1966) that K resulting from linear elastic fracture mechanics is valid so long as the plane strain plastic zone correction, r_y, is less than a/50. Therefore, it is desirable to keep the size of the special element smaller than r_y so that linear elastic fracture mechanics would be valid as yield spreads to r_y. Again this points to the a/64 model. Another reason for selecting the a/64 is that it gives results

closer to the crack tip. Hence, despite its stiffness, the a/64 special element model is used for problems involving extensive yielding.

B. Singularity as a Function of Notch Opening Angle

In addition to testing out the special element for plastic analyses a series of elastic problems has been devised to determine SPECEL's response to notch opening angle. The analytical work was done by Williams (1952) and gave the result

$$\sin[p2\alpha] = p \sin 2\alpha$$

where $2(\pi-\alpha)$ is the notch opening angle and p, a function of α only, is the exponent of the leading radial term of the Airy stress function $\chi(r,\theta)$ where

$$\nabla^4 \chi = 0$$

assuming

$$\chi = r^{p+1} f(\theta)$$

Displacements are on the order of r^p ($p>1$ for finite displacements at the tip), and stresses and strains behave like r^{p-1}. For α equal to π a straight crack exists and $p = 1/2$.

A finite element map for a zero notch angle is shown in Fig. (8). Only half the specimen is shown due to symmetry at $y = 0$. In order to develop a specified notch angle all the points are rotated about the crack tip towards the symmetry line ahead of the tip - the symmetry line remains fixed. This method increases the aspect ratios of the finite elements and also the angular resolution.

An arbitrary elastic modulus and Poisson's ratio are supplied as elastic material parameters. Loading is in the form of a vertical

nodal extension of node A. Although symmetry is enforced throughout this problem Williams' result only requires a symmetrical notch and no loading on the notch faces. Results of these test cases are presented in Chapter IV.

C. Power Hardening Material (PH)

This section describes the set up for the elasto-plastic solution of a center cracked specimen with power hardening material characteristics. The chief reason for selecting such a problem is that it may be compared with the HRR theory. Principally, the distinguishing feature of SPECEL, the variable (accumulated) exponent, should agree with the HRR model at some point in the loading process provided certain criteria are met. Also, there may be a direct comparison with the stresses (Hutchinson, 1968a,b) as well as J values and crack opening profiles (Goldman and Hutchinson, 1973).

The geometry and the finite element map for one quarter of the specimen (due to two degrees of symmetry) can be seen in Fig. (9). In order to insure insensitivity to the vertical dimension a length to width ratio of three has been chosen. The crack length is one half the specimen width. As stated earlier, the special element size is a/64.

In the finite element map one special element with twenty-four sectors is used in conjunction with 228 regular elements. There are 173 nodes and 347 degrees of freedom, two degrees for each node plus one exponent. The band width is fifty-six.

Tractions are applied to the upper boundary perpendicular to the plane of the crack to achieve a uniform tensile load. The direction of the tractions is fixed while the magnitude is increased three percent

of the previous accumulated value for each increment. On the remainder of the boundary the tractions are always kept at zero. Since the direction of the tractions is fixed while their magnitude is everywhere proportional to a single load parameter, the stress at each point in the body also should vary linearly with the load parameter, provided $\varepsilon_{ef} = \alpha\sigma_e^N$ where α and N are constants. This was shown first by Ilyushin (1946) and restated by Goldman and Hutchinson (1976). Ilyushin then points out that the solution is rigorously correct for both deformation and incremental plasticity theories. It will be shown below that although the tractions are linearly proportional to a single parameter, the stresses, particularly near the tip, are not in proportion to this parameter. Keep in mind, however, that the stress-strain relationship used by SPECEL is different than the one described by Ilyushin.

Defining a stress-strain curve proves to be somewhat of a problem. Hutchinson (1968a) ignores the elastic contribution. He argues that near the tip the plastic terms dominate due to the plastic singularity. However, in the SPECEL formulation it is impossible to neglect the elastic component. In the HRR theory an octahedral stress-strain curve of the form

$$\frac{\varepsilon^p}{\varepsilon_L} = \alpha \left(\frac{\tau}{\tau_L}\right)^n$$

is employed, where τ and ε^p are the octahedral stress and plastic strain quantities, respectively; ε_L and τ_L are the octahedral quantities at yield and related by $\varepsilon_L = \tau_L/2G$, where G is the shear modulus; α is some constant and n is the constant strain hardening exponent ($n \geq 1$).

After some consideration it was decided that the stress-strain curve to be used in SPECEL should have the form

$$\frac{\varepsilon}{\varepsilon_L} = \frac{\tau}{\tau_L} \qquad \text{for } \tau \leq \tau_L$$

$$\frac{\varepsilon}{\varepsilon_L} = \left(\frac{\tau}{\tau_L}\right)^n \qquad \text{for } \tau > \tau_L$$

where ε is the total octahedral strain; τ, ε_L, τ_L are the same quantities as in the HRR model; for this case α has been set to one and n is three. For a given state of stress both the HRR and SPECEL analyses consider the same area under the stress-strain curve. The SPECEL formulation is not quite the same as the HRR model, but by including an elastic response it is a more realistic representation.

Elastic numerical constants have been selected to keep the elastic contributions small. The octahedral yield stress is 1000 psi which converts to a tensile, or effective, yield stress of 2121 psi. Poisson's ratio is 0.3 and the elastic modulus is 1×10^7 psi. This gives an octahedral strain of less than 0.0003 at yield. Besides keeping the elastic contributions small, these constants enable quite a bit of loading before finite deformations become important.

D. Bilinear Material (BIL)

This problem is identical to the PH problem with the exception of a different stress-strain curve. It is a pseudo bilinear curve where a smooth curve joins the two linear portions of the curve. A bilinear curve has been chosen because it can be compared directly to analytical work done by Hutchinson (1968a) which is independent of the analysis for power hardening materials.

The two linear portions of the BIL curve as well as the PH curve can be seen in Fig. (10). In the next figure the small strain region which includes the transition between the two linear regions is shown.

Both BIL and PH problems have the same elastic constants. The second linear segment of the BIL curve has been chosen such that it closely approaches the PH curve in the region of critical loading. This region of critical loading, $2.0 \leq \tau/\tau_L \leq 5.0$, has been determined after analysis of the PH problem. Most Gauss points in the special element are in this range between net section yield (yield extends from the crack tip to the outer boundary) and gross yield (applied stress exceeds yield stress). So the second linear portion of the BIL curve is found by merely running a straight line through the points of the PH curve where τ/τ_L equals two and five. The slope of this second linear segment is 2.5% that of the elastic line.

As stated above the two linear portions of the bilinear curve are joined by a smooth curve in the region $1 \leq \tau/\tau_L \leq 2$. This curve is drawn such that continuity of the stress-strain curve and its first derivative is maintained as nearly as possible at the curve's intersection with the two linear portions. Attempts at meeting these requirements analytically have not been successful. The reason that such a curve is necessary is that a strict bilinear curve could lead to a significant overshooting of the stress-strain curve when a point yields initially or a very costly analysis would be necessary to turn the corner sharply.

E. A533B STEEL (RS)

This problem also involves a center crack panel but with different geometry, loading, and material properties than the previous two. Actually, it was the first problem in the sequence and was used as a test case in comparison with another numerical result, Riccardella and Swedlow (1973). This problem affords the opportunities to use a real

stress-strain curve and to compare with actual laboratory results.

The finite element map for one quarter of the problem (two degrees of symmetry) is shown in Fig. (12). The dimensions of the specimen agree with the subsized finite element map used by Ricardella and Swedlow. This subsized model has been developed to avoid the complexities of the pin loaded, center cracked specimen used in the laboratory. The upper boundary of the subsized model is a region of uniform displacement. Dimensions for the problem analyzed by SPECEL are as follows: half height - 1.75 in.; half width - 1.5 in.; half crack length - 0.5 in. The special element is embedded in a map with 232 regular elements. There are 174 nodes, 350 degrees of freedom (two for each node and two exponents), and the band width is 56.

Loading is imposed by uniform vertical displacement along the upper edge. The sides are traction free. Increments of load are five percent of the previous accumulated applied displacement.

Tensile stress-strain relations are shown in Riccardella and Swedlow (1973), p. 136. The actual curve exhibits a yield point instability which cannot be handled numerically. So the curve used in SPECEL is the dashed curve in the same figure. The tensile yield stress is 60,000 psi, which converts to 28,284 psi in octahedral quantities. Young's modulus is 3.158×10^7 psi, and Poisson's ratio is 0.3.

F. Task Group - Round Robin (Bend)

The final problem in the sequence has been proposed by the E-24 Task Group of ASTM. It is a three point bend problem. A number of analysts have solved this problem using various finite element techniques. Solving such a problem invites an evaluation of SPECEL with other in-service programs. This type of problem also offers a different

geometry not seen in the previous problems.

A finite element map of the specimen is shown in Fig. (13). Due to the symmetry of y=0 only half of the problem is modelled. Displacement at node A is applied in the horizontal direction. Node B is held fixed and the remainder of the boundary is traction free. Displacement increments are no more than five percent of the previous accumulated load.

Two hundred thirty-six regular elements serve as host to the special element. There are 174 nodes, 349 degrees of freedom (only one exponent), and the band width is 56. The specimen half length is two inches, its width is one inch, and the crack length is one-half inch.

The uniaxial (effective) stress-strain curve is of the form

$$\varepsilon = \sigma/E \qquad \text{for } \sigma < \sigma_y$$

$$\varepsilon = \frac{\sigma}{E} + \left(\frac{\sigma}{B_0}\right)^n \qquad \text{for } \sigma \geq \sigma_y$$

where $E = 3.158\times10^7$ psi

$B_0 = 1.20\times10^5$ psi

$\sigma_y = 3\times10^4$ psi

$n = 10$

Poisson's ratio is 0.3. Effective quantities are converted to octahedral quantities for use in SPECEL. This problem has the least amount of strain hardening of the four considered. Little plastic strain occurs until σ exceeds $2\sigma_y$.

These four problems will serve as the basis for the evaluation by SPECEL of the elasto-plastic flow process. The power hardening and bilinear problems provide a comparison with the HRR theory. A chance to study a real material with actual laboratory data is offered by the A533B steel. SPECEL's numerics can be compared with other computational methods in the Task Group problem. With this carefully selected problem set the analyst is in a position to pose questions regarding material and geometric effects in elasto-plastic flow. This is done in the next chapter.

CHAPTER IV

DISCUSSION OF THE RESULTS

A. Notched Disks

SPECEL's ability to determine the elastic singularity as a function of notch angle is shown in Fig. (14). The displacement exponent, p, is plotted against the angle of the notched disk, 2α, and compared with the analytical Williams solution. Each point representing SPECEL's result is actually the average of four values. These four values of p are found through the minimization procedure and for each of the four the minimization begins at a different guess for p which is within ±10% of the analytical value. The coefficient of variation for the final four p values is less than 2%. In order to obtain this agreement among the final values it is necessary to tighten the convergence criterion of the minimization process (see Chapter II) from 10^{-3} to 10^{-6}. This tightening is a result of the large scatter in initial guess for p. For the elasto-plastic problems the initial guess is much closer to the desired value since the increments are so small. Hence, the 10^{-3} convergence criterion is acceptable.

SPECEL's prediction for the exponent is consistently about 4% less than the analytical values. A contributing factor for this deviation is that the size of the special element is 5.2% of the notch depth. When the relative size of the special element is reduced to less than 2% of the notch depth by using the geometry of any of the elasto-plastic problems for a straight crack (PH,BIL, etc.) SPECEL's p value is within 3% of the analytical value. In view of this and the

fact that the initial guess for the exponent for each increment of the elasto-plastic problems is close to the "true" value a high degree of confidence is placed in SPECEL to select the best exponent for these problems.

B. Power Hardening Material (PH)

One of the reasons for studying this particular problem is to compare SPECEL's exponential response at high loading with the HRR theory. Of course, some transition from elastic to plastic is to be expected. Figure (15) shows the response of the incremental displacement exponent versus the applied load. It begins at the preset elastic value of 0.5 and then drops sharply until yielding exceeds the special element (applied stress, $\bar{\sigma}$, is 0.16 times the tensile yield stress, σ_y). After levelling off for a time the incremental exponent reaches a minimum at $\bar{\sigma}/\sigma_y = 1.09$ before increasing. This increase is accompanied by two other events which may explain the unexpected rise. First, since there is so much yielding near the tip the small strain theory used in SPECEL no longer may be applicable for this region. McMeeking and Rice (1975) argue that small strain theory breaks down when the tangential modulus ($2\mu_0^p$) of the material is comparable to the magnitude of the stresses. Up to $\bar{\sigma}/\sigma_y = 1.09$, $2\mu_0^p$ is greater than stress levels at all Gauss points, but for higher loads the near tip Gauss points have stresses that exceed $2\mu_0^p$. The second possible explanation of the exponential increase may be that the Gauss points have yielded so much that they have exceeded the limits of the inputted stress-strain curve. These points are using an approximate extension of the stress-strain curve. Results show that points using this extension technique have difficulty following the desired curve.

Figure (16) shows the accumulated exponent for selected steps.

These steps are: step 1 (elastic response), step 60 (yield exceeds the special element), step 115 (net section yield, NSY), and step 125 (applied stress exceeds tensile yield stress). As described in Chapter II the accumulated displacements are put into the form

$$u = a + br + cr^{p^*}$$

where p^* is the accumulated exponent. Results for both the radial and tangential displacements are shown.

As expected the elastic step shows exact agreement between incremental and accumulated exponents. When yield first exceeds the special element there is some θ dependence in p^* as well as some spurious results for small and large θ values. From the point of net section yield there is a nearly constant p^* and very good agreement with the HRR prediction.

A comment about the accuracy of this accumulated exponent method is in order. The coefficient of determination for all of the points except two in Fig. (16) is 1.000000. This accuracy indicates that the accumulated displacement form is suitable for summing the incremental displacements. The two points which are the exception are the first two θ values of the tangential exponent at step 60. These points have a coefficient of determination of 0.998 which may explain their curious behavior.

An average p^* is computed for a number of steps by averaging six p^* values for tangential displacements near 90° (56°, 71°, 86°, 94°, 109°, and 124°). These values typify the response for the whole element and show the most constant p^* for all load levels. This average p^* is plotted in Fig. (17) as a function of the applied load. The transition

from elastic to HRR response is clearly seen although the rate slows considerably for $\bar{\sigma}/\sigma_y > 0.2$. The deviation from the HRR prediction for large loads corresponds to the rise in the incremental exponent and may be explained by the same reasoning.

An attempt at characterizing the strain energy density exponent is shown in Fig. (18). Accumulated values of the energy density for the seven radial positions of the Gauss points for a fixed θ are fitted to the form

$$W = A + Br^{s^*}$$

where A and B are constants and s* is the strain energy density exponent. The A term is included to account for the T effect (Larsson and Carlsson, 1973) of the stresses. Both elastic and HRR theories predict a value of minus one for this exponent. The results show reasonable agreement with this prediction except for small and large θ. For some large θ values no value of s* is found within the range shown. All except two of the plotted points have a coefficient of determination of 0.99997 or greater. It seems that the form used to pick off the energy exponent is not as suitable as the one for displacements, and for small and large θ perhaps an entirely different form should be used.

In addition to the exponential response, stresses also may be compared with the HRR theory. Figures (19-23) plot various stresses at fixed angular positions versus the radial position for a number of load levels. The purposes of these graphs are to see how far in the radial direction the HRR singularity dominates and to determine which radial position offers the best comparison with HRR stress results. The normalizing factor in all these graphs is the maximum effective

stress. This maximum is found for each r value in the range $0° \leq \theta \leq 180°$. Also shown on the plots are the HRR prediction from the first term of the Hutchinson eigenanalysis and the elastic prediction from the first two terms of the Williams eigenanalysis. The first term of the Williams solution is taken from Tada, et.al. (1973) and the second term is from Larsson and Carlsson (1973).

Figure (19) shows the radial stress at $\theta = 3.75°$ (measured from the line of symmetry ahead of the crack tip). The HRR prediction is constant with respect to r because for a one term solution the singularity in the stresses is normalized out by $\sigma_{e\ max}$ term; whereas in the two term Williams solution the r dependence cannot be totally negated. SPECEL's results for the elastic step are quite good and pick up the effect of the second term. As the transition to HRR takes place the closest Gauss point (r/a = 0.0004) exhibits erratic behavior. The second Gauss point comes the closest to the HRR prediction while the rest of the points trail off, perhaps indicating the effect of a second term. At $\theta = 93.75°$, Fig. (20), there is little difference between the elastic and HRR predictions. Again the first Gauss point deviates from the theory but all of the other points show reasonable agreement with the HRR value at high loads.

Tangential stress for both θ values is shown in Fig. (21). The nearest Gauss point for both θ values must be regarded with suspicion. At $\theta = 3.75°$ there is a clear transition from elastic to the HRR prediction for the last six Gauss points. At 93.75° the transition is not that good but again the second Gauss point comes the closest to the HRR value.

Figures (22,23) show the effective stress at 3.75° and the shear stress at 93.75°. Both these plots show good elastic agreement for all radial positions but the Gauss points nearest the tip, excluding the first, compare best with the HRR theory.

From these plots it can be seen that results for the first Gauss point are often erratic, much like regular finite elements nearest the tip. For some stresses and angular positions the HRR prediction dominates the entire special element while for other values SPECEL's agreement with the HRR theory trails off with increasing distance from the tip. Keep in mind that the HRR solution is asymptotic in r. Based on these observations the complete stress field at the second Gauss point (r/a = 0.002) from the tip is presented in the next figures.

The effective stress is shown in Fig. (24) for the same load levels described for Fig. (16) with the addition of a load step with a very high applied stress ($\bar{\sigma}/\sigma_y = 1.7$). (Note that $\hat{r} = 1/2$ r/a.) There is very good agreement with the elastic prediction for all angular positions. As stated previously, the theoretical elastic result comes from the first two terms of the Williams analysis. SPECEL gives $\sigma_{e\ max}$ at 86.25° and the theory predicts $\sigma_{e\ max}$ between 80° and 90°; it is nearly constant in that range. The minimum that occurs before 180° is a result of including the second term of the eigenseries. Its effect is to cause the radial stress to be zero at the θ value corresponding to the minimum effective stress rather than at 180°.

As loading proceeds $\sigma_{e\ max}$ drops to 71° but moves back to 93° at $\bar{\sigma}/\sigma_y = 1.7$. The HRR prediction for $\sigma_{e\ max}$ is at 95°. For θ greater than 90° fairly good agreement exists between SPECEL and the HRR theory, including the value along the crack flank. For angles less than 90° the numerical results overpredict the analytical results.

In Figs. (25-27) the individual stress components are presented for the same five load levels. The radial stress in Fig. (25) shows good agreement with the elastic theory and then a slow progression toward the HRR prediction takes place. At $\bar{\sigma}/\sigma_y = 1.7$ quite a bit of instability in the results is present. This probably indicates that this loading range is at or exceeds the credibility limit of SPECEL for this problem. It is interesting to note that for $\theta > 135°$ there is not much deviation from the elastic prediction for all load levels. This is probably due to the fact that yield progresses most slowly in this region.

Similar trends can be seen in Fig. (26) for the tangential stress. A good elastic response, a slow transition to the HRR prediction, and quite a bit of instability at the fifth load level are common to both normal stresses. The pattern of the shear stress, Fig. (27), is somewhat different. Although the elastic agreement is good the transition to the HRR result is not as observable. SPECEL's peak shear stress occurs at a smaller θ value than the HRR prediction. And the shear stress does not approach zero near the crack flank ($\theta = 180°$). But on the whole the stresses demonstrate a clear transition from an elastic state to one closely resembling the HRR prediction.

Another comparison with the HRR theory is presented in Fig. (28). Both the Hutchinson and the Rice-Rosengren results are shown. The maximum shear angle* is plotted against the angular position around

*The maximum shear direction is found by first using the cartesiam components of stress to construct the Mohr circle. The angle between the smaller principal stress, the center of the Mohr circle, and the point (σ_x, τ_{xy}) - measuring the angle positive clockwise from the smaller principal stress - represents the principal stress direction. Add 90° to this angle to obtain the angle representing maximum shear. Then, take one-half of this value to get the true maximum shear direction (one-half is needed because the Mohr circle angular measurement is twice the true angle).

the crack tip. SPECEL's results are shown only for $\bar{\sigma}/\sigma_y = 1.09$ although the pattern holds (±2°) for $\theta < 135°$ at an applied stress of $0.52 \leq \bar{\sigma}/\sigma_y \leq 1.26$. Again, the discrepancy with the HRR theory occurs for large θ values.

Now that the shape of the stress field has been presented, its amplitude, in terms of J, is studied. Figure (29) plots normalized J as a function of the effective radius of the J path, $\hat{r}$, measured from the crack tip. The definitions of Y and the effective radius are given in the figure. Two striking observations are noticeable. Between the second and third load steps presented Y deviates from the elastic or small scale yielding results (Y is constant as a function of load for small scale yielding). And between the same two load steps a significant deviation in Y as a function of $\hat{r}$ is apparent. From Rice's analytical results (1968) it has been shown that J, and hence Y, is independent of $\hat{r}$ for elastic materials and those behaving according to the laws of deformation plasticity. For the elastic response SPECEL shows a small deviation in Y. The coefficient of variation for the eleven Y values in the figure is 3.5% and for J it is 6.0%. But at the time when $\bar{\sigma}/\sigma_y = 1.09$ the coefficient of variation for Y is 18.2% and for J it is 37.4%. These results indicate that at sufficient loading J is no longer path independent.

Figure (30) follows up on the first of these observations. The plastic strain intensity (defined in the figure) is plotted as a function of the applied load. Deviation from small scale yielding occurs in the range $\bar{\sigma}/\sigma_y = 0.6$. This compares favorably with the results of Hilton and Hutchinson (1971).

The more startling observation shows that J is path dependent. An explanation of this phenomenon is lengthy. Goldman and Hutchinson (1975) argue that as a result of Ilyushin's work (1946) J is proportional to $\bar{\sigma}^{n+1}$ ($\bar{\sigma}$ is the applied stress, n is the power hardening exponent) for a body loaded such as this one (traction loaded, loading direction fixed, magnitude of traction proportional to a single parameter). The result of $J/\bar{\sigma}^4$ (n=3 for this problem) versus applied load is shown for J paths outside the special element in Fig. (31). From the point of net section yield ($\bar{\sigma}/\sigma_y = 0.81$) the paths furthest from the special element exhibit a relationship of the form

$$J \propto \bar{\sigma}^4$$

to within ±10%. For the paths nearer the special element this relationship breaks down. This seems to indicate that far field J results might be following deformation theory.

This indication is confirmed in the next figure. Y values, normalized on the elastic average, for near and far field J paths are plotted versus applied load. The near field Y value represents an average for three J paths within the special element and the far field Y value is the average for three J paths far from the special element. Superimposed on these results are the elastic prediction from Tada, et al. (1973) and deformation theory results from Goldman and Hutchinson (1975). The far field Y value follows the small scale yielding (elastic) prediction until $\bar{\sigma}/\sigma_y = 0.6$ at which point it begins to follow the deformation theory prediction, showing agreement to within 15%. The near field Y value shows a deviation (7%) from the small scale yield result at low loads ($\bar{\sigma}/\sigma_y < 0.6$). For higher loads Y_{near} increases but does not approach the deformation theory prediction.

Why the path dependence in J?

One possible reason may be found by examining the near and far field stress results. A sufficient condition for deformation theory to work (Ilyushin, 1946) is that all stresses increase in proportion with a parameter, in this case, the applied load. It can be seen from Figs. (25-27) that the shape of the near field stresses is changing. A replotting of the near field stresses, this time normalized on the applied load, is shown in Figs. (33-35). There is a major redistribution of the initial elastic response until some proportional loading pattern (or nearly proportional) is reached around net section yield.

In contrast to this behavior are the far field stresses which are plotted in Figs. (36-38). Except for a few points a proportional loading pattern is maintained for loading up to $\bar{\sigma}/\sigma_y = 1.7$.

Proportional loading is only a sufficient condition for incremental and deformation theories of plasticity to agree. The necessary condition for agreement is that the tensor of similitude remain constant during the loading process (Ilyushin, 1946). The tensor of similitude is defined as:

$$\Pi_{ij} = \frac{s_{ij}}{\sigma_e}$$

where s_{ij} and σ_e have been defined in Chapter II.

Figures (39-40) show the tensor of similitude as a function of applied load for near and far field stresses ahead of (near 0°) and above (near 90°) the crack tip. It can be seen that near the tip there is a nonconstant tensor of similitude, particularly ahead of the crack. But the far field tensor shows a constant behavior, except for some small deviations at high loads. This evidence indicates that

a proportional/nonproportional stress pattern leads to a constant/nonconstant tensor of similitude. For future problems only the proportionality of stresses will be checked to determine whether deformation theory requirements are satisfied. For this problem it is expected that far field J values agree with the deformation theory prediction. However, no such stipulations can be placed on the near field J. More discussion about J can be found in the last section of this chapter.

Figure (41) shows the crack opening profile within the special element. Results are normalized on the displacement of the Gauss point furthest from the tip. Progressive blunting can be seen up to gross yield (step 125). At higher load levels there is a resharpening of the crack shape.

The same information along the entire crack flank can be seen in Fig. (42). Again there is progressive blunting until gross yield and then a slight resharpening near the tip. SPECEL's displacement results are slightly lower than both the elastic and power hardening profiles given by Goldman and Hutchinson.

Figure (43) shows the crack mouth opening as a function of the applied load. The mouth opening is the displacement between the two crack faces at the center of the panel. There is good agreement between the two elastic predictions and SPECEL's result and after net section yield SPECEL approaches the power hardening prediction. However, the agreement is not as strong as that exhibited by the far field Y.

In summary, SPECEL shows excellent agreement with the predicted elastic results. For this power law material there is a reasonable convergence to the HRR theory as elastic strains become relatively small, but this does not occur until net section yield is approached.

The major deviation from the HRR theory is the path dependent J, which will have more discussion. But the unmistakable conclusion is that the method works.

C. Bilinear Material (BIL)

This problem is identical to the power hardening problem except for the material stress-strain curve. The four key steps (elastic, yield exceeds the special element, NSY, and applied stress exceeds tensile yield stress) are the same for the two problems.

For this case the inputted stress-strain curve is extended far enough so that yielded points never exceed the limits of this curve. Also, the tangential modulus ($2\mu_0^p$) is always substantially larger than the stresses so small strain theory is unobjectionable. Therefore, results at the final step ($\bar{\sigma}/\sigma_y = 2.28$) sometimes are presented.

Following the same order as for the PH material the exponential response will be examined first. Again, there is only one exponent. The incremental displacement exponent is plotted as a function of applied load in Fig. (44). Translating these values into accumulated numbers is done next. Accumulated exponents are computed for a few load steps. The coefficient of determination for all points is 1.000000. Results show that it is reasonable to talk of an average accumulated exponent. A plot of this average based on the same angular values used in the PH problem is given in Fig. (45). Hutchinson (1968a) predicts that the dominant plastic singularity is the same as the elastic singularity, namely, 0.5. SPECEL shows the singularity beginning at 0.5 for the elastic step, dropping to a minimum of 0.24, and then climbing towards Hutchinson's prediction. It is not clear if the accumulated exponent will eventually reach 0.5. Apparently

quite a bit of loading is necessary to reach this value. Remember that the stress-strain curve is not strictly bilinear. One interesting feature occurs in the range between NSY and gross yield (step 125) where most points in the special element have an octahedral stress of $2 < \tau_0/\tau_{Lim} < 5$. In this region the PH and BIL stress-strain curves are reasonable approximations of one another and the accumulated exponents for the two problems are very close, roughly 0.25.

Figure (46) shows the results of the energy exponent analysis. The elastic response is identical to the PH material, but the other steps exhibit a different behavior. There is reasonable agreement with the minus one prediction up to the point of gross yield. All but two of the points are within 20% of the minus one prediction and only four have a coefficient of variation less than 0.99997. The scheme seems to break down for step 150.

The stress components in the special element, normalized in $\sigma_{e\ max}$, are plotted against radial position in Figs. (47-51). All plots include the elastic prediction and the power hardening result for n=3. The bilinear and elastic predictions, with the exception of $\sigma_e/\sigma_{e\ max}$, are identical save for the second term of the elastic Williams solution. The difference occurs for $\sigma_e/\sigma_{e\ max}$ due to the fact that for elastic plane strain results

$$\sigma_z = \nu(\sigma_x + \sigma_y)$$

but for plastic results

$$\sigma_z = 1/2(\sigma_x + \sigma_y)$$

and

$$\sigma_e = f(\sigma_x, \sigma_y, \sigma_z, \tau_{xy})$$

Yielding appears to take place in two phases. First there is a shift from an elastic to a power hardening response. Recall that the Gauss points for the BIL material are in that part of the stress-strain curve that closely approximates the PH material between NSY and gross yield. Then the stresses proceed in a direction back towards the elastic results. As expected, the points nearest the tip sense this change in material behavior first. It appears that the plastic singularity dominates the stress results throughout the special element, with the possible exception of σ_r at 3.75°. Occasionally the first Gauss point exhibits erratic behavior but not to the degree of the PH material.

It seems most sensible to plot the entire stress field for the second Gauss point so that a direct comparison can be made with the PH material. Results for the effective stress, Fig. (52), are similar to SPECEL's results for the PH material. There is reasonable agreemen- with the HRR, n=3 prediction for $\theta > 90°$ at NSY. For $\theta < 90°$ both materials overpredict the effective stress. At step 150 the effective stress has moved near the elastic (not the bilinear) prediction except for large and small θ. Individual stress components are shown in the next three figures. The radial stress, Fig. (53), shows very good agreement at NSY with the HRR, n=3 prediction for $\theta < 165°$. At step 150 the results are very rough but the trend is toward the bilinear prediction. The behavior of the tangential stress component, Fig. (54), is similar to the radial stress. As in the case of the effective stress, the shear stress, Fig. (55), demonstrates good agreement with SPECEL's results for the PH material at NSY. The agreement with the HRR, n=3

prediction at NSY is only modest. Again the trend is towards the bilinear prediction at step 150 except for $\theta > 120°$. In general, the two phase transition is observable for all stresses.

J values, in the form of Y, are presented as a function of the distance from the crack tip in Fig. (56). Deviation from small scale yielding is evident at NSY and a definite path dependence in Y is present at gross yield. The deviation and path dependence are not as noticeable as for the PH material at corresponding load levels. This is due to the fact that there is little plastic strain until $\tau_0 > 1.5\ \tau_{Lim}$ in the BIL stress-strain curve. Consequently elements first yielding at NSY exhibit very little plastic response so that, in effect, NSY is delayed somewhat.

Path dependence is examined by plotting near and far field Y values as a function of applied load in Fig. (57). As with the PH material the near field value shows a decrease before NSY. Path dependence is clearly evident after NSY. However, the far field Y value does not show much resemblance to the Goldman and Hutchinson prediction for n=3. Extrapolated curves of the near and far field values are seen reaching plateaus in this figure. The Y value for an elastic material that behaves solely like the second linear portion of the BIL curve is superimposed on this figure. The far field Y value of the BIL material might reach this limit but apparently only at unreasonably high loads.

Proportionality of the near and far field stresses is examined in Figs. (58, 59) to determine causes of path dependence in J. Only the radial component is examined since the other stresses possess the same behavior. As expected, no proportional loading pattern is evident in the near field stresses, even after NSY. However, the far field

stresses exhibit proportional loading for most points; there are some shifts in the data at step 150. Hence, the tensor of similitude is nearly constant for far field values and deformation theory is acceptable. The same statement cannot be made for the near field stresses.

Crack opening profiles within the special element, Fig. (60), show a blunting of the crack tip with continued loading. But after gross yield a resharpening occurs. Figure (61) shows progressive blunting along the crank flank until gross yield. At $\overline{\sigma}/\sigma_y$ the transition back to the elastic response has spread through the near tip area while the crank flank from the tip shows agreement with the Goldman and Hutchinson n=3 results.

A direct comparison between the PH and BIL materials is made in the next series of graphs. Differences in the near field octahedral stress are plotted as a function of θ in Fig. (62). The range (maximum minus minimum) of the BIL octahedral stress at $\hat{r} = 0.001$ and corresponding load level is used as a normalization factor. Fluctuations about the line $\gamma=0$ in the figure coincide well with the relative magnitude of the two stress-strain curves for equivalent strain values. Between NSY and gross yield most Gauss points for both materials are in the range $2 < \tau_0/\tau_{Lim} < 5$ and the PH stress-strain curve has greater values. Outside this stress range the BIL curve has larger stress values at equivalent strains.

In contrast, the far field octahedral stress values, Fig. (63), shows no such pattern and the overall agreement between PH and BIL materials is much greater. Of course, the points of the far field stress pattern are either on the linear elastic portion of the stress-strain curve (which is identical for both materials) or in the region

of initial plastic yield. At the highest load level shown ($\bar{\sigma}/\sigma_y = 1.7$) the two materials do not have identical stress fields. However, the overall deviation of the far field at this load is not as great as the deviation in the near field at $\bar{\sigma}/\sigma_y = 1.6$. At these instances both the near and far field points occupy the same region of the stress-strain curve. It may be argued that the near field stress pattern is dependent primarily on material type. But far field stress behavior is affected by loading as well as material type.

A comparison of J, both near and far, as well as crack mouth opening is given in the next figure. All three parameters plotted are the ratio of values for the PH material to the BIL material. It is interesting to note the ratio for all three parameters may be expressed as a single number, allowing a reasonable amount of scatter (±5%) except for the far field J value in the region of gross yield ($0.8 < \bar{\sigma}/\sigma_y < 1.3$).

One possible explanation for the fluctuations about unity for these three parameters might lie in the energy input to the specimens. J values and displacements should reflect energy input. Since both specimens have the same geometry and the same loading, the energy input may be inferred, at least roughly, from the average displacement at the applied traction (Energy $\doteq$ Force (traction) × Displacement).

$\bar{\sigma}/\sigma_y$	Displacement	
	PH	BIL
0.39	0.0002566	0.0002560
0.81	0.0005804	0.0005472
1.09	0.0009454	0.0007914
1.70	0.0028460	0.0029398

It can be seen that the trends in the energy input (displacement) are mirrored in the values for J and mouth opening.

Although the agreement with the HRR theory is not as good for the BIL material as for the PH material there are some similarities. It appears that the displacement exponent and near field stresses might reach the HRR prediction, but only after a tremendous amount of loading. J results again show path dependence. Despite the fact that the BIL stress-strain curve serves as a reasonable approximation to the PH curve for $\tau_0/\tau_{Lim} < 5$ there are noticeable differences in the two solutions after small scale yielding, particularly in the J values.

D. A533B STEEL (RS)

Much of the data for this problem is reported by Swedlow and Karabin (1977). Information is reported for the four key load levels: elastic, yield exceeds the special element, NSY, and net applied stress exceeds tensile yield stress (gross yield). Only the pertinent results of that paper will be discussed here.

Unlike the two previous problems this material has a real stress-strain curve and, therefore, does not lend itself to a direct comparison with the HRR theory. Also, it uses two displacement exponents. Chronologically, it is the first elasto-plastic problem in the sequence. Due to the fact that the two exponents are relatively equal and the fact that this two exponent scheme is not coordinate system independent all other problems have only one exponent. Figure (7) of the Swedlow and Karabin report show the incremental displacement exponents. p and q represent the radial and tangential incremental displacement values respectively. The sharp rise of these exponents (step 48) occurs when the Gauss points closest to the crack tip extend past the limit of the

inputted stress-strain curve. As mentioned in the PH problem the curve extension method is not that exact. The largest octahedral strain within the special element at this point is 0.16.

Accumulated values for these exponents are presented here:

Step	p*	q*
1	0.4999	0.5002
38	0.3119	0.2463
73	0.2321	0.2404
93	0.2794	0.2982

The coefficient of determination for these numbers is typically 0.99999. Attempting to characterize this material as a power hardening type by fitting such a curve through the last segment of the real stress-strain curve would lead to an expected accumulated exponent of 0.13 - 0.16. SPECEL's results show a trend in this direction until those near tip Gauss points exceed the inputted stress-strain curve. However, exact agreement with the HRR theory cannot be expected because the entire stress-strain curve cannot be characterized by a single hardening exponent.

Average values for the strain energy density exponent are given here:

Step	s*
1	-0.979
38	-0.858
73	-0.975
93	-1.012

Candidate values for the average are taken for $55° < \theta < 125°$ and the coefficient of determination for each is in excess of 0.999. The last two steps use only the six Gauss points furthest from the crack tip. There is some consistency with the minus one prediction of the HRR model. However, there is significant deviation from the above figures for large and small θ, indicating that possibly another form for fitting the strain energy density should be used in these regions.

No attempt will be made to compare the near field stresses with the HRR theory. Instead, the near field cartesian displacements and principal stresses are plotted in Figs. (2a,2b and 3a,3b) of the Swedlow and Karabin report. These quantities are normalized on the applied load (loading produced via displacements, but to within a few percent this may be represented by net tension) and this information is reported at Gauss points with $\hat{r} = 0.0039$ as opposed to $\hat{r} = 0.0010$ for the two previous problems. However, the pattern of redistribution of these near field quantities from an elastic to a plastic response is unmistakable. Displacements remain smooth for all load levels but roughness develops in the stress data for the highest load shown.

The normalized J parameter is shown in Fig. (65). Its response is not unlike the results for the previous two materials. Y is fairly path independent for the elastic step. As yielding progresses there is a slight decrease in the near field Y. Then, at NSY, the far field Y has increased substantially and the path independence begins to break down. At gross yield no semblance of path independence remains.

Near and far field stresses are compared to determine the degree of proportionality. As mentioned above the near field stresses, normalized on applied load (stress), show nonproportional loading. The far field stresses, although not shown here, exhibit a proportional

loading pattern. This demonstrates that the tensor of similitude is independent of load and the deformation theory of plasticity is acceptable in the far field region.

Although this stress-strain curve is not of the power hardening variety a couple of approximations to the curve are shown in Fig. (66). They are of the form

$$(1) \quad \varepsilon/\varepsilon_{Lim} = 3.11\ (\tau/\tau_{Lim})^{7.74}$$

$$(2) \quad \varepsilon/\varepsilon_{Lim} = \frac{\sigma}{E} + 0.514 \left(\frac{\sigma}{\sigma_y}\right)^{10}$$

where the two curves are in octahedral and effective quantities respectively. (The second curve is used in the next problem.) The first curve characterizes the total strain in a power hardening form while the second curve just characterizes the plastic response in this form. Figure (67) shows the near and far field Y in comparison with the Goldman and Hutchinson results using these two curves. Although the far field Y agrees with neither of the Goldman and Hutchinson predictions it does have the same shape and relative magnitude after NSY. The near field Y is clearly different. It is interesting to note that even though stress-strain curves (1) and (2) are a reasonable approximation of one another, their Y responses, via Goldman and Hutchinson, are substantially different (more than 50% at gross yield). Comparison of J with laboratory experiments will be given later in this chapter.

Crack opening profiles, both within the special element and along the entire crack flank, are shown in the next two figures. Within the special element a progressive blunting of the tip can be seen until NSY. The same is true along the entire crack flank. But after

NSY the crack flank deforms dramatically. Near the tip the profile resharpens while further away the crack is still blunting. This resharpening of the tip has been seen in all three center cracked specimens. Figure (70) offers a comparison of the crack mouth opening from SPECEL with the Goldman and Hutchinson results for the two power hardening approximations. Note the disparity between the two Goldman and Hutchinson results. For this reason the degree of agreement between SPECEL's response and the Goldman and Hutchinson results for curve (2) is considered somewhat of a lucky coincidence.

There is a number of similarities with this problem and the other center crack problems: near versus far field stresses, Y and its path dependence, crack flank opening, among others. Some agreement can be seen with the deformation theory results for J and crack mouth opening. This is so despite the fact the accumulated displacement exponent does not behave as the HRR theory predicts.

E. E-24 Task Group Problem - Round Robin (Bend)

As stated in the previous chapter this problem has been solved in accordance with the ASTM E-24 committee guidelines. These guidelines include the reporting of specific results. The format for this problem will be to study some of this required information first and then proceed with the results that are inherent to SPECEL.

The elastic stiffness for this problem is given in terms of the ratio of force per unit thickness (P/B) to the applied displacement (u_A)

$$\frac{P}{EBu_A} = 0.0216$$

where E is the elastic modulus. This is 10-15% higher than results for

six other finite element solutions of the same problem. So the finite element map that is used by SPECEL is too stiff due to an insufficient number of constant strain triangles. Force versus applied displacement in Fig. (71) exhibits this extra stiffness throughout the loading process (as compared to the finite element results of other analysts, Wilson (1977)).

Stresses and strains are plotted along the symmetry line ahead of the crack tip. The hydrostatic stress is shown in Fig. (72) as a function of distance from the tip for a number of load levels. Large nonzero values of this parameter occur both near the tip and near the pinned node ($x/(W-a) = 1.0$) though with different signs. At $x/(W-a) \doteq 0.45$ the hydrostatic stress is zero which agrees with other analysts' findings, Wilson (1977). One result peculiar to SPECEL is the 10% discontinuity that occurs between the special element and the adjacent regular element at an applied displacement of 0.0020 inches. Accompanying this result is a rise in the stress for subsequent regular elements. It appears that the built-in incompatibility is causing some problems. However, the limit for the parameter study, excluding the ASTM required plots, is $u_A = 0.0015$ inches. This is a sufficiently high load - it is more than twice the applied displacement at net section yield. A check of this incompatibility is done for one of the center crack panels (PH) in the next figure. A slight discontinuity (about 5%) develops at $\bar{\sigma}/\sigma_y = 1.7$. The accompanying rise in the stress develops about four regular elements away from the discontinuity. Therefore, it appears that SPECEL can handle fairly high loads before this incompatibility becomes noticeable.

Effective stress is plotted in Fig. (74). Although no discontinuity develops as for the hydrostatic stress a relative maximum

occurs at the interface of the special and regular elements ($x/(W-a) = 0.016$). The peak near the pinned node is an accident of the finite element map. Since the pinned node acts as a loaded point a rise in the stress is expected. The element along the symmetry line that shares this node shows a slight drop in the stress because the regular element with the same diagonal side (both elements are right triangles) absorbs most of the load. This is typical of constant strain elements in bend problems.

J, normalized on the square of the applied displacement, is plotted in Fig. (75) as a function of distance from the crack tip. The elastic step shows quite a bit of scatter in J - a coefficient of variation of 9% exists. By contrast the PH problem has a coefficient of variation of only 6% for the corresponding range of effective radius. This can be attributed to the relatively poor job constant strain elements do in bending. Other analysts do not show this scatter in elastic J values but SPECEL's average J agrees to within a few percent (±3) of their results. Notice that J remains proportional to applied displacement squared for paths with $R_p/(W-a) > 0.1$ up to $u_A = 0.005$. But the near field J exhibits a marked decrease. Average J*, plotted as a function of the applied displacement, is shown in the next figure. It is evident that J is proportional to applied displacement squared for lower loads and then a linear relationship develops for $u_A > 0.01$ inches. Other graphs required by the E-24 Committee will not be discussed or will be commented upon later (i.e. crack opening).

*Average J is taken from the four paths in the special element furthest from the tip and the four paths in the regular elements.

Turning to the exponential discussion, a typical incremental displacement exponent response can be seen in Fig. (77). The value drops from the inputted one-half for the elastic step to a minimum at u_A = 0.005 inches. Here the octahedral strains at the nearest Gauss points are as high as 0.47. In terms of the McMeeking-Rice criterion for small strain theory limitations this means that the stresses at these Gauss points are more than twice the tangential modulus. Yet the trend in the exponent is correct. In the subsequent load steps the yielded points exceed the limits of the inputted stress-strain curve and the exponent begins to rise. This seems to indicate that it is primarily the unfaithful representation of the stress-strain curve past the input limits rather than large strains that cause a rise in the exponent. The limit of the inputted stress-strain curve for this problem is γ_0 (octahedral strain) = 0.66.

Accumulated exponents are calculated for a few steps at a number of angular positions. The response shows a fairly constant exponent although slightly higher values are found near the symmetry line. However, it does seem reasonable to take an average exponent as a representation and this is shown in the next figure. In view of the incremental plot the result is not unexpected. The HRR theory predicts a displacement exponent of 0.09 for fully plastic behavior whereas SPECEL exhibits higher values. Still the transition from elastic to plastic behavior is expected.

The strain energy density exponent shows agreement (to within 10%) with the minus one prediction for the first three load levels plotted in Fig. (79). There is a bit of discrepancy for small and large θ. All values for these first three steps use all seven Gauss points in a curve fit and the coefficient of determination is 0.99997 or better.

At step 93 six, or even five, of the Gauss points are used in the curve fitting to find the few values shown. Some s* values are not found and for those that are, the coefficient of determination is worse than before. Tangential stress distribution in the radial direction for certain angles is shown in Fig. (80). Other stress components have similar behavior. The two term Williams solution as well as the HRR prediction for a material with a hardening exponent of thirteen are plotted. The two term Williams solution appears constant in r because the second term is practically negligible in bend problems. Although the bend problem has an exponent of ten, both types of power law materials have little strain hardening and there should be some degree of agreement between the two. As before, the normalization factor is $\sigma_{e\ max}$. Note the load is given in terms of applied stress via applied force. There is good agreement for all stresses throughout the special element with the elastic prediction indicating the elastic singularity dominates this region. As yielding progresses there is a transition to some new state. Some agreement with the HRR, n=13 result can be seen. The plastic singularity does not show the same dominance exhibited in the elastic step - the stress values are not constant with r. Erratic behavior can be seen for the first, and in some instances, the second Gauss point. But since for all other materials the full stress field for the second Gauss point is presented the same is done here. The results are shown in Figs. (81-84).

The effective stress, Fig. (81), shows excellent agreement with the elastic prediction. Note that the rise near 180° has disappeared. This is due to the fact that there is no buildup of radial compressive stress for the bend geometry on the crack flank. Transition is evident as yield exceeds the special element, step 40, and a fair

agreement with the power hardening case (n=13) can be seen at NSY, step 77. There is some discrepancy in the range $30° < \theta < 80°$. At step 93 the stress field at $\hat{r} = 0.001$ deteriorates so the stresses at $\hat{r} = 0.0023$ are plotted. This shows the same degree of agreement with the power hardening (n=13) result as the closer Gauss point does at NSY.

Components of stress exhibit the same trends as the effective stress. The radial stress, Fig. (82), is greater than the HRR prediction at NSY but it does have a peak (maximum) for small θ and a valley is almost achieved for large θ. At higher loads the smoothness of the stress field vanishes at $\hat{r} = 0.0010$ and at $\hat{r} = 0.0023$ only the peak is visible. Tangential stress demonstrates excellent correspondence with both elastic and plastic predictions (except for very small θ). The plateau predicted for the shear stress in the mid-θ range is found in SPECEL's result but near the crack flank the numerical values do not approach the analytical limit. However, there is a very clear overall transition from elastic to plastic behavior.

Some of the J behavior that has been seen in the E-24 required graphs is replotted in other forms in the next few graphs. Normalized J, in terms of Y, versus the effective radius of the J path is shown in Fig. (85). The two J values furthest from the crack tip ($\hat{r} > 0.5$) are ignored because they show an unnatural rise in J, even for the elastic step. These J paths include that portion of the boundary with singular (point) loading which is not accurately represented by the large constant strain elements comprising these paths. The remaining J paths, although not that constant for the elastic step, do not show much increase in scatter between Y_{near} and Y_{far} as the center crack panels.

The usual comparison of the proportionality of near and far field stresses has been done but is not shown. As expected, the near field stresses exhibit a major redistribution. The far field stresses are proportional up to step 93 except for a few points in front of the crack tip. During the period of near field stress redistribution the scatter increases between near and far field J as was seen in Fig. (75).

Crack opening profiles are shown in Figs. (86 and 87). As with the center crack panels there is a progressive blunting at the tip. Unlike the center crack panels resharpening at the tip does not occur until very high loads (at $u_A = 0.05$, roughly seven times the applied displacement at NSY) and the profile is nearly linear along the entire profile. This linearity will be exploited to obtain a projected crack opening displacement.

Despite the fact that the model for this problem is crude relative to those used by other analysts some interesting results have been shown. Although the exponent did not reach the HRR prediction the near field stresses exhibited reasonable agreement with the HRR model for a low strain hardening material. J and the displacements along the crack flank show a marked difference from the center crack geometry which will be explored further in the next section.

F. J, COD, δ_M

Another procedure for measuring J is given by Rice, et al. (1973). It is based on the definition

$$J = \int_0^{\delta} \left(-\frac{\partial P}{\partial a}\right) d\delta$$

which relates J to the rate of change of the area under the load versus

load-point displacement curve (P-δ) to the crack size (a). For an internally notched plate in tension this reduces to

$$J = J_{elastic} + \left[2\int_0^{\delta_{plastic}} (P/b)d\delta_{plastic} - (P/b)\delta_{plastic}\right]$$

where P/b is the load per unit thickness for each ligament of the center crack panel and δ is the total displacement between load points. In the case of a deeply notched plate subject to bending by forces the formulation reduces to

$$J = 2\int_0^{\delta_{crack}} (P/b)d\delta_{crack}$$

where δ_{crack} is that part of the total displacement due to the crack alone. Unfortunately for this exercise it would necessitate rerunning the Bend problem with the crack zipped up. The return/investment ratio makes this prohibitive. However, it is a trivial matter to find the plastic component of displacement required for the center crack specimens.

Figures (88-90) show the Rice estimate for J in comparison with the near and far field J from SPECEL. For the RS problem there is excellent agreement between the far field J and Rice's estimate. It should be noted that Rice's procedure is based upon the deformation theory of plasticity. This ignores plastic dissipation that is significant near the crack tip but not as important in the far field. Rice's estimates of J for the PH and BIL problems do not show this good agreement with the far field J of SPECEL but they do overestimate all the J values within the special element.

A possible explanation of why the good correlation between Rice's

procedure and far field SPECEL J values exists for the RS problem but not for the BIL and PH materials may involve the type of loading. Displacement loading of a finite element map has more energy input than a real specimen due to the extra stiffness of the map, whereas the applied traction loading of a finite element map underpredicts the energy input to a real specimen. And a tensile load applied with constant displacements results in loading by a moment in addition to a constant stress. This hypothesis could be checked simply by running one of these three problems with the other type of loading.

J is plotted as a function of crack mouth opening (δ_M) in Figs. (89-92). In all four problems the near field J has a near linear relationship with the mouth opening after NSY. The worst case of this relationship is the Bend problem. Goldman and Hutchinson predict that J, based on deformation theory, should be related to δ_M by

$$J = C \delta_M^{\frac{n+1}{n}}$$

for tension loaded center crack panels. C is a constant and n is the hardening exponent. For the PH case, Figs. (89 and 90), the far field J behaves like $\delta_M^{1.55}$ as opposed to the $\delta_M^{1.33}$ dependence predicted by Goldman and Hutchinson. Although not in close agreement, SPECEL's far field J values behave quite unlike the near field J with respect to δ_M. The BIL material exhibits the same type behavior in Figs. (89 and 90). In the case of the RS problem, Fig. (91), the hardening exponent has been estimated between seven and ten. It can be seen how the large exponent flattens out the far field J,δ_M relationship.

Much in the literature has been devoted to finding a relationship between J and crack opening displacement (COD). A number of definitions

for COD have been proposed and two of them will be used in this discussion. Both are employed in Fig. (93) for the Bend problem. One definition of COD is twice the displacement perpendicular from the crack plane at positions along the crack flank. These points are close to the crack tip, either within or near the special element. The second definition involves the linear extrapolation of the crack flank displacement to the tip using displacements at the crack mouth and halfway along the crack flank. This second definition is used only for bend specimens. Also shown in the figure is Wells' result (1971) using extrapolation. SPECEL's and Wells' extrapolations show reasonable agreement and are considerably larger than COD based on near tip Gauss point displacements (radius of special element is 0.0076 inches). These near tip Gauss points have displacements that behave in a quadratic fashion with δ_M for low load levels. However, in the region (before and after) NSY the entire crack flank displacements are linear with respect to δ_M.

Plotting J with COD does not yield a pure linear relationship for the Bend problem as seen in Fig. (94). The J - COD relationship is of the form

$$J \propto (COD)^{\frac{m+1}{n}} \quad , \qquad m > 1$$

Here m is not the power hardening exponent, but the relationship is of the form predicted by Goldman and Hutchinson. For materials with little strain hardening (large exponent) the Goldman and Hutchinson relationship is nearly linear. And for this problem a straight line for the J - COD relationship is not a bad approximation after $\frac{\delta E}{\sigma_y W} > 0.6$. Also shown is the straight line which relates J to COD by the factor $2\sigma_y$. $2\sigma_y$

represents the knee in the stress-strain curve and is the same proportionality factor used by Hayes and Turner (1974). There is modest agreement with this relationship and near field COD.

Extrapolated COD cannot be found for center crack specimens due to the nature of the crack flank. However, near and far field J are plotted against COD using the first definition of COD for the PH problem. In Figs. (95 and 96) the PH specimen has a nearly linear J - COD relationship but, actually, it is more like the power law relationship given above. The same may be said of the RS problem.

Assuming J is related to some crack flank opening another possible explanation for J path dependence can be given. Figures (97-99) plot crack flank opening (δ) against δ_M for the center crack panels. The striking feature common to all three is the near bilinear δ-δ_M relationship for near tip points. The knee in these "bilinear" curves occurs near NSY, except it is delayed slightly for the BIL material due to the insignificant amount of plasticity in the stress-strain curve until yield has been greatly exceeded ($\tau_0/\tau_{Lim} > 1.5$). The sharpness of the knee is greatest near the tip and dies out at further distances. It is still evident at $\hat{r} = 0.0176$, more than twice the radius of the special element, but cannot be seen at $\hat{r} = 0.0705$ or less than 15% of the crack length. This is another manifestation of the crack tip "resharpening" itself that was seen in the previous sections. If one were to extrapolate a COD using the crack flank information far from the tip ($\hat{r} > 0.0705$), the value would overestimate the actual COD. The sense of the resharpening has been lost outside the near tip area. Employing the assumption that J is proportional to COD (not necessarily linear) far field J, using far field crack flank opening to sense a COD, would overestimate J. Near field J are affected by this resharpening

and do not overpredict J.

Remember this resharpening is not present in the bend problem. The entire crank flank is proportional to δ_M for nearly all load levels. This would suggest that resharpening is not a factor in J path dependence for the bend specimen. Consider the coefficient of variation for the Bend and PH problems for nine identical J paths $0.0010 < \hat{r} < 0.2821$:

	BEND	PH
elastic	0.09	0.06
NSY	0.17	0.21
GY	0.22	0.31

GY denotes gross yield - step 93 for the Bend, step 125 for the PH. At GY the applied displacement is 2.03 times the displacement at NSY for the Bend; for the PH the ratio between the two displacements is 1.63. It is evident that the rate of path dependence is growing much faster for the PH problem. This would support the claim that the resharpening of the crack tip in center crack panels causes a path dependence in J. So path dependence may be dependent upon the amount of plastic dissipation and tip resharpening in the near field.

Finally, it is possible to compare the near versus far field J against actual laboratory results for the RS problem. The information is provided by Riccardella and Swedlow (1974) and is shown as vertical and horizontal lines in Fig. (88). Two values of J_{IC} are plotted as horizontal lines. The largest J_{IC} is the result of thirty-six standard J_{IC} tests (Fig. 6 of Riccardella and Swedlow). However, most (thirty) of the specimens are an inch thick or less. There does seem to be something of a size effect for thicker specimens and the second J_{IC}

estimate represents the average for two four inch thick specimens. It should be noted that J_{IC} is determined from the load displacement curve of compact tension specimens. The compact tension is essentially a bend specimen so resharpening should not be a factor in J path dependence, but the method of computing J uses far field parameters.

The two vertical lines in the figure represent initial fracture predictions at given applied displacements. The one on the left represents the applied displacement when an average J reaches the J_{IC} predicted by the thirty-six specimens. This average J is determined from a numerical analysis by Riccardella and Swedlow using an average of ten J paths (some of which may be considered near field). On the right, the initial fracture is determined by laboratory experiments. It corresponds to the applied displacement when an actual four inch thick center crack specimen begins to fracture. This fracture prediction is based on acoustic emission results which can be seen in Fig. (19) of the Riccardella and Swedlow report. Fracture initiation corresponds to an enormous increase in acoustic emissions occurring at an applied displacement of 0.015 inches or an applied stress of 53,300 psi. Although the acoustic technique has not been calibrated with respect to crack growth this prediction does fall within the scatter band of the other fracture prediction. It is evident that the far field J shows better agreement than the near J with the fracture initiation point predicted by the thirty-six specimen J_{IC} test and numerical result of Riccardella and Swedlow. However, the fracture initiation point predicted by the four inch thick J_{IC} tests and acoustic emissions from a four inch thick center crack panel show good agreement with SPECEL's near field J. The far field J overpredicts this point by a factor of three whereas the near field J is twenty percent less

than this J_{IC}. While certainly not conclusive perhaps this is an indication that far field J is not the parameter that governs fracture. Although near field J loses its physical significance in terms of a deformation theory type measurement, it still reflects the amplitude of the near tip stress and strain fields. In the next chapter an experiment will be proposed that should determine whether or not the near field J is a relevant number.

CHAPTER V

PROPOSAL FOR EXPERIMENTATION

In this chapter an experiment will be proposed whose purpose is to determine whether or not the difference between near and far field J is real. A flow chart for the experiment can be seen in Fig. (100). Unfortunately, the only apparent method of measuring J near the crack tip is by numerical techniques. Far from the tip J can be determined by energy as well as numerical methods.

It has been suggested earlier that J path dependence is caused by two factors: 1) significant dissipation of energy near the tip due to plastic deformation; and 2) a resharpening of the crack tip in center crack specimens. Quantitative measurement of the energy expended for plastic deformation is not possible. But displacement measurements near the tip would detect resharpening. Therefore, the proposed experiment will place more emphasis on this aspect of path dependent J.

As was seen in the previous chapter materials with little strain hardening cause difficulties with the incremental exponent technique if the stress-strain curve is not extended far enough, at least in light of the HRR model. At least on the first pass of the experiment a material with high strain hardening and ductility characteristics should be selected to increase the confidence in the numerical results. The material stress-strain curve will be determined from a number of tensile tests analogous to the procedure used by Riccardella and Swedlow (1974).

The most important material parameter to determine accurately is a G_{IC}, or the energy made available per unit increase in crack surface

area at fracture initiation. This quantity is determined such that it is independent of specimen thickness. To determine G_{IC} two independent series of tests will be run - K_{IC} and J_{IC} tests - on three point bend specimens.

Standard K_{IC} test procedure is given in ASTM E399-74 (1974). K is related to G by

$$G_{IC} = \frac{K_{IC}^2(1-\nu^2)}{E}$$

where E and ν have been determined from the tensile tests. This test has the advantage of measuring K (which is directly related to G and J) in an essentially elastic material. In such a material J (and hence G and K) has been shown to be path independent (Rice, 1968). Although there may be a small plastic zone around the tip the size of the zone is such that J is still path independent as seen from SPECEL's results. However, it does have the disadvantage that K_{IC} is measured at 2% crack growth.

J_{IC} testing procedure is given by Landes and Begley (1974) and modified by Clarke, et al. (1976). J and G are equivalent. Care should be taken so that the specimen size effect seen in the RS report is eliminated. This test determines J by using the area under the load-displacement curve of a bend specimen. It is a change in energy/change in crack area method which uses far field parameters. From the previous chapter it was shown that the change in energy/change in crack area method always overpredicts near field J and sometimes agrees with far field J from numerical analyses of center crack specimens. However, the J_{IC} test procedure does seek to measure J at no crack growth and when the specimen has attained significant yield. And by using a

bend specimen the crack resharpening does not come into play after NSY.

Hopefully, these two numbers should agree with one another - to within 10-20% - indicating that G_{IC} is unique. In that case let $G_{IC} = J_{IC}$. If the G value computed from K_{IC} is significantly lower than J_{IC} denote $G'_{IC} = f(K_{IC})$ and $G''_{IC} = J_{IC}$. The reason for denoting two G's for this case is that the difference between the two may be the result of path dependent J values. G''_{IC} is measured from far field parameters when significant yield is present, whereas G'_{IC} is path independent. If the J_{IC} test leads to significantly lower G values then $G_{IC} = J_{IC}$.

The next step in the experiment is to conduct numerical analyses of the three point bend and center crack specimens with SPECEL for this material. It was seen that the bend problem had a significant amount of path dependence in J for the elastic step due to an insufficient number of constant strain elements. Therefore, enough elements should be included in the analysis to eliminate most of this effect. Also, it is advisable to run the bend problem with the crack zipped up in order to measure J by the change in energy/change in crack area method and compare with the far field J results of SPECEL. When the numerical far field J reaches J_{IC} the numerical near field J should be noted. Call this value G_{ICN}. For the case when G'_{IC} does not equal G''_{IC} agreement between near field J and G'_{IC} should be checked at the time far field J equals G''_{IC}. If near field J and G'_{IC} are close let $G'_{IC} = G_{ICN}$. This is an indication that the G_{IC}'s found by the K_{IC} and J_{IC} tests reflect near and far field quantities respectively. If near field J (equal to G_{ICN}) and G'_{IC} are not approximately equal to one another then this indicates that G_{IC} found by the elastic K_{IC} test does not have any relation to the J in a plastic analysis.

The numerical analysis of a tension loaded center crack specimen of the same material is to be done next. Loading may be induced by tractions or displacements, whatever is easier to replicate with an actual specimen. The applied load should be noted when the far field J reaches G_{IC} and when the near field J reaches G_{IC} and G_{ICN}. Denote the corresponding loads L_F, L_{N0}, L_{N1} ($L_F<L_{N1}<L_{N0}$). There should be a substantial difference between these far and near field quantities. But if $L_F \doteq L_{N1}$, disregard L_{N1} and G_{ICN} concept since G_{ICN} parallels G_{IC}.

The final step of the experiment is to reproduce the numerical center crack problem in the lab with an actual specimen. The point of fracture initiation is to be determined and the corresponding load is L*. There may be a problem determining precisely the initial of crack growth. Acoustic emission tests, like those used by Riccardella and Swedlow (1974), might be employed. Assuming that L* is obtained by this method the credibility of SPECEL's results can be tested. If L* agrees with L_F this indicates SPECEL's J path dependence is not real but a result of the numerical modelling. However, if L* and L_{N0} are relatively close this indicates that the path dependence in J is real, at least for the center crack specimens. And it probably means that the dependence is caused by resharpening near the tip. This resharpening can be confirmed by taking displacement measurements along the crack flank. If L* agrees with L_{N1} this again indicates that J is path dependent. More importantly, fracture initiation is associated with a near field parameter, G_{ICN}, for two specimen types. G_{ICN} is affected by dissipation of plastic energy near the tip and accounts for re-sharpening in center crack specimens. Different specimen tests would be needed to confirm that G_{ICN} is truly a material property. Near

field J, although not a measure of change in energy input/change in crack area, may be a measure of

$$\Delta(EI - DE) / \Delta A$$

where EI is energy input, DE is dissipation energy, A is crack area, and Δ's represent change. The problem with this formulation is that no apparent method of measuring DE is available.

If the acoustic technique is not acceptable for measuring fracture initiation another, more costly, less exact method is proposed. This method probably will not be able to distinguish between L_{N0} and L_{N1} since they should be relatively close and the margin of error in this technique is large. Take a number of center crack specimens, save five, and apply the following loads: L_F, $L_F + \Delta/4$, $L_F + 3\Delta/4$, L_N, $L_N + \Delta/4$. L_N represents an average of L_{N0} and L_{N1} and Δ is the difference between L_N and L_F. After loading heat tint the specimen and then break them open to measure any crack growth. If fracture initiation occurs between L_F and $L_F + \Delta/4$ or earlier then no real path dependence in J is present; between $L_F + \Delta/4$ and $L_F + 3\Delta/4$ the results are inconclusive; between $L_F + 3\Delta/4$ and $L_N + \Delta/4$ J path dependence is real but the contributing factors are not that easy to separate and identify.

This proposal will either confirm or refute the path dependent J behavior found in SPECEL. The accompanying computational problems should use very refined finite element maps to diminish elastic J variation (noise). Although it was suggested that a material with a large amount of strain hardening be chosen first other materials might be used provided the stress-strain relationship is extended far enough, even approximately, on input to SPECEL. The most critical part of the exercise is the laboratory work on the real specimens. Without good experimental numbers the purpose of the proposal is defeated.

CHAPTER VI

SUMMARY, CONCLUSIONS AND SUGGESTIONS

Through this series of problems it has been shown that SPECEL adds a new dimension to fracture analysis. Bounded by fully plastic and fully elastic theories SPECEL offers a reasonable bridge between these two. Although somewhat more expensive than conventional finite element solutions of elasto-plastic problems SPECEL is able to provide well behaved data much closer to the crack tip, thus shrinking the zone of blindness there.

The method itself is based on an analog to the theorem of minimum potential energy, the same as other finite element techniques. It includes the singularity within the special element as a degree of freedom. However, the minimization is carried out in an iterative manner unlike the usual procedure. First, the energy is minimized with respect to the regular degrees of freedom, then the exponent. The change in energy of the body is checked before and after exponent minimization to safeguard the iterative method. Also unlike conventional finite element analyses there is a built-in incompatibility between the special element and surrounding regular elements. But with the current model this proves not to be a problem till well after net section yield. Despite these two deviations (iterative minimization, incompatibility) from usual finite element procedure SPECEL's results indicate the method works.

In all elasto-plastic problems the incremental exponent shows a trend in the direction expected. But the incremental exponent itself is meaningless until translated into an accumulated value by functional fitting techniques. The typical coefficients of determination demonstrate

that the accumulated exponent procedure works quite well. For the power hardening material the accumulated exponent eventually agrees with the HRR prediction. The exponent for the bilinear material approaches the analytical value but appears it only will reach it for enormous load levels. Materials with little strain hardening, RS and Bend, near their theoretical predictions then deviate sharply. It has been shown that the unnatural sharp rise in the displacement exponent is caused primarily by stresses and strains exceeding the limits of the inputted material curve. The method for tracking points on the inputted curve is self-correcting and provides excellent results. But the curve extension method only provides the correct slope at a given stress and once the material gets off the intended curve the errors accumulate. Therefore, it is suggested that on input the material curve be extended far past sensible limits.

Attempts at characterizing the strain energy density exponent meet with modest success. There is decent agreement with the minus one prediction of the elastic and plastic analytical theories for the central θ range. Keep in mind that the inverse r singularity is predicted not for each angular value, but only in the average angular sense. In light of this, SPECEL's results are very reasonable.

Near field stresses show a major redistribution between elastic and plastic responses. All four problems have excellent agreement with the elastic prediction. With the possible exception of the shear component the stresses of the PH problem reach the HRR, n=3 prediction. The Bend problem exhibits decent agreement with the HRR, n=13 prediction although the two stress-strain curves are slightly different. A two phase transition is evident in the stresses of the bilinear material. First, a migration from the elastic step to a response

resembling the HRR, n=3 prediction occurs. This happens when points within the special element are on that portion of the stress-strain curve that closely approximates the PH curve. Such agreement, as well as the similarity between the Bend and HRR, n=13 results, indicates that specimens with like stress-strain curves produce, under mode I loading, the same pattern of near field stresses. However, the amplitude, or J, of the near field stresses is highly sensitive to material type. The second phase of the transition for the BIL problem takes the stresses from the n=3 toward the bilinear prediction. It is evident that quite a bit of loading is necessary to reach a true bilinear stress field. The crack would probably grow before the material behaved in a bilinear fashion. Therefore, expecting a bilinear response from a material is probably unreasonable.

The most surprising of SPECEL's results involve J and COD. J shows an increase in path dependence as yield spreads through the specimen and a dramatic growth in the vicinity of net section yield. A certain amount of path dependence may be due to the fact that the finite deformation definition of J is not used. Atluri, et al. (1977a,b) show that such a definition reduces path dependence near the tip. However, this explanation would not totally account for the degree of J variation seen by SPECEL.

Far field J results show some agreement with other analyses (Goldman and Hutchinson, change in energy input/change in crack length) which are based on the deformation theory of plasticity. Near field J values are always less than their far field counterparts. Two reasons for path dependence in SPECEL's results have been suggested:
1) dissipation of plastic energy near the crack tip which results from use of incremental as opposed to deformation theory of plasticity;

2) resharpening of the crack tip after net section yield in center crack specimens. The Bend specimen does not exhibit the resharpening which leads to a smaller increase in path dependence for this case. This problem also possesses a linear crack flank from which a COD is extrapolated. J and COD are not linearly related in any specimen. Rather, their relationship has a slight curvature typical of the form suggested by Goldman and Hutchinson. Some credence is given to the near field J in predicting fracture when the laboratory results of Riccardella and Swedlow are analyzed.

In order to demonstrate the fact that J path dependence is a real phenomenon an experiment is proposed. It involves the use of numerical solutions in conjunction with actual material tests. By using two types of specimens, the bend and the center crack, the path dependence of J due to resharpening can be detected easily. And it may be possible to determine the effect of plastic energy dissipation near the tip. Of course, if the experiments disprove the J path dependence then SPECEL must be reexamined in terms of its numerics.

But assuming the experimental evidence supports SPECEL's findings a number of problems are worth investigation. Mode II or mixed mode loading might be applied to another power hardening material. The results could be compared to the analytical work of Shih (1974). The effect of unloading might be checked. This would be important in single specimen J_{IC} tests. Net tension loading versus net extension loading could be studied for their effect on far field J and change in energy/change in crack length as discussed in Chapter IV. Many different specimens of the same material would provide a geometric study. SPECEL might be used to obtain a near field J_{IC} or predict

the fracture of an actual specimen.

Regardless of the outcome of the experiments SPECEL has proved to be a useful and interesting tool. It has shown that some aspects of the HRR theory are applicable to problems which use the incremental theory of plasticity. Materials that are characterized as bilinear do not behave as such until enormously high loads are applied. Similar materials have similar variations in near field stresses but the amplitude of the stresses is sensitive to material type. Advanced applications of the variable exponent technique (Marino, 1978) may shed additional light on these findings.

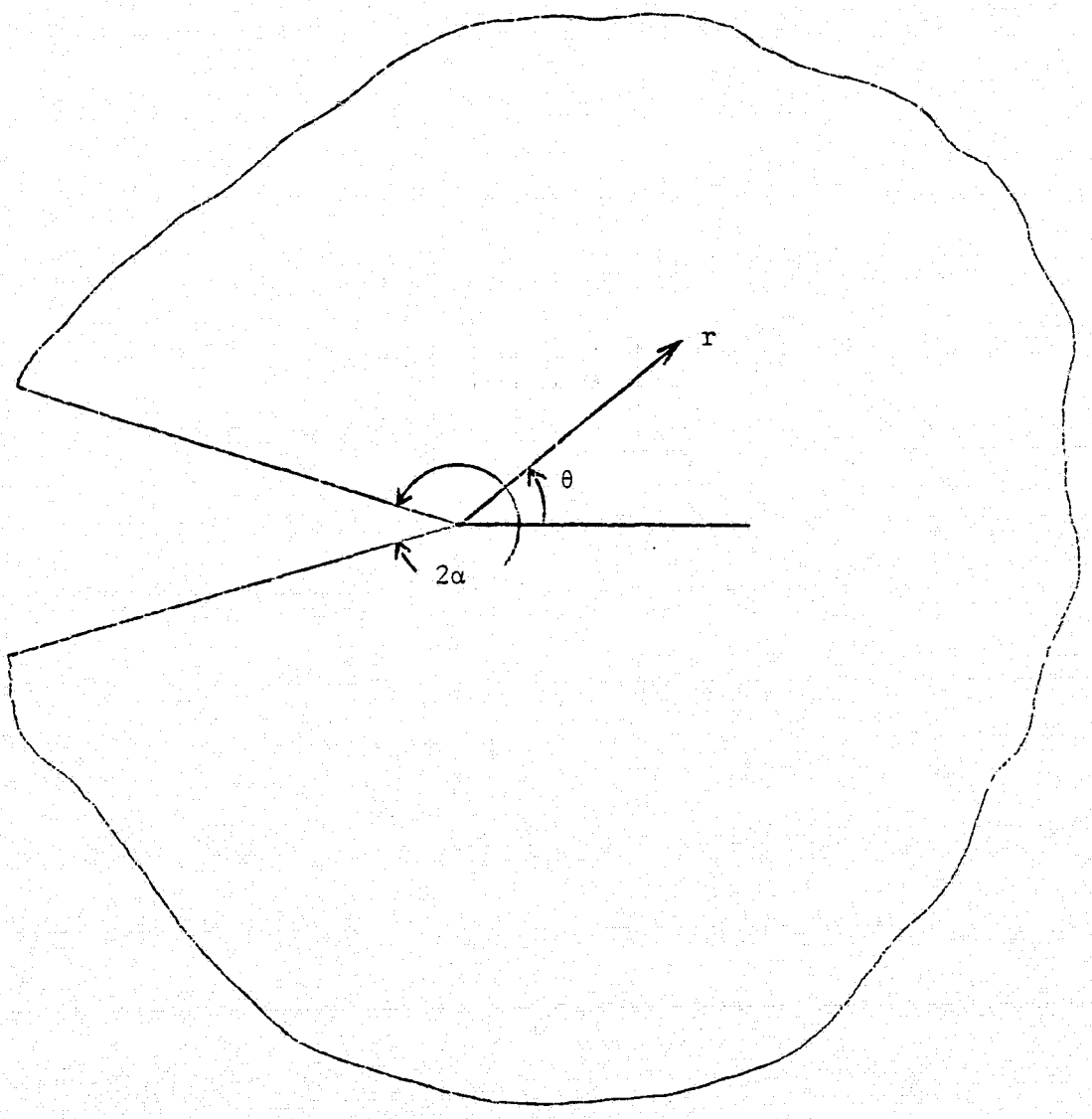

FIG. 1: Notch Tip Geometry

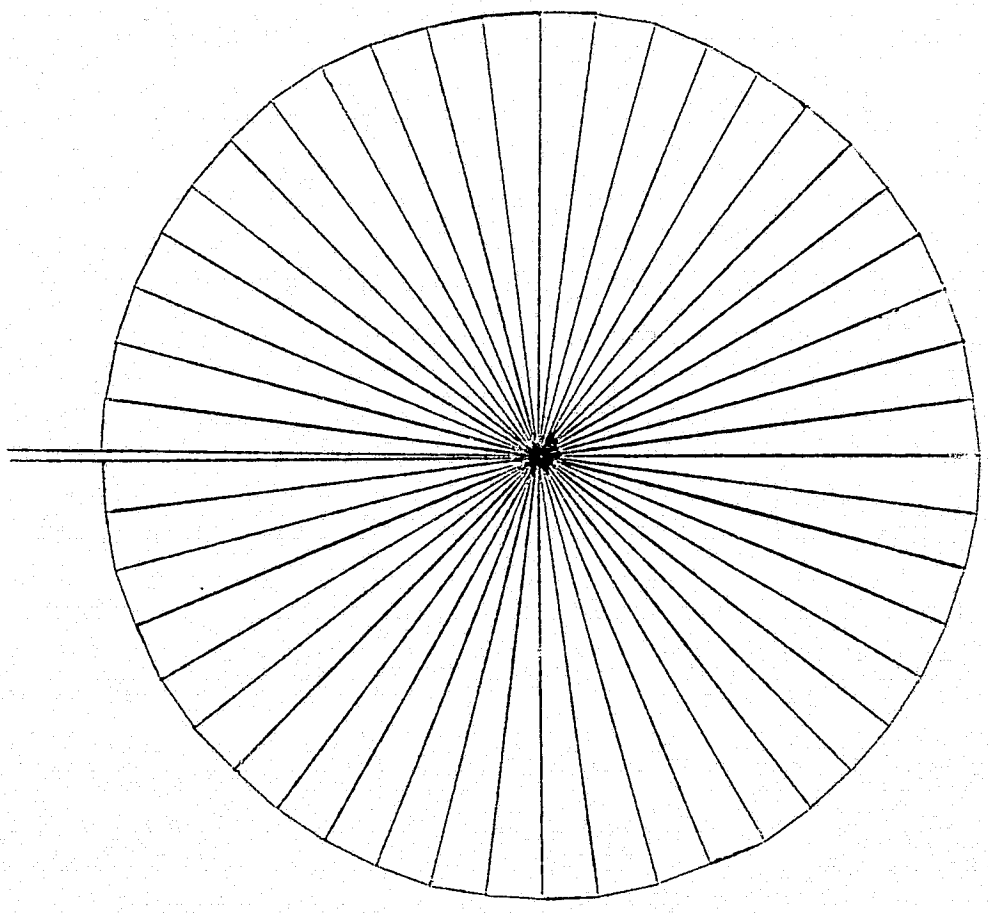

FIG. 2: Sectors Comprising Special Element
Surrounding Crack Tip

Figure 3 - Flow chart for SPECEL

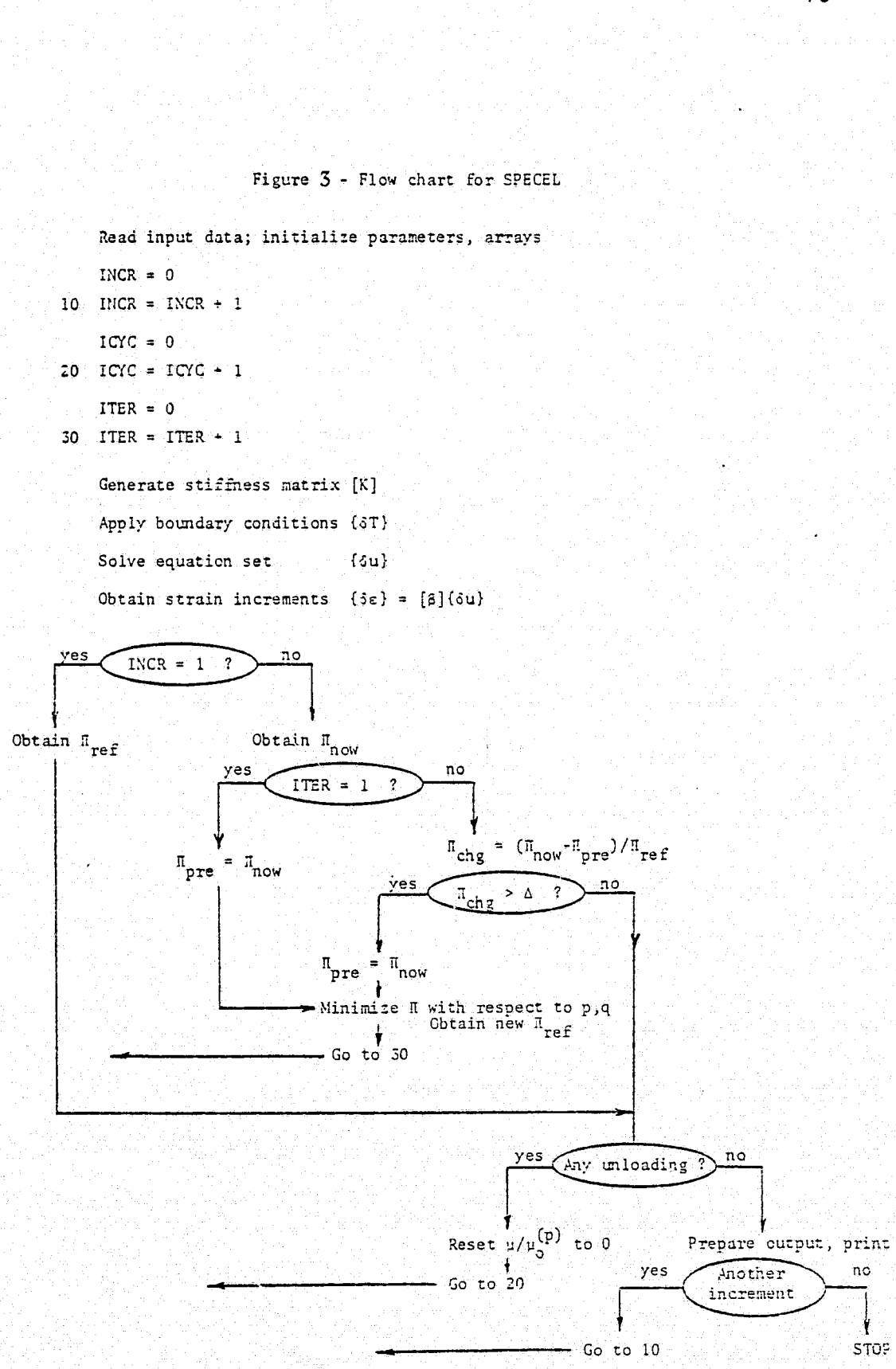

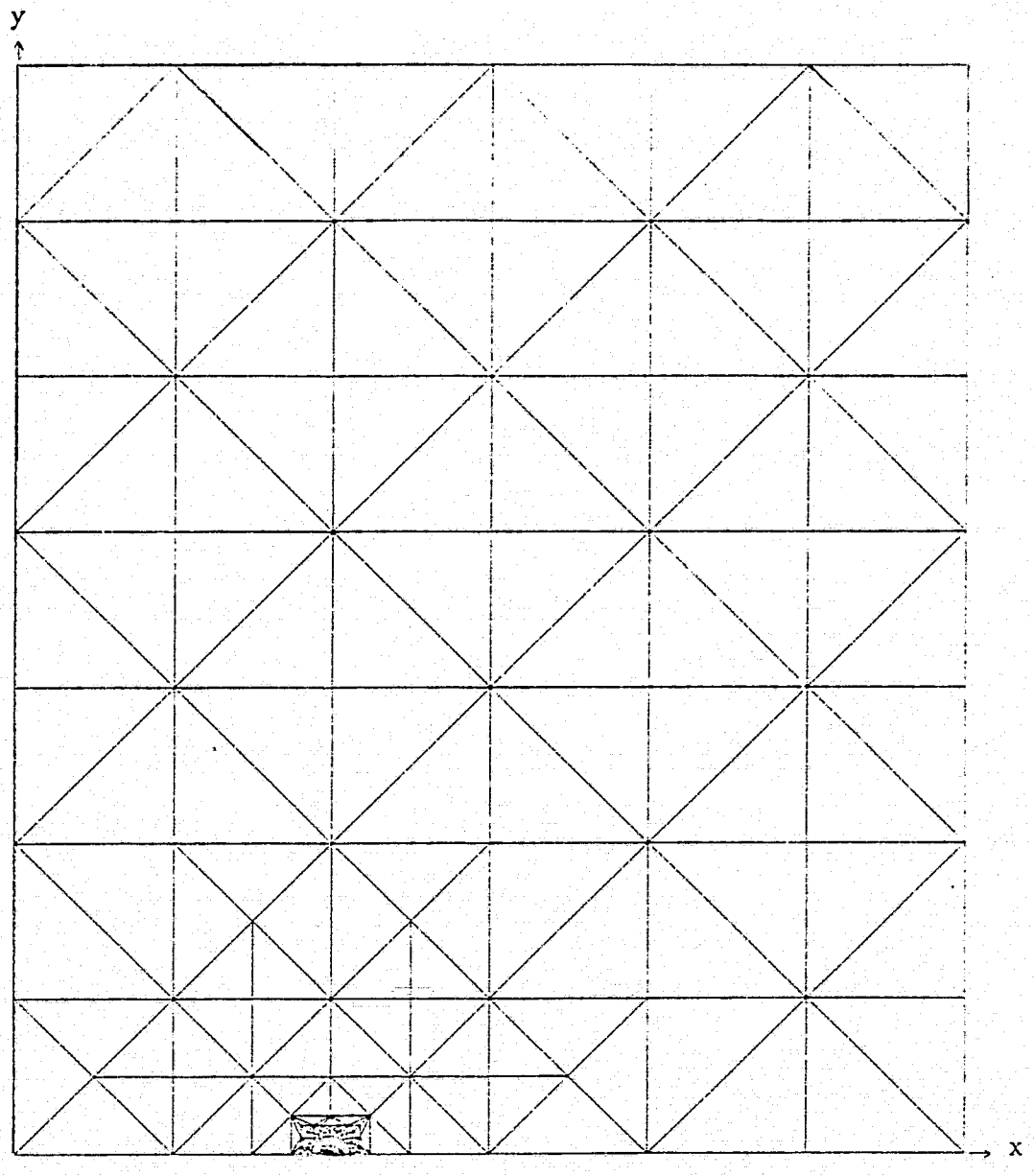

FIG. 4: Finite Element Map, Special Element Size a/16

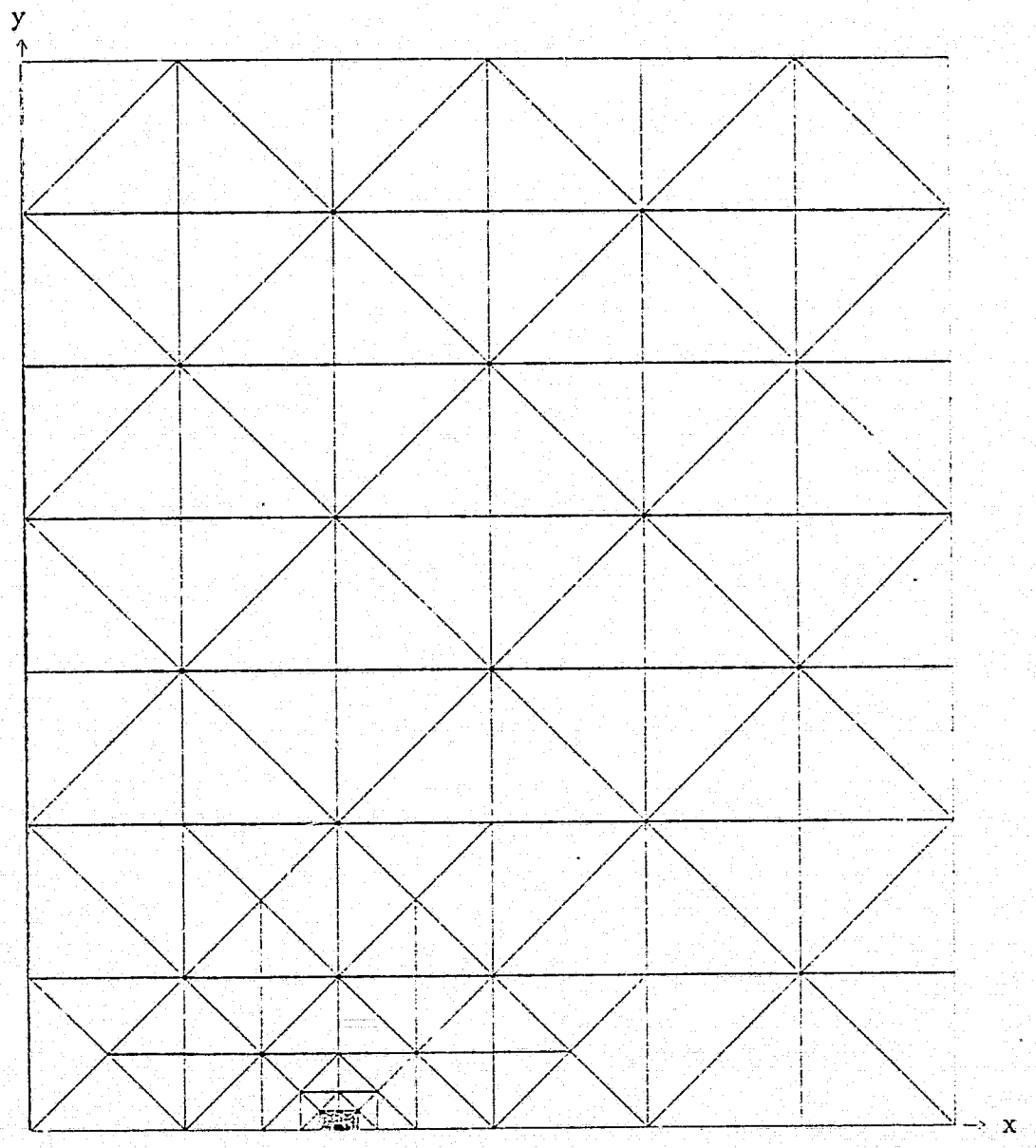

FIG. 5: Finite Element Map, Special Element Size a/32

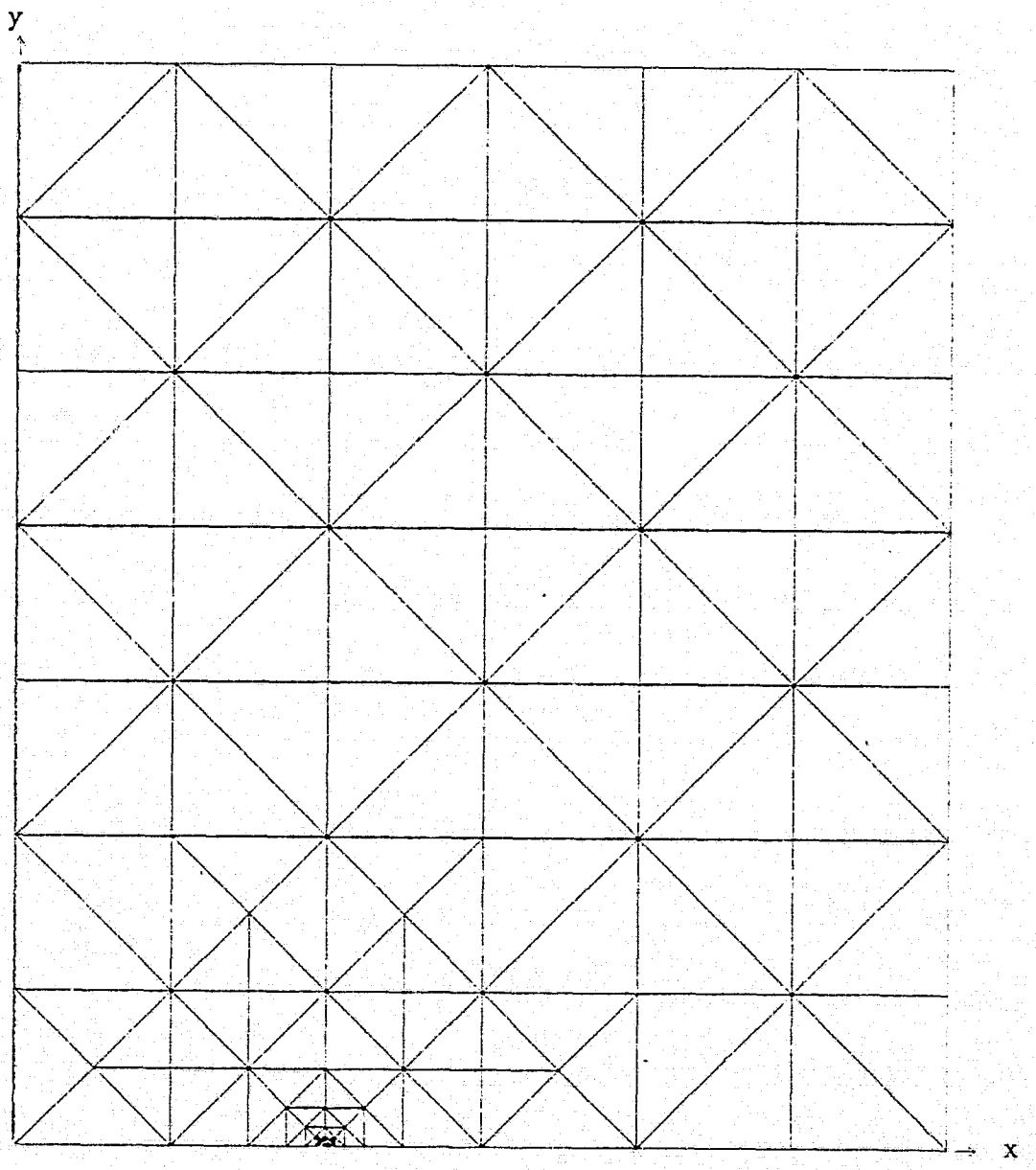

FIG. 6: Finite Element Map, Special Element Size a/64

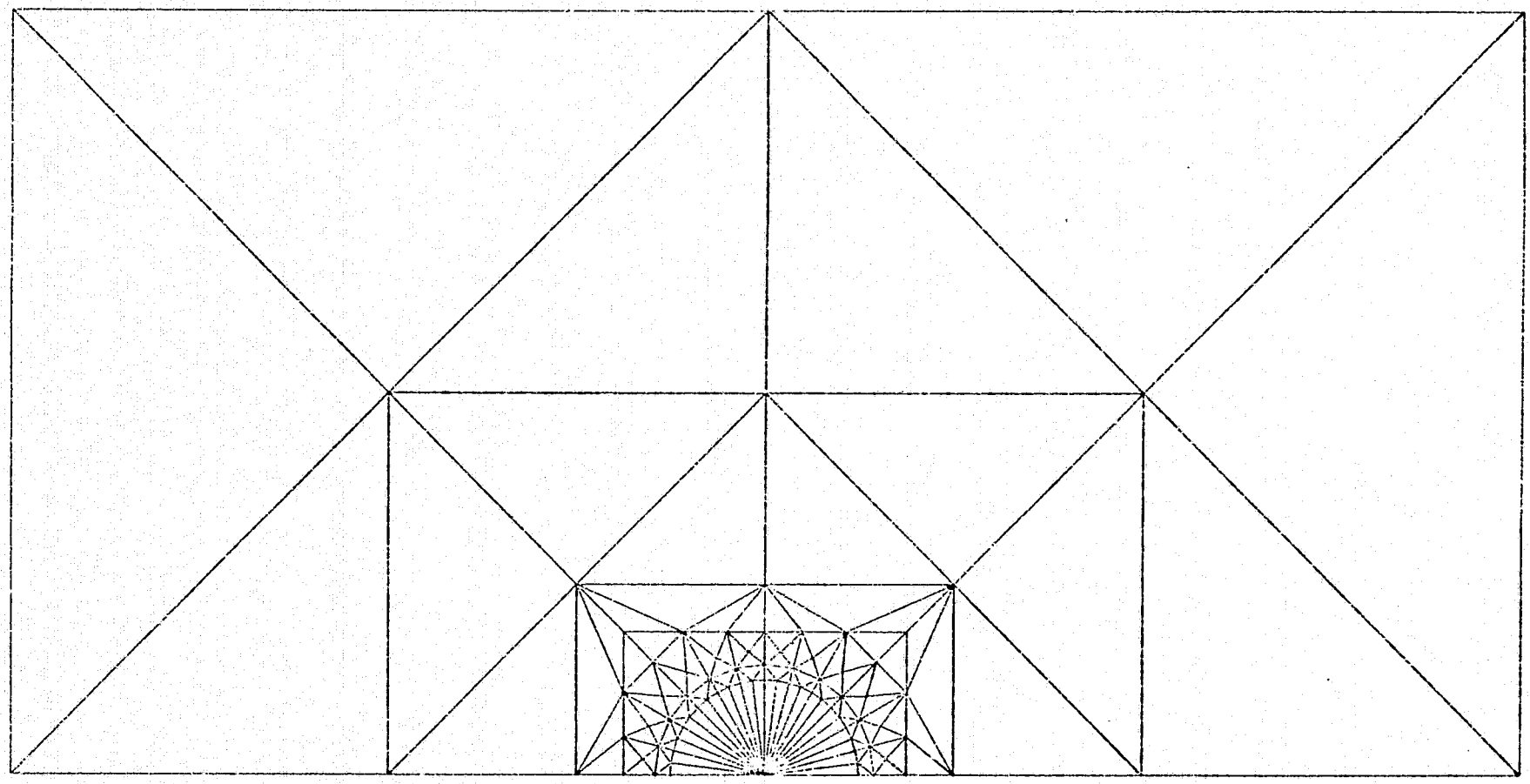

FIG. 7: Special Element Embedded in Regular Elements

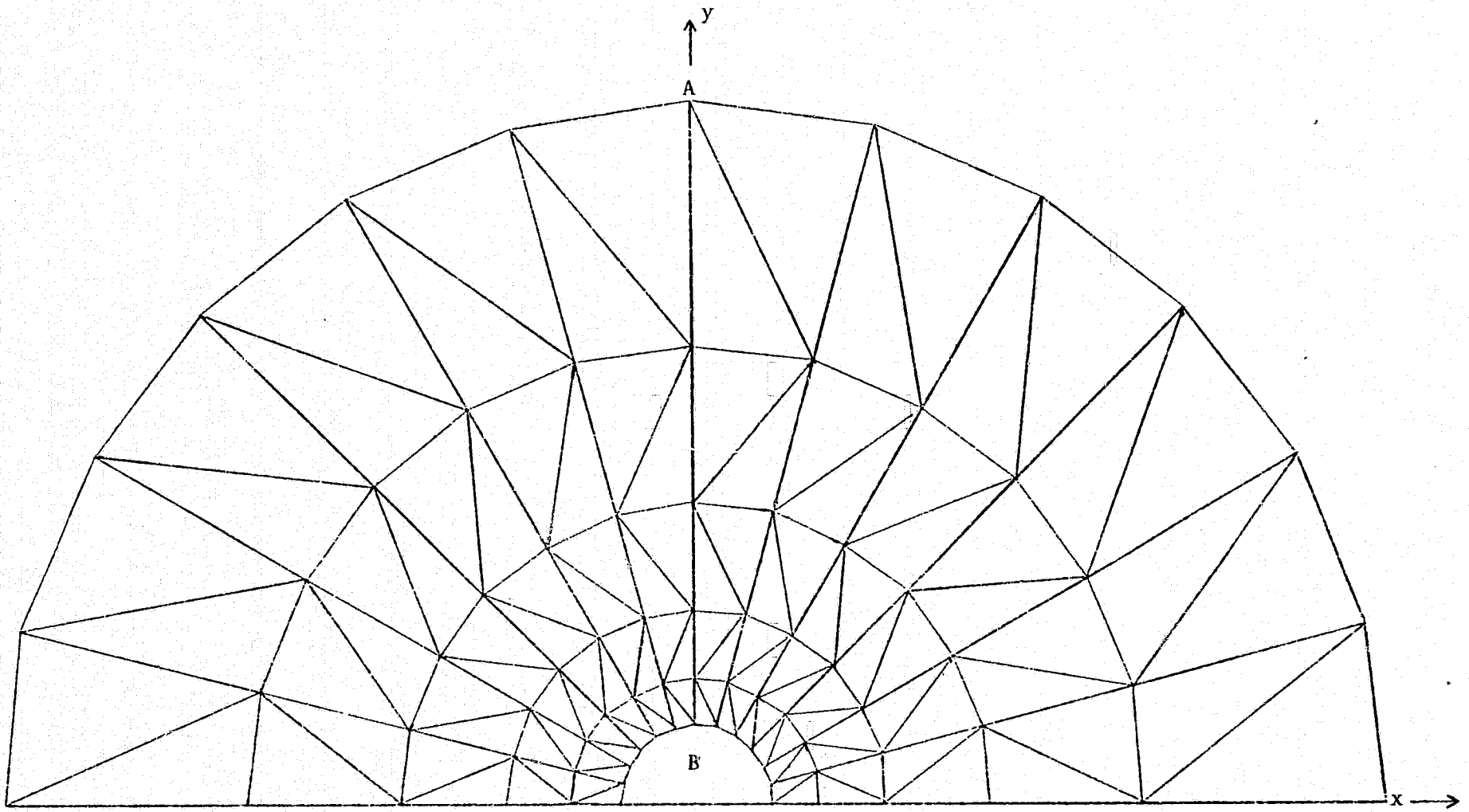

FIG. 8a: Finite Element Map for Notch Problems.
Section B shown in FIG. 8b.

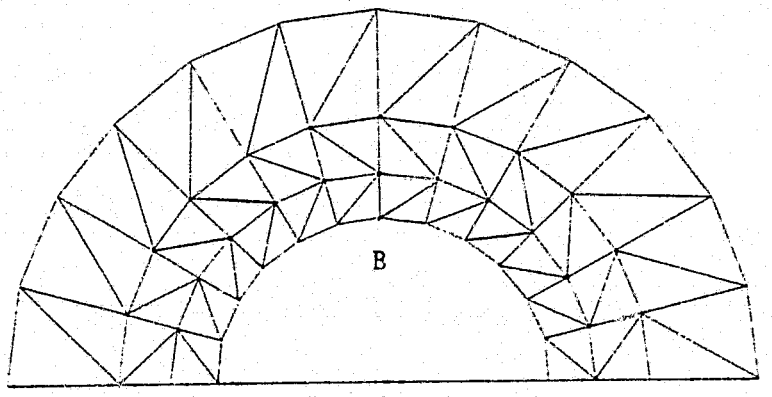

FIG. 8b: Insert for FIG. 8a, Section B shown in FIG. 8c.

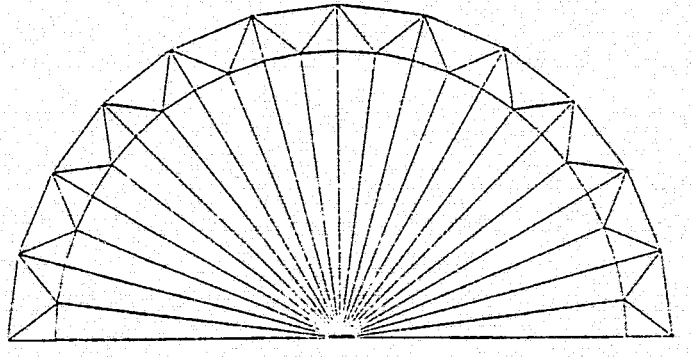

FIG. 8c: Insert for FIG. 8b.

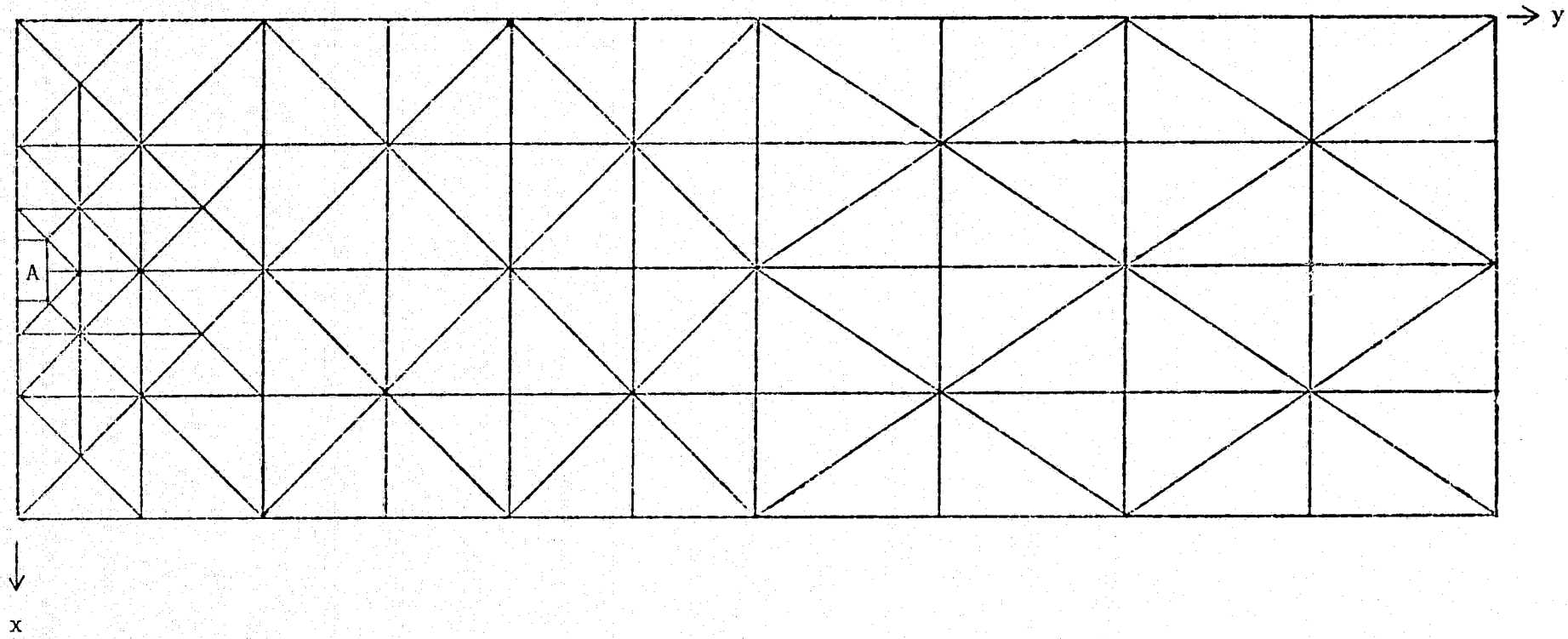

FIG. 9: Finite Element Map for Power Hardening and Bilinear Problems.
Section A shown in FIG. 7.

FIG. 10: Octahedral Stress-Strain Relationships for Power Hardening and Bilinear Materials

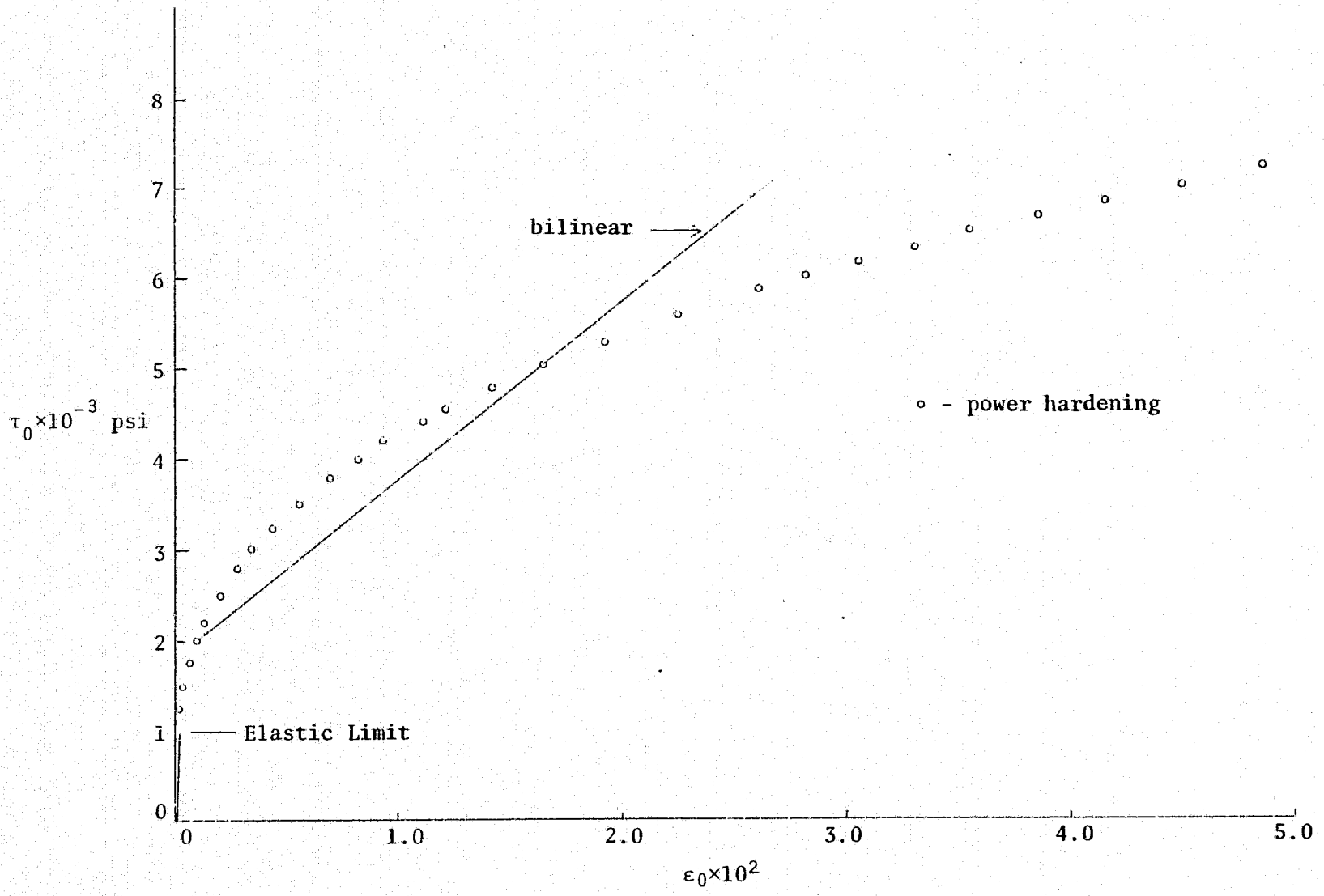

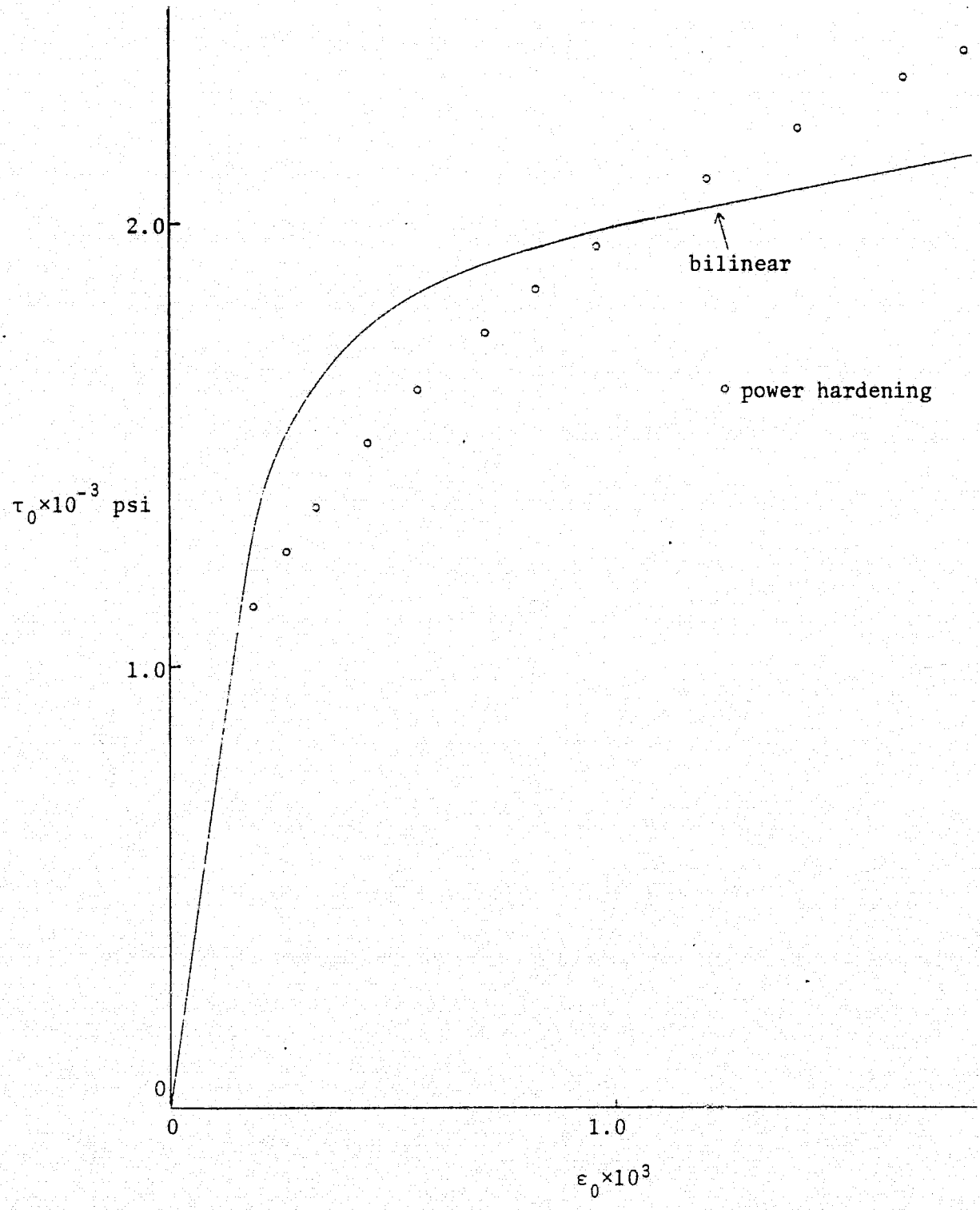

FIG. 11: Small Strain Octahedral Stress-Strain Relationships for Power Hardening and Bilinear Materials

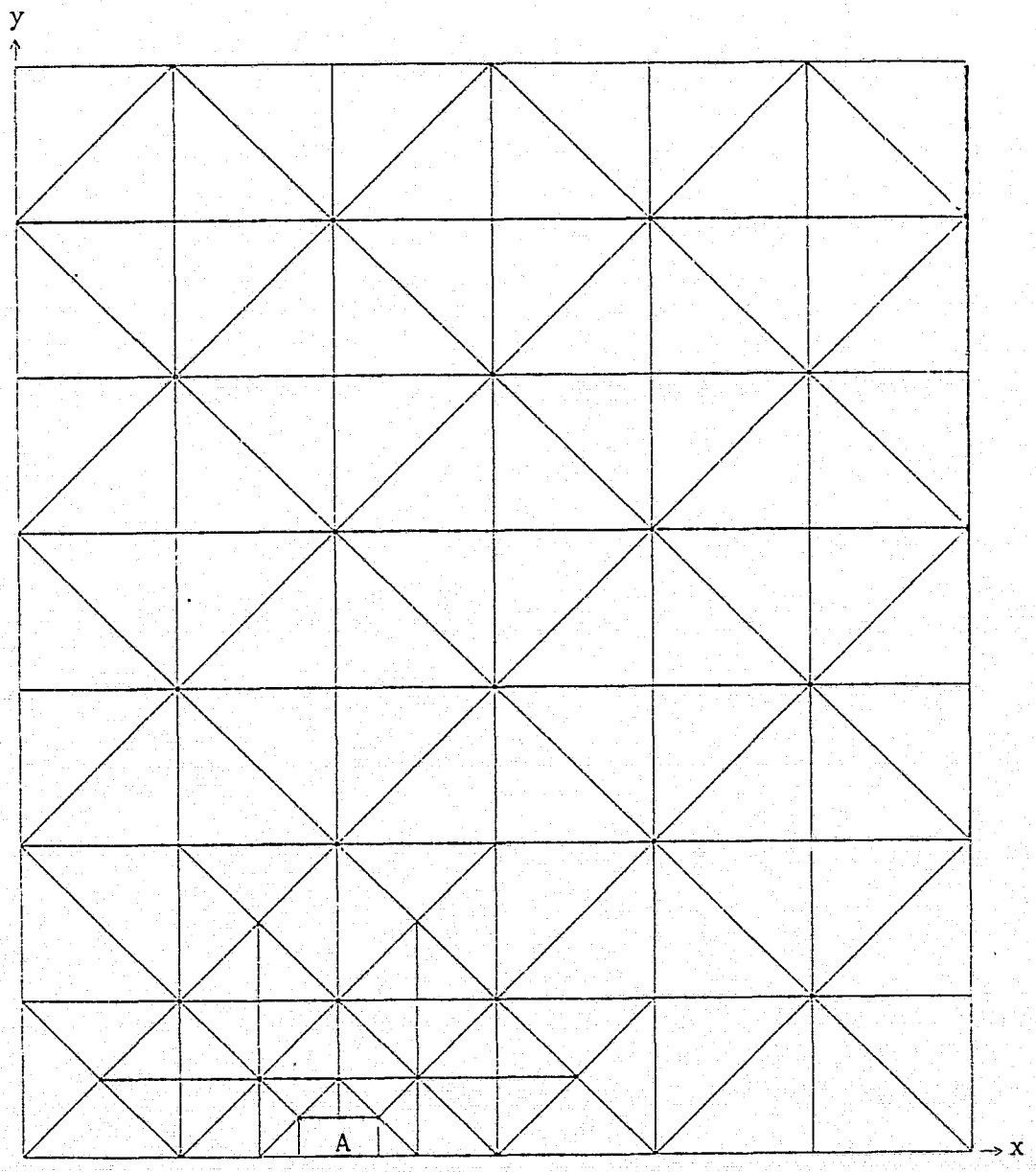

FIG. 12: Finite Element Map for RS Problem. Section A shown in FIG. 7.

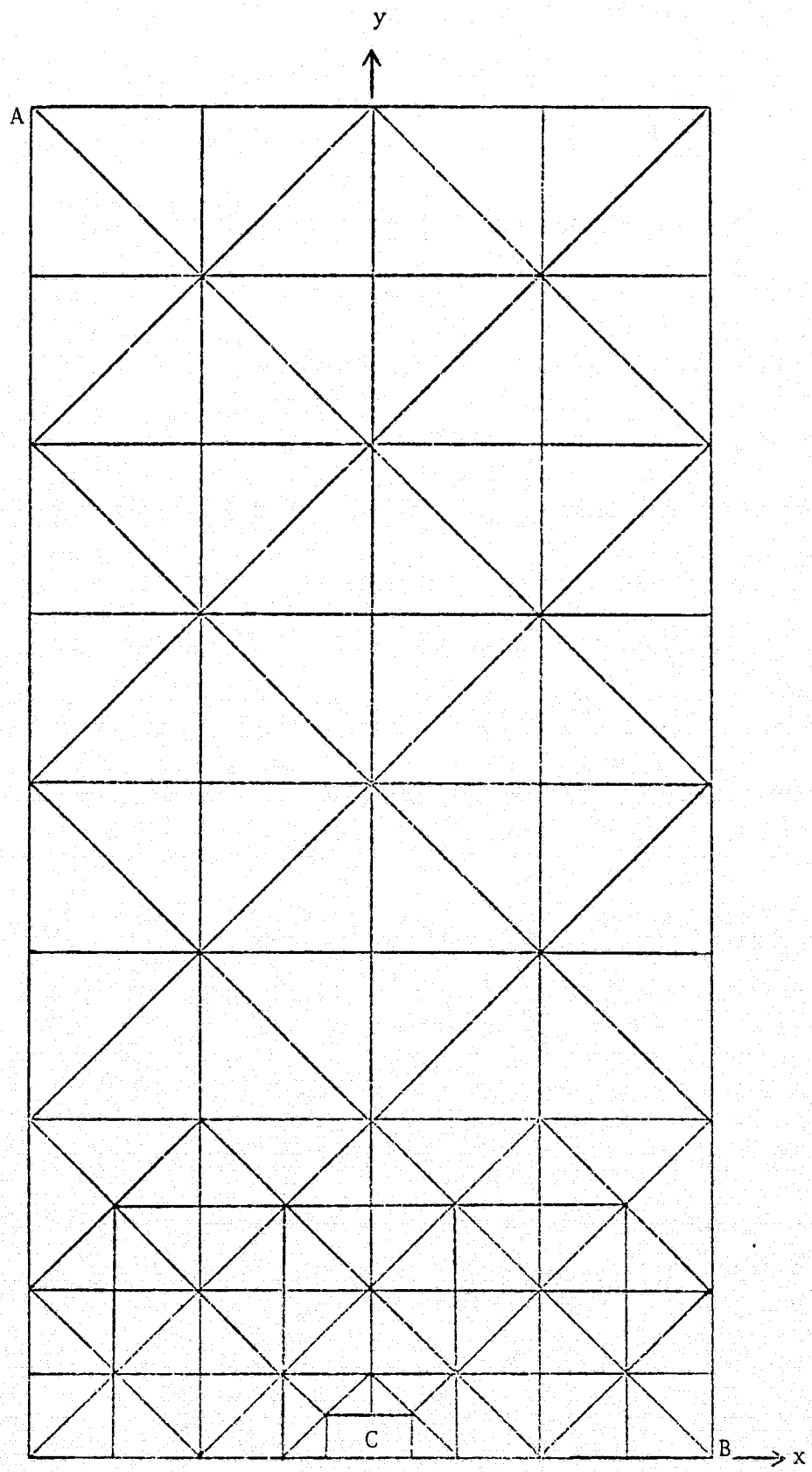

FIG. 13: Finite Element Map for Bend Problem.
Section C shown in FIG. 7.

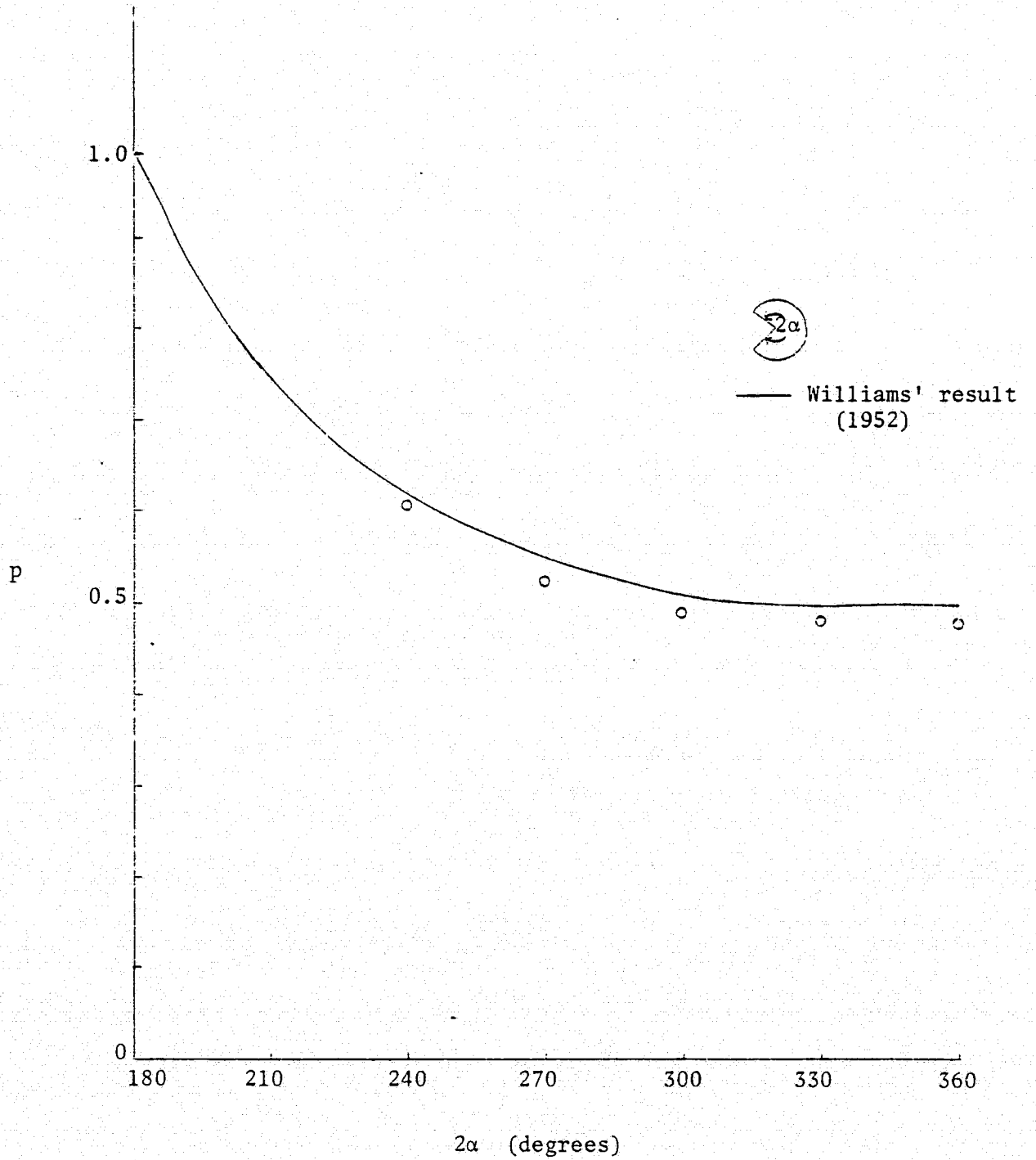

FIG. 14: Elastic Exponent (p) VS. Notch Enclosure Angle (2α)

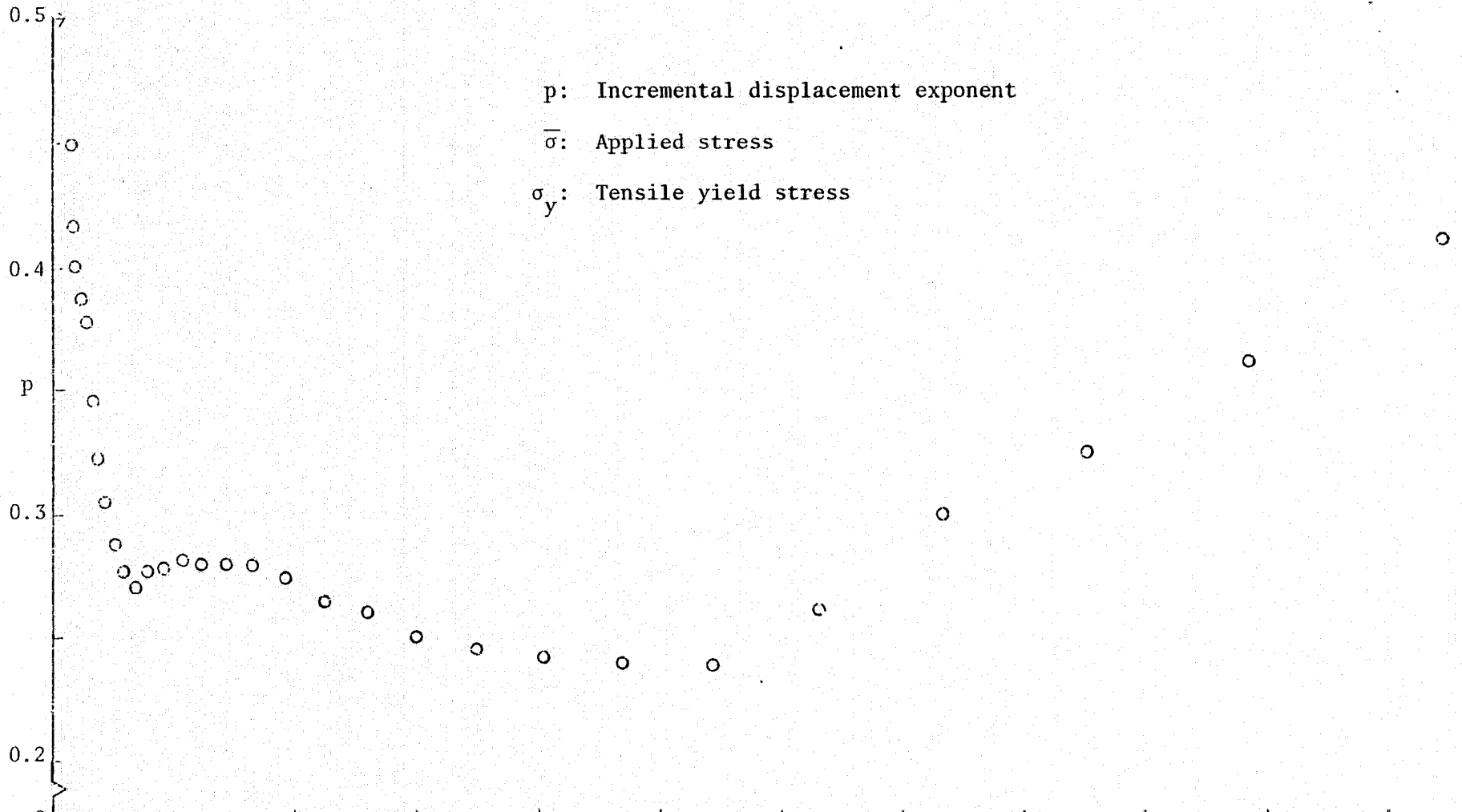

FIG. 15: Incremental Exponent VS. Applied Load for Every Fifth Load Step (PH)

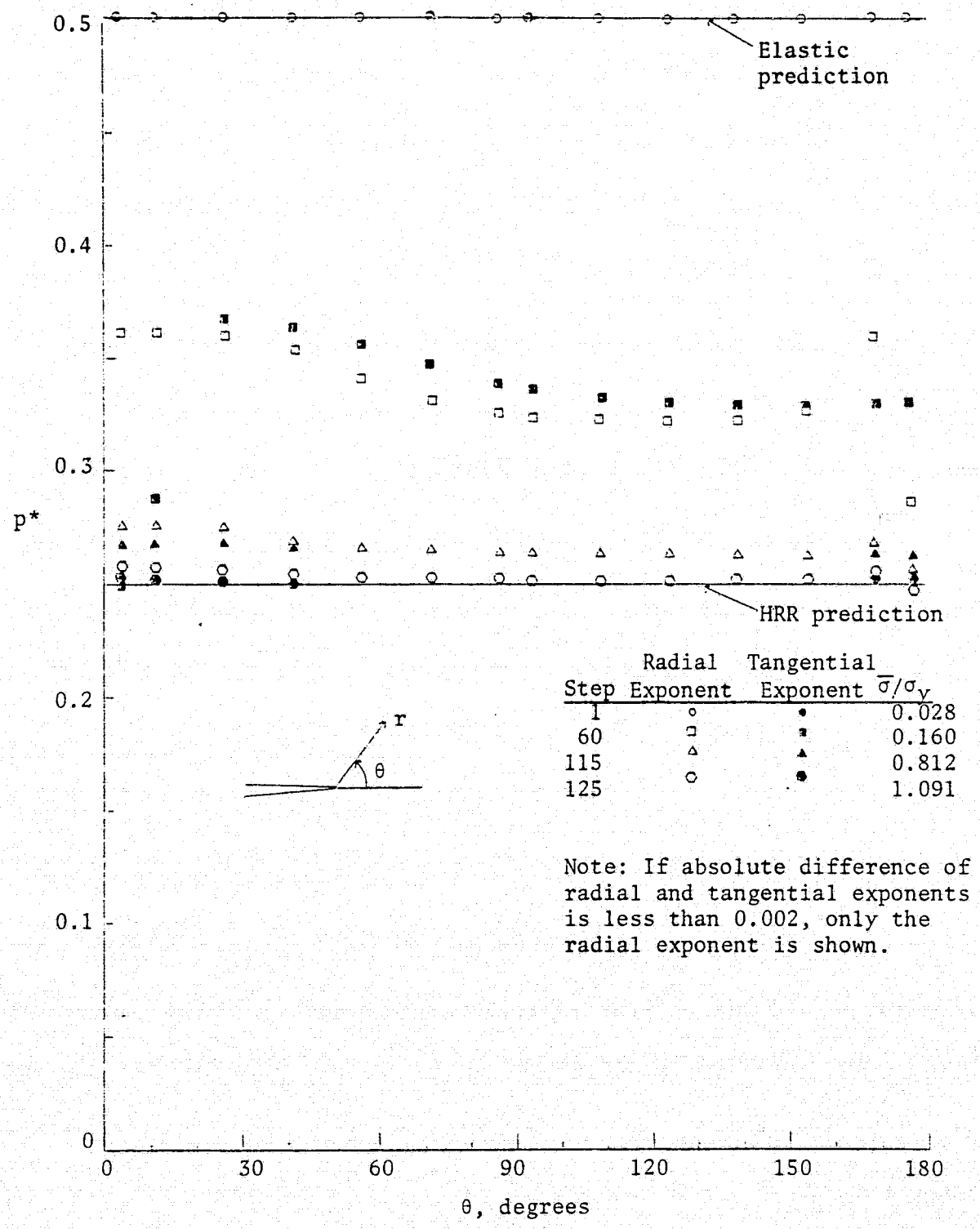

FIG. 16: Accumulated Exponent VS. Angular Position (PH)

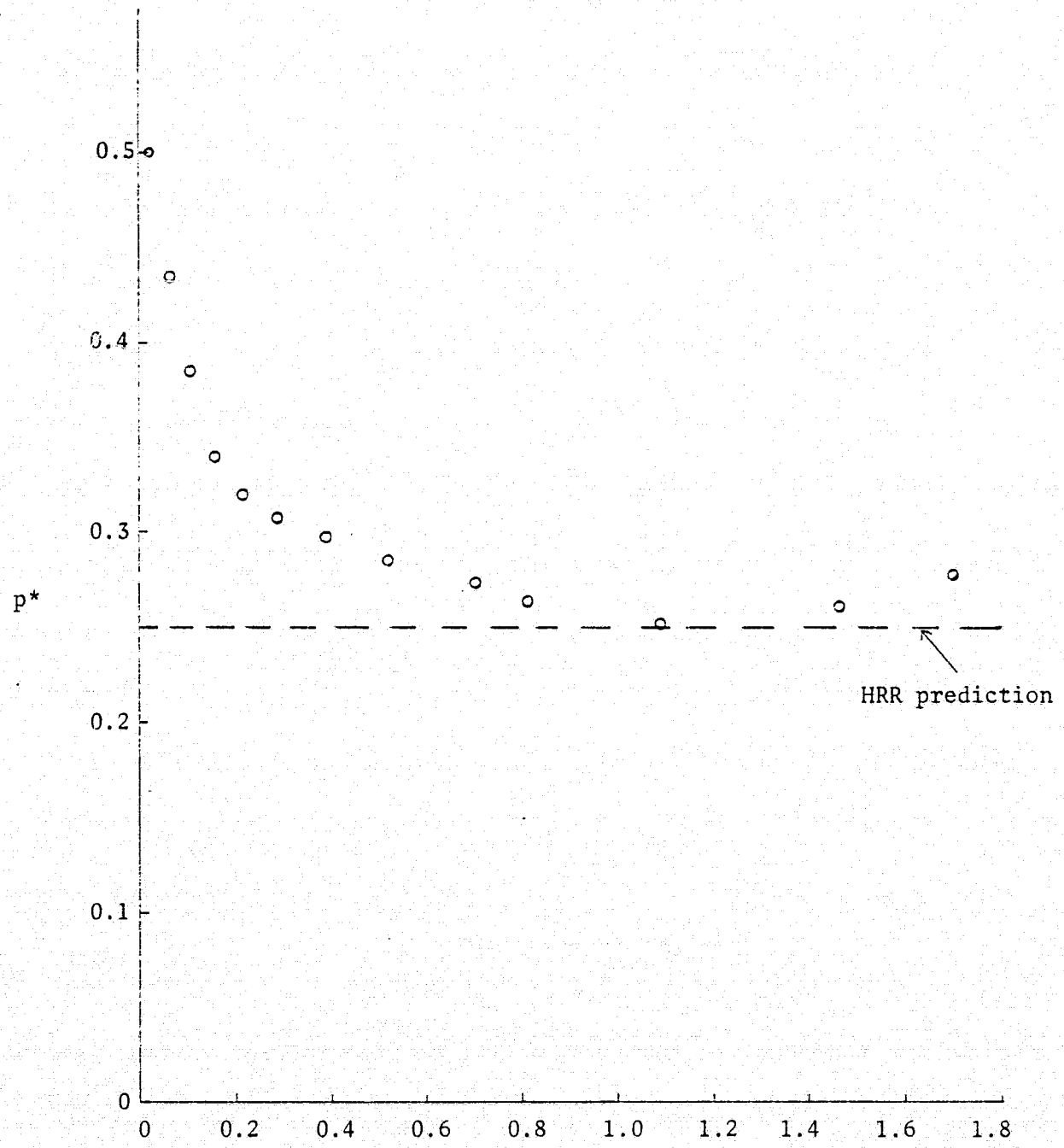

FIG. 17: Accumulated Exponent VS. Applied Load (PH)

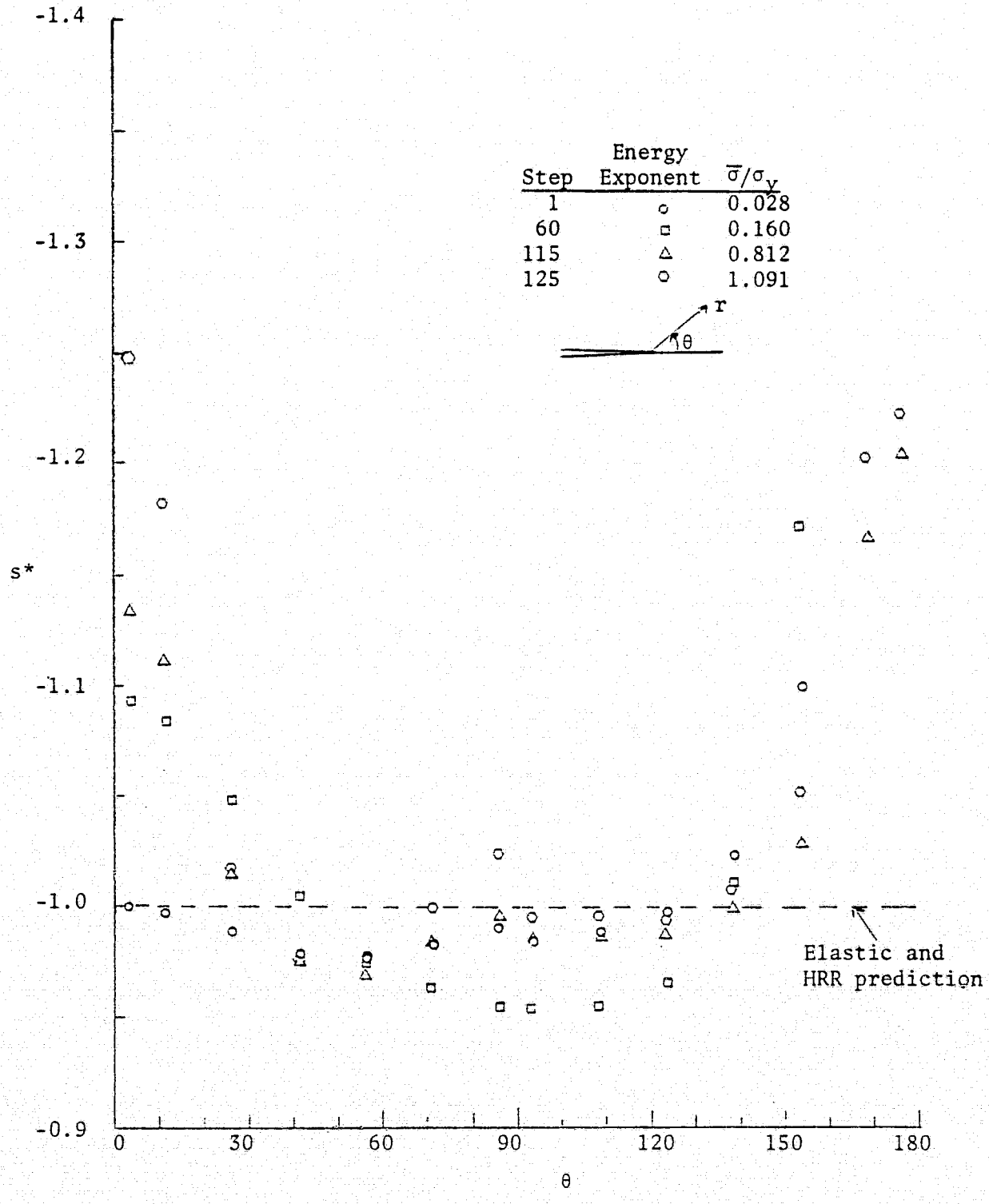

FIG. 18: Energy Exponent VS. Angular Position (PH)

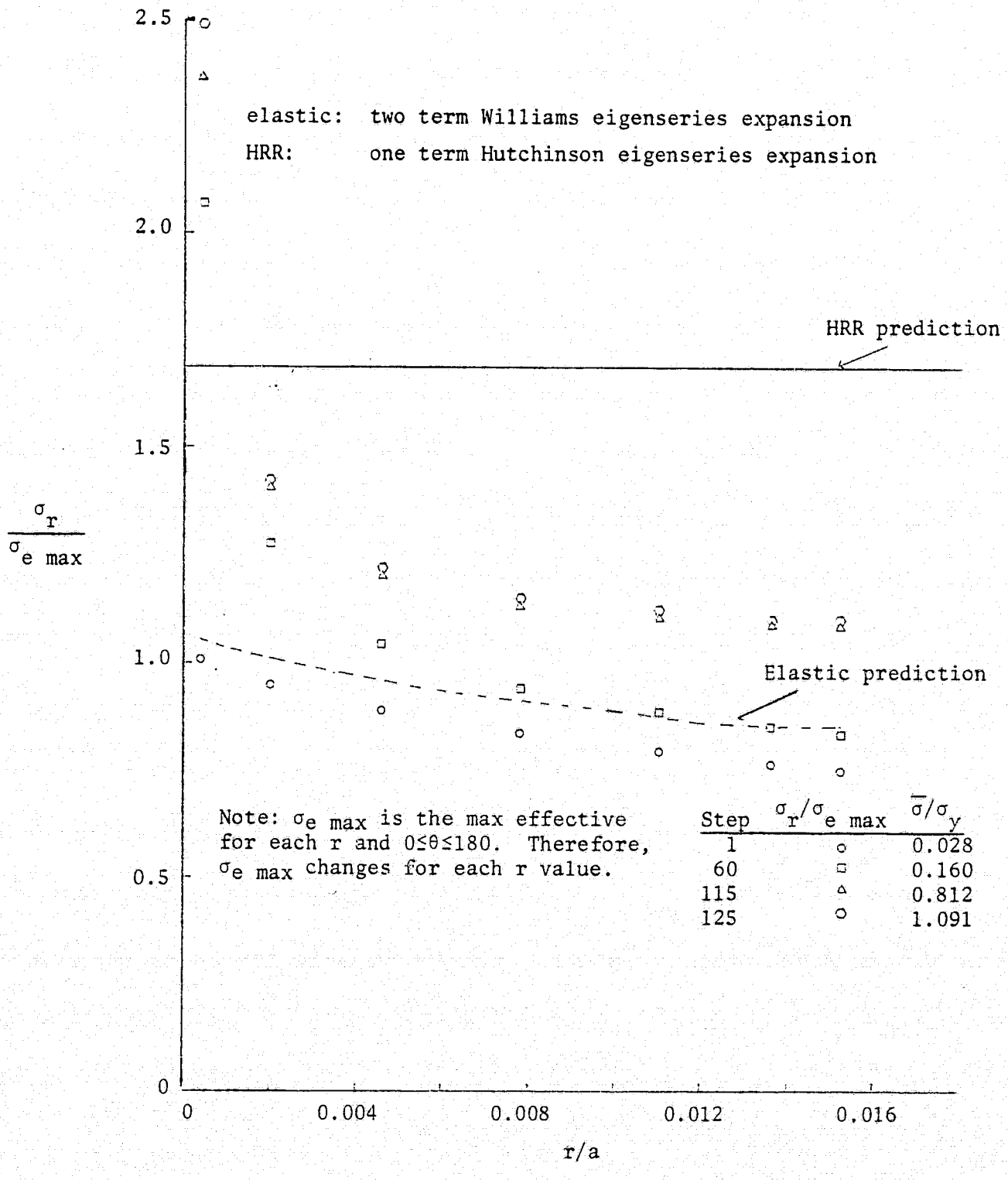

FIG. 19: $\sigma_r/\sigma_{e\ max}$ VS. r/a at $\theta = 3.75°$ (PH)

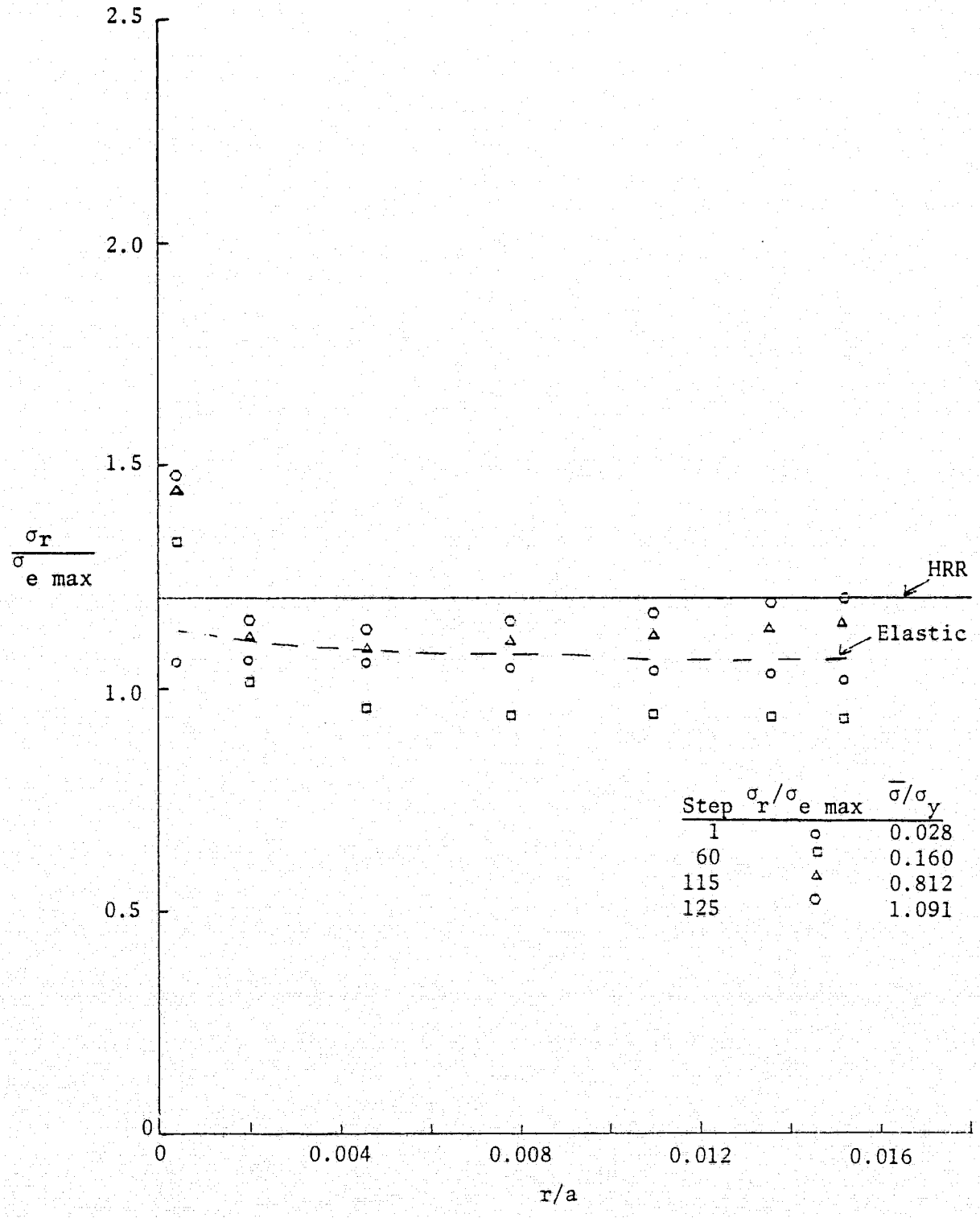

FIG. 20: $\sigma_r/\sigma_{e\ max}$ VS. r/a at $\theta = 93.75°$ (PH)

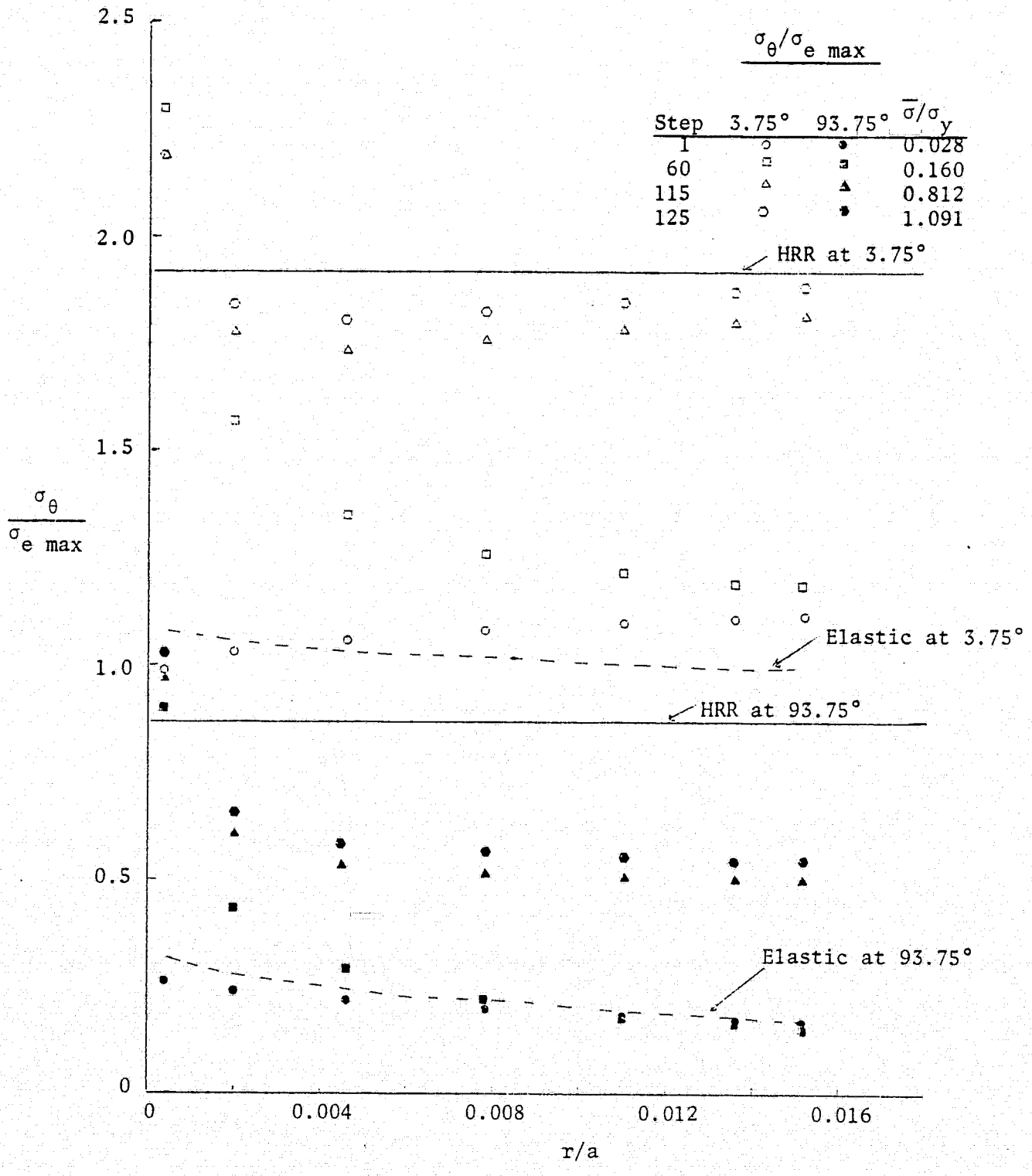

FIG. 21: $\sigma_\theta/\sigma_{e\ max}$ VS. r/a at 3.75° and 93.75° (PH)

FIG. 22: $\sigma_e/\sigma_{e\ max}$ VS. r/a at 3.75° (PH)

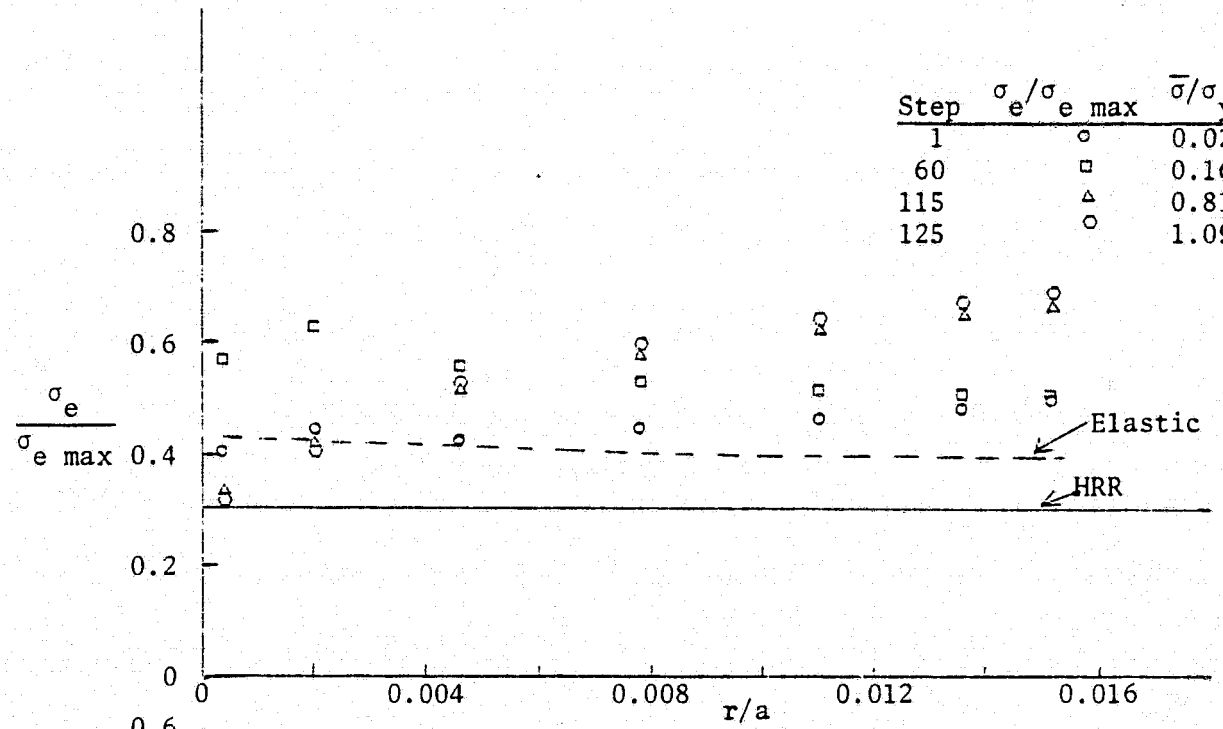

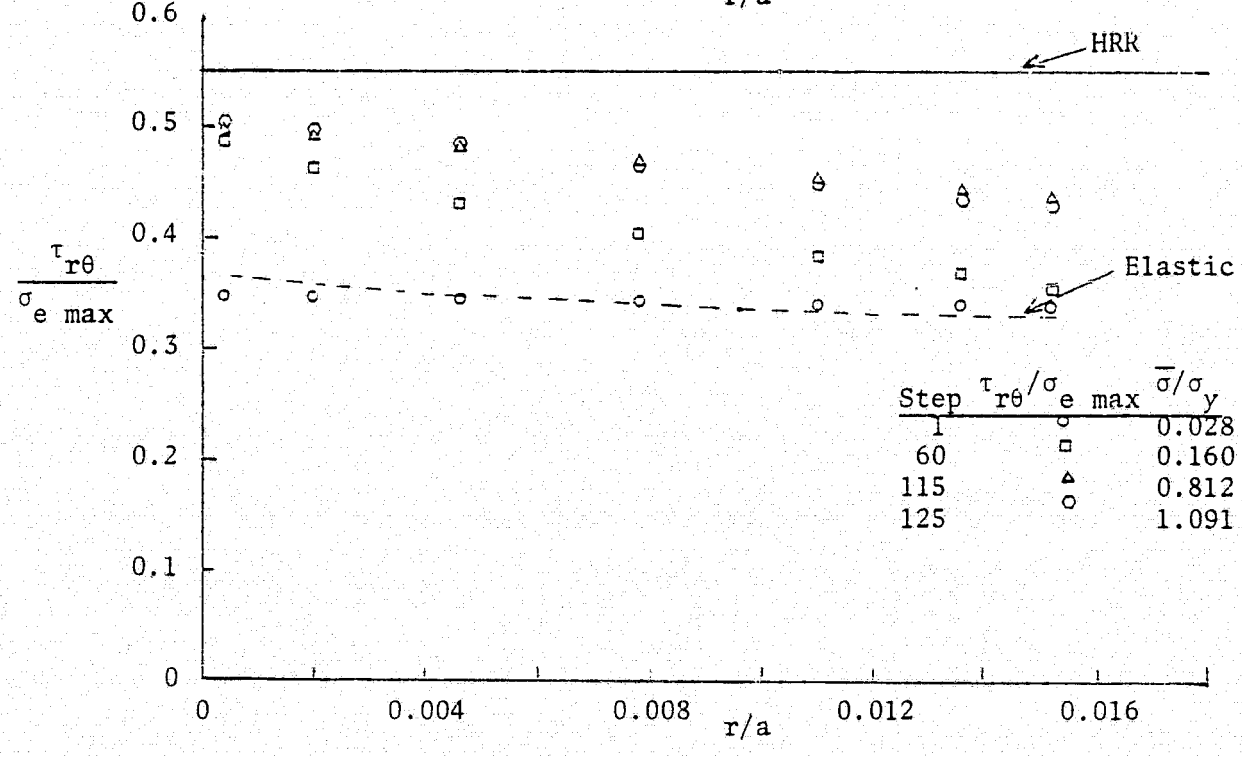

FIG. 23: $\tau_{r\theta}/\sigma_{e\ max}$ VS. r/a at 93.75° (PH)

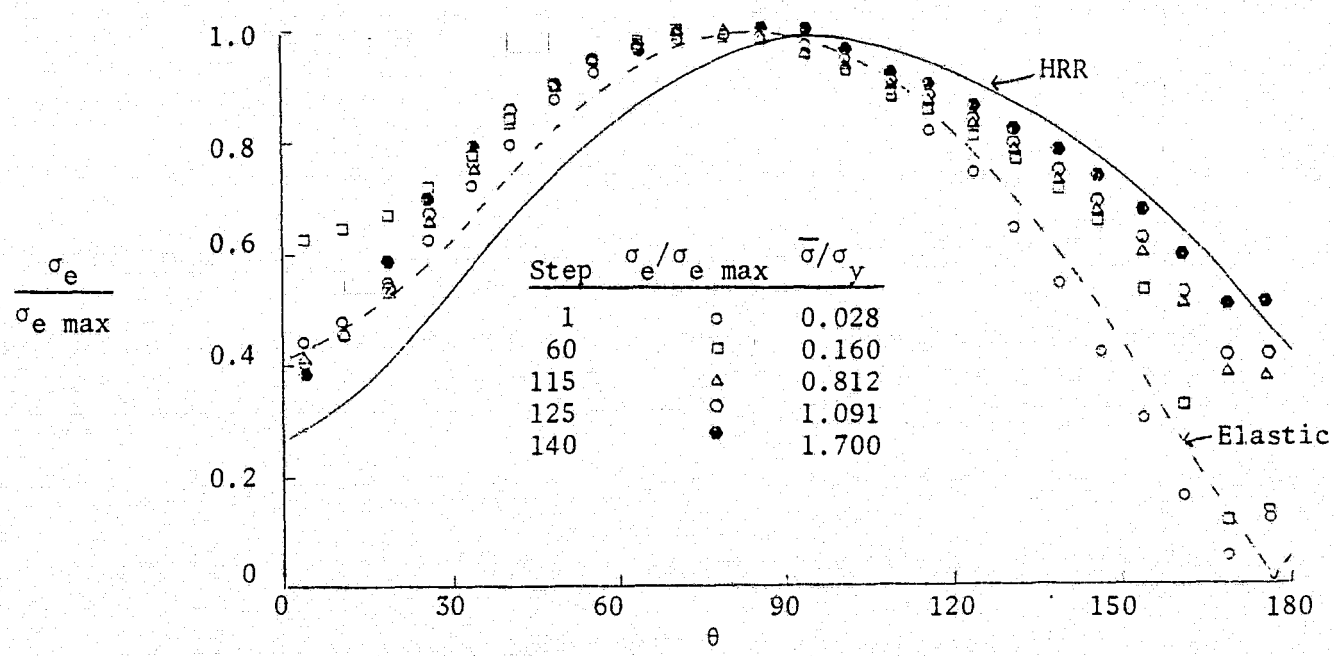

FIG. 24: $\sigma_e/\sigma_{e\ max}$ VS. θ for $\hat{r} = 0.001$ (PH)

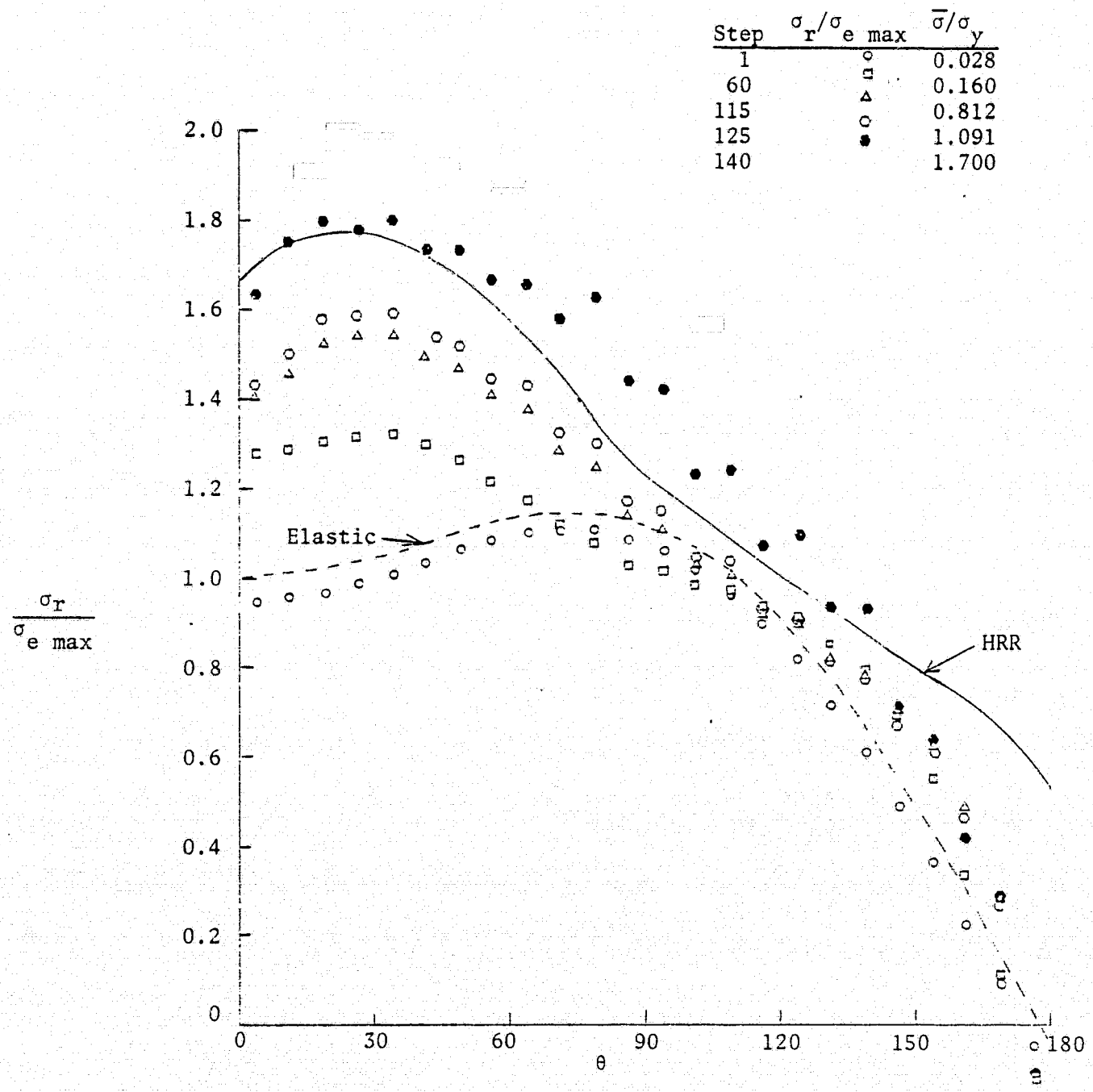

FIG. 25: $\sigma_r/\sigma_{e\ max}$ VS. θ for $\hat{r} = 0.001$ (PH)

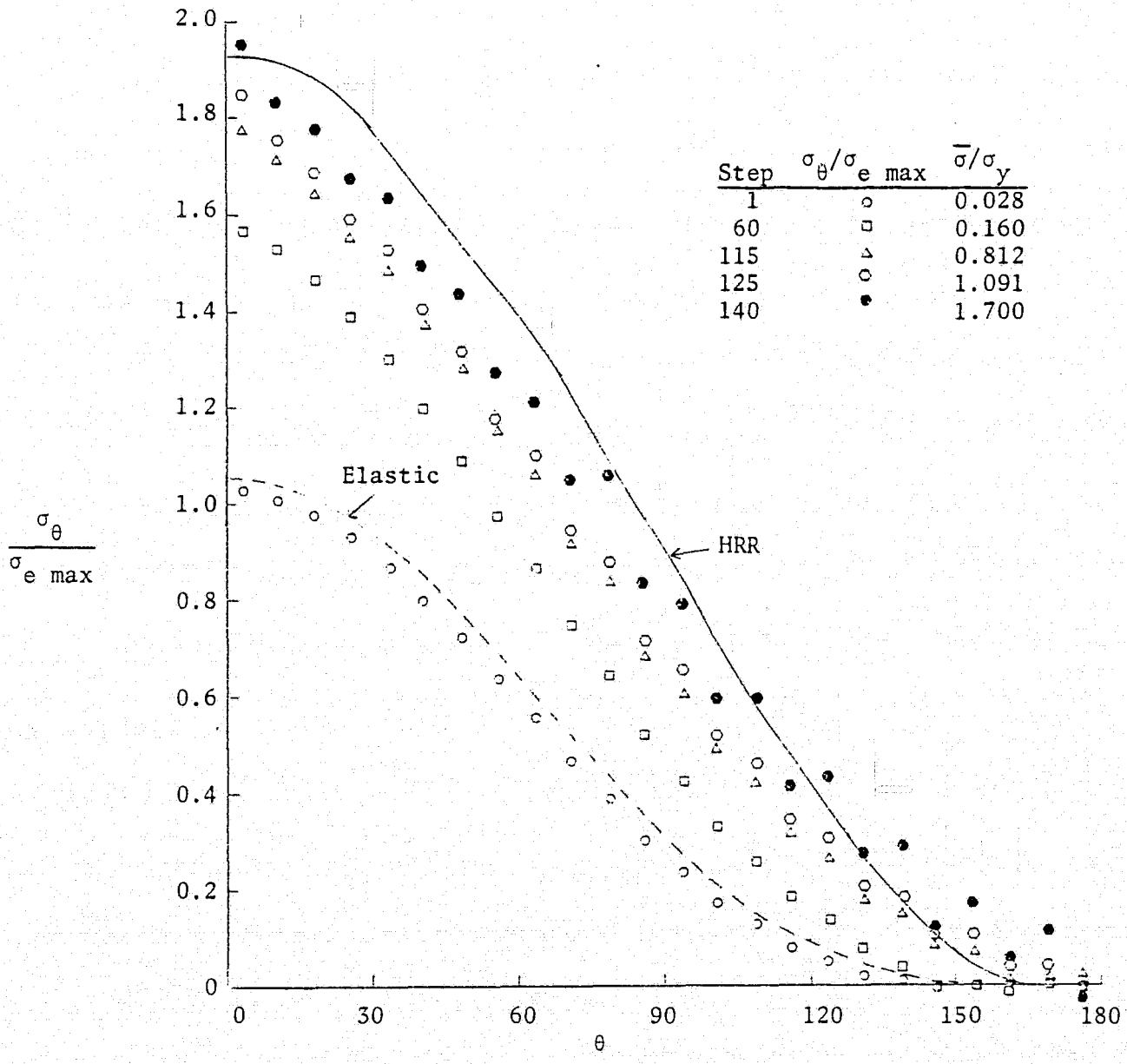

FIG. 26: $\sigma_\theta/\sigma_{e\ max}$ VS. θ for $\hat{r}$ = 0.001 (PH)

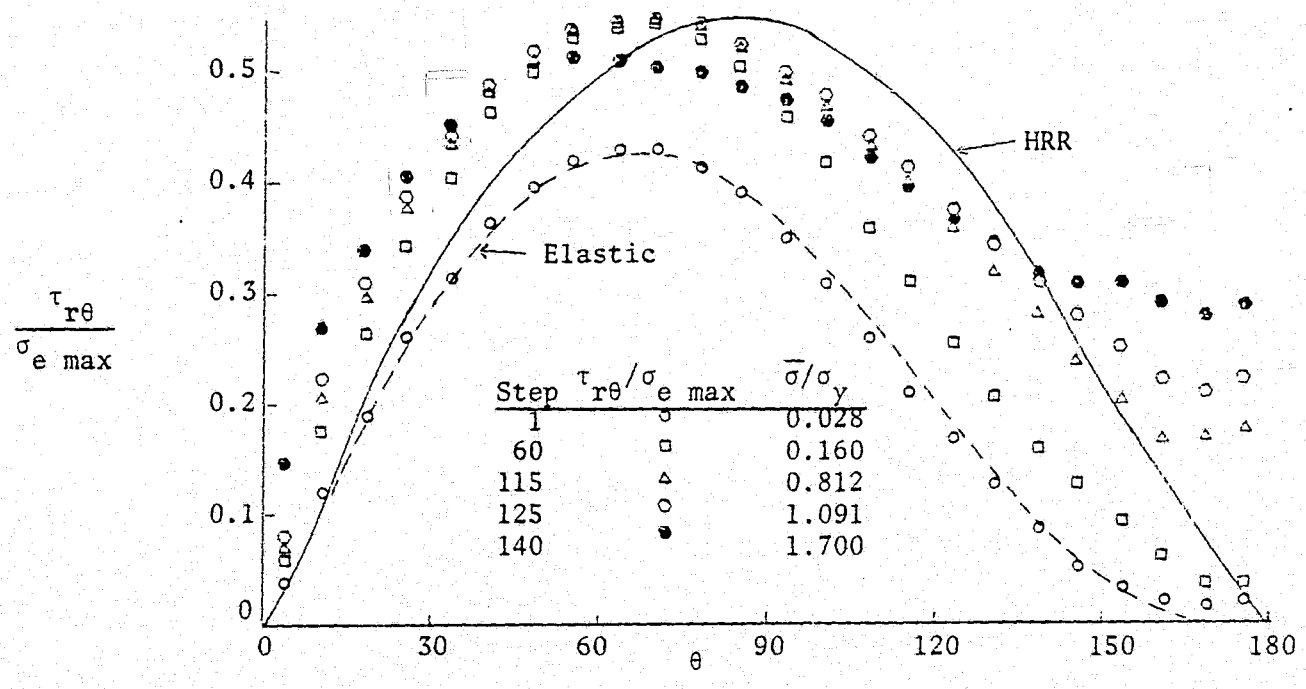

FIG. 27: $\tau_{r\theta}/\sigma_{e\ max}$ VS. θ for $\hat{r} = 0.001$ (PH)

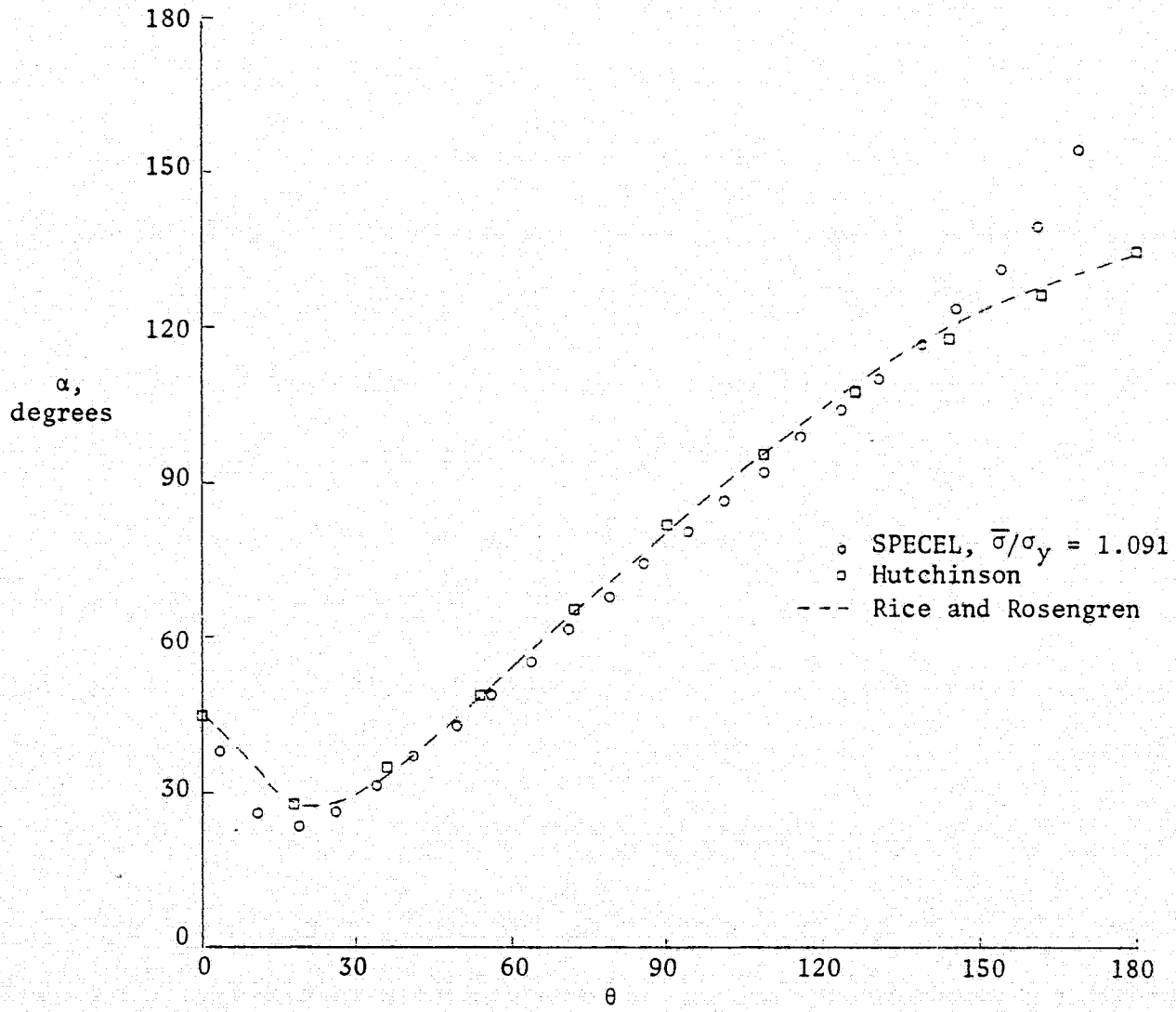

FIG. 28: Max Shear Direction (α) VS. θ (PH)

FIG. 29: Normalized J VS. Distance from the Crack Tip (PH)

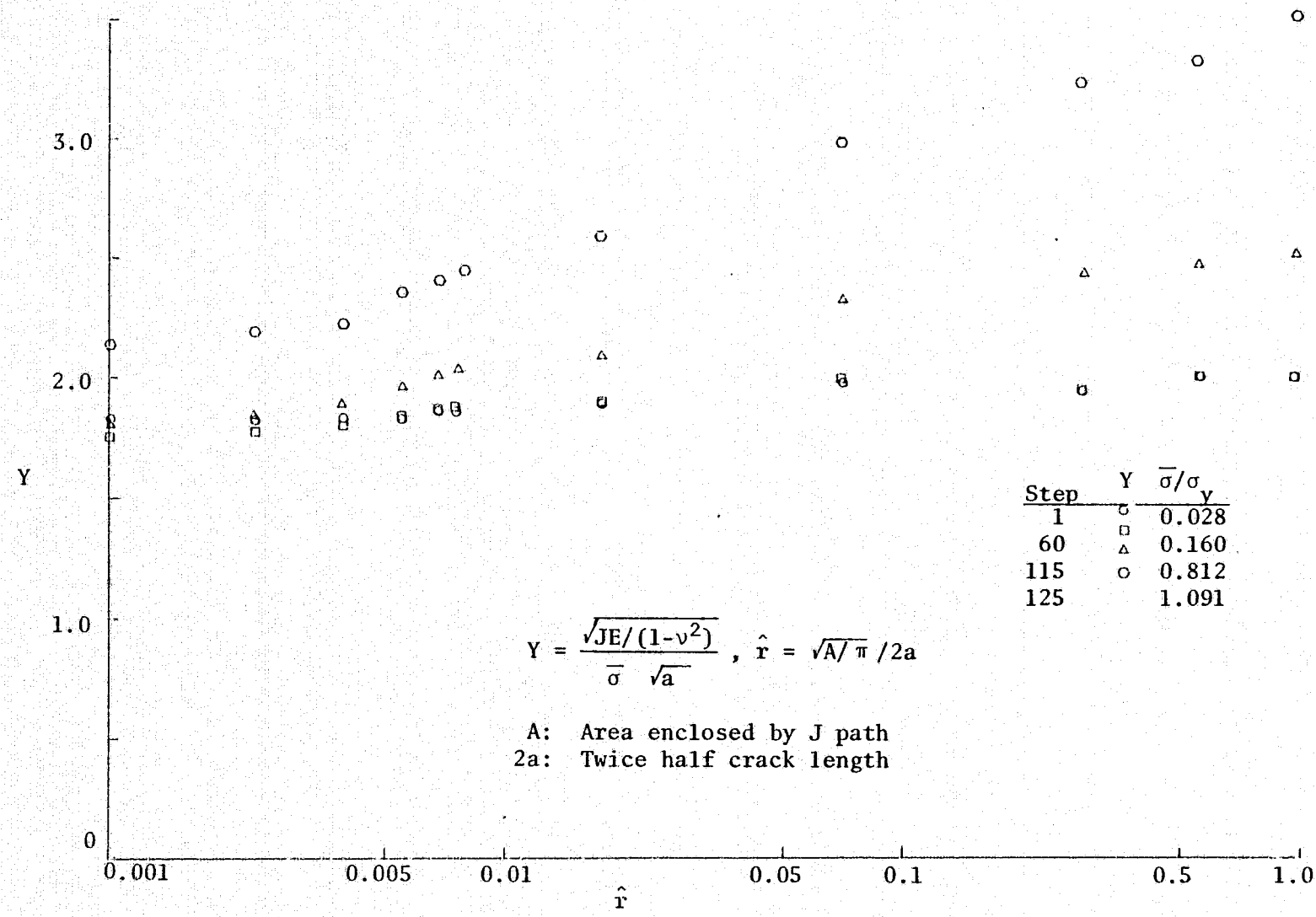

Step	Y	$\bar{\sigma}/\sigma_y$
1	○ □	0.028
60	△	0.160
115	○	0.812
125		1.091

$$Y = \frac{\sqrt{JE/(1-\nu^2)}}{\bar{\sigma}\ \sqrt{a}}\ ,\ \hat{r} = \sqrt{A/\pi}\ /2a$$

A: Area enclosed by J path
2a: Twice half crack length

FIG. 30: Plastic Strain Intensity Factor VS. Applied Stress (PH)

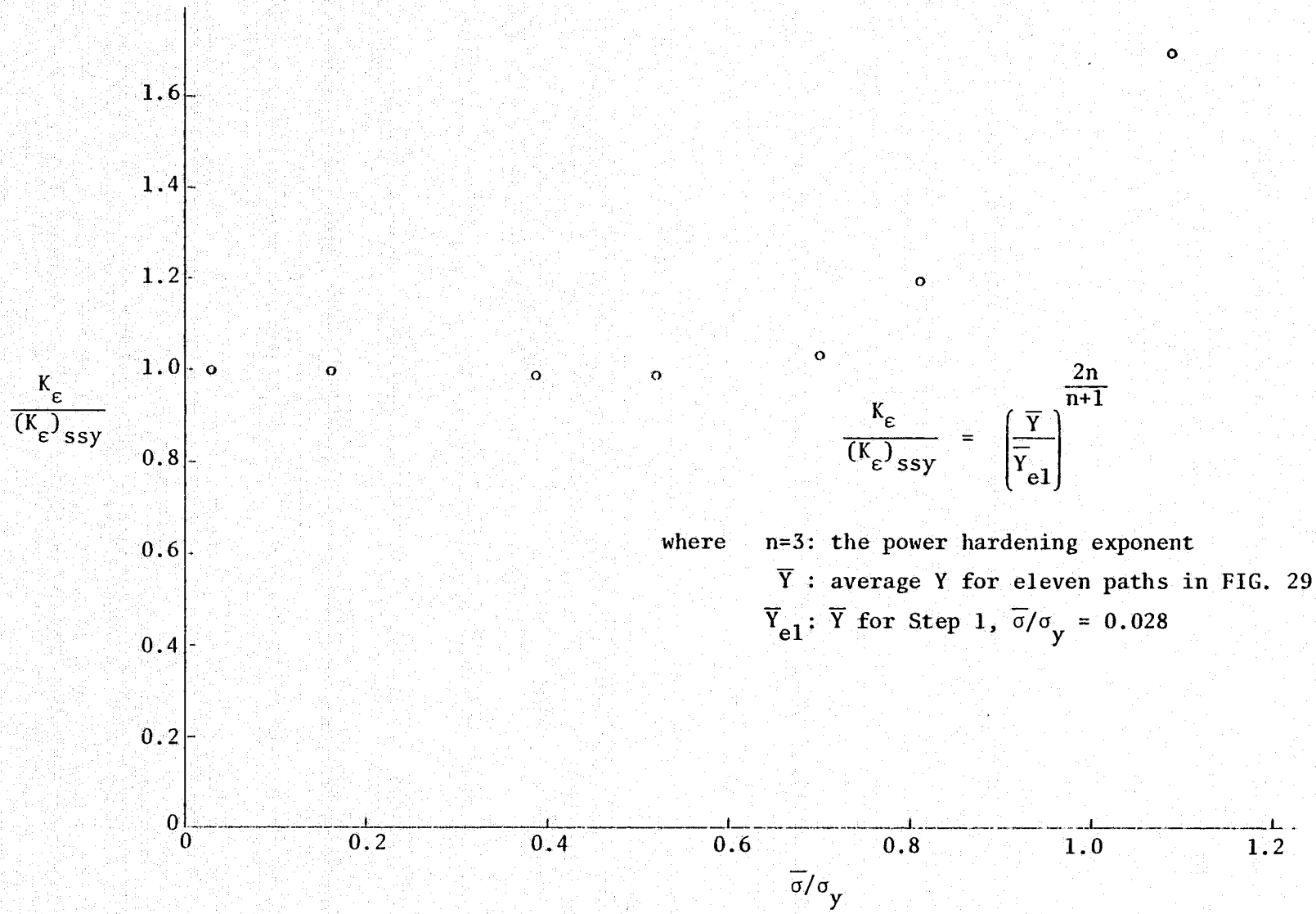

FIG. 31: J* VS. $\bar{\sigma}/\sigma_y$ for J Paths Outside the Special Element (PH)

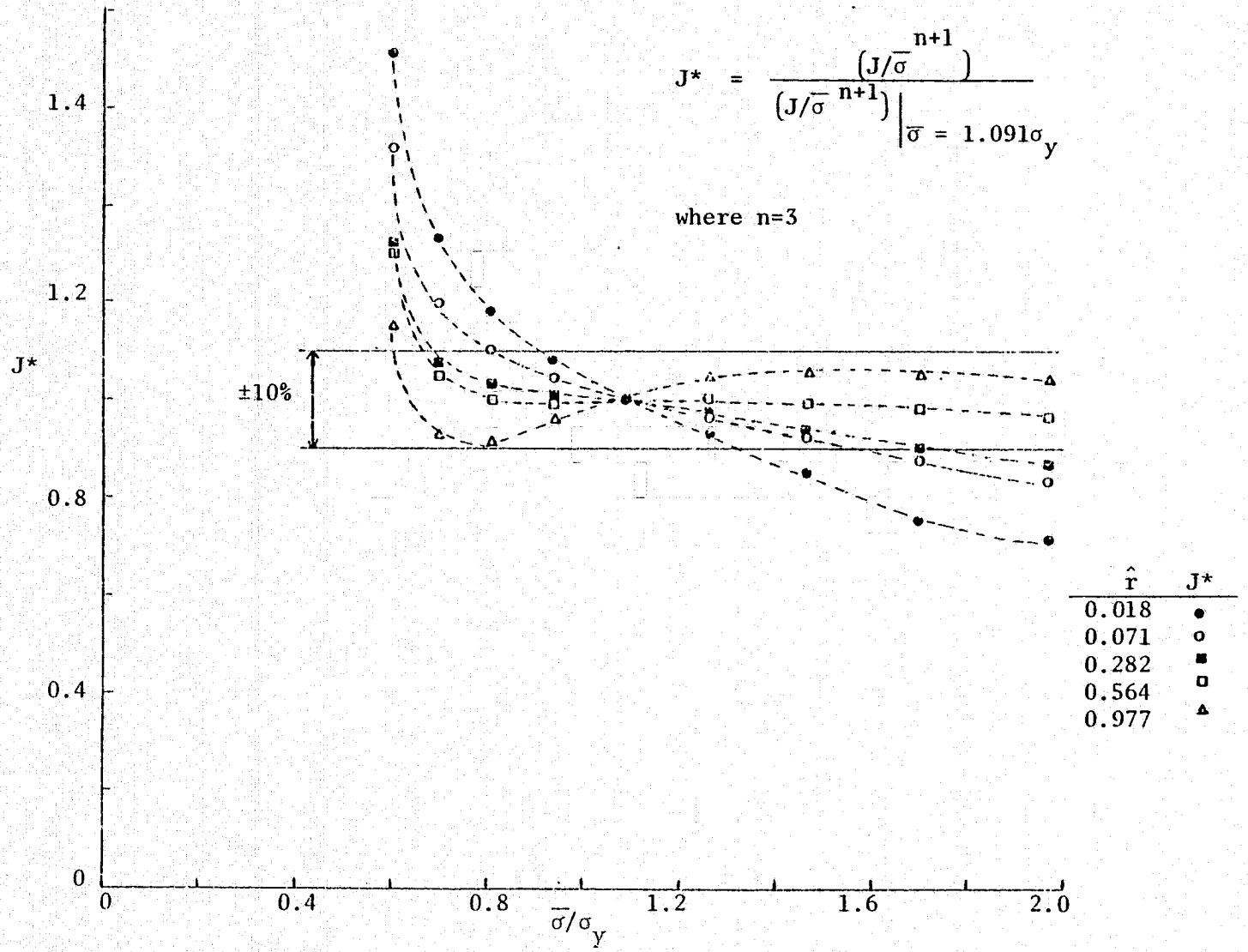

FIG. 32: Y/Y_{el} VS. $\bar{\sigma}/\sigma_y$ for Near and Far Field Paths (PH)

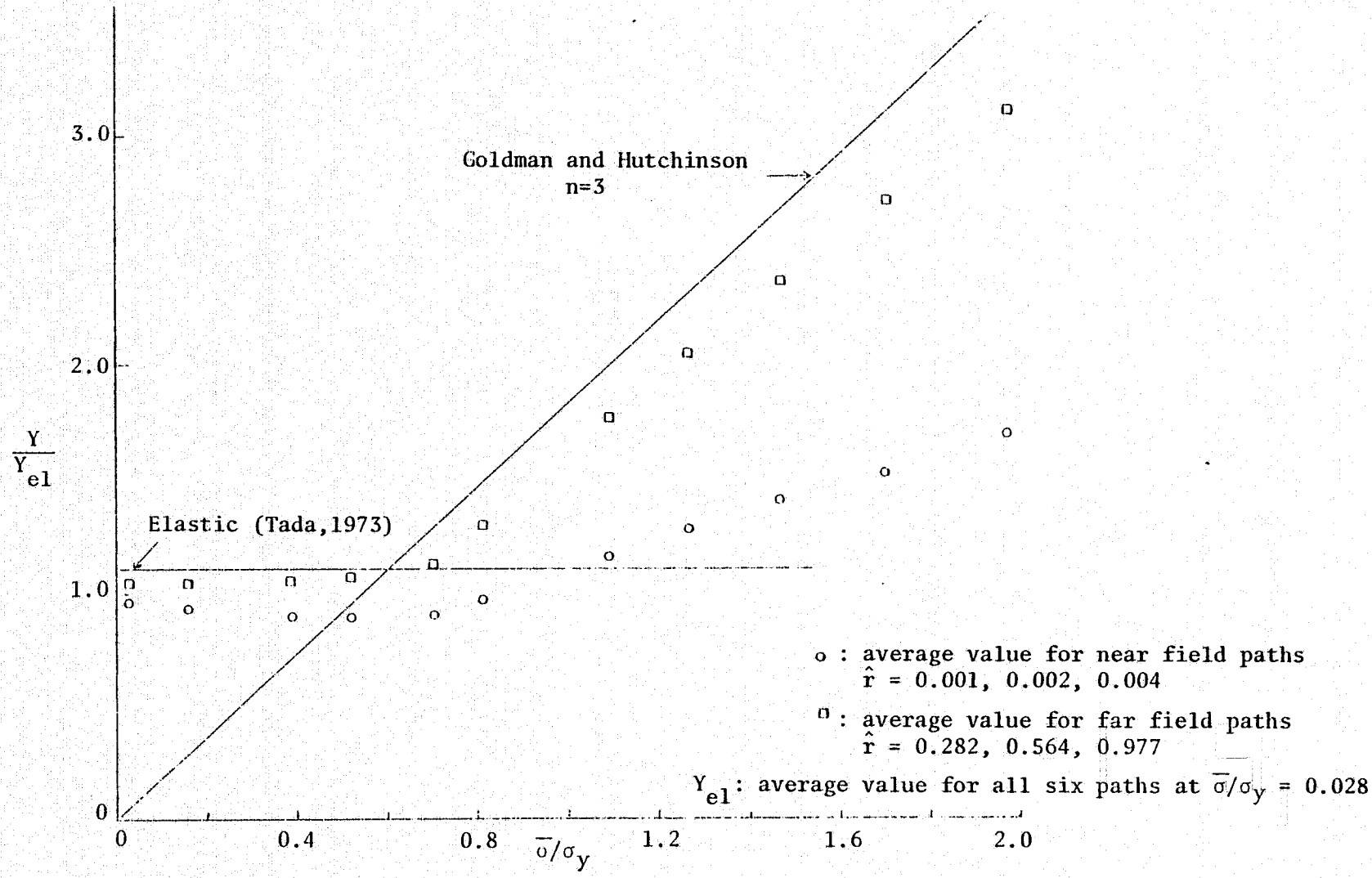

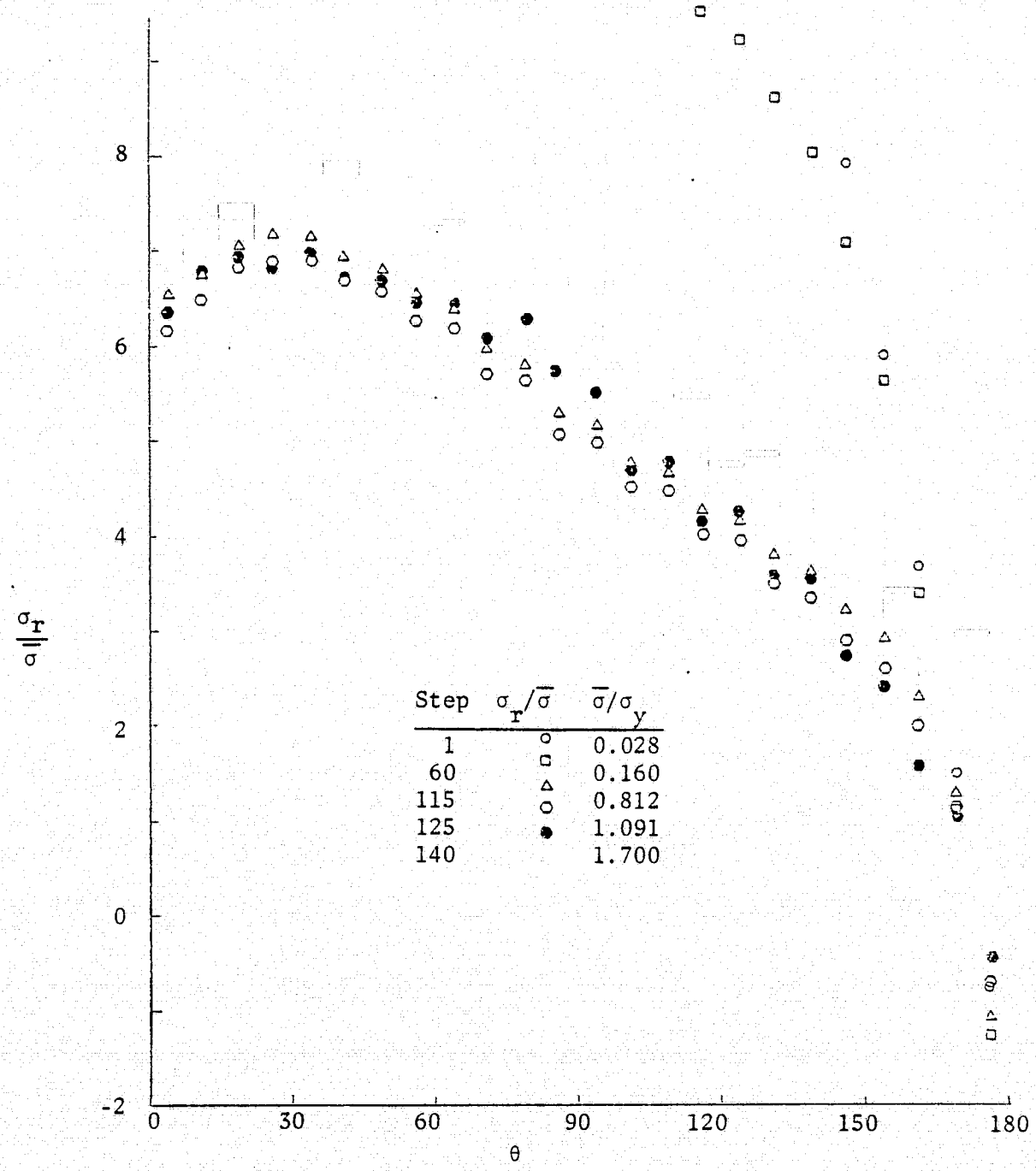

FIG. 33: $\sigma_r/\bar{\sigma}$ VS. θ for $\hat{r} = 0.001$ (PH)

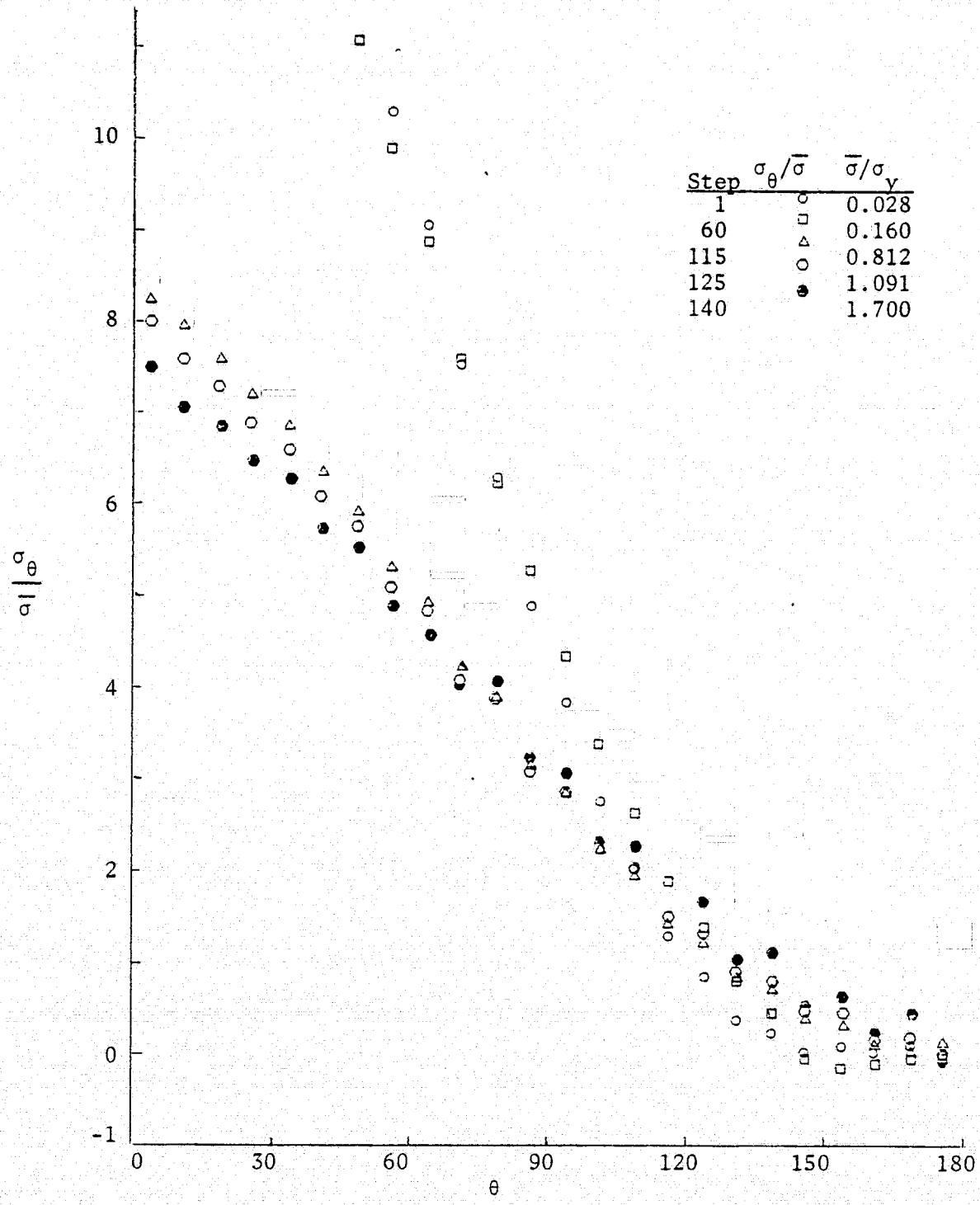

FIG. 34: $\sigma_\theta/\bar{\sigma}$ VS. θ for $\hat{r} = 0.001$ (PH)

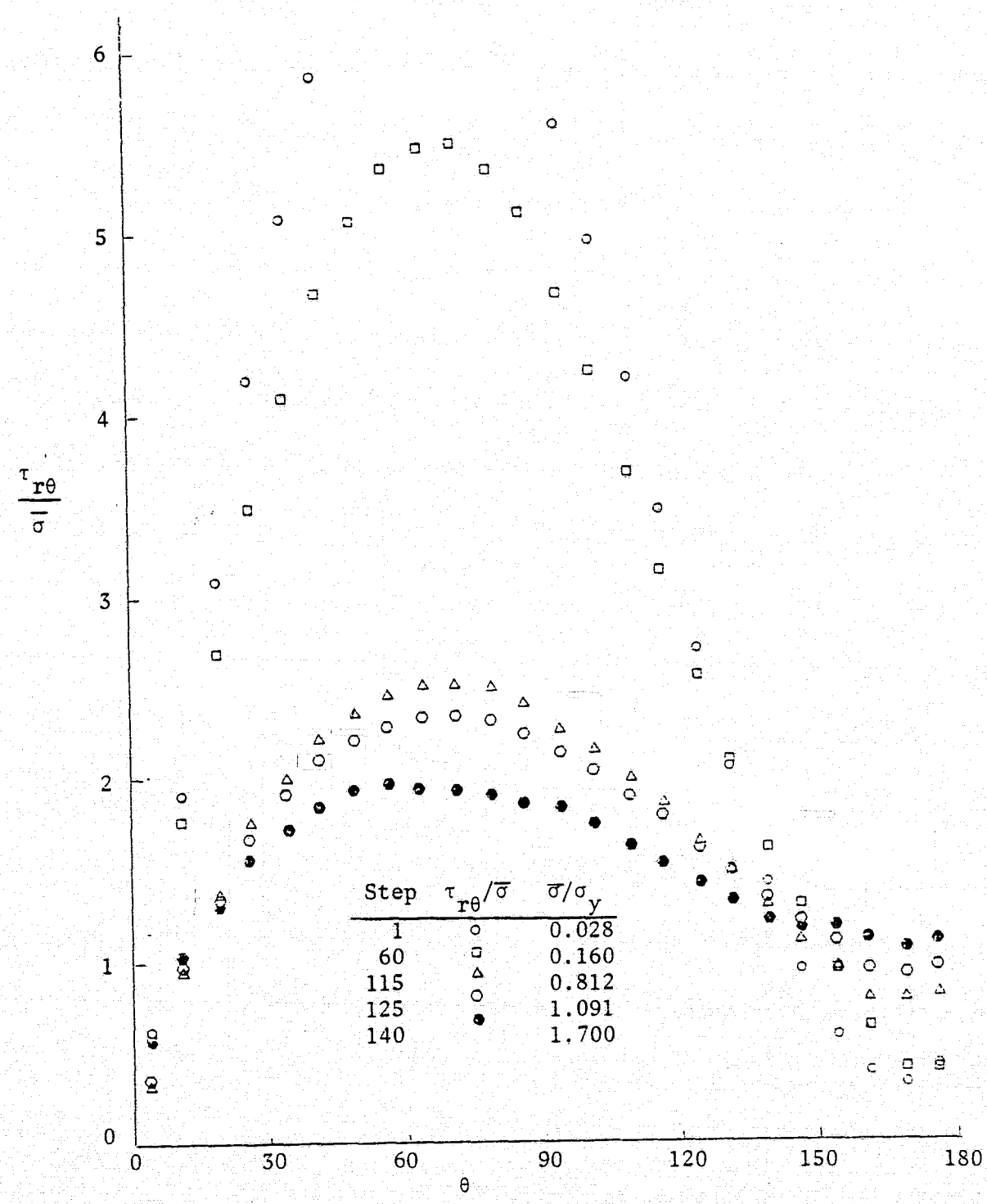

FIG. 35: $\tau_{r\theta}/\bar{\sigma}$ VS. θ for $\hat{r} = 0.001$ (PH)

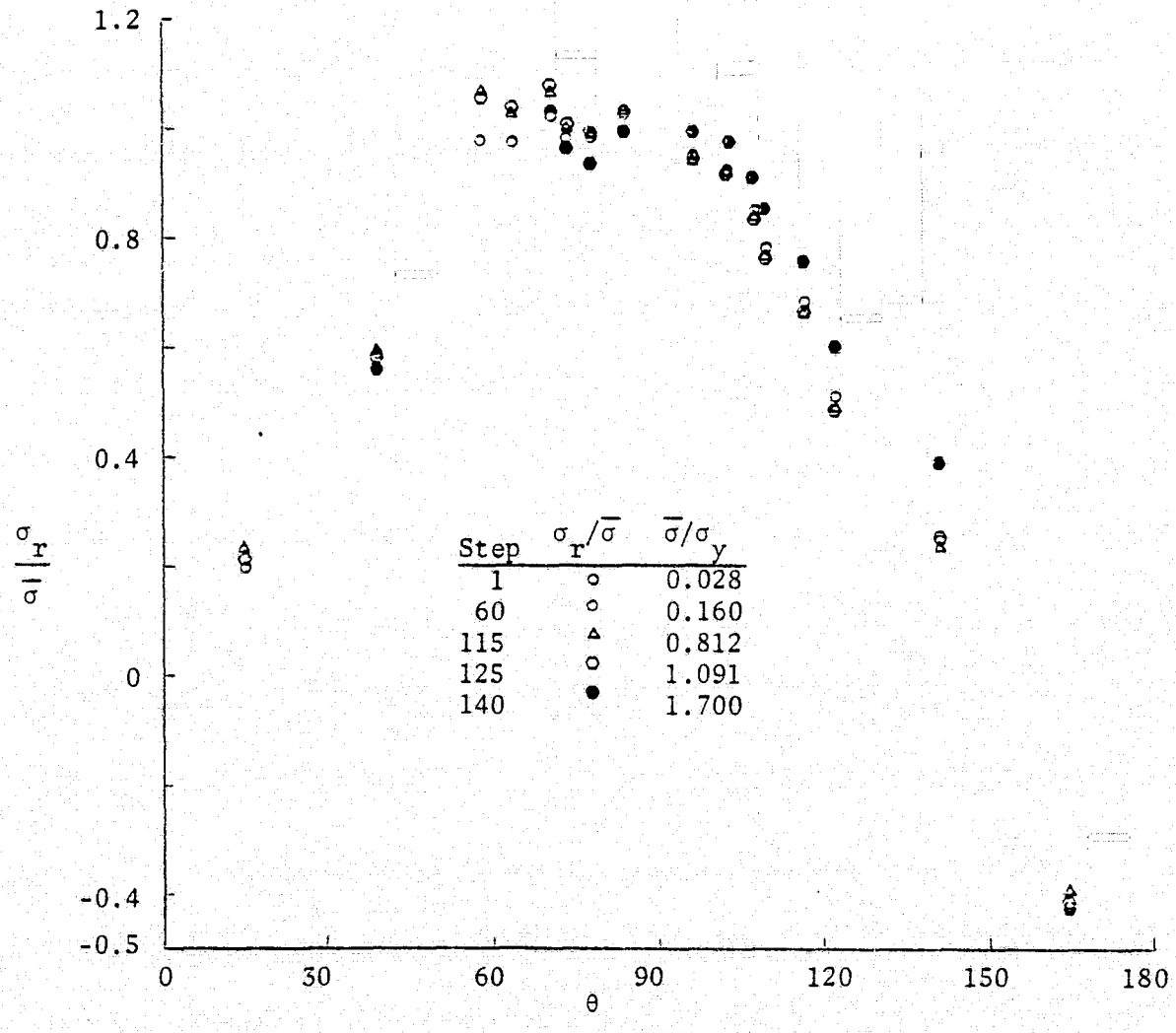

FIG. 36: $\sigma_r/\bar{\sigma}$ VS. θ for $\hat{r} = 0.977$ (PH)

FIG. 37: $\sigma_\theta/\bar{\sigma}$ VS. θ for $\hat{r}$ = 0.977 (PH)

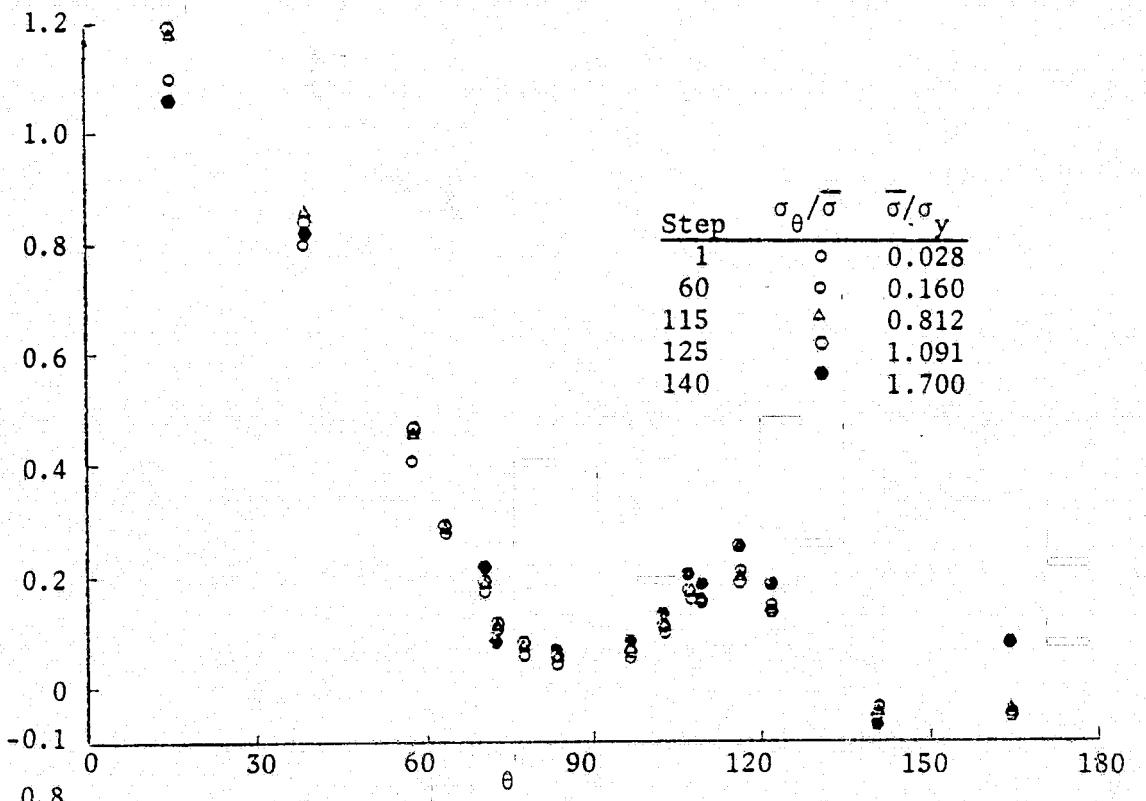

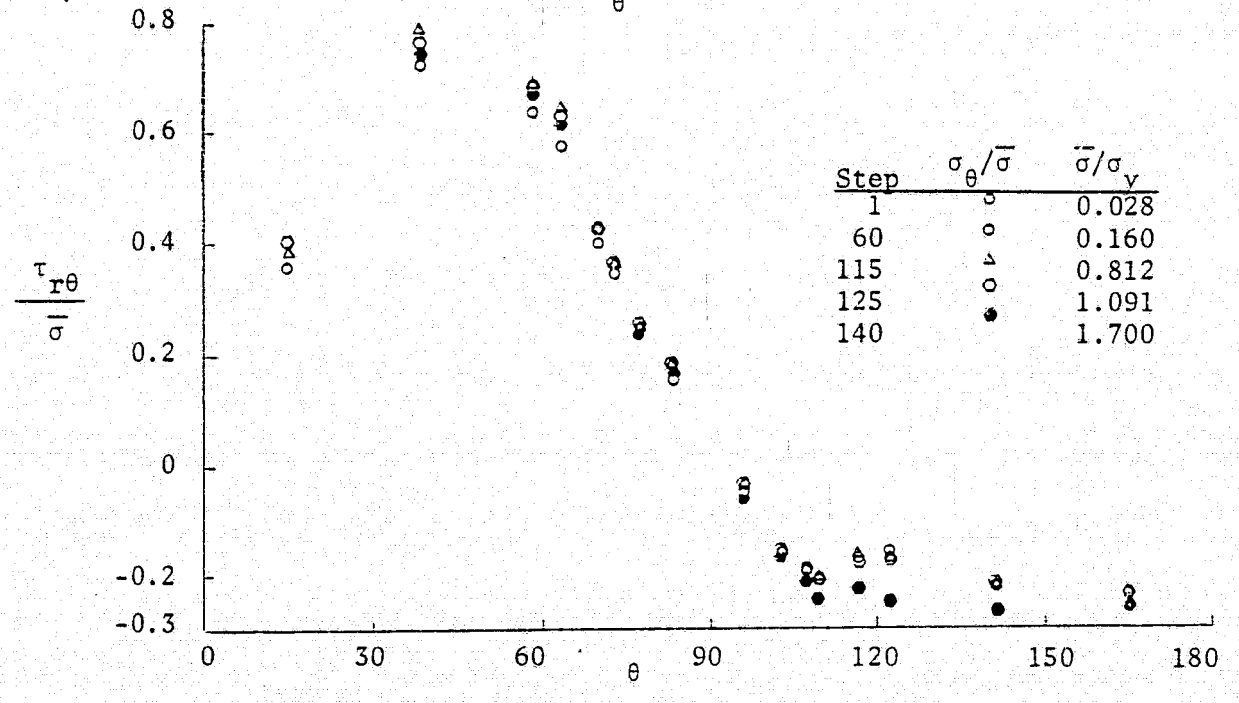

FIG. 38: $\tau_{r\theta}/\bar{\sigma}$ VS. θ for $\hat{r}$ = 0.977 (PH)

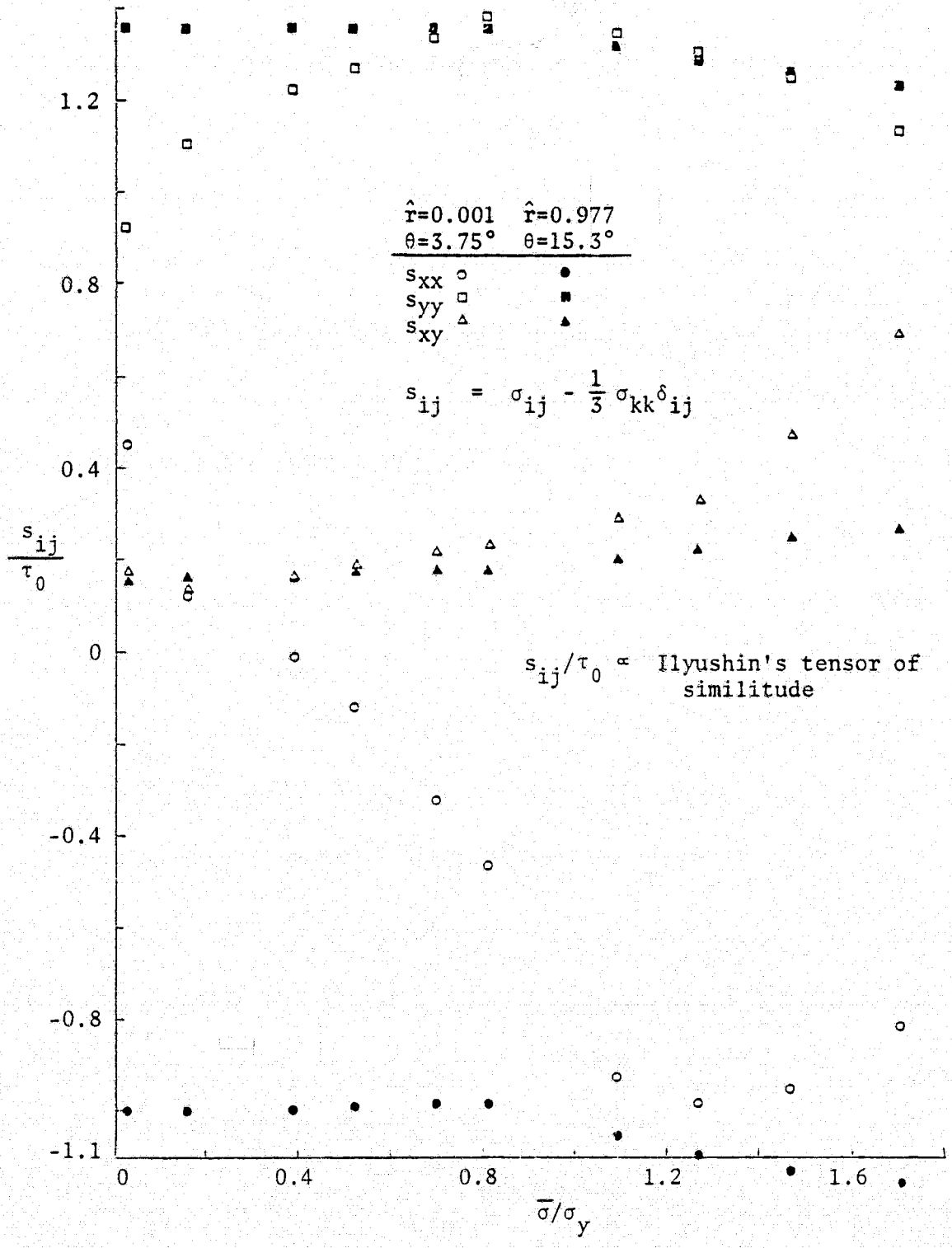

FIG. 39: s_{ij}/τ_0 VS. $\bar{\sigma}/\sigma_y$ Ahead of Crack Tip (PH)

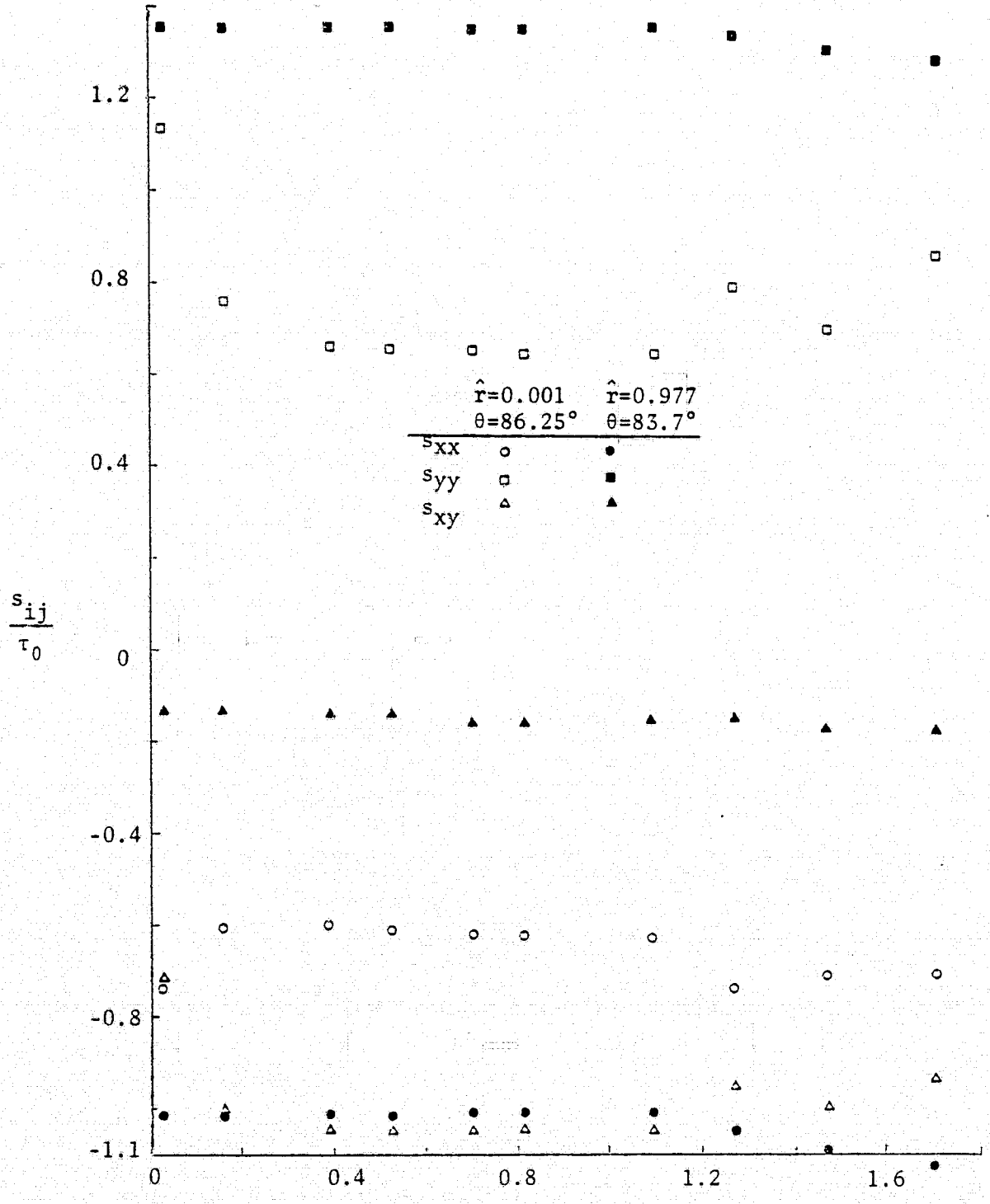

FIG. 40: s_{ij}/τ_0 VS. $\bar{\sigma}/\sigma_y$ Above Crack Tip (PH)

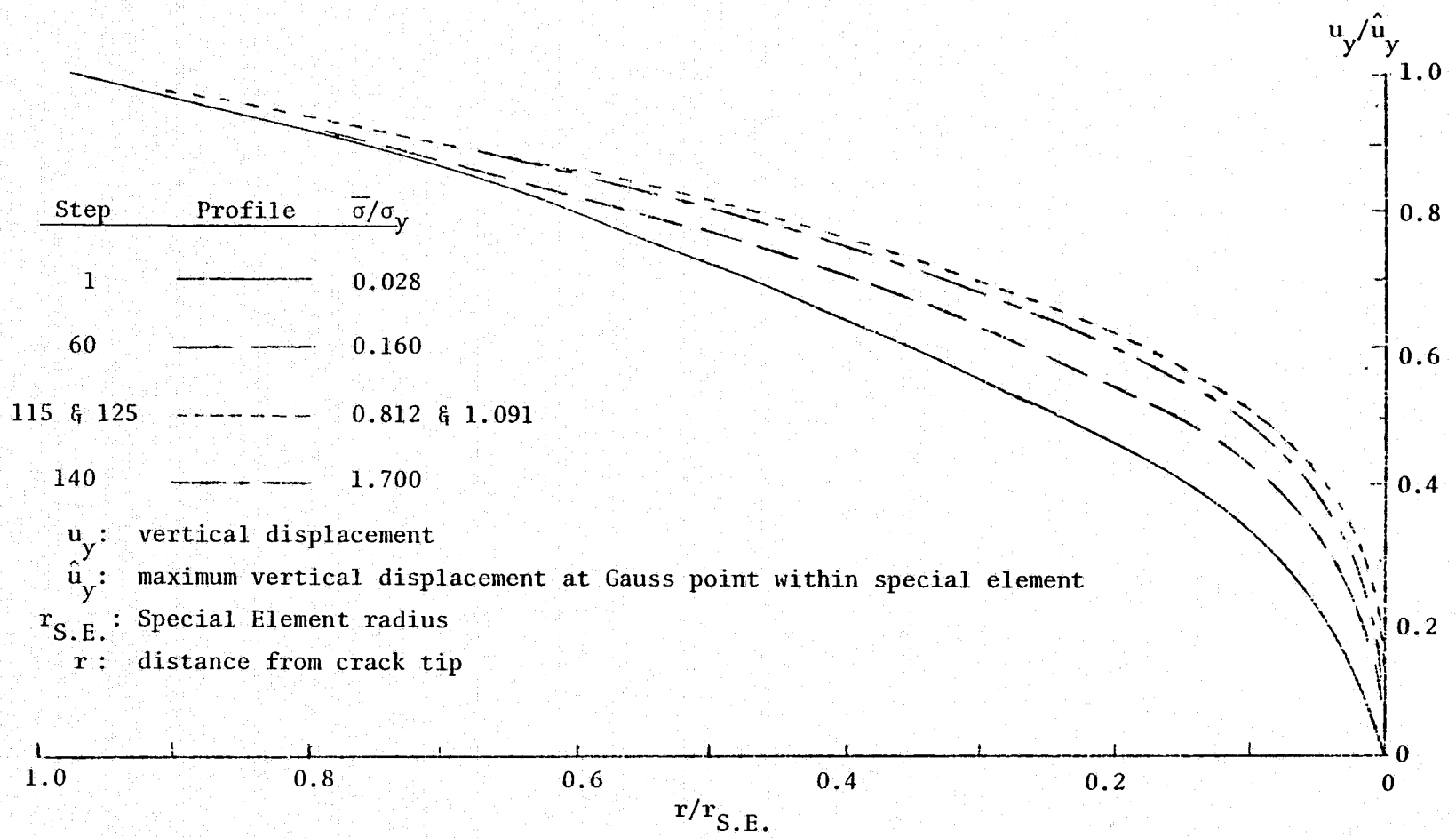

FIG. 41: Crack Opening Profiles within the Special Element (PH)

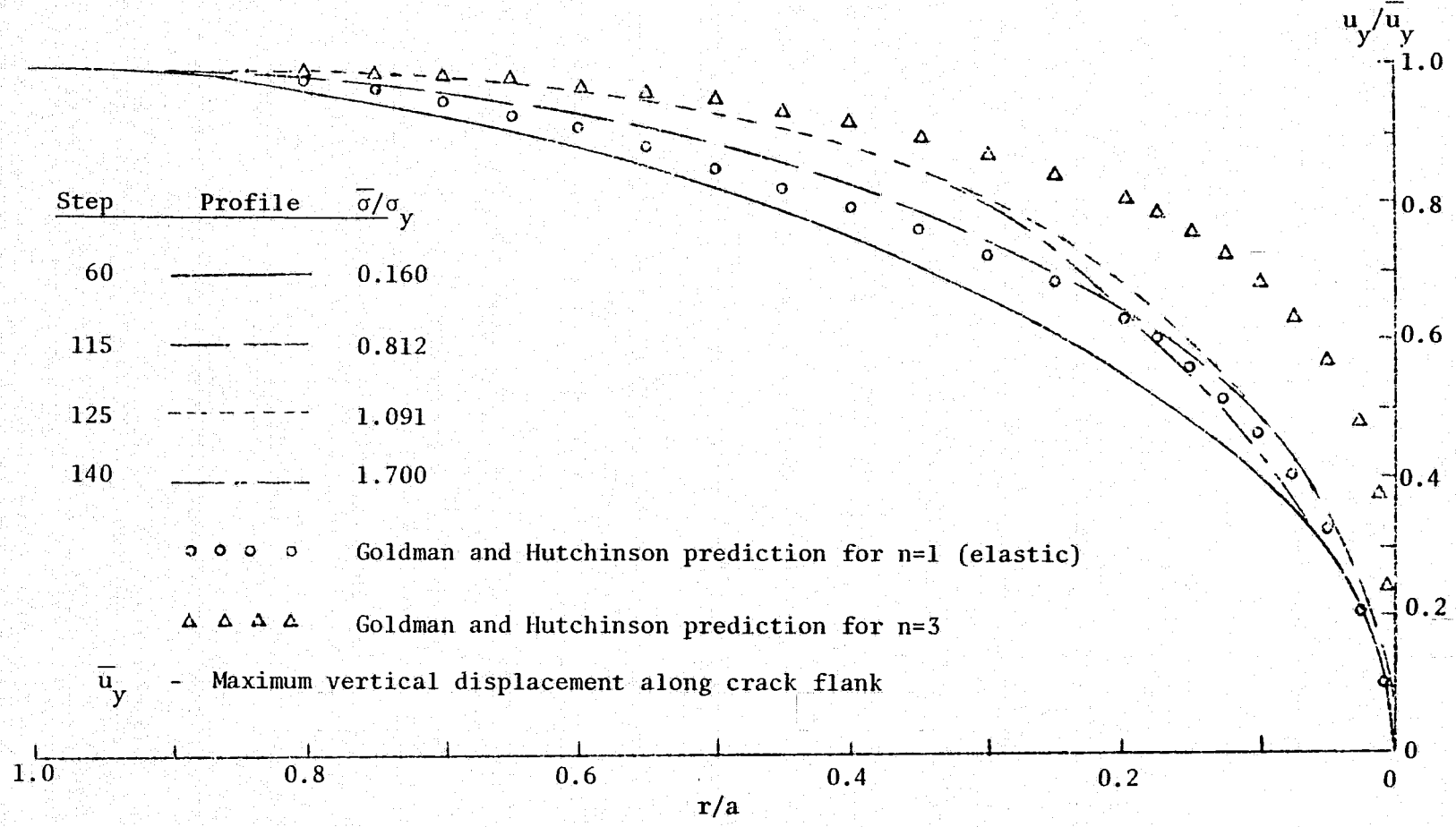

FIG. 42: Crack Opening Profiles along Entire Crack Flank (PH)

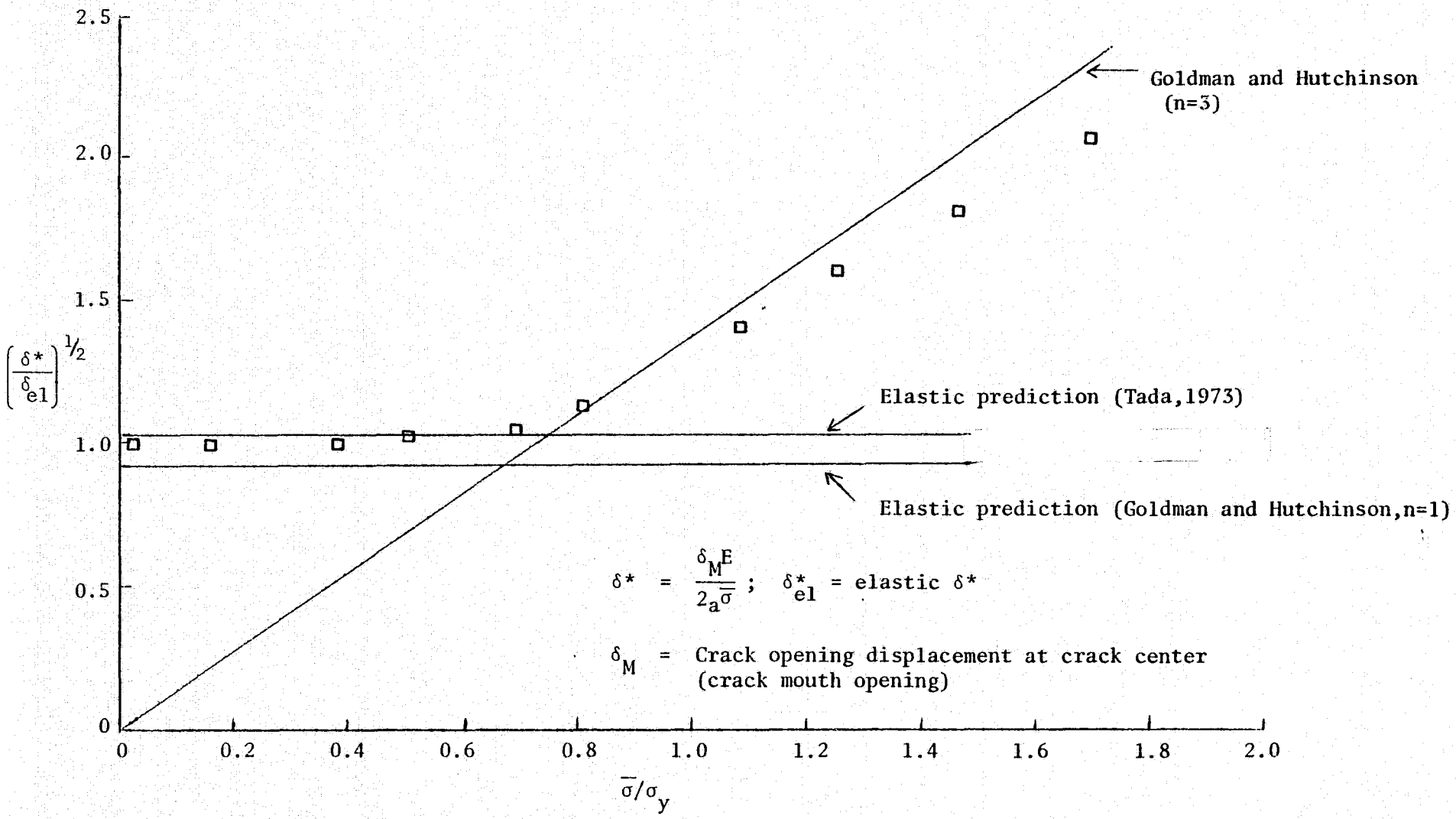

FIG. 43: Crack Mouth Opening VS. Applied Load (PH)

FIG. 44: Incremental Exponent VS. Applied Load for Every Fifth Load Step (BIL)

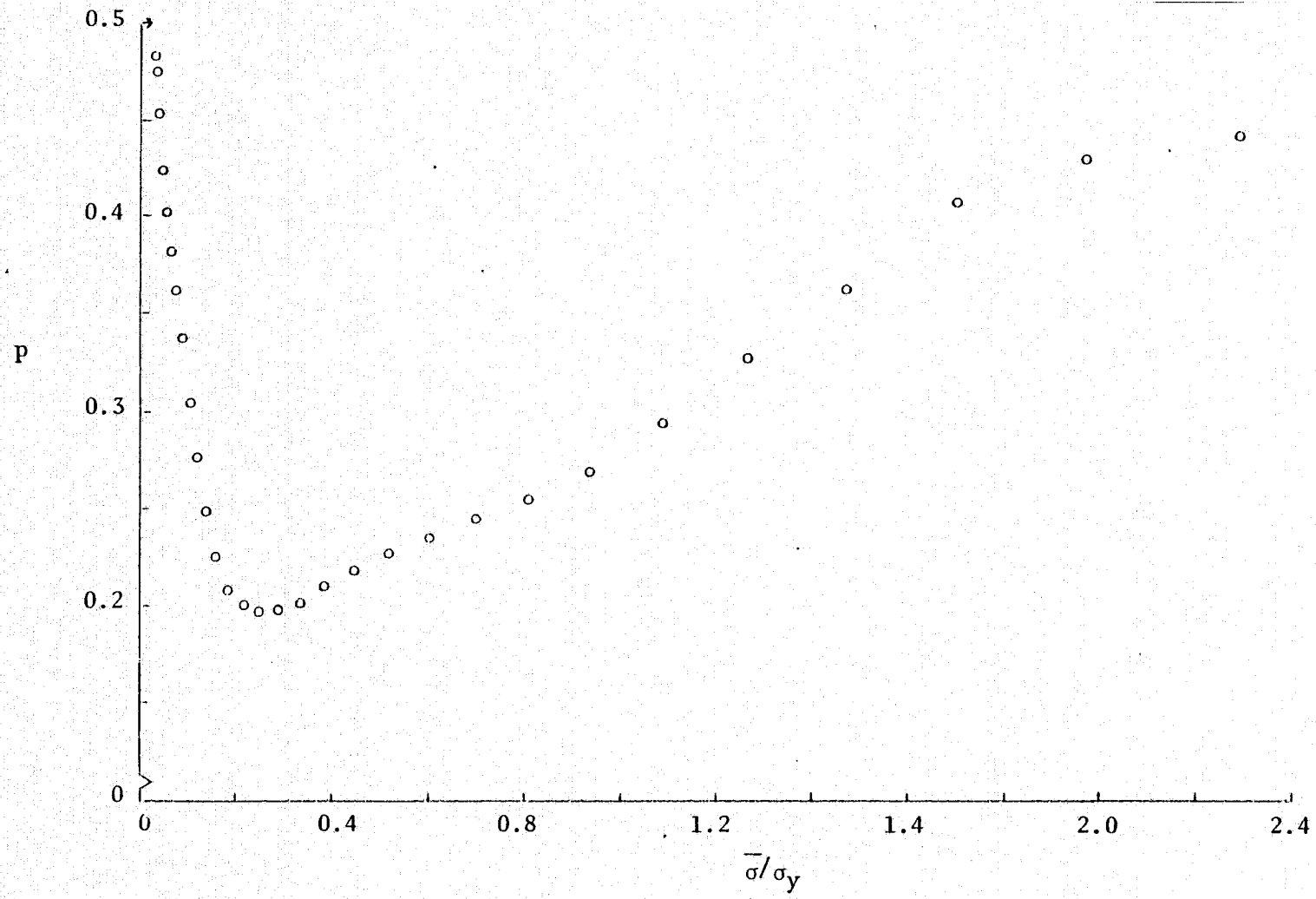

FIG. 45: Accumulated Exponent VS. Applied Load (BIL)

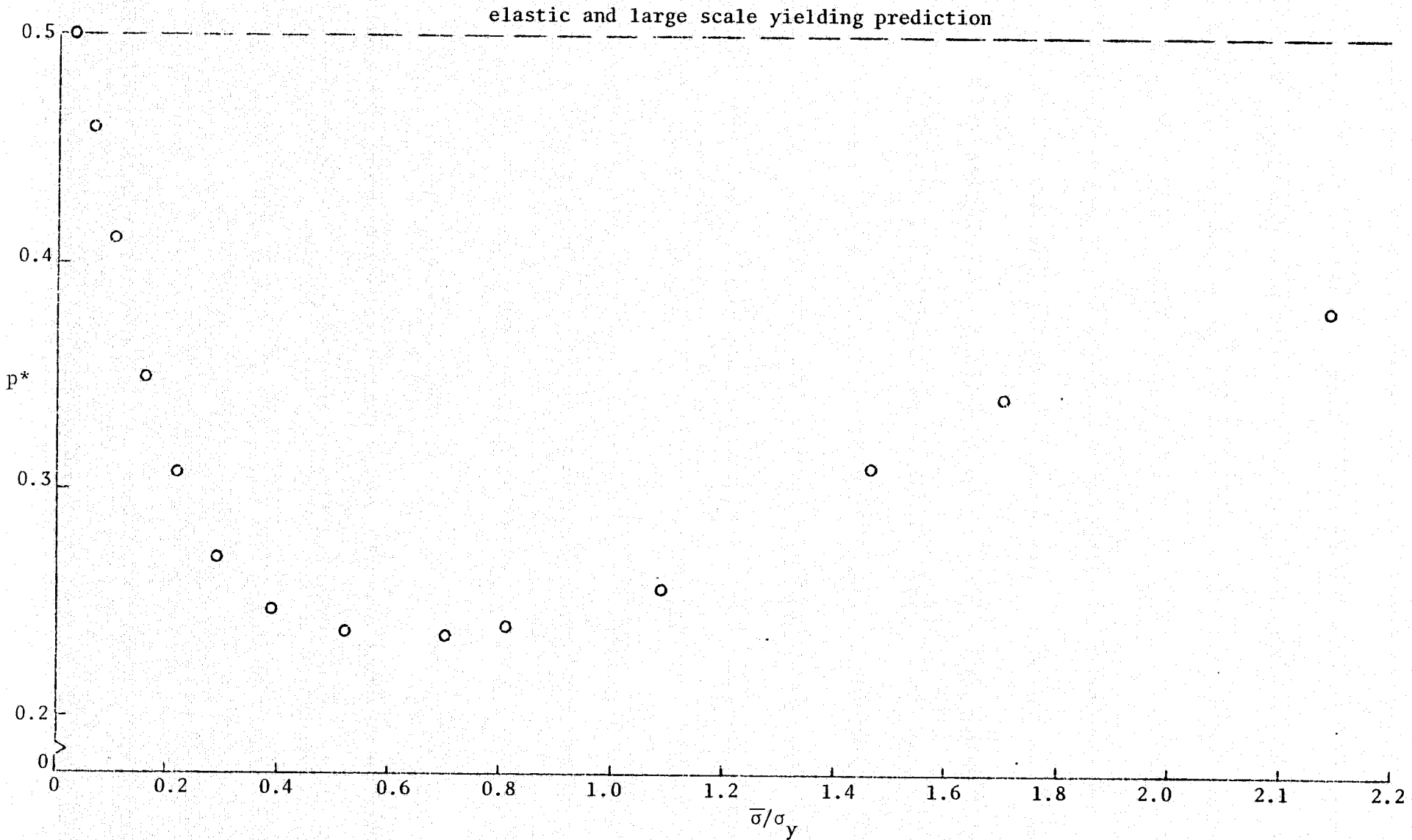

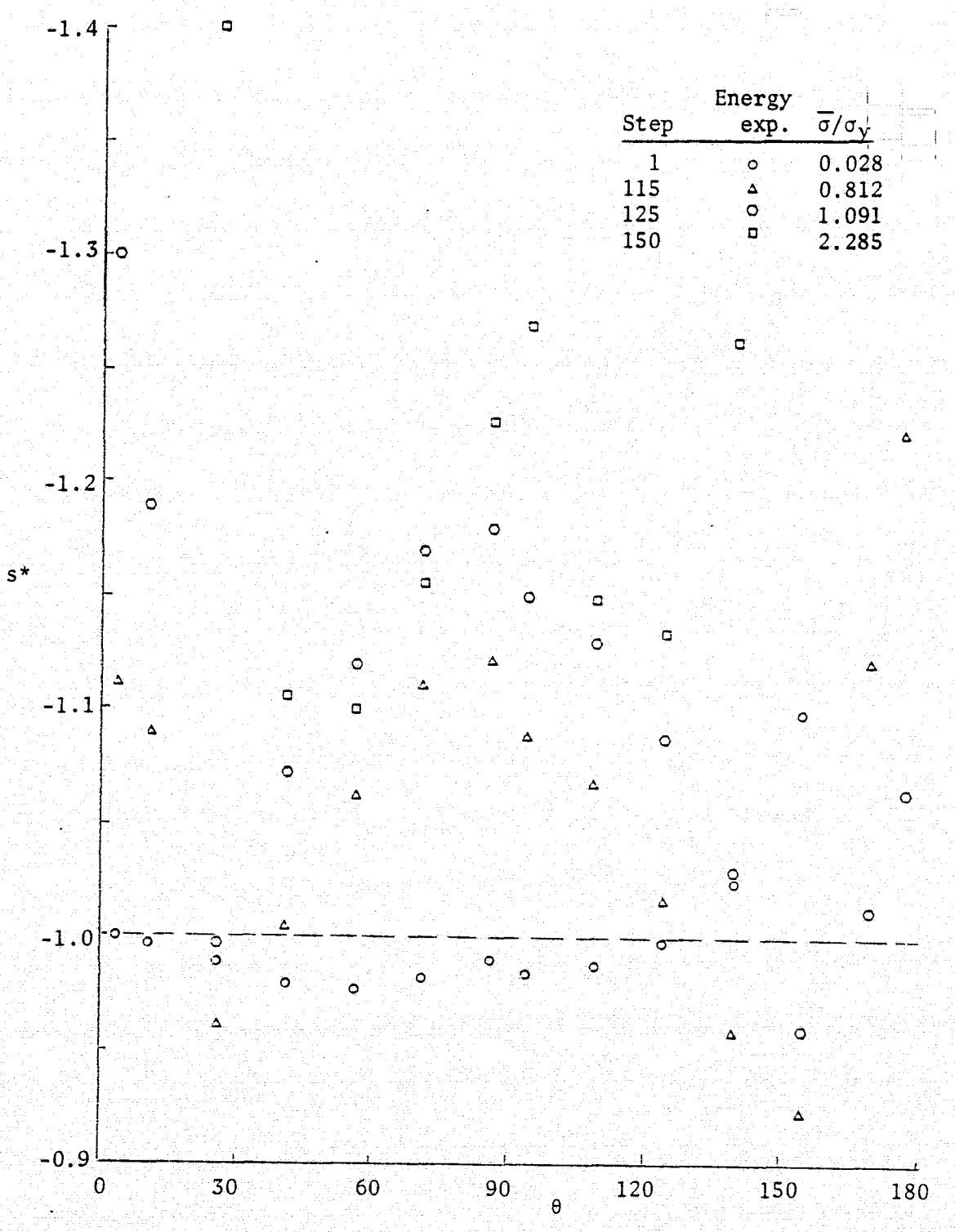

FIG. 46: Energy Exponent VS. Angular Position (BIL)

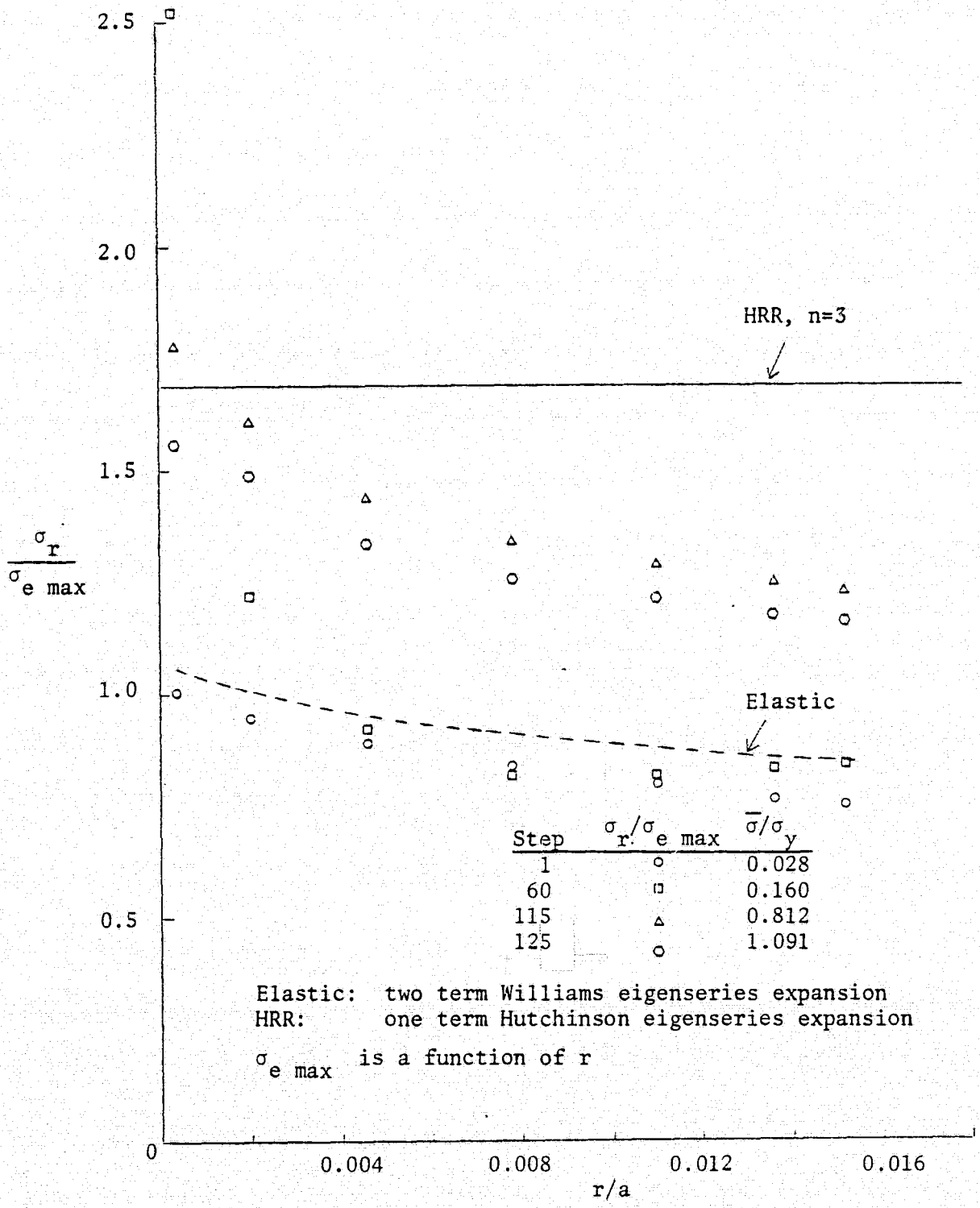

FIG. 47: $\sigma_r/\sigma_{e\ max}$ VS. r/a at $\theta = 3.75°$ (BIL)

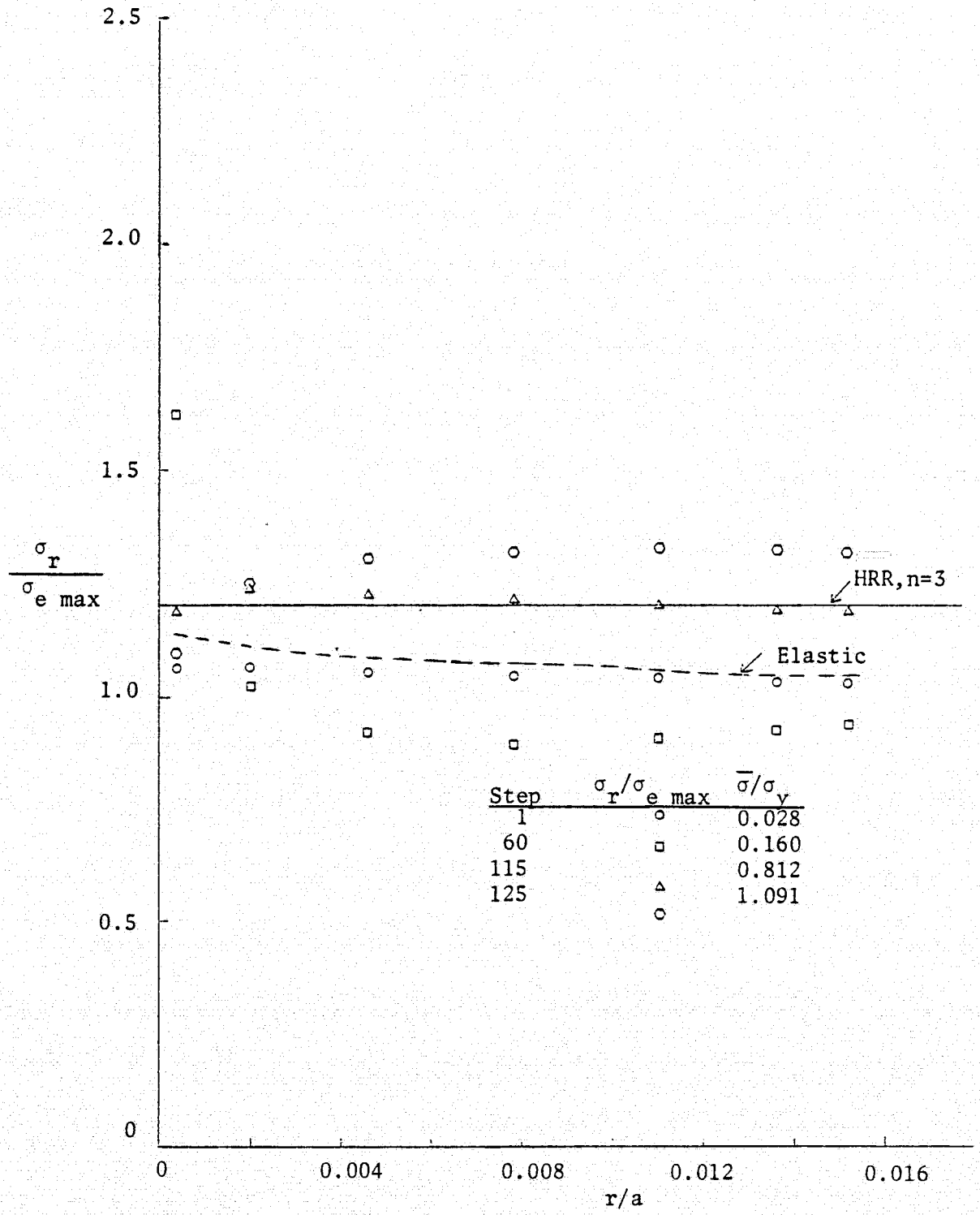

FIG. 48: $\sigma_r/\sigma_{e\ max}$ VS. r/a at $\theta = 93.75°$ (BIL)

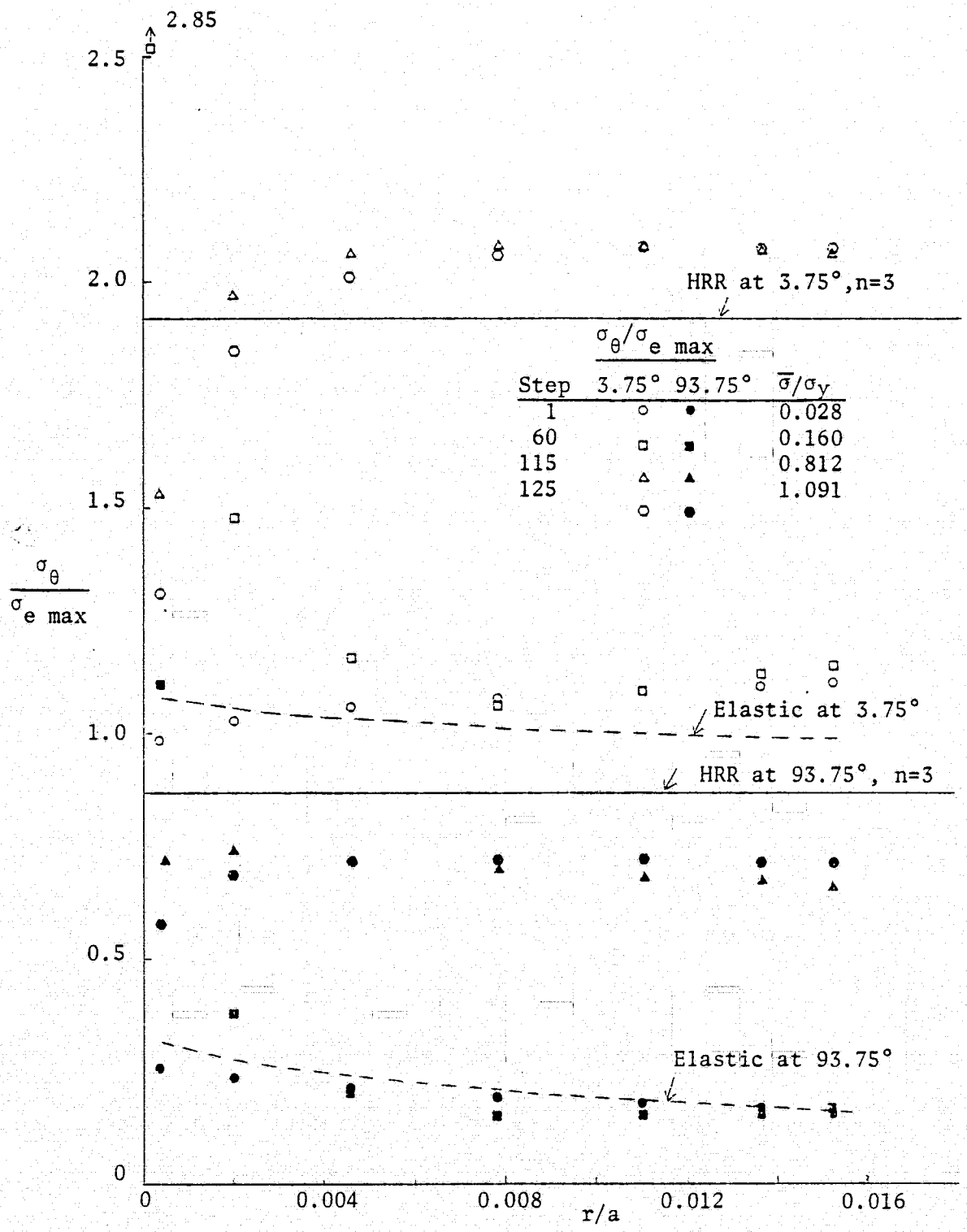

FIG. 49: $\sigma_\theta/\sigma_{e\ max}$ VS. r/a at θ = 3.75° and 93.75° (BIL)

FIG. 50: $\sigma_e/\sigma_{e\ max}$ VS. r/a at $\theta = 3.75°$ (BIL)

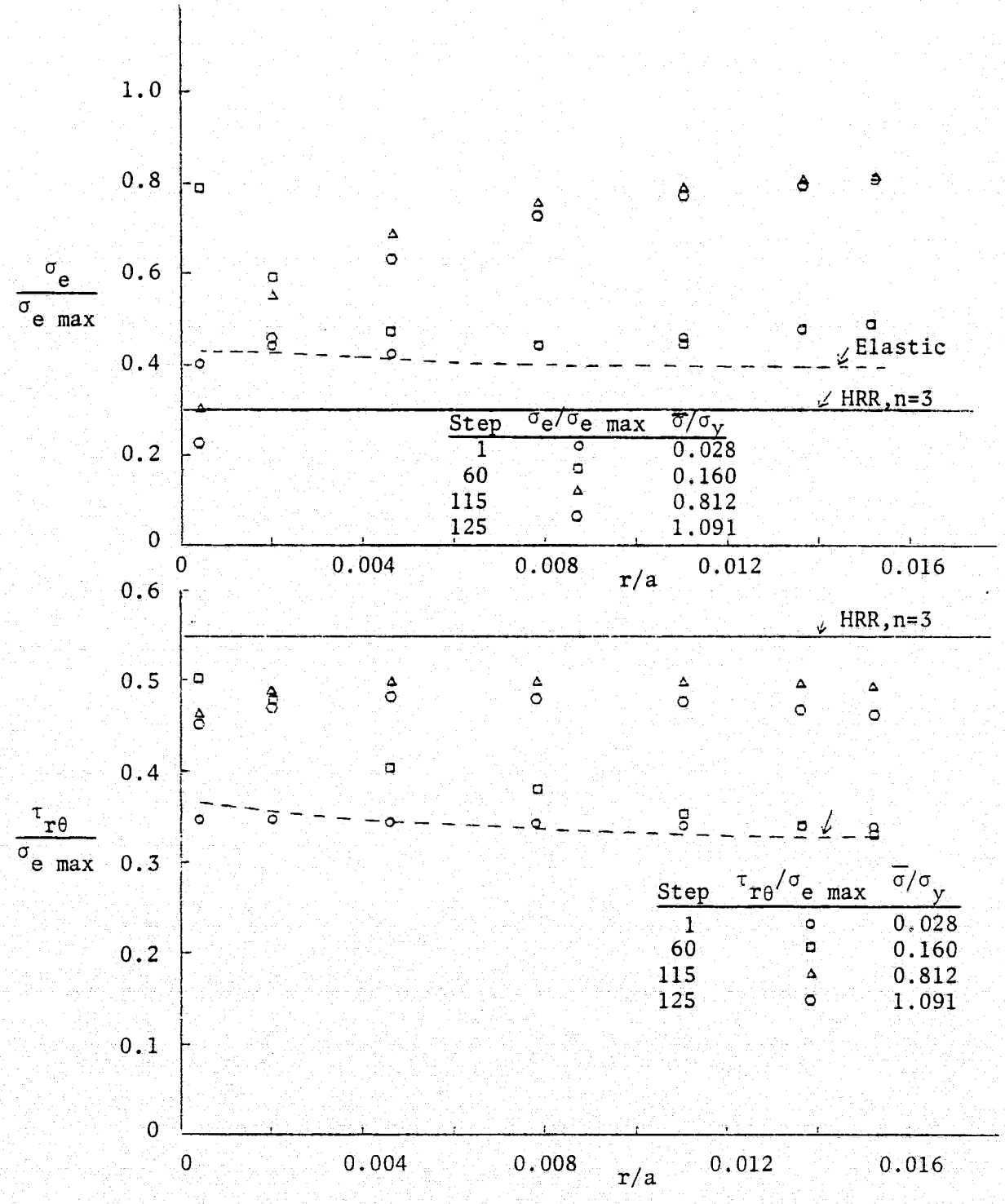

FIG. 51: $\tau_{r\theta}/\sigma_{e\ max}$ VS. r/a at $\theta = 93.75°$ (BIL)

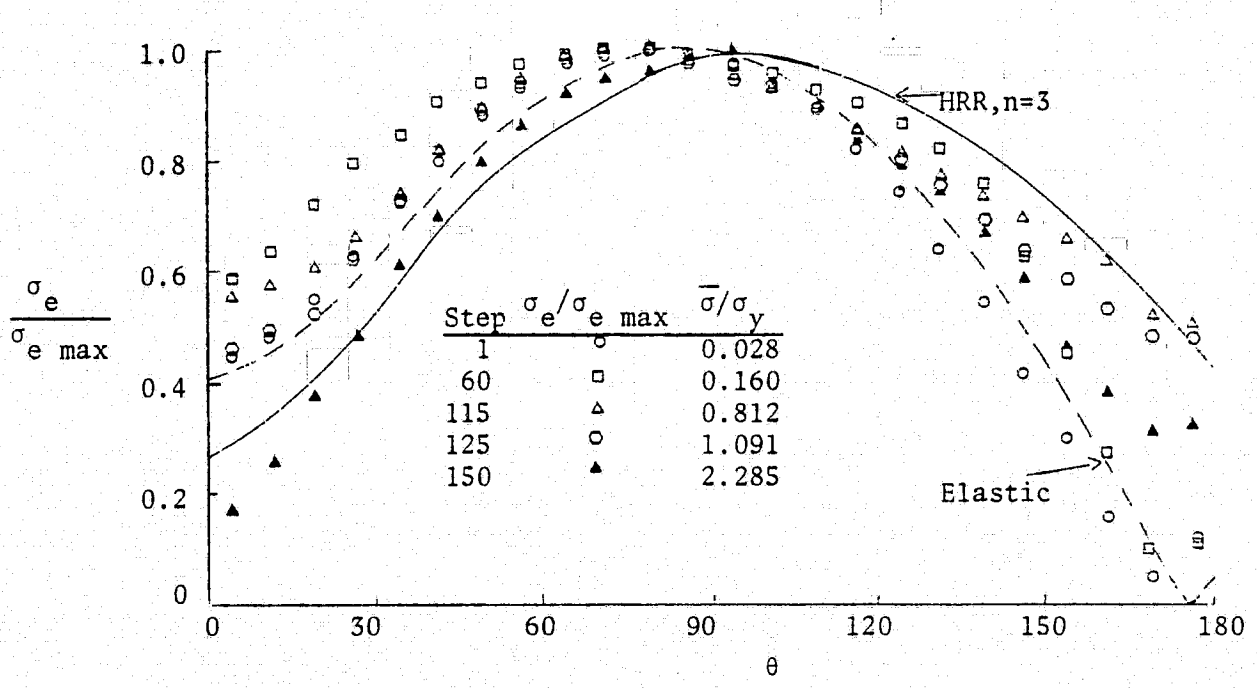

FIG. 52: $\sigma_e/\sigma_{e\ max}$ VS. θ for $\hat{r}$ = 0.001 (BIL)

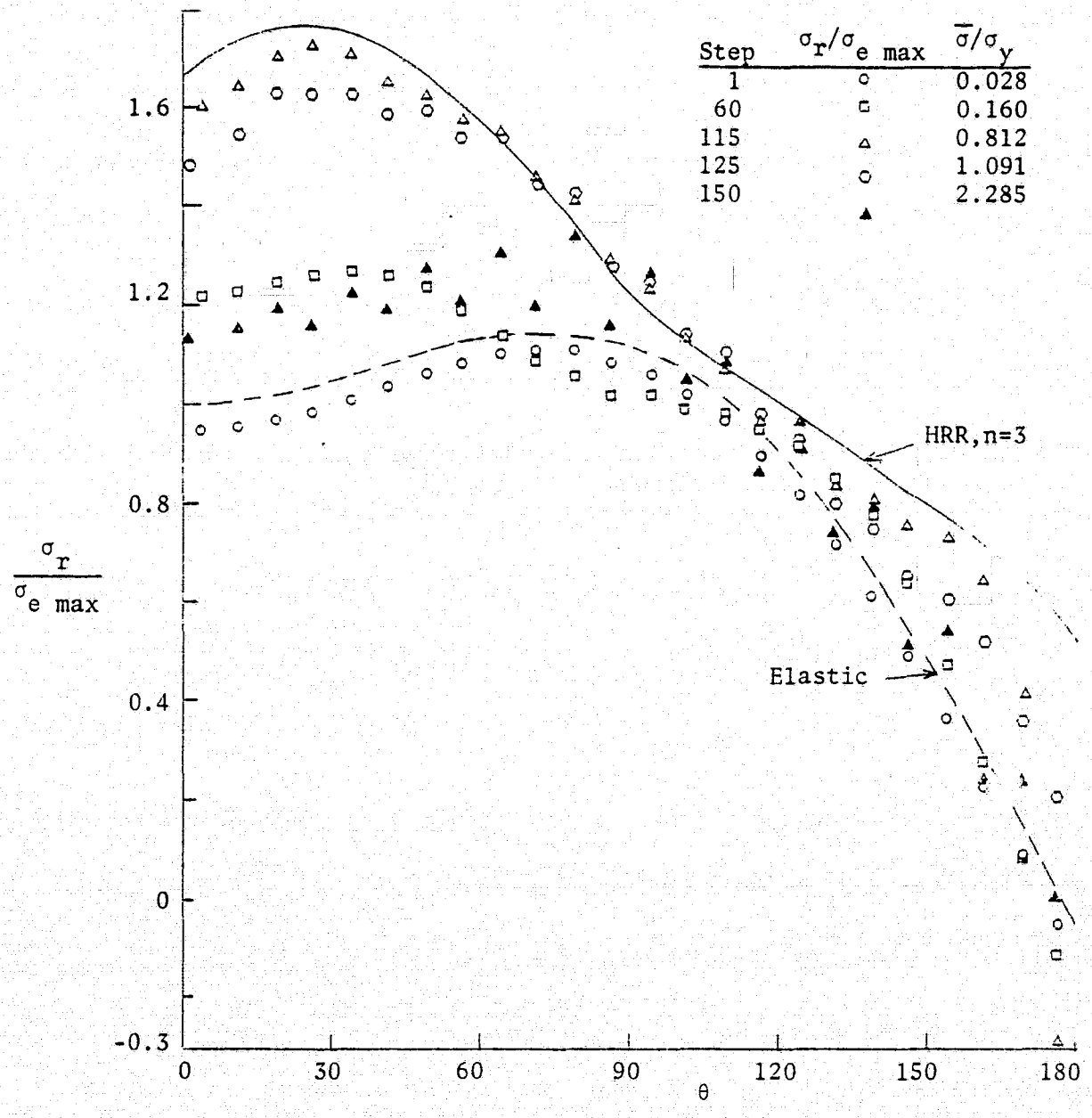

FIG. 53: $\sigma_r/\sigma_{e\ max}$ VS. θ for $\hat{r}$ = 0.001 (BIL)

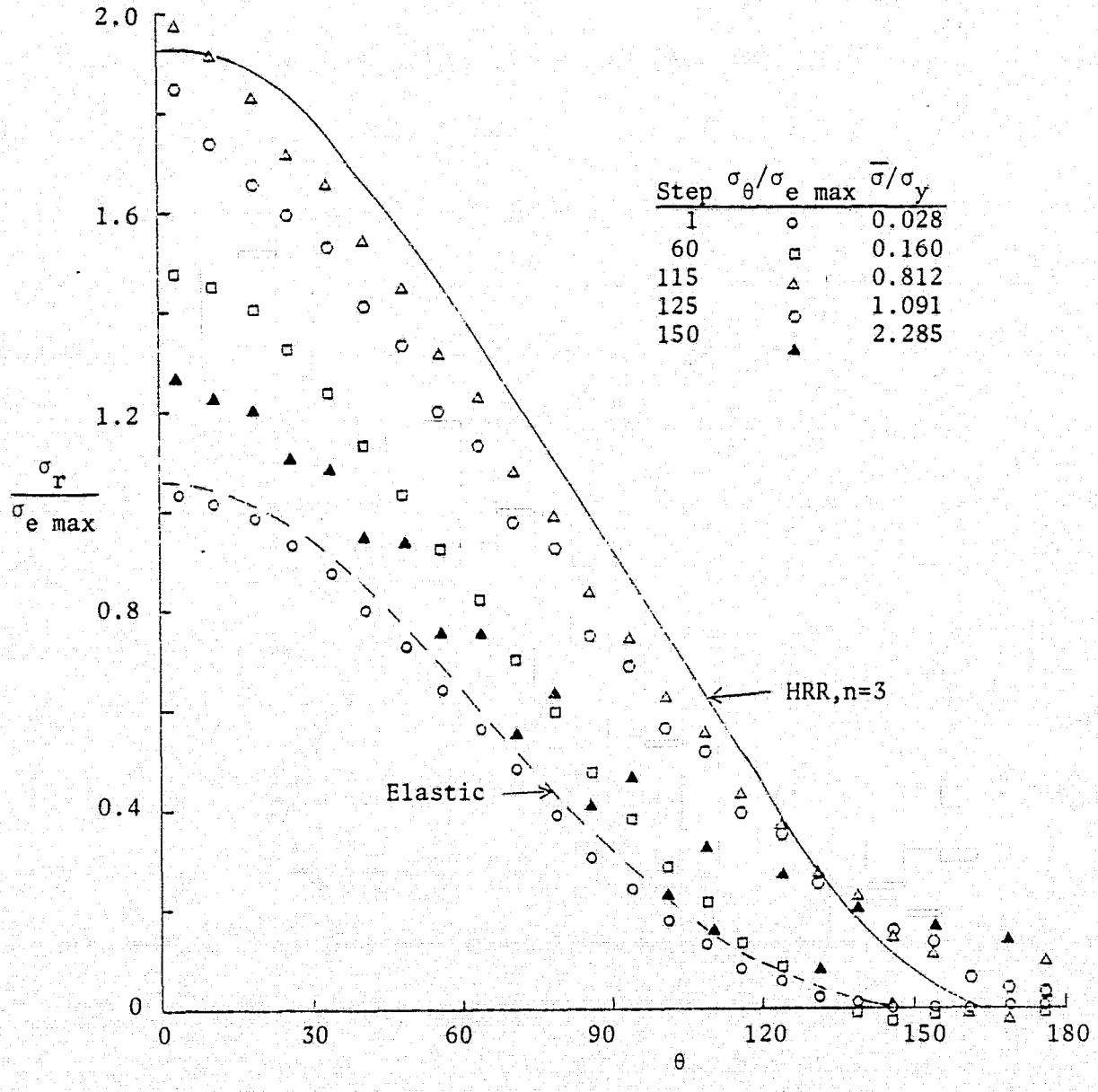

FIG. 54: $\sigma_\theta/\sigma_{e\ max}$ VS. θ for $\hat{r}$ = 0.001 (BIL)

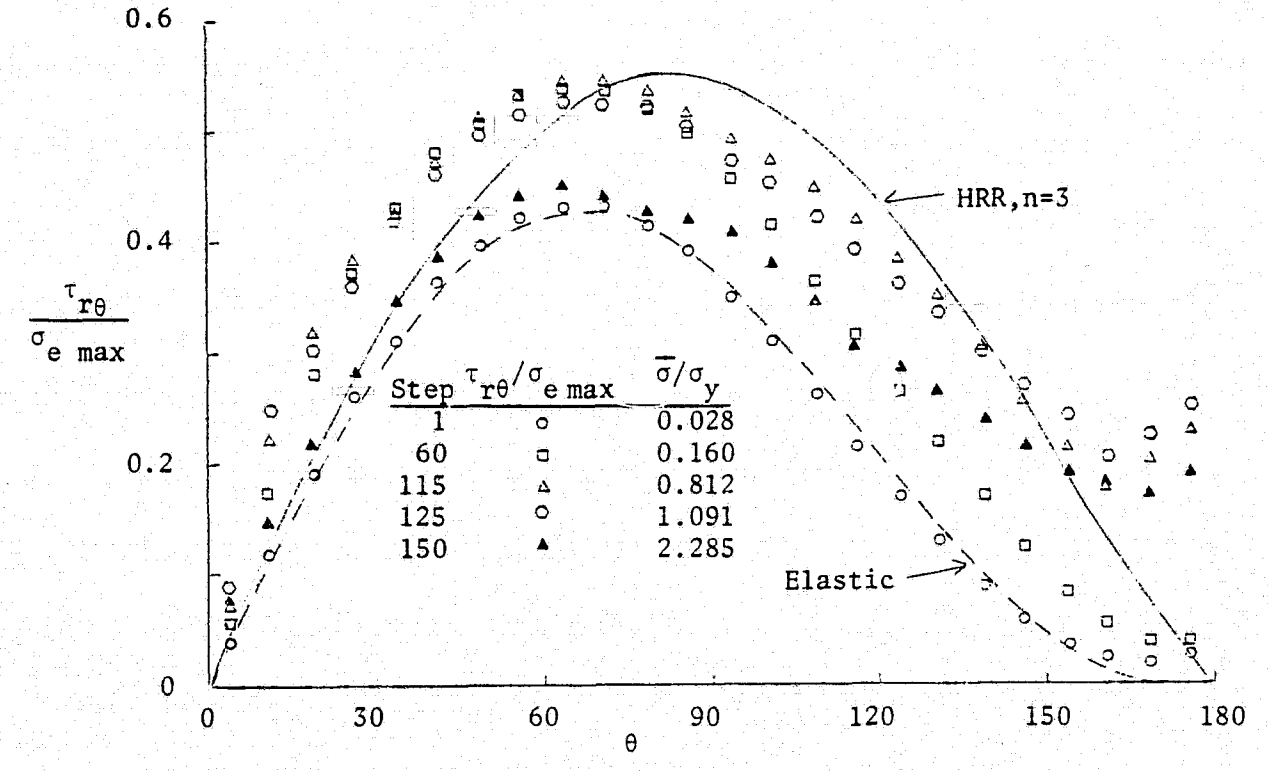

FIG. 55: $\tau_{r\theta}/\sigma_{e\ max}$ VS. θ for $\hat{r}$ = 0.001 (BIL)

FIG. 56: Normalized J VS. Distance from the Crack Tip (BIL)

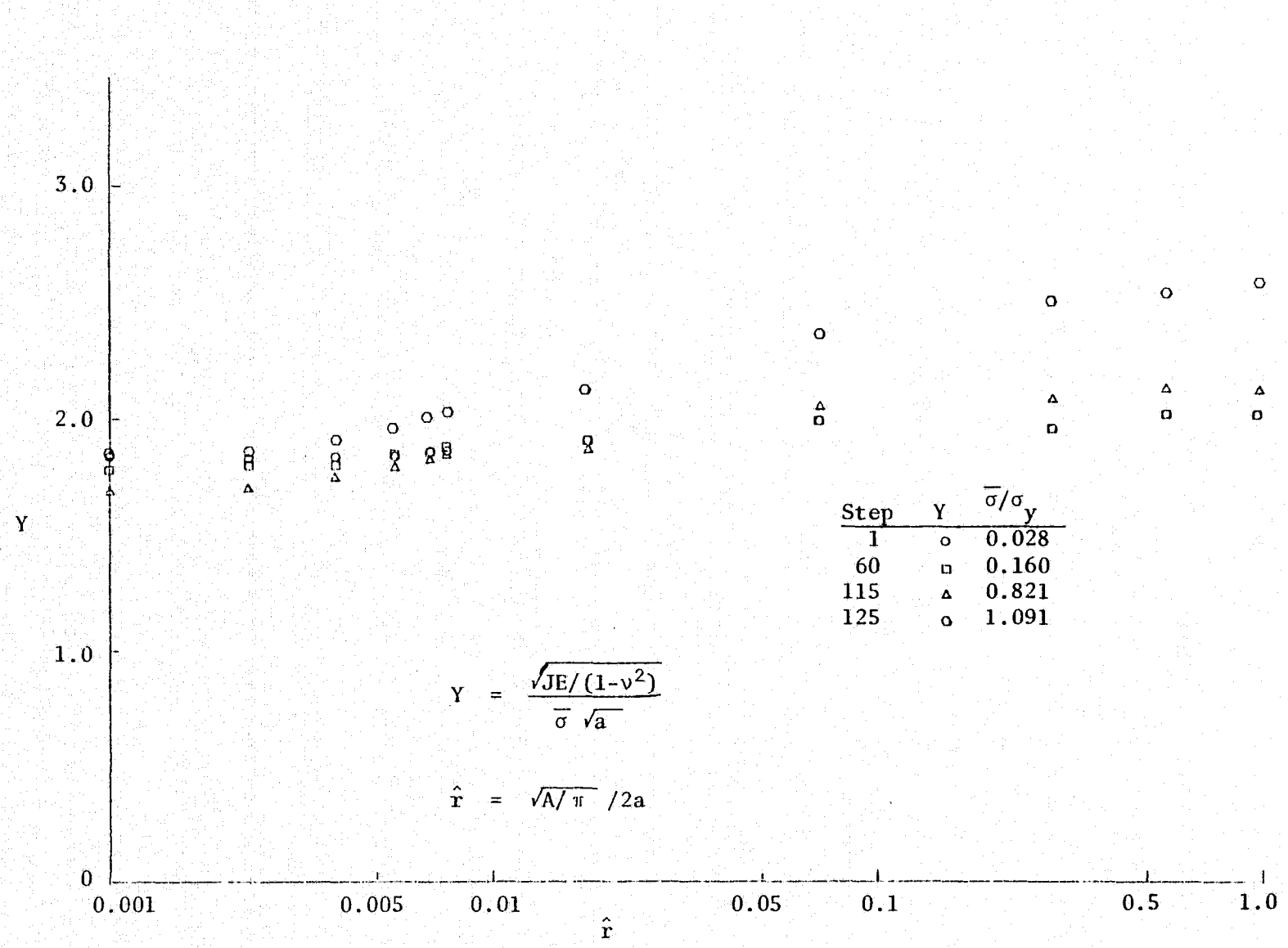

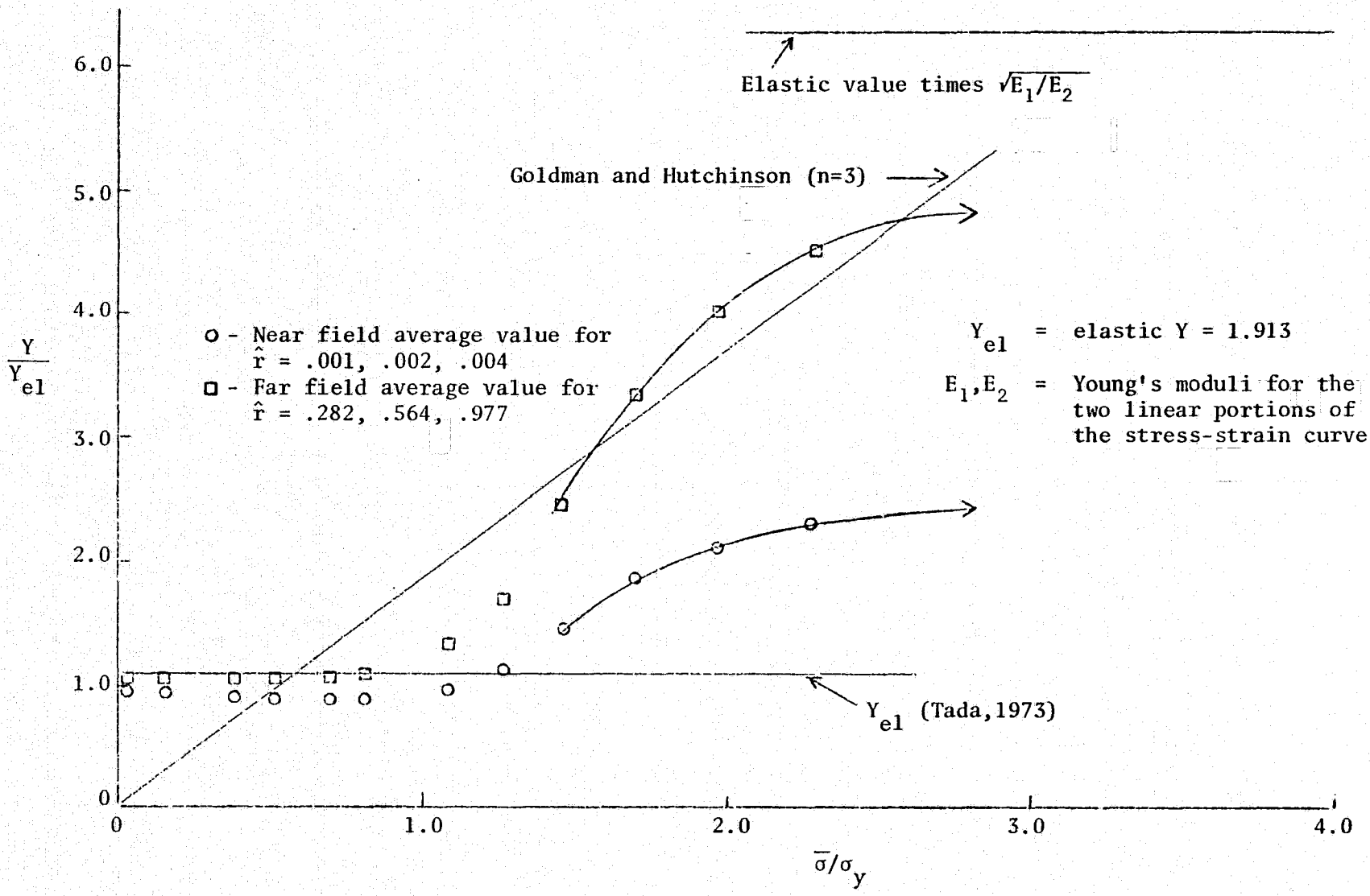

FIG. 57: Near and Far Field J Values VS. Applied Load (BIL)

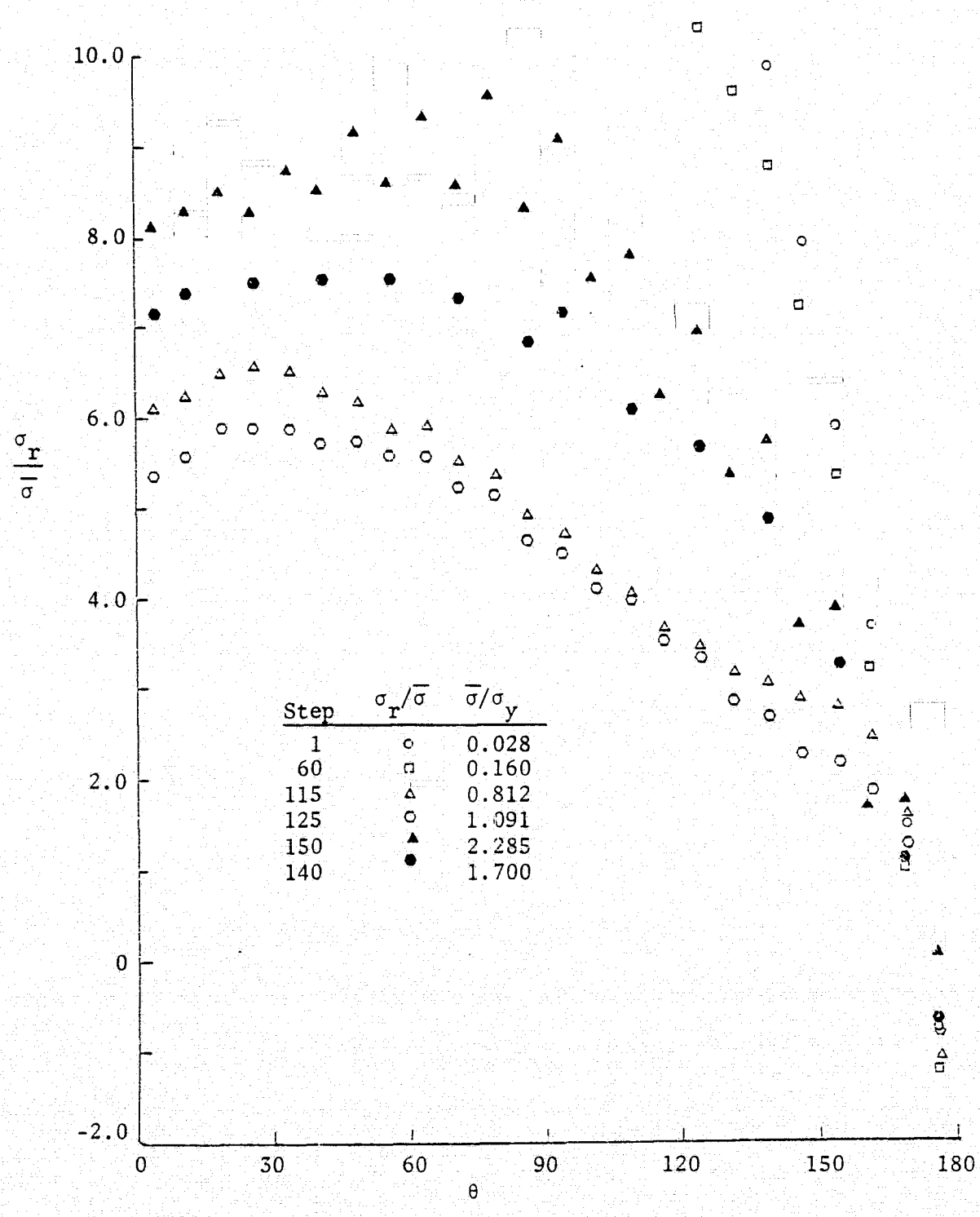

FIG. 58: $\sigma_r/\bar{\sigma}$ VS. θ for $\hat{r} = 0.001$ (BIL)

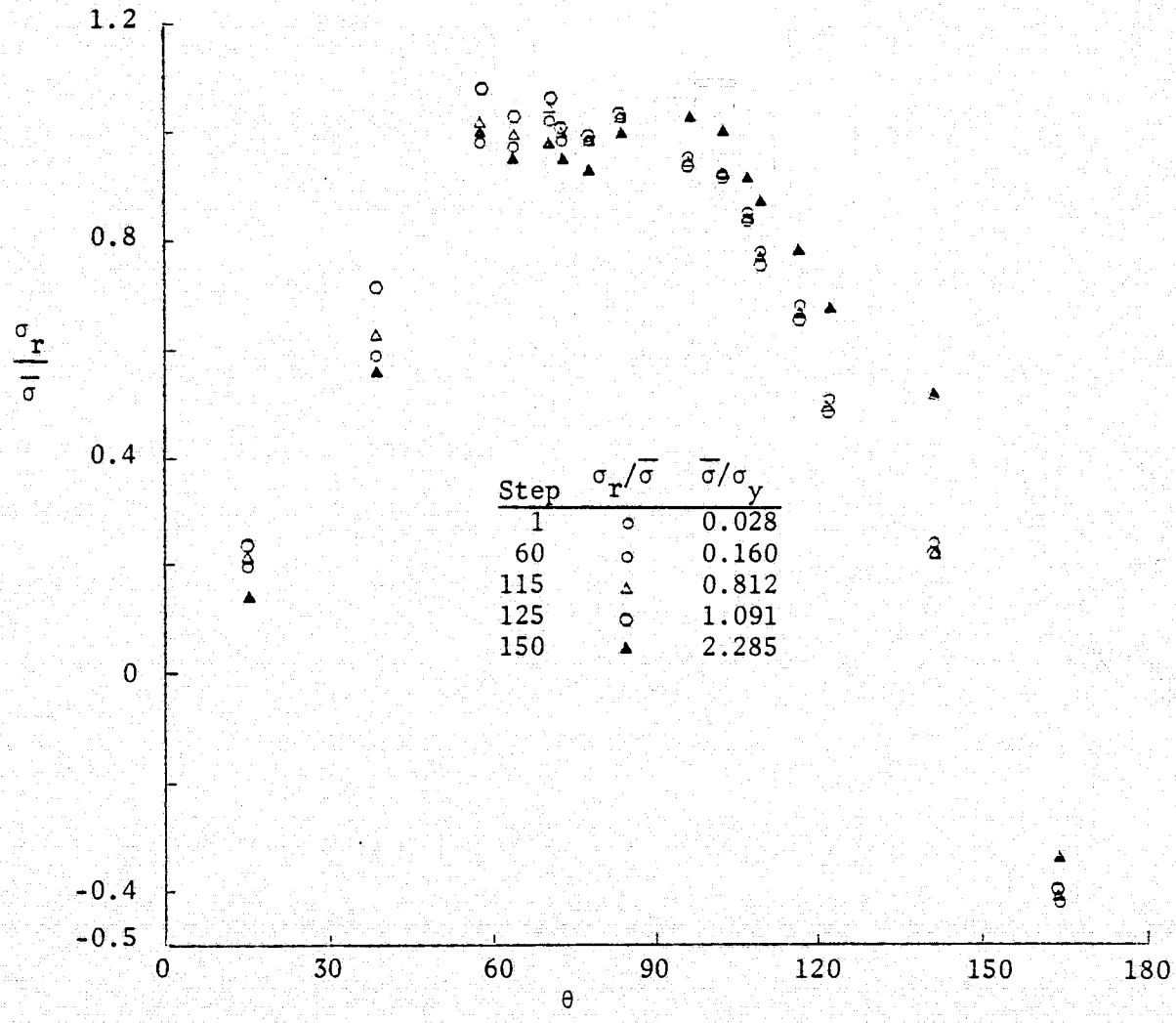

FIG. 59: $\sigma_r/\bar{\sigma}$ VS. θ for $\hat{r}$ = 0.977 (BIL)

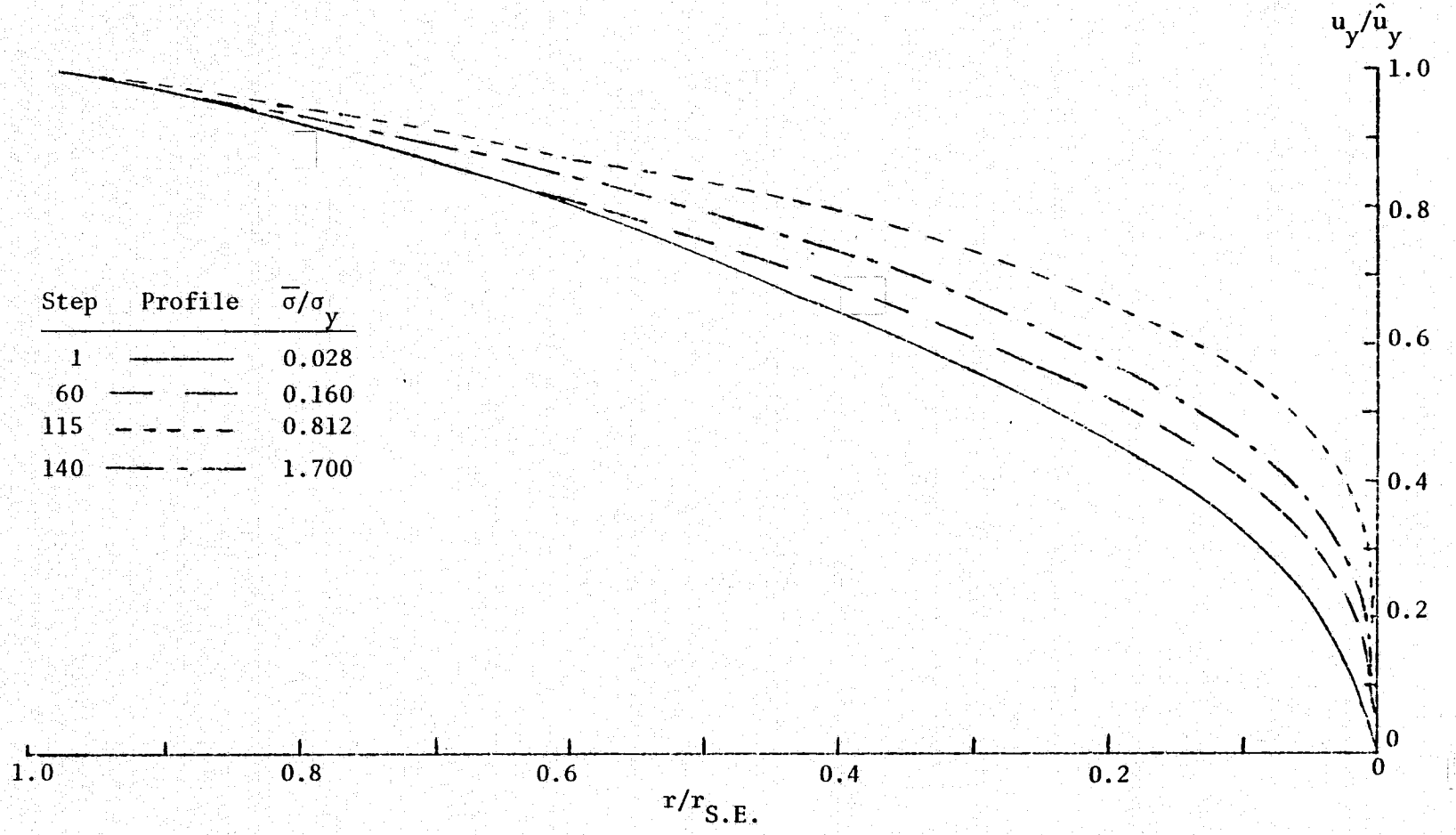

FIG. 60: Crack Opening Profiles within the Special Element (BIL)

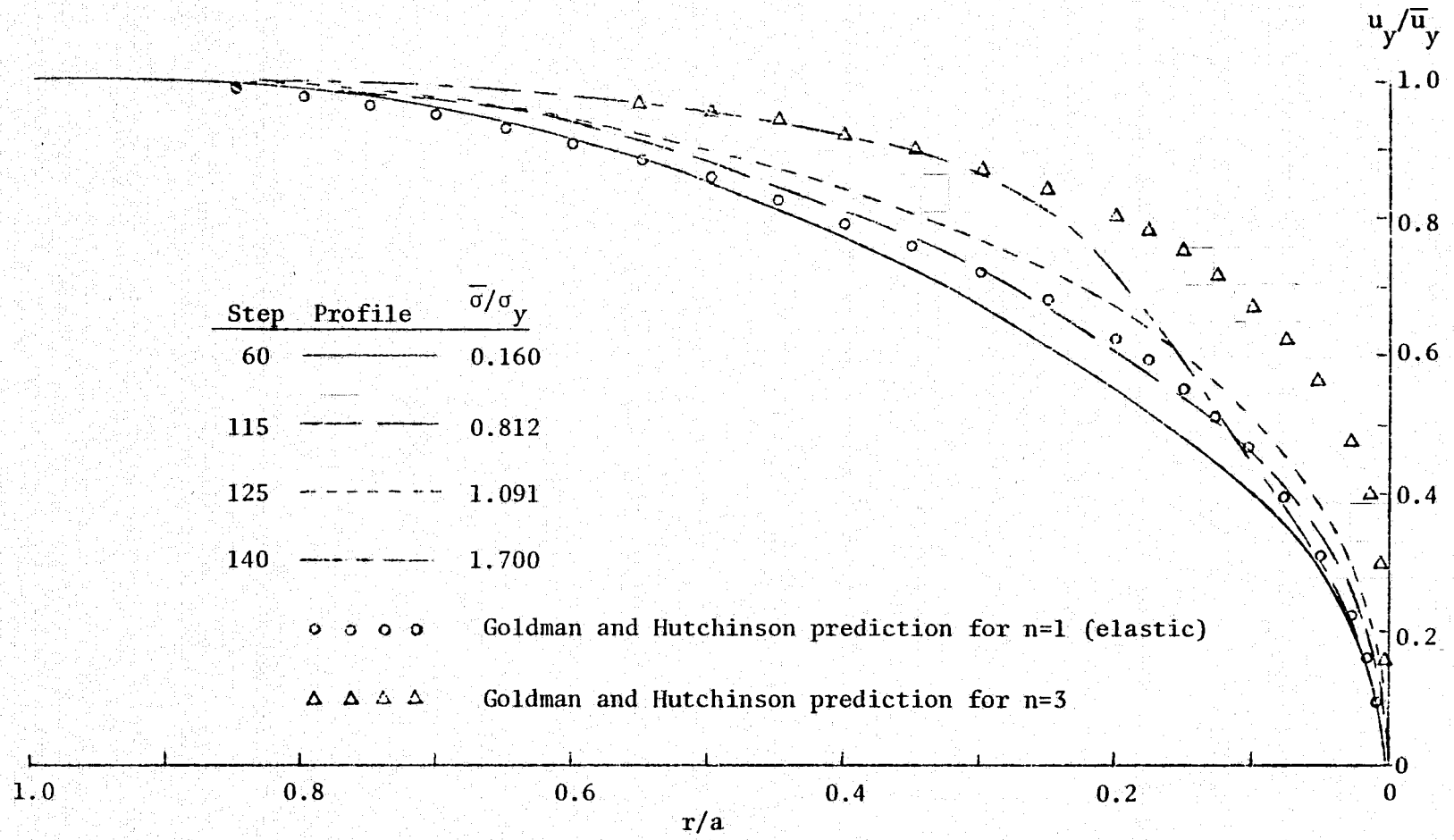

FIG. 61: Crack Opening Profiles along Entire Crack Flank (BIL)

FIG. 62: Octahedral Stress Comparison of Power Hardening and Bilinear Materials at $\hat{r}$ = 0.001 (BIL and PH)

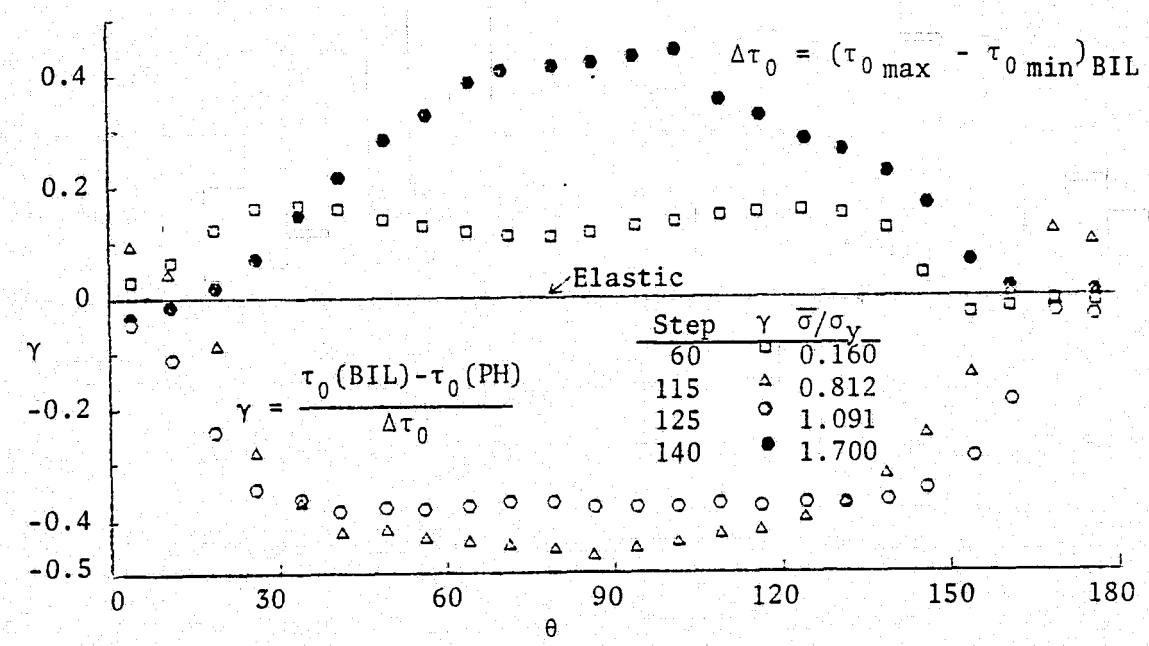

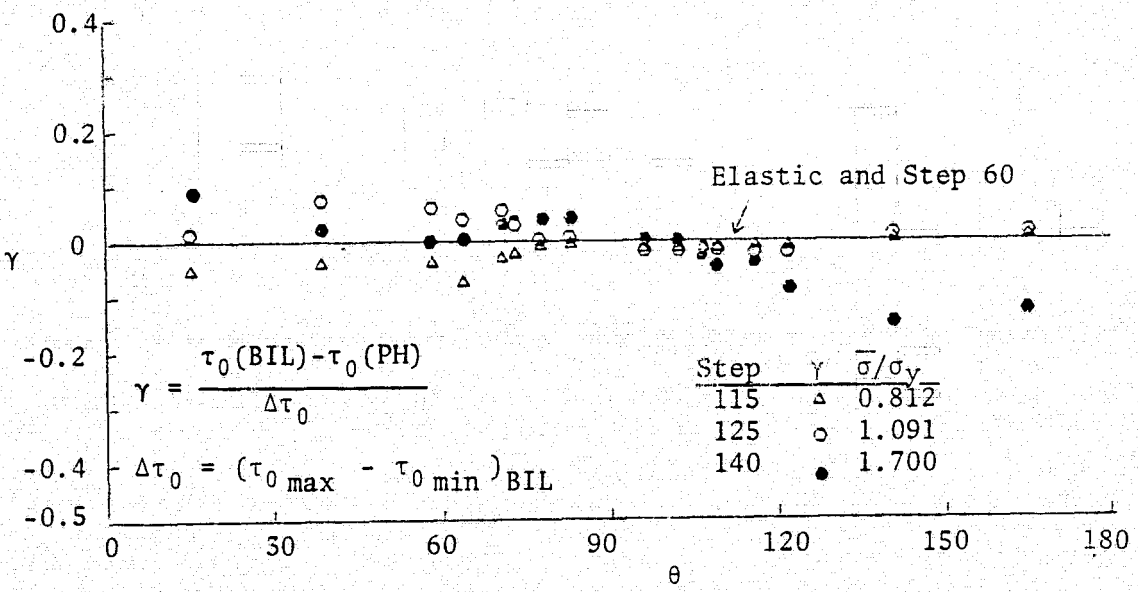

FIG. 63: Octahedral Stress Comparison of Power Hardening and Bilinear Materials at $\hat{r}$ = 0.977 (BIL and PH)

FIG. 64: Comparison of Power Hardening and Bilinear Parameters (BIL and PH)

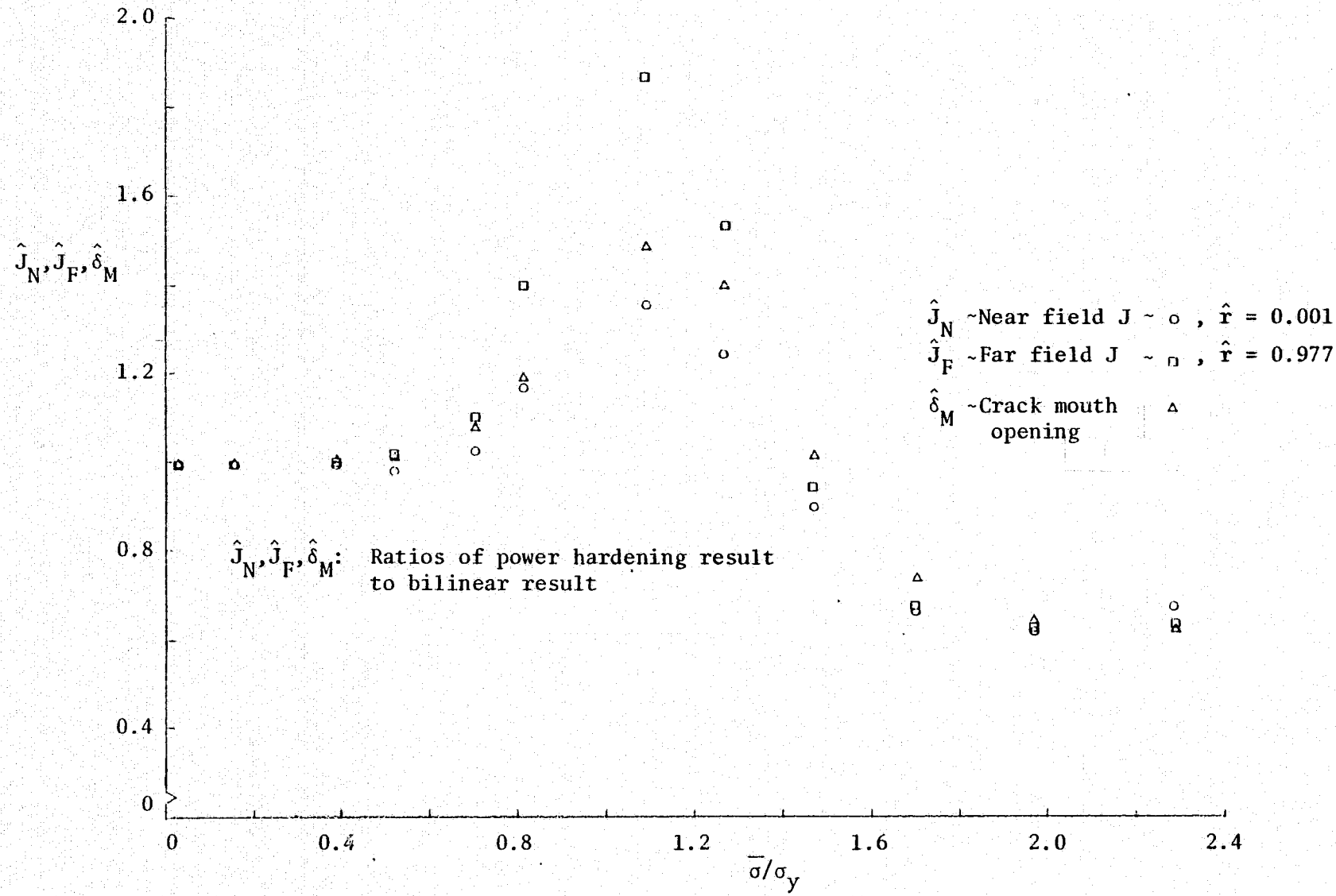

FIG. 65: Normalized J VS. Distance from the Crack Tip (RS)

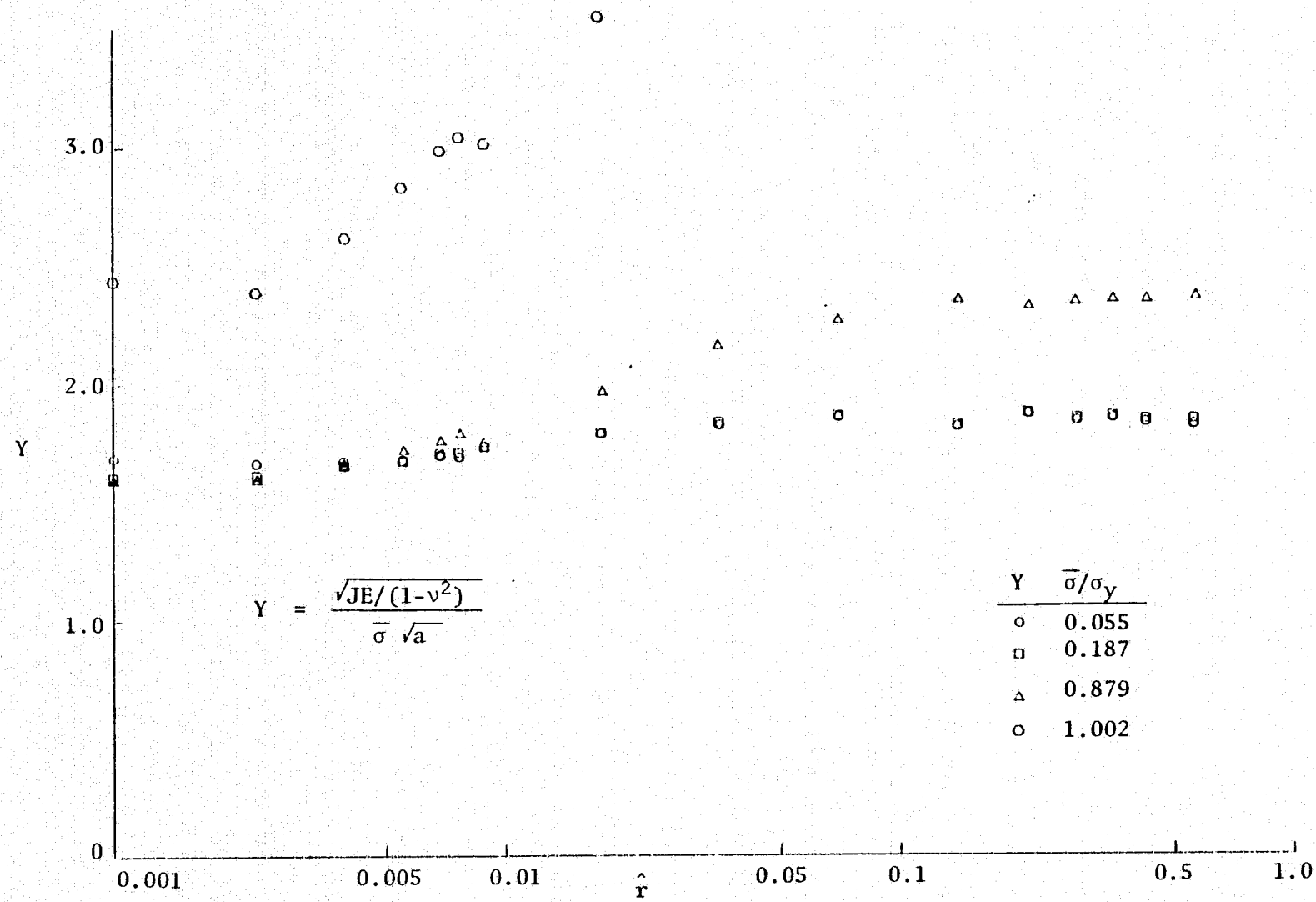

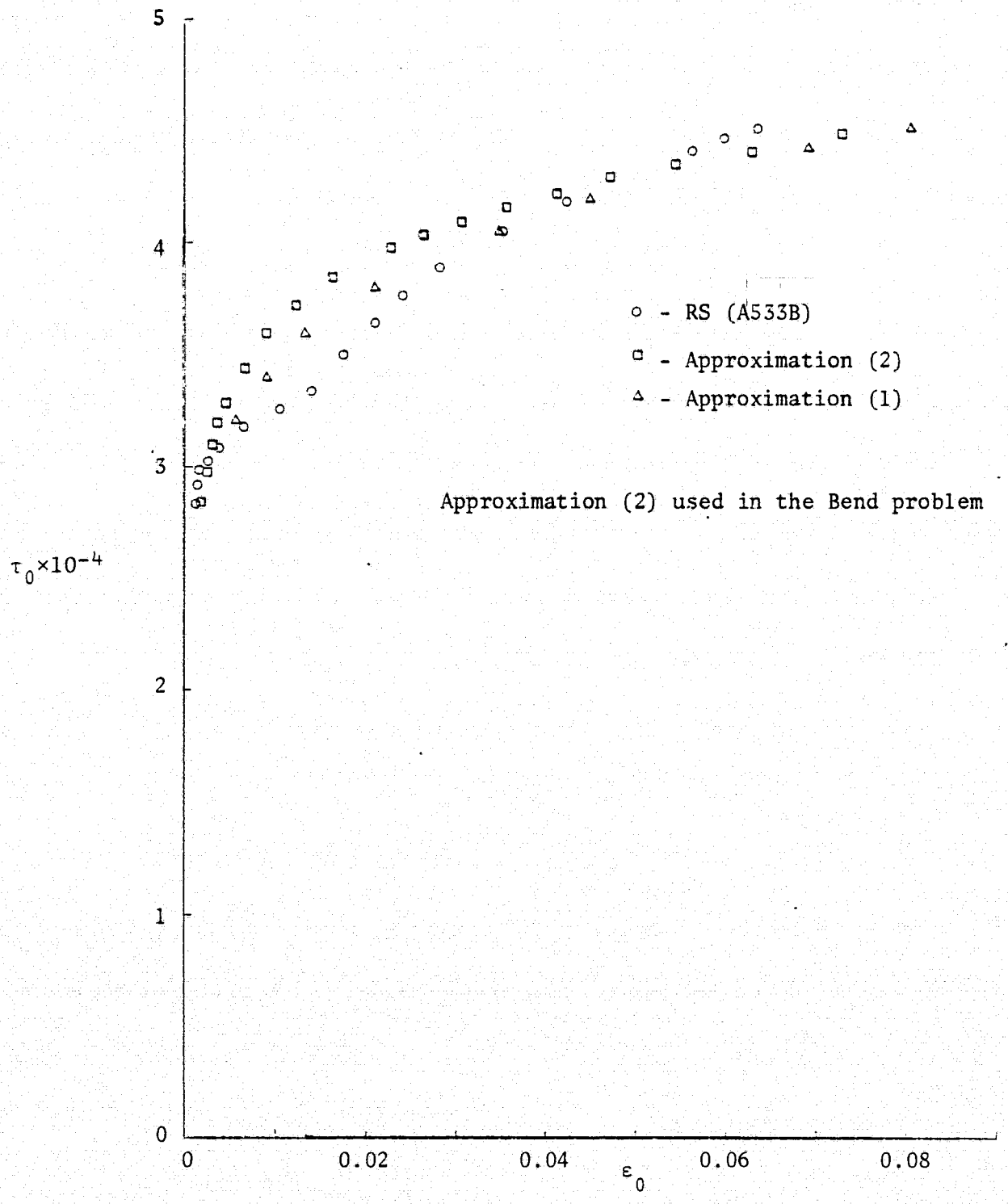

FIG. 66: Octahedral Stress-Strain Curves (RS)

FIG. 67: Near and Far Field J Values VS. Applied Load (RS)

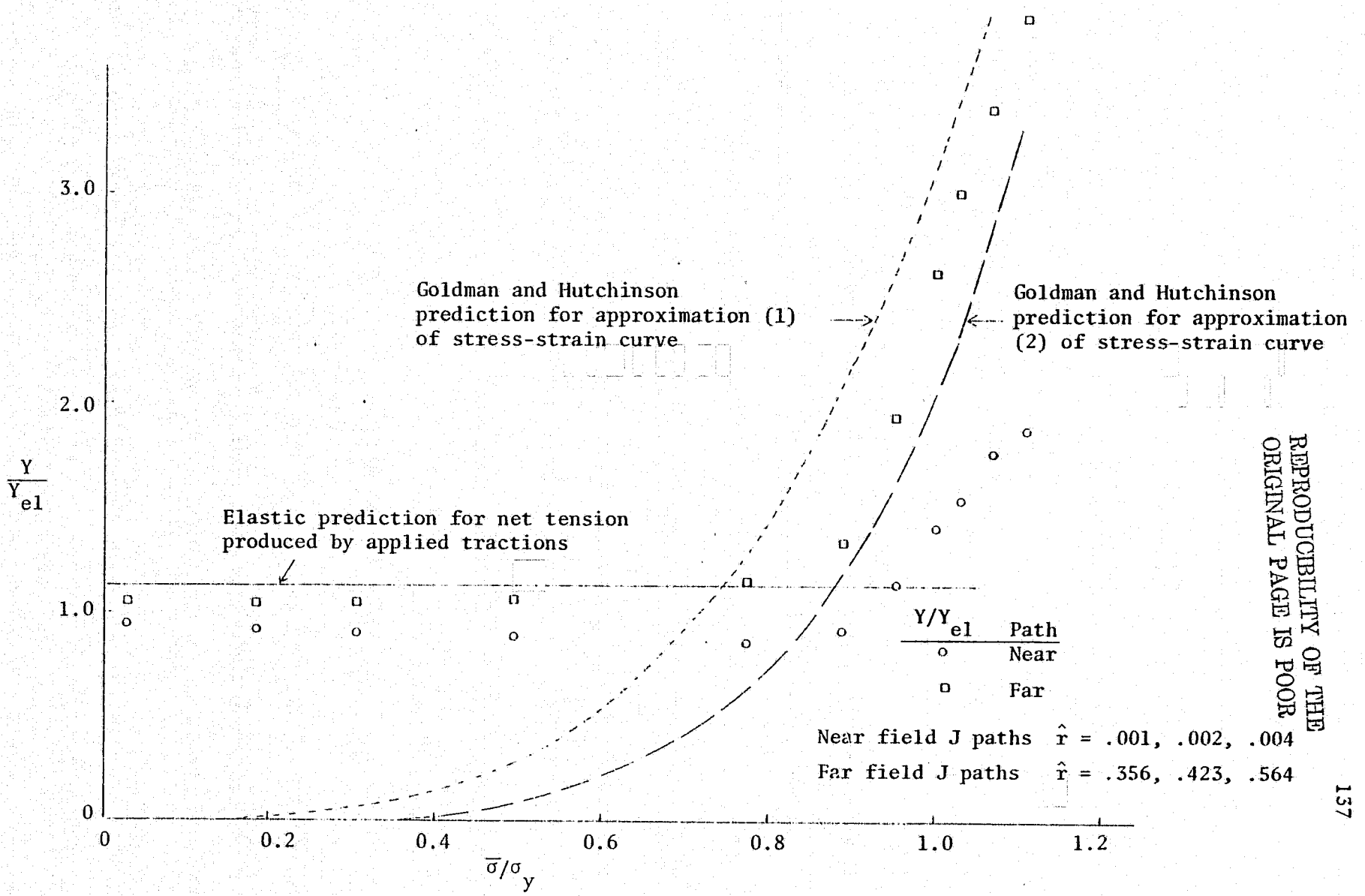

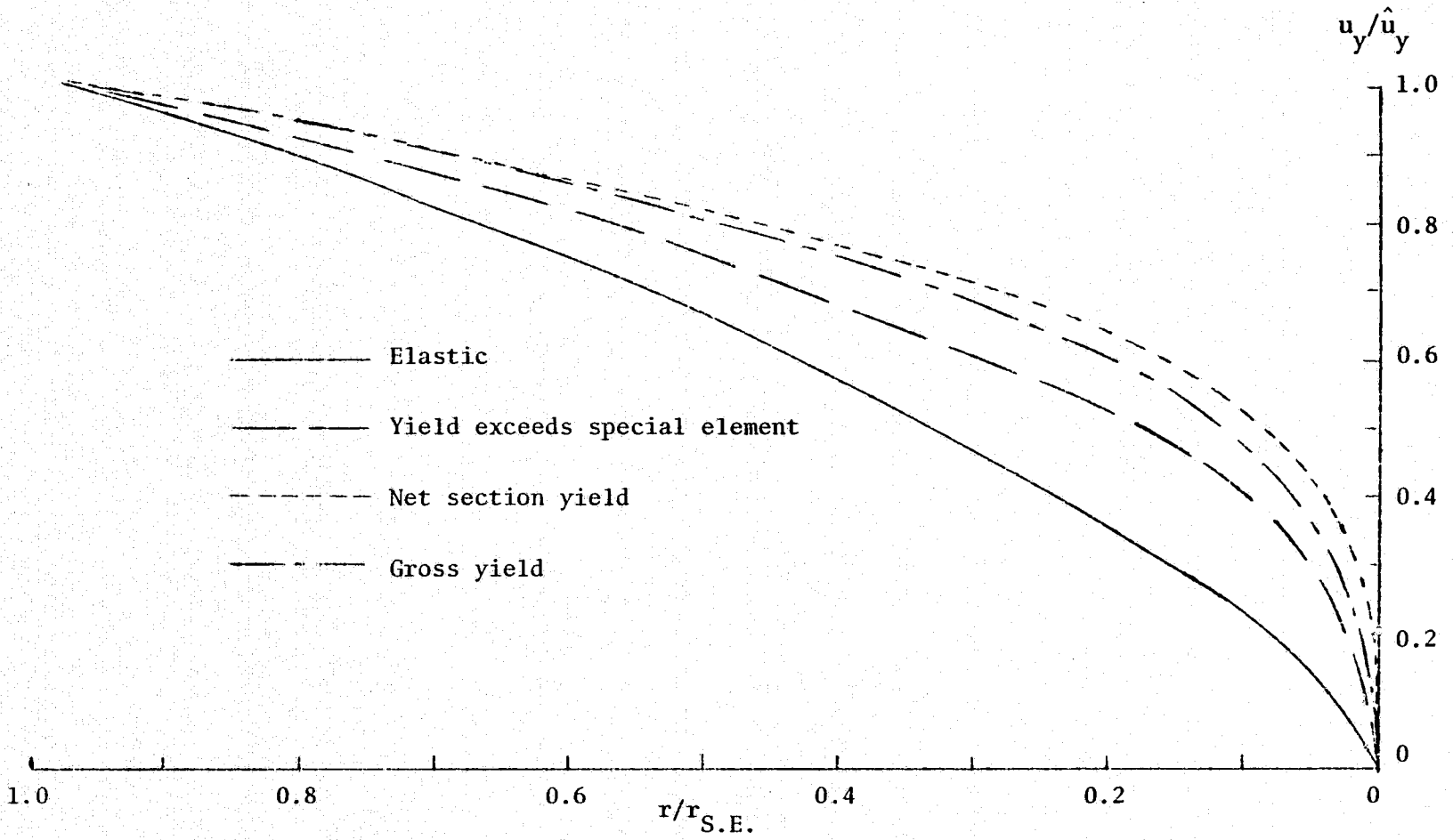

FIG. 68: Crack Opening Profiles within the Special Element (RS)

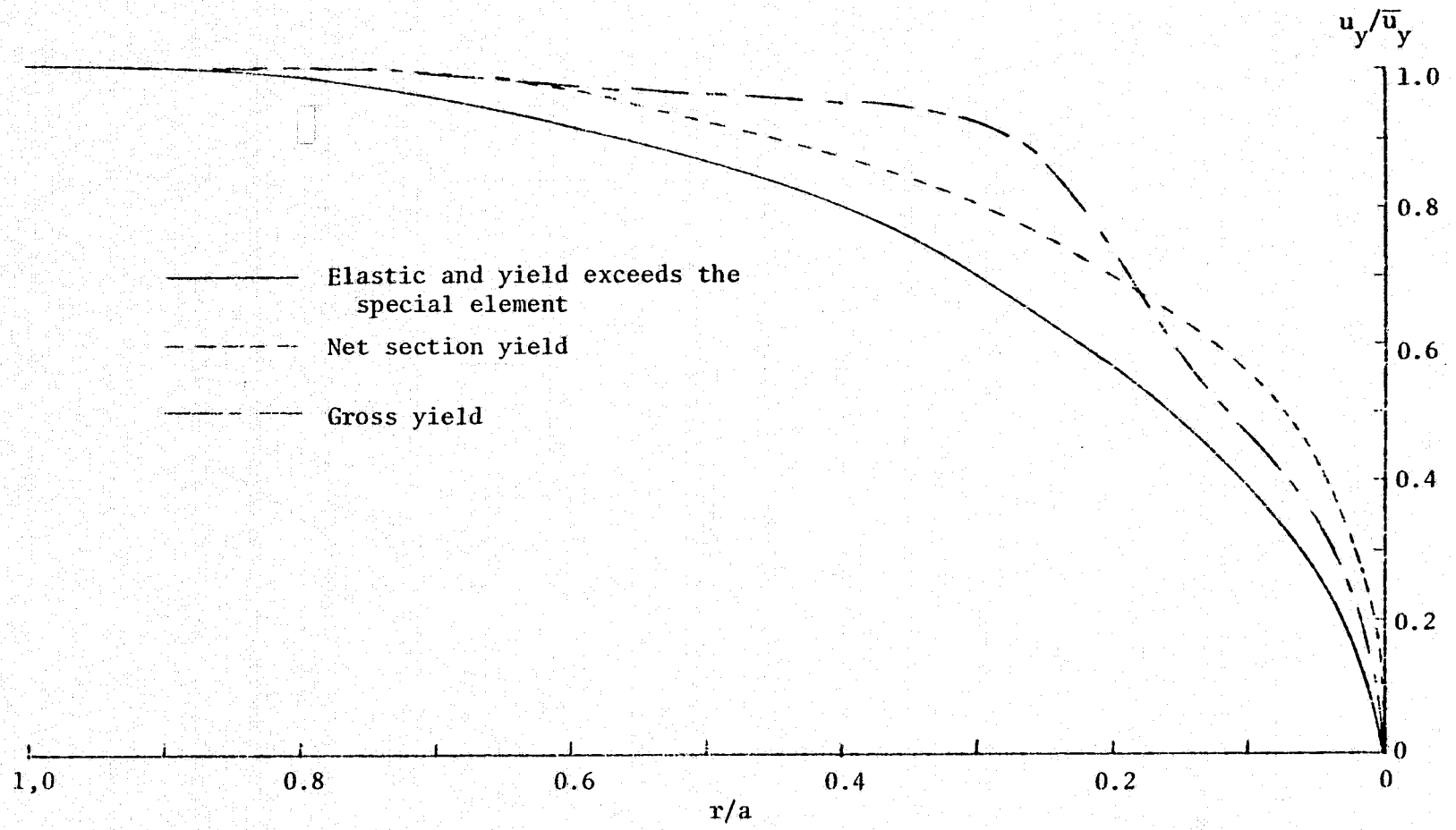

FIG. 69: Crack Opening Profile Along Entire Crack Flank (RS)

FIG. 70: $\left(\delta^*/\delta^*_{el}\right)^{1/2}$ VS. $\bar{\sigma}/\sigma_y$ (RS)

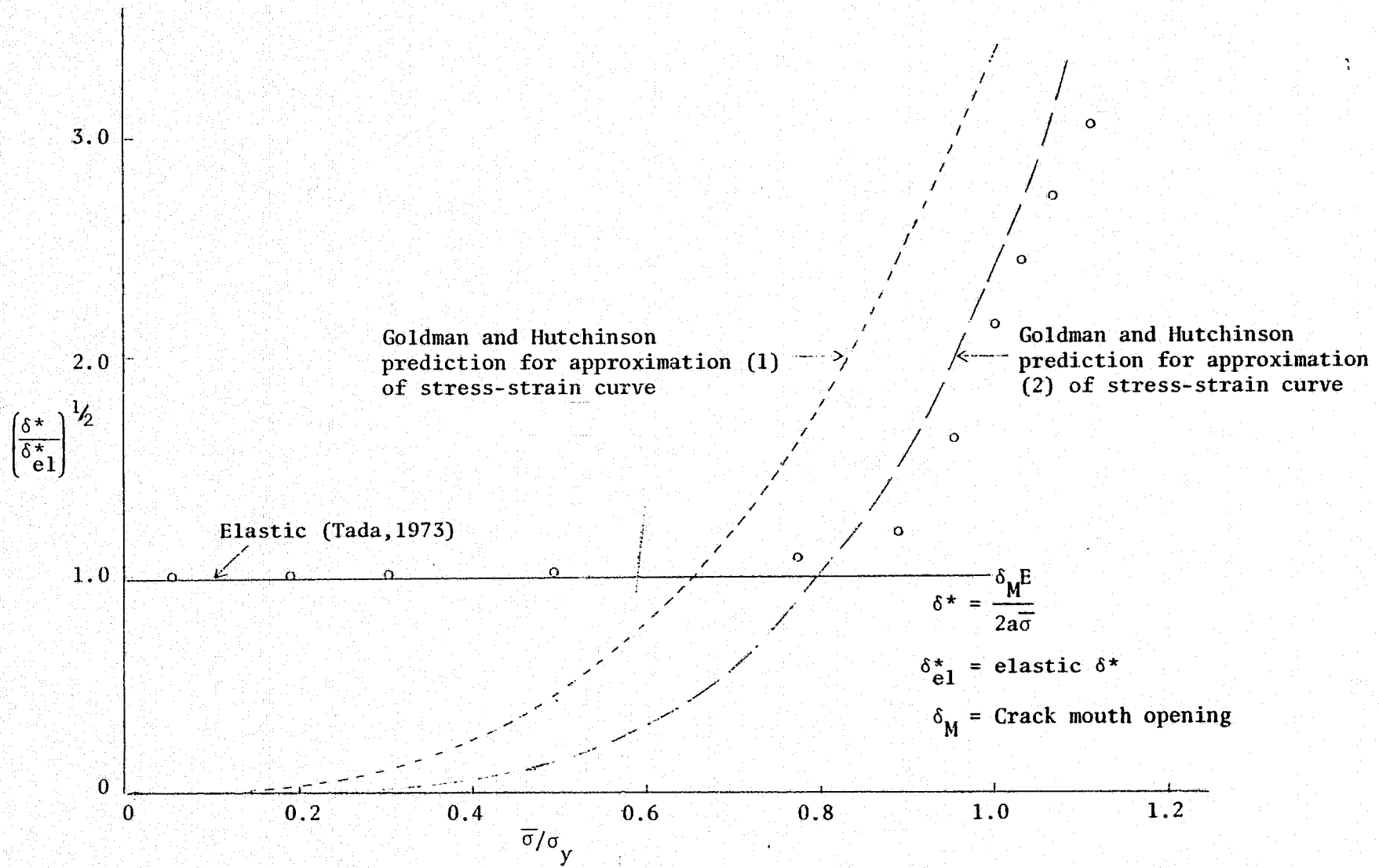

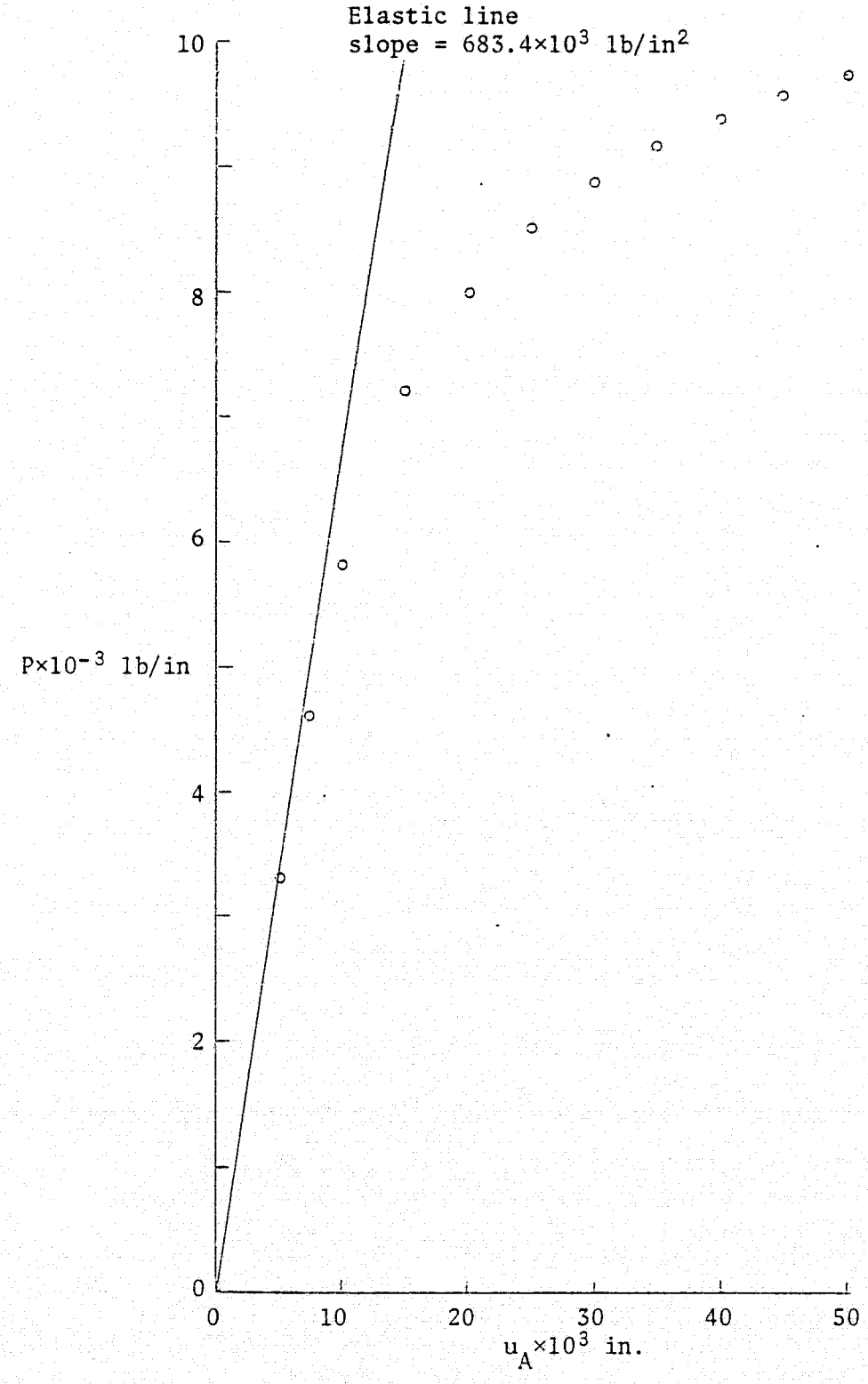

FIG. 71: Load-Deflection Curve (Bend)

FIG. 72: Hydrostatic Stress along Crack Ligament (Bend)

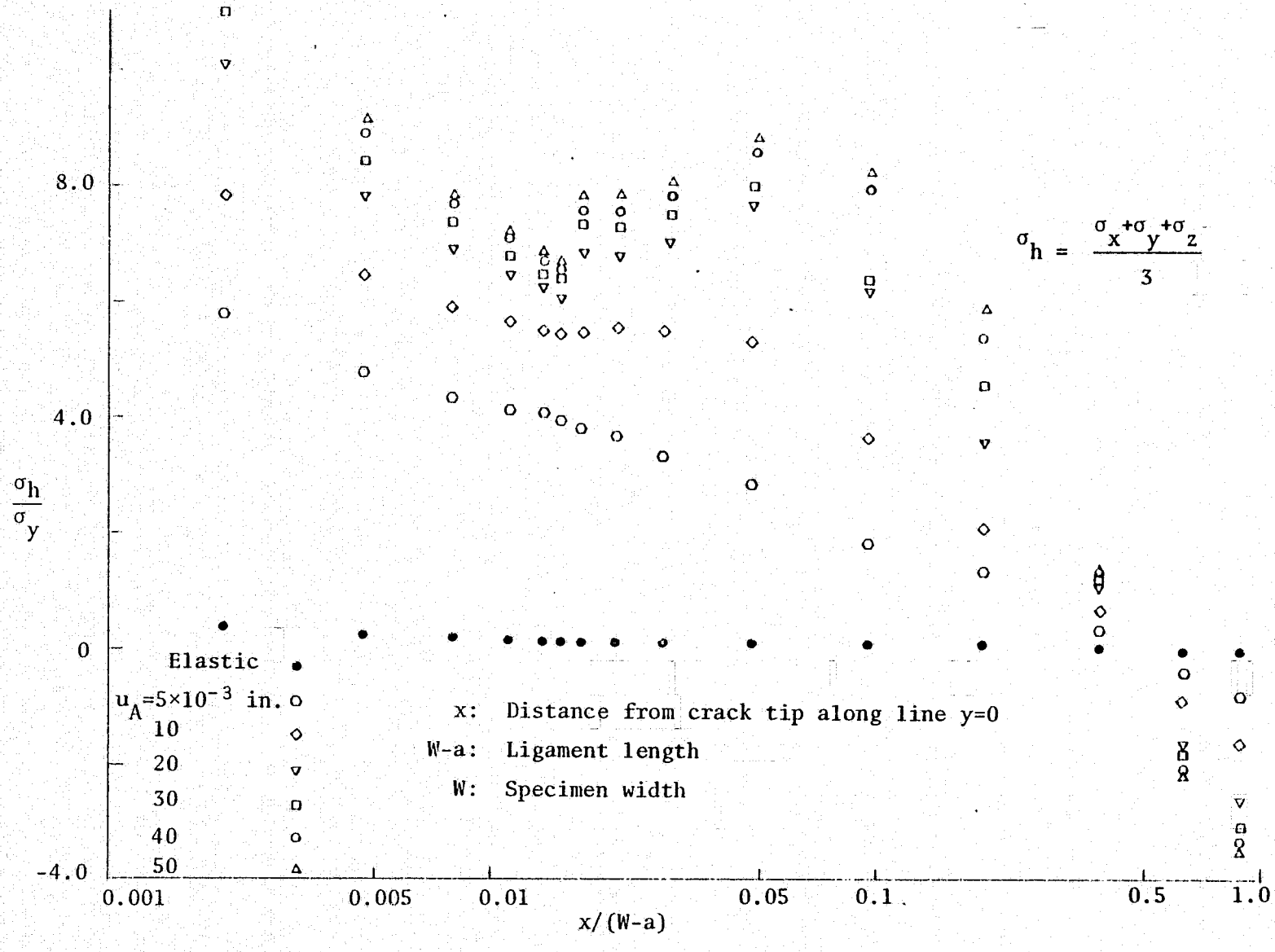

FIG. 73: Hydrostatic Stress along Crack Ligament (PH)

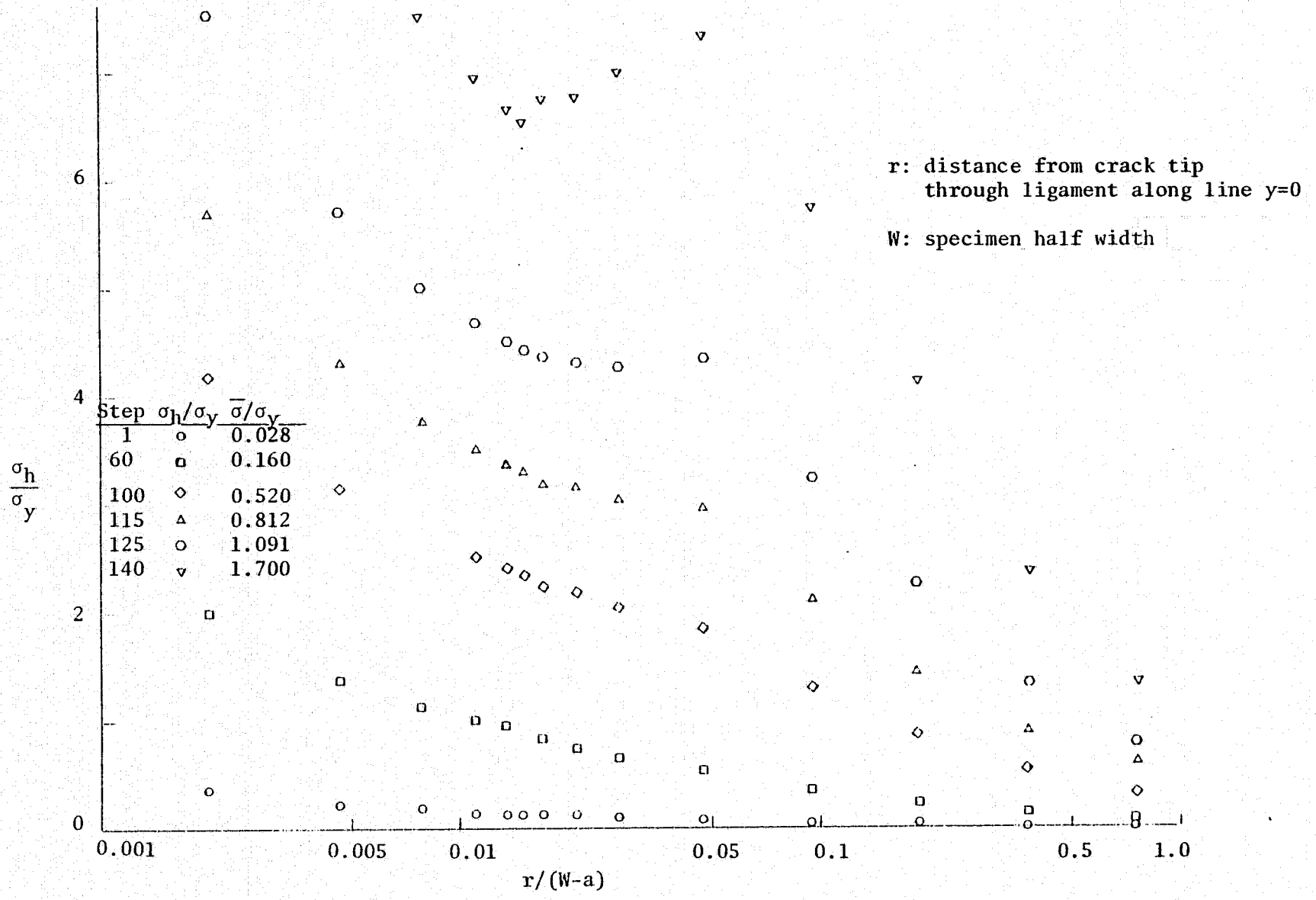

FIG. 74: Effective Stress along Crack Ligament (Bend)

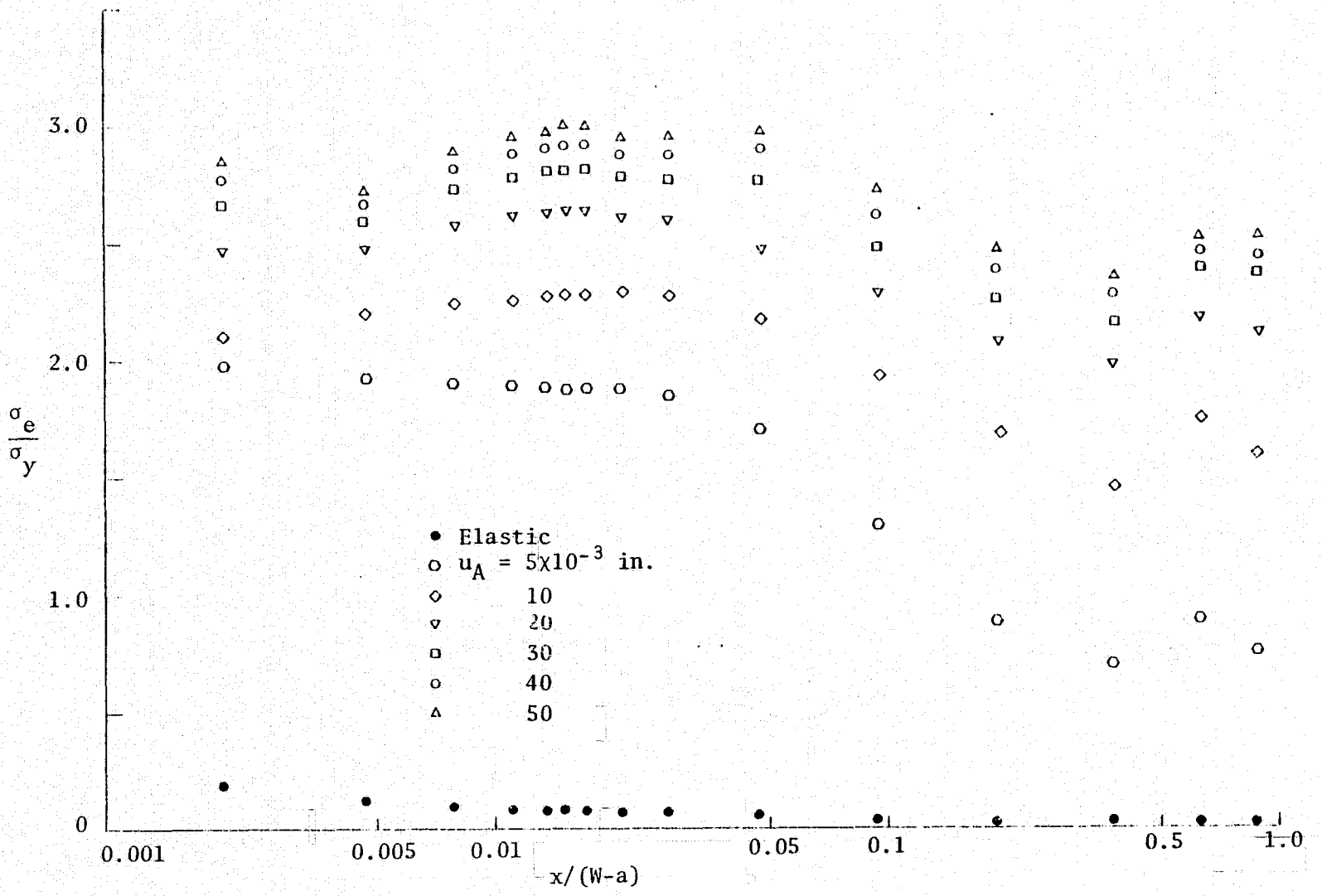

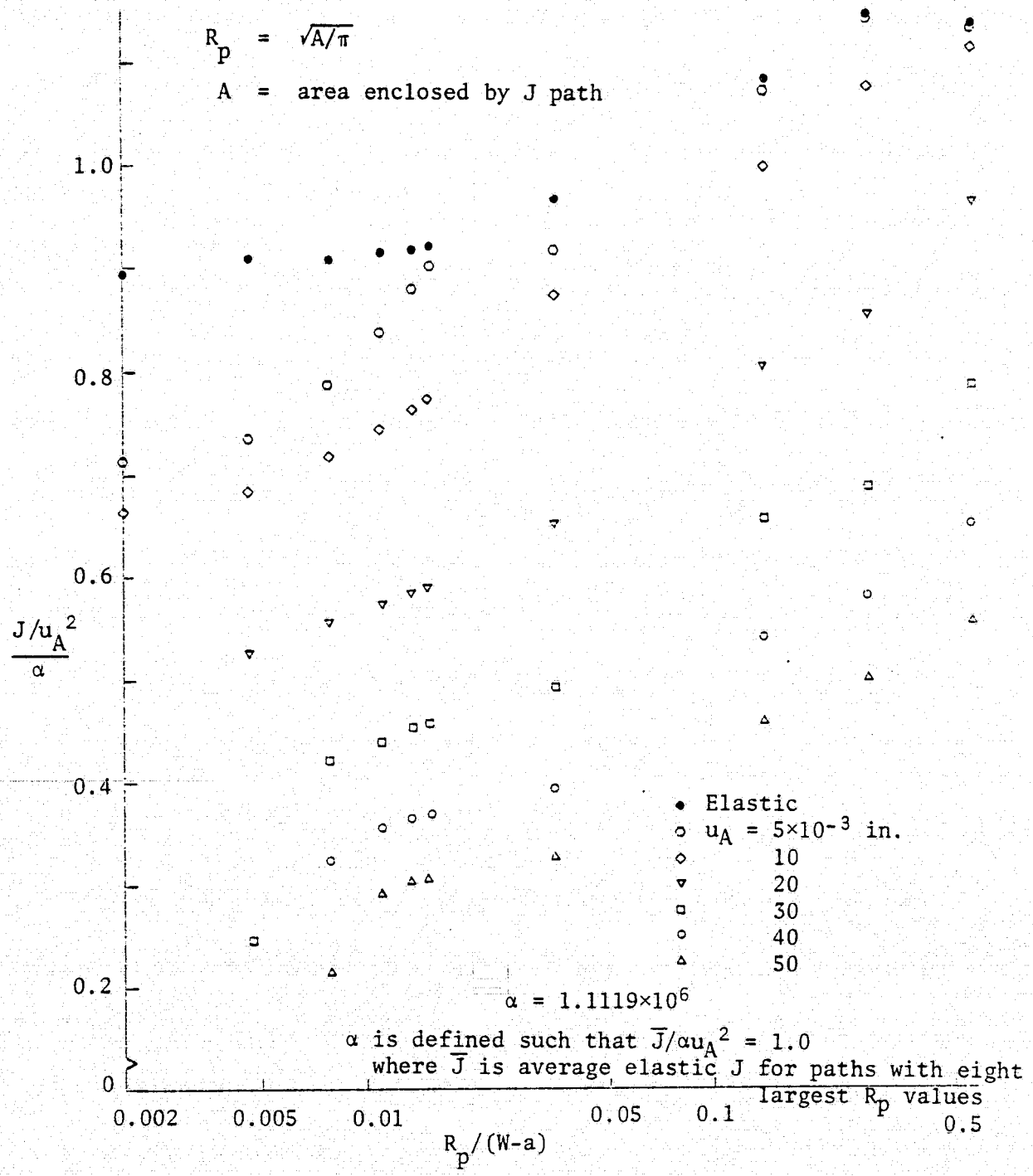

FIG. 75: J as a Function of Distance from the Tip for a Number of Load Levels (Bend)

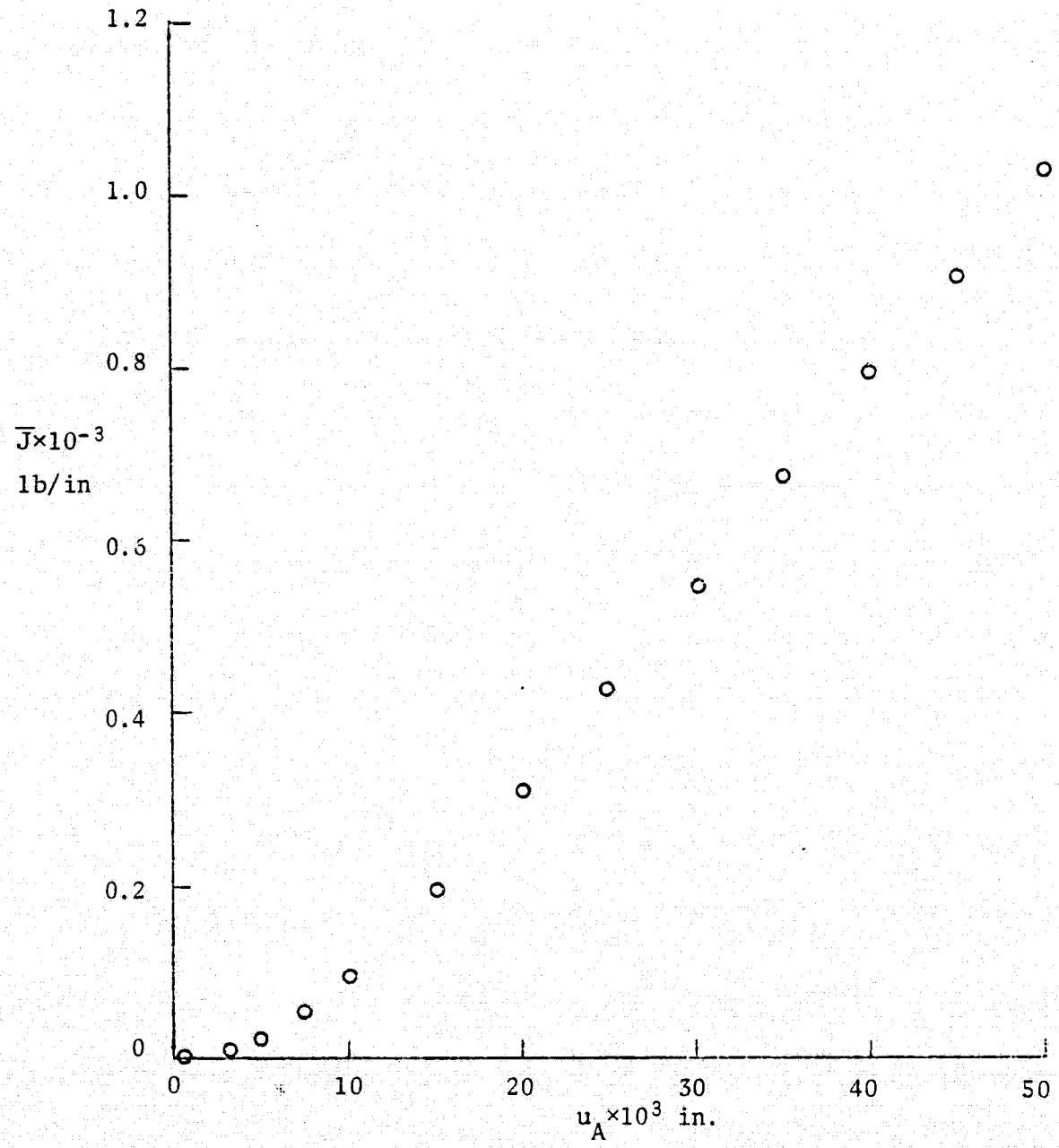

FIG. 76: $\overline{J}$ VS. Applied Displacement (Bend)

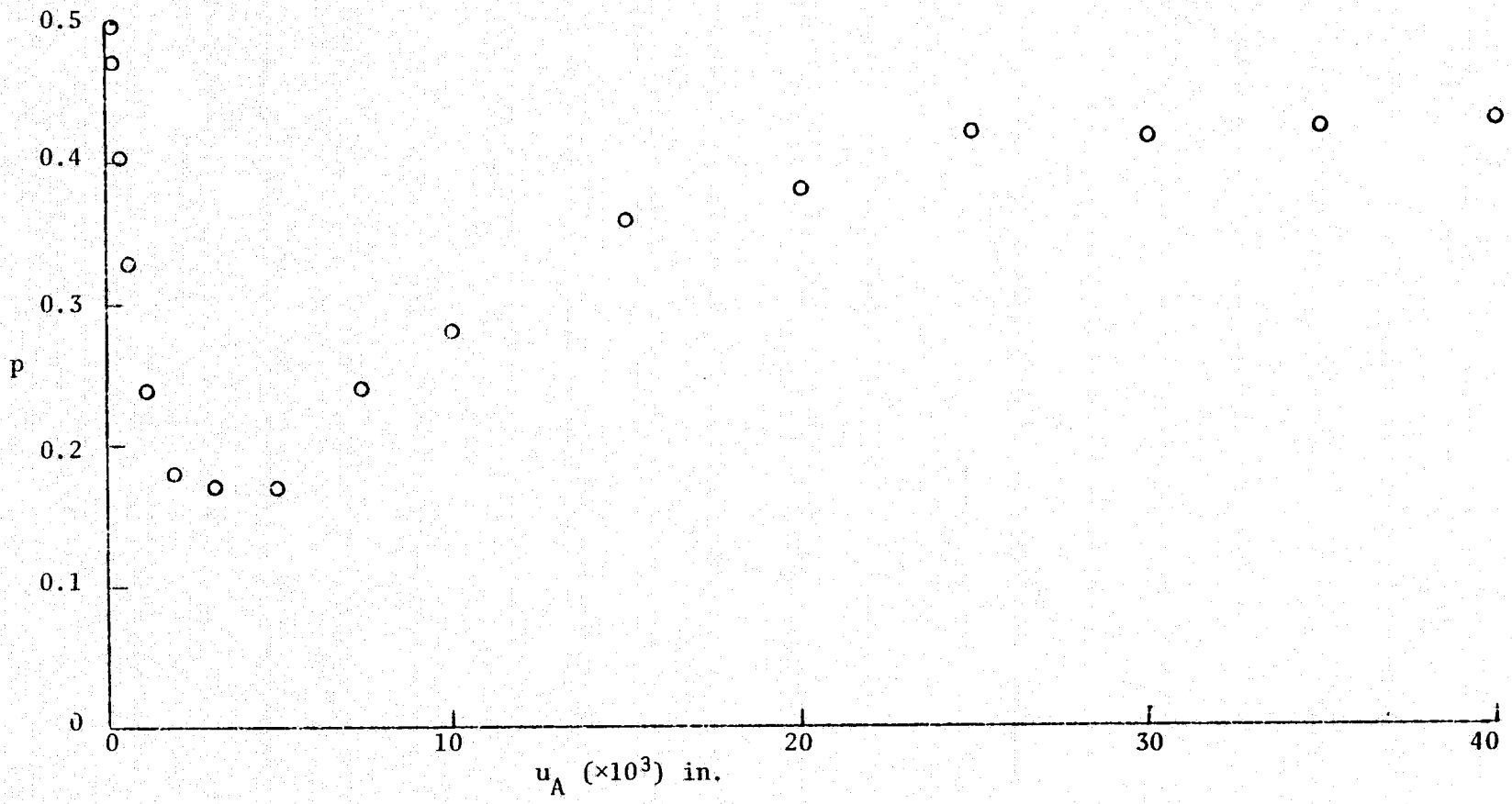

FIG. 77: Incremental Exponent VS. Applied Displacement (Bend)

FIG. 78: Accumulated Exponent VS. Applied Displacement (Bend)

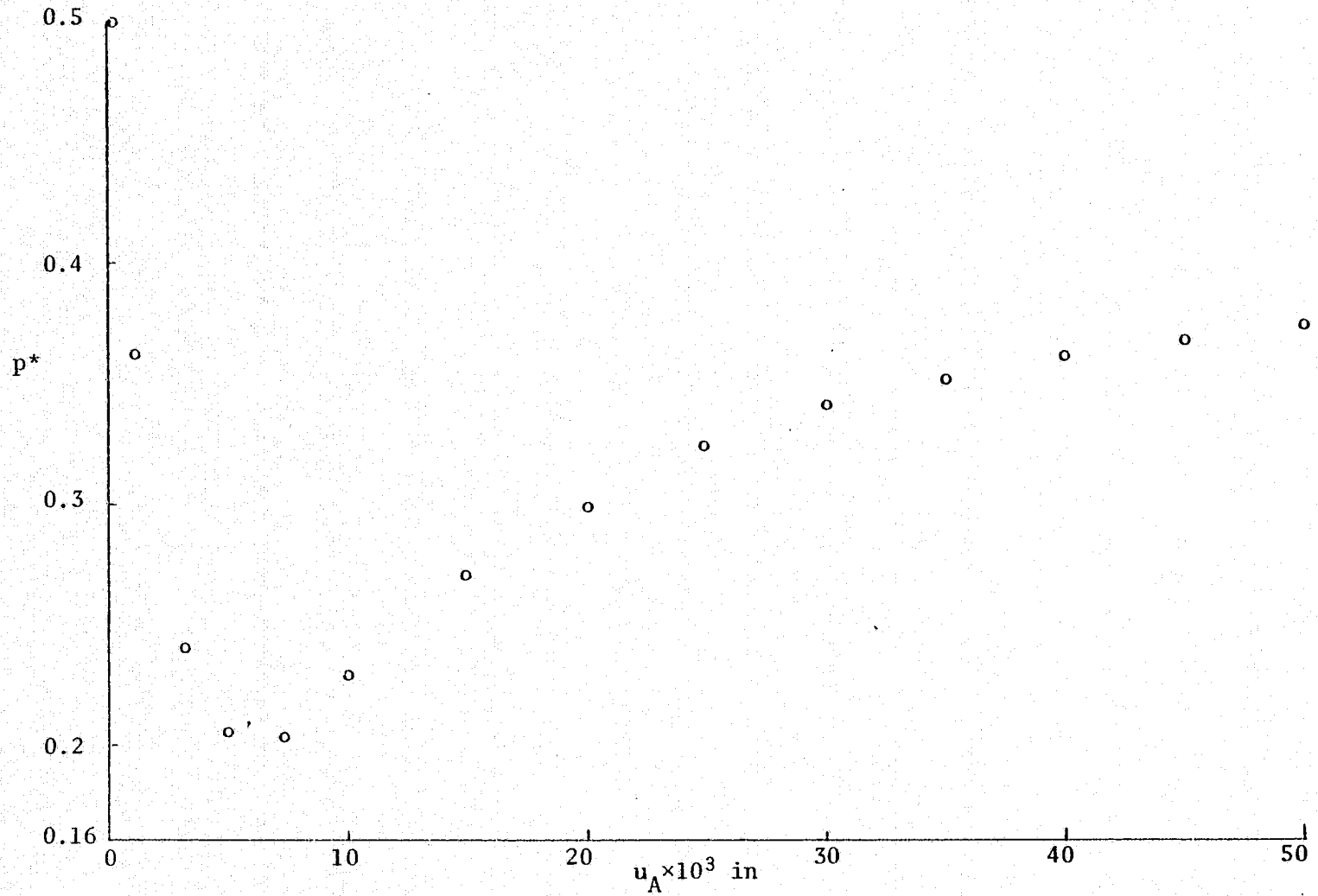

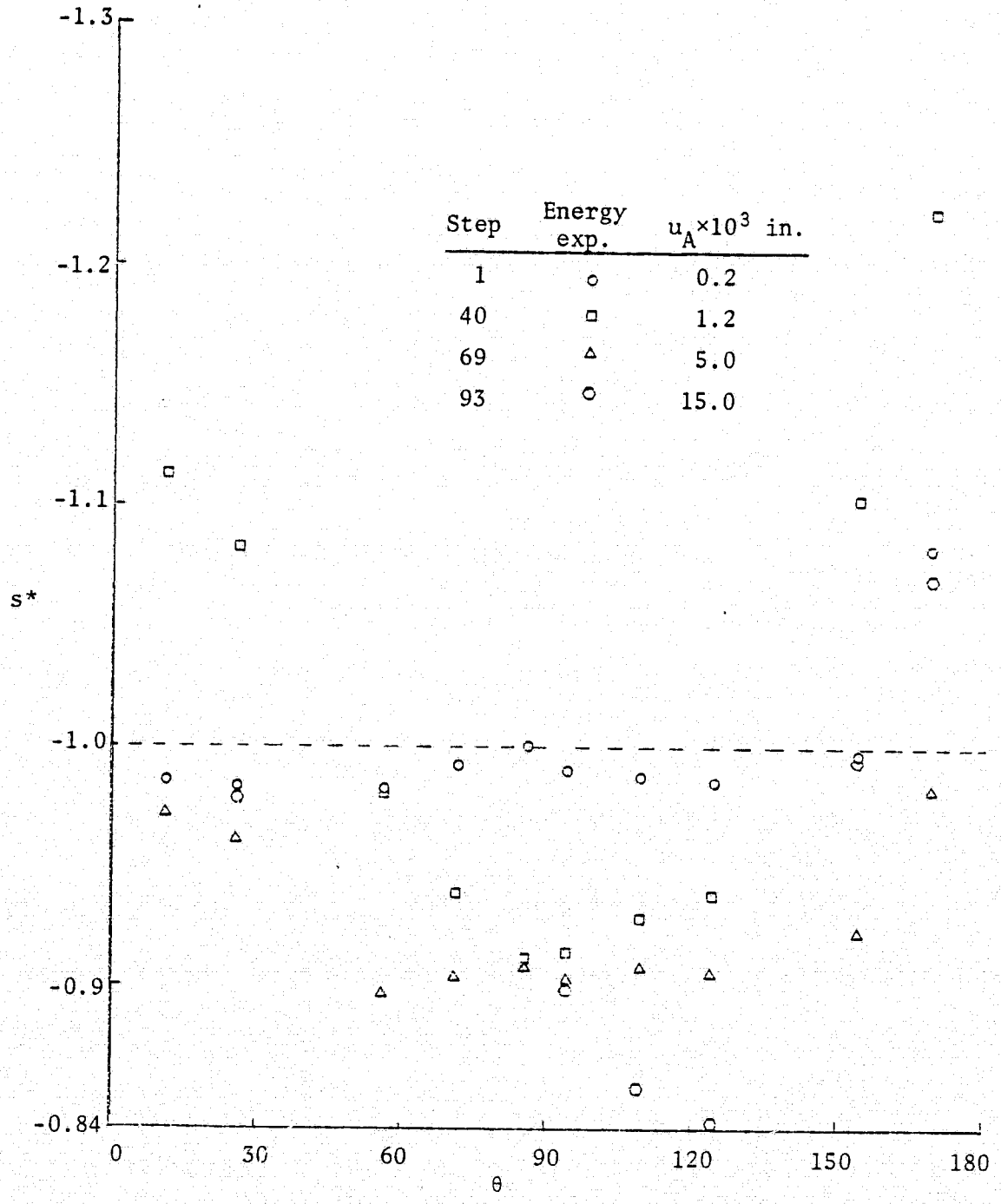

FIG. 79: Energy Exponent VS. Angular Position (Bend)

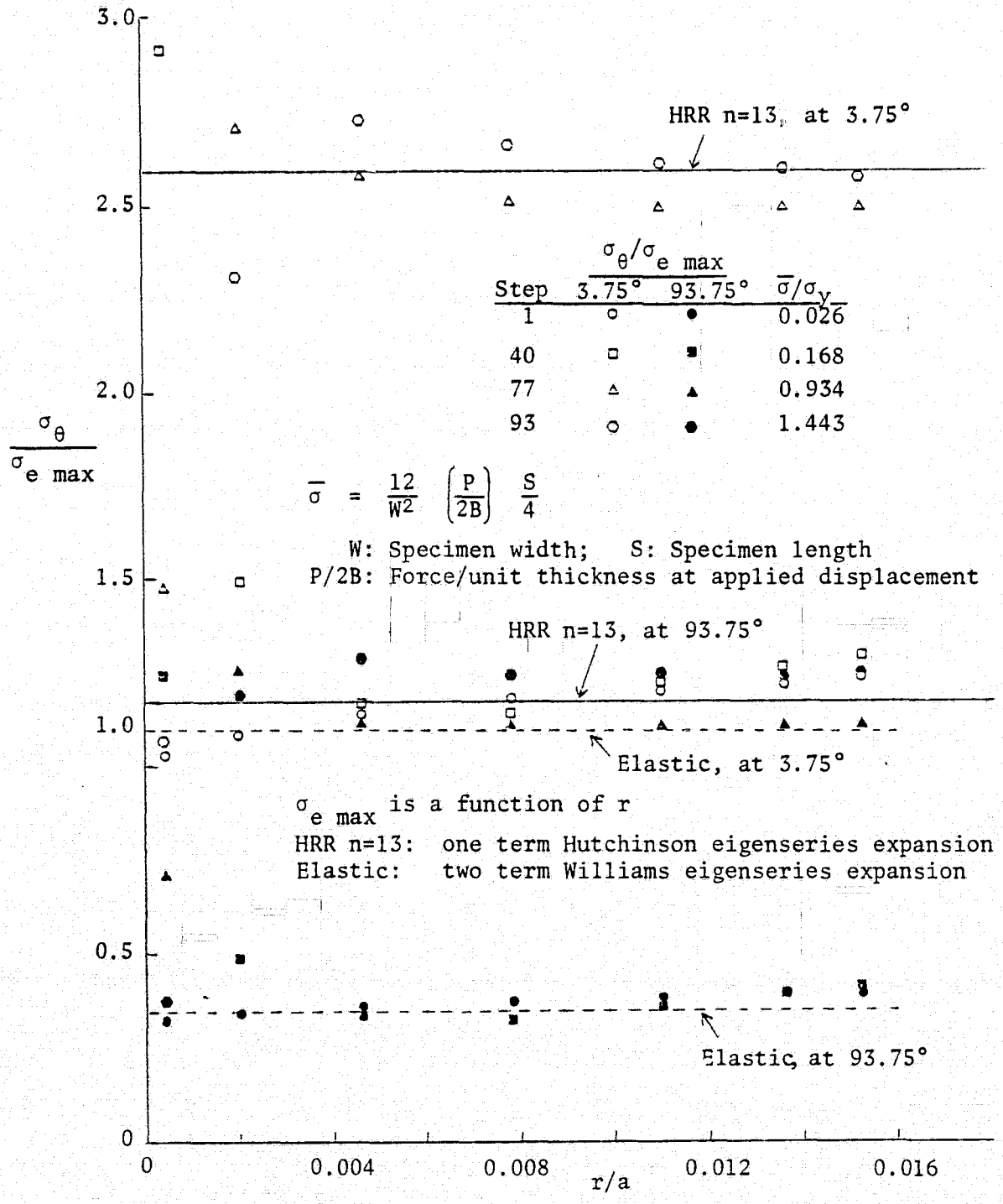

FIG. 80: $\sigma_\theta/\sigma_{e\ max}$ VS. r/a at θ = 3.75° and 93.75° (Bend)

$$\bar{\sigma} = \frac{12}{W^2}\left(\frac{P}{2B}\right)\frac{S}{4}$$

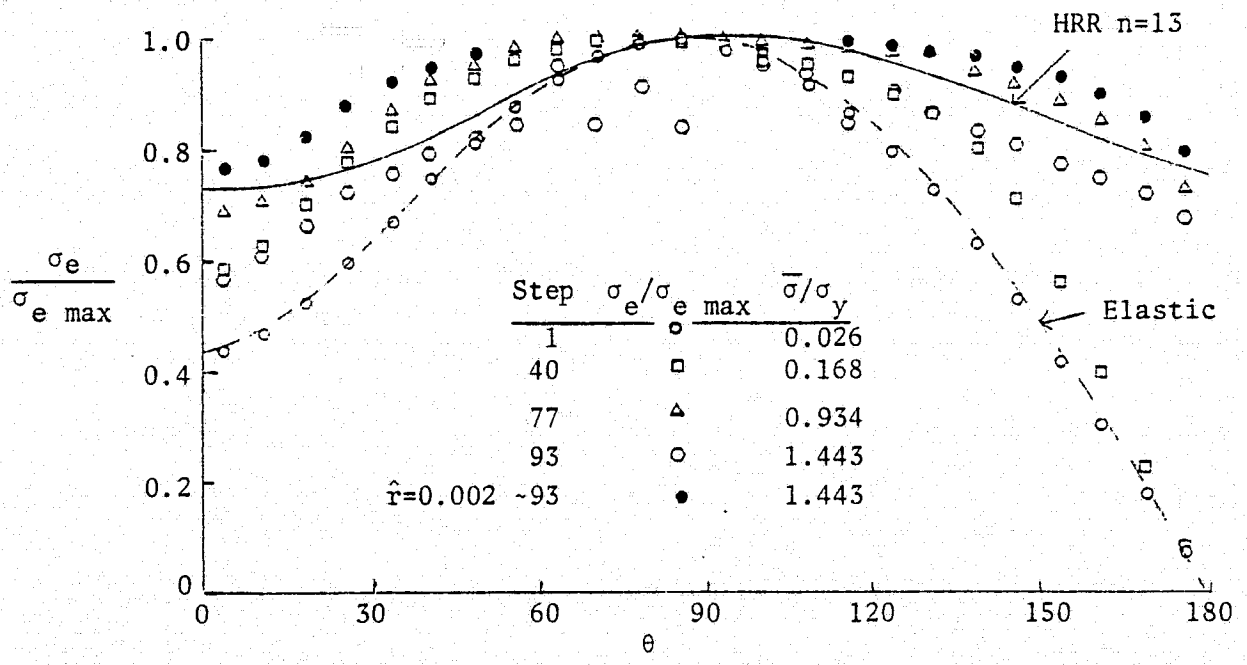

FIG. 81: $\sigma_e/\sigma_{e\ max}$ VS. θ for $\hat{r}$ = 0.001 (Bend)

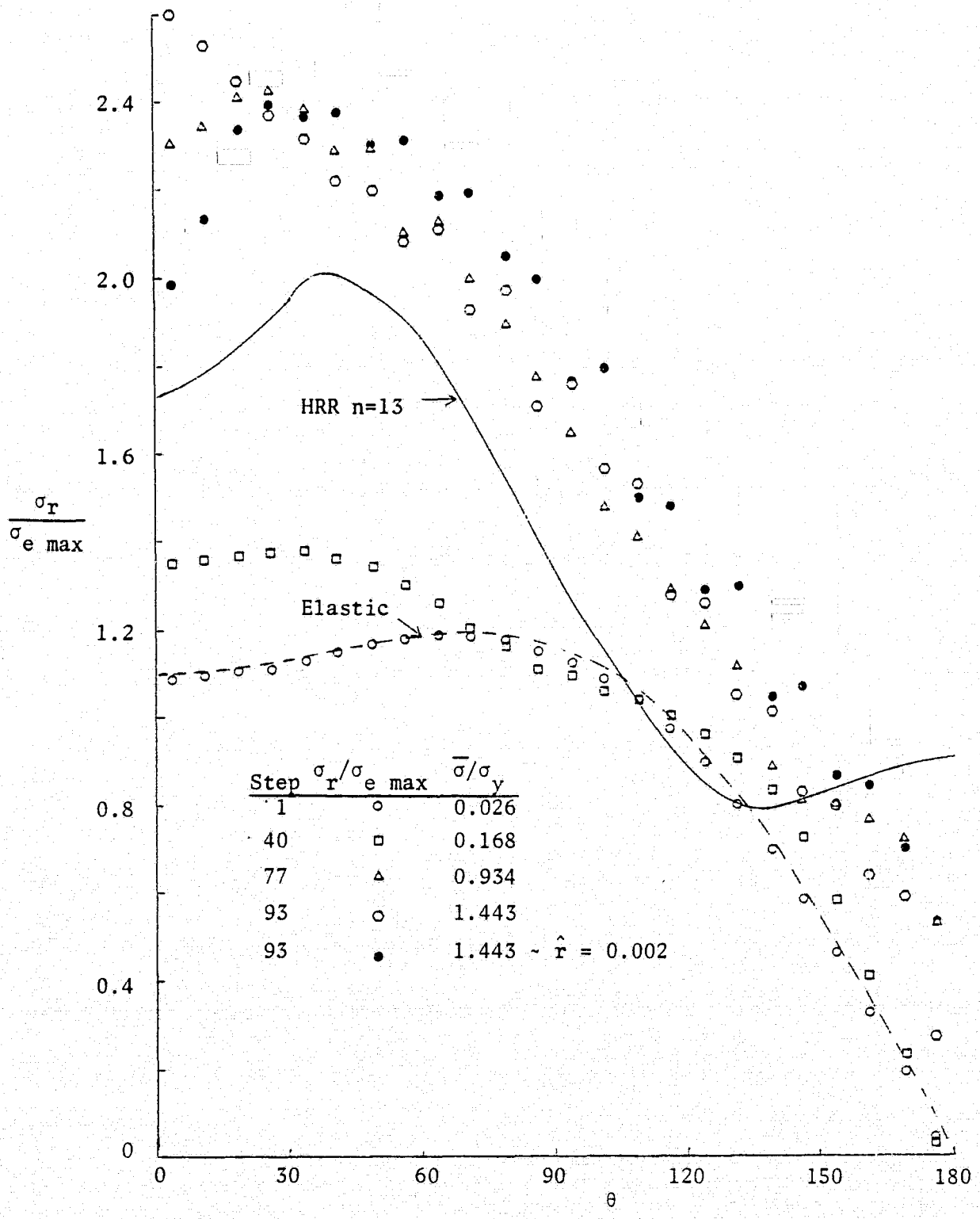

FIG. 82: $\sigma_r/\sigma_{e\ max}$ VS. θ for $\hat{r}$ = 0.001 (Bend)

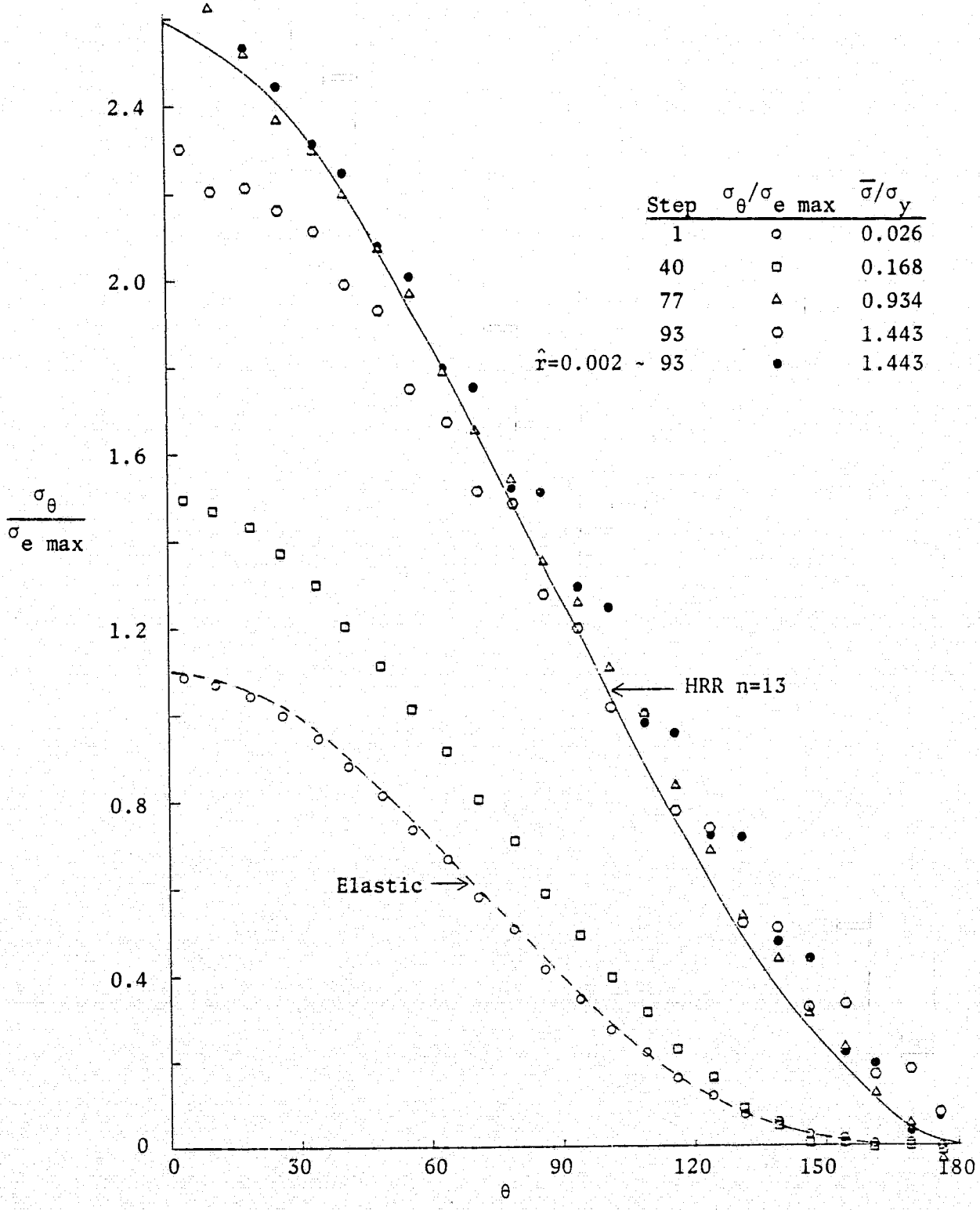

FIG. 83: $\sigma_\theta/\sigma_{e\ max}$ VS. θ for $\hat{r}$ = 0.001 (Bend)

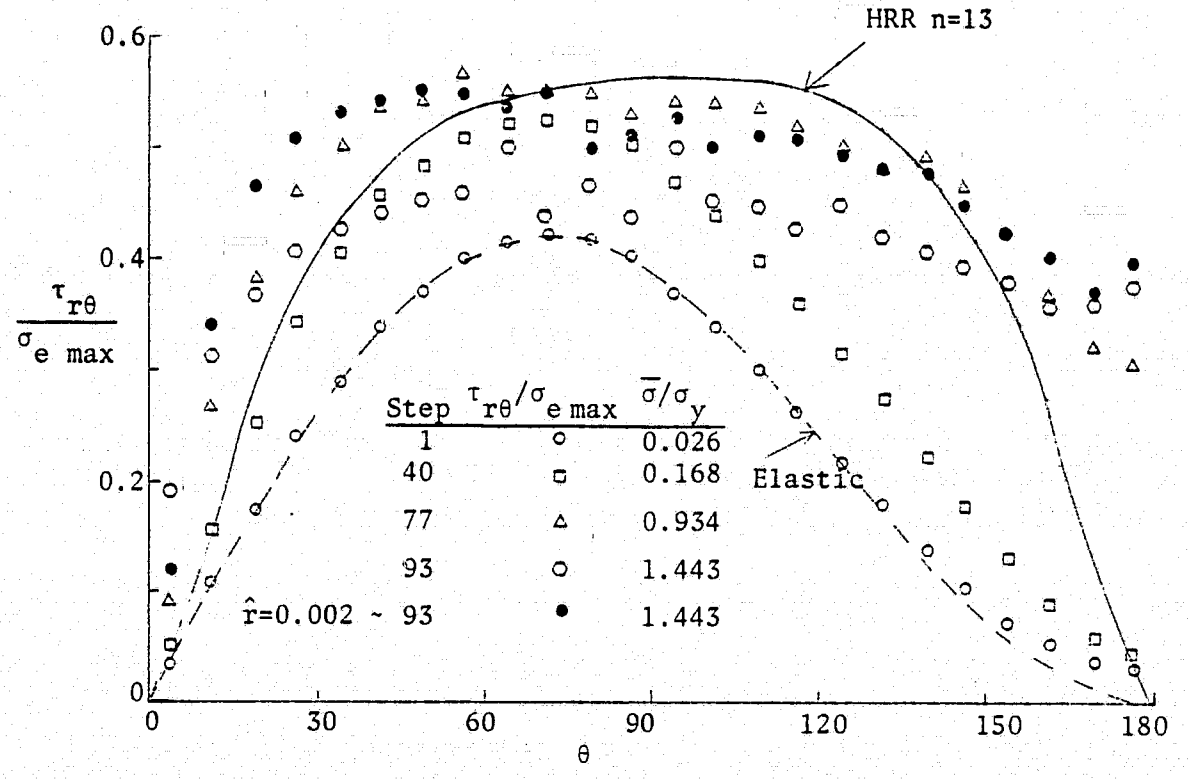

FIG. 84: $\tau_{r\theta}/\sigma_{e\ max}$ VS. θ for $\hat{r}$ = 0.001 (Bend)

FIG. 85: Normalized J VS. Distance from the Crack Tip (Bend)

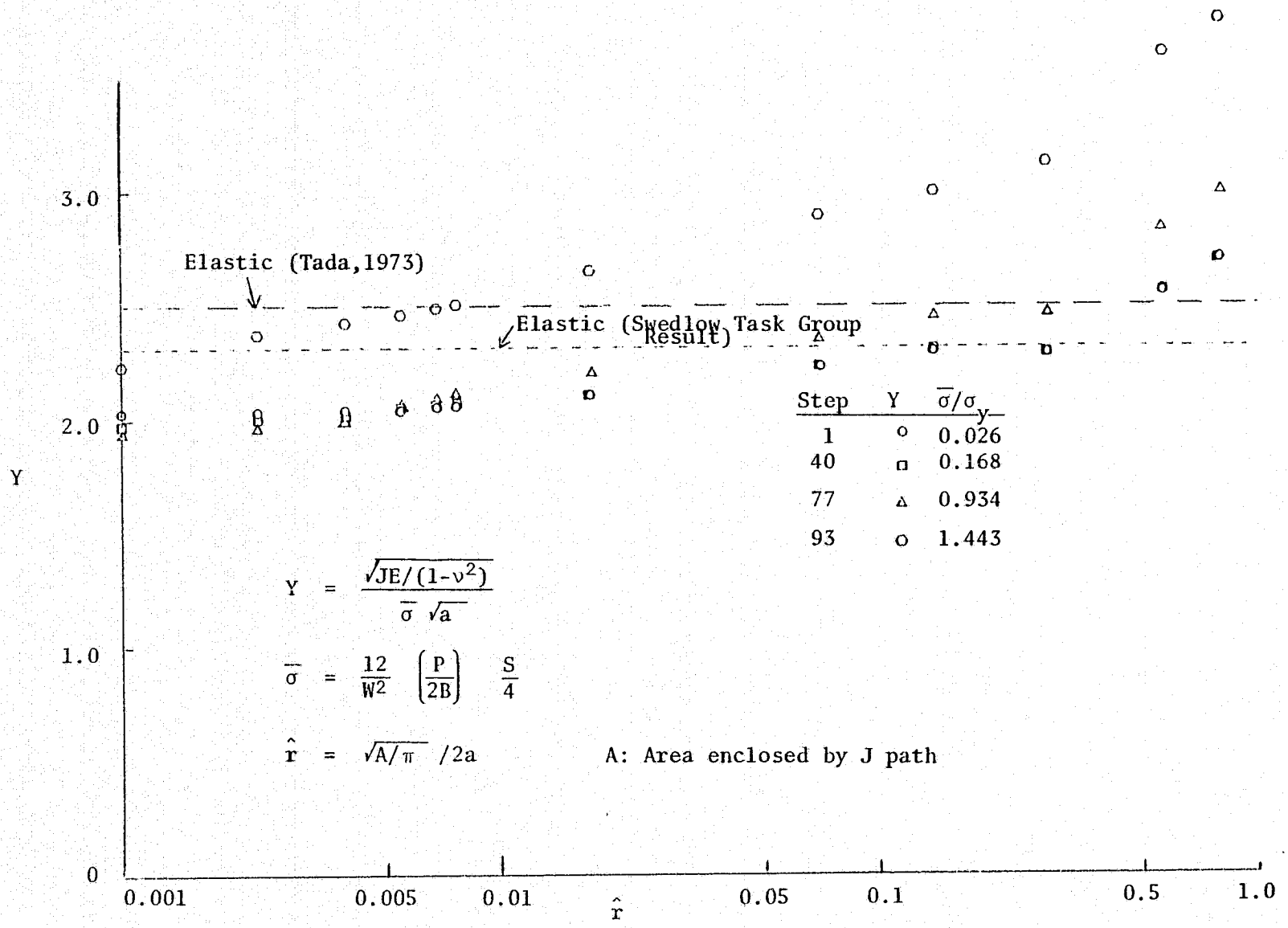

FIG. 86: Crack Opening Profiles near the Crack Tip (Bend)

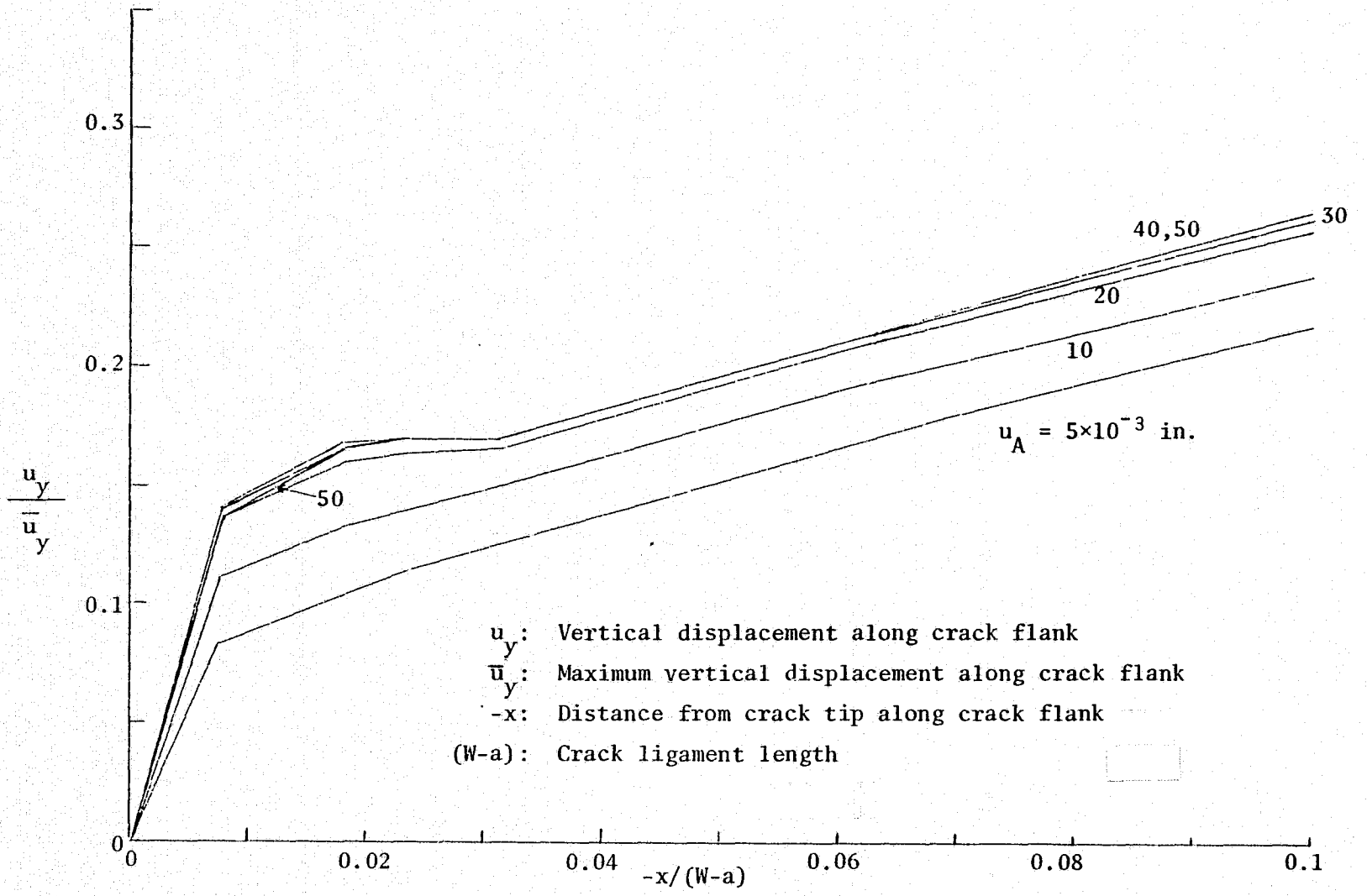

FIG. 87: Crack Opening Profiles along Remainder of Crack Flank (Bend)

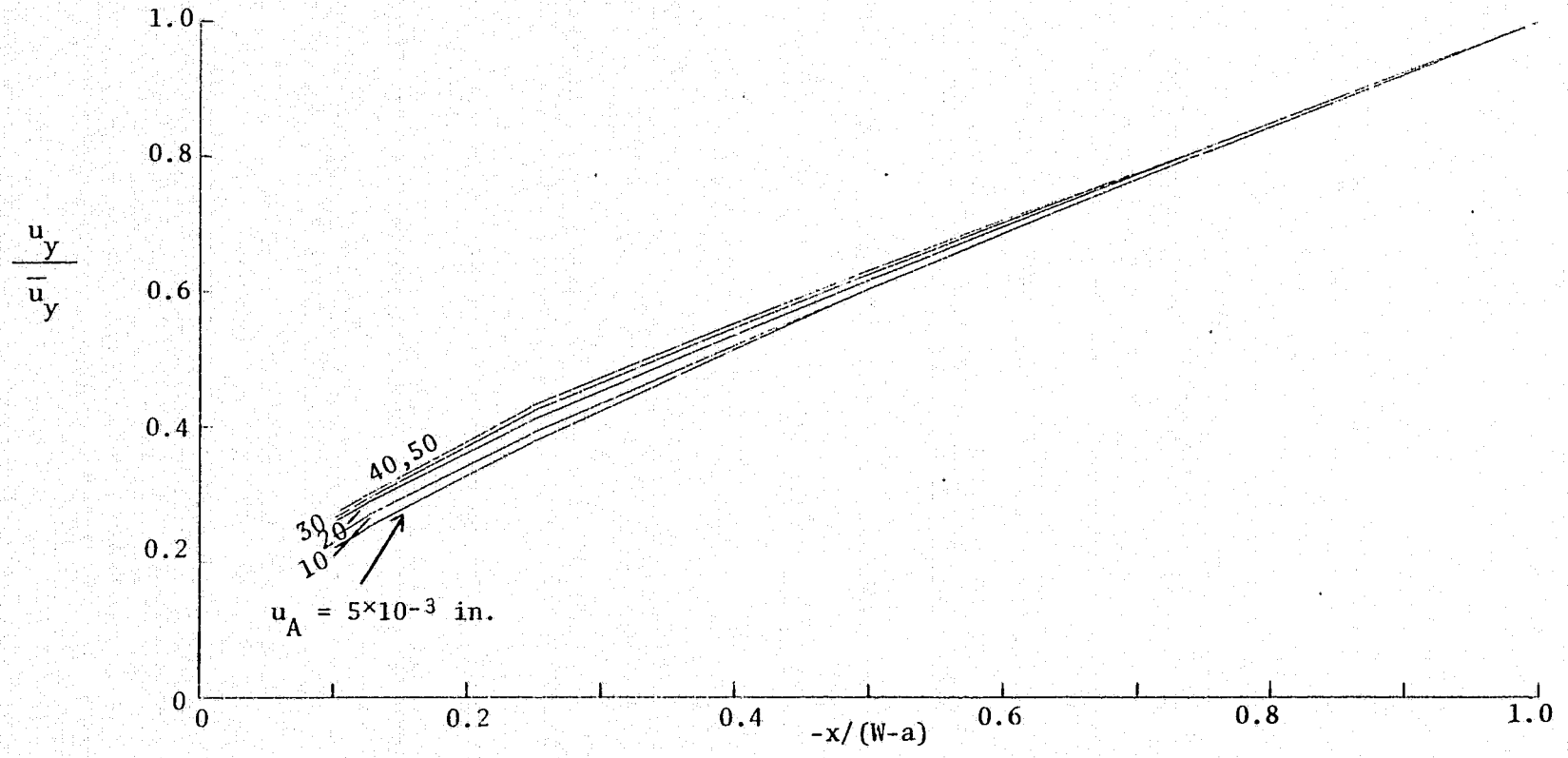

FIG. 88: J VS. Applied Displacement (RS)

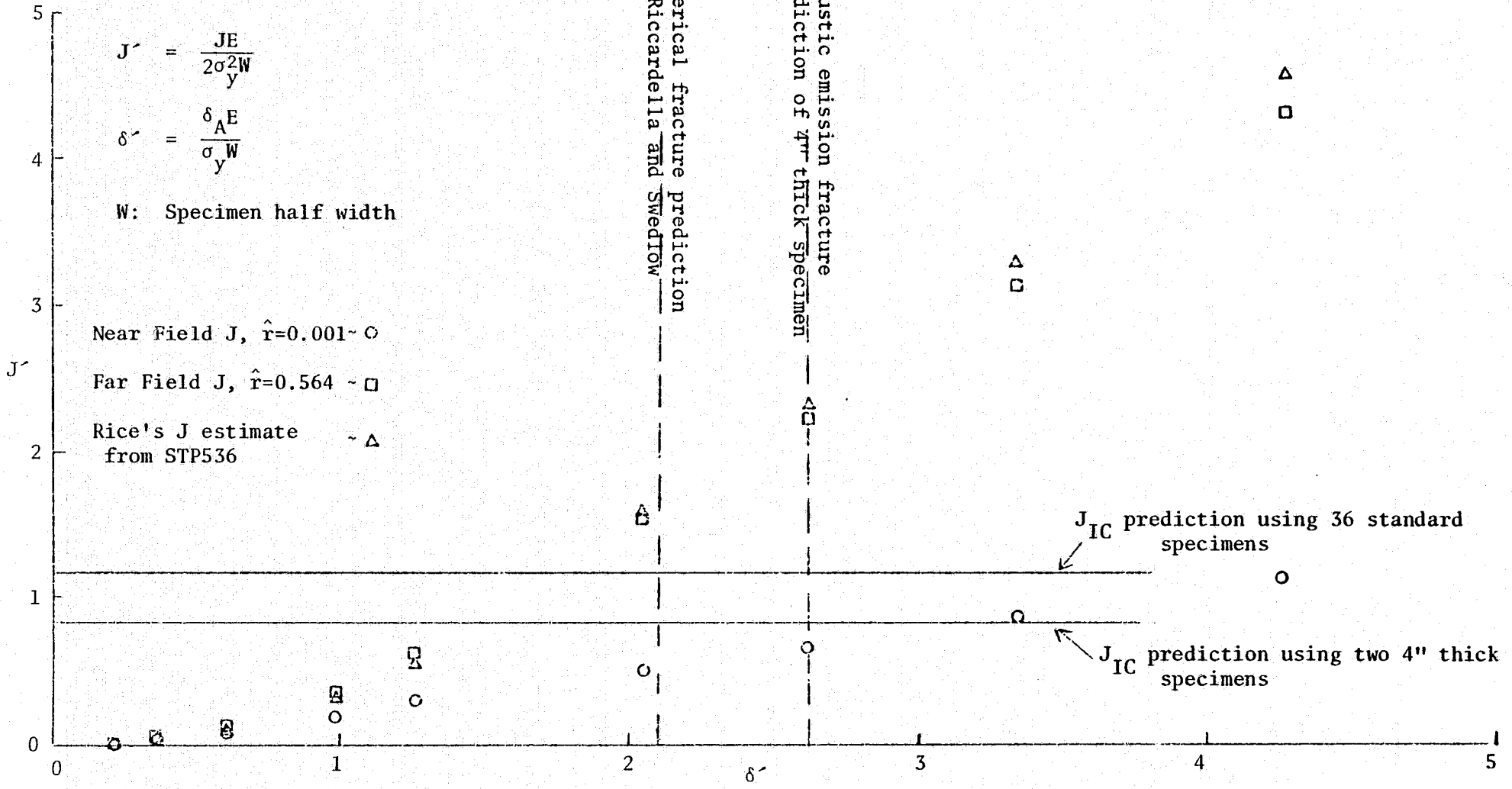

FIG. 89: J VS. Crack Mouth Opening (PH and BIL)

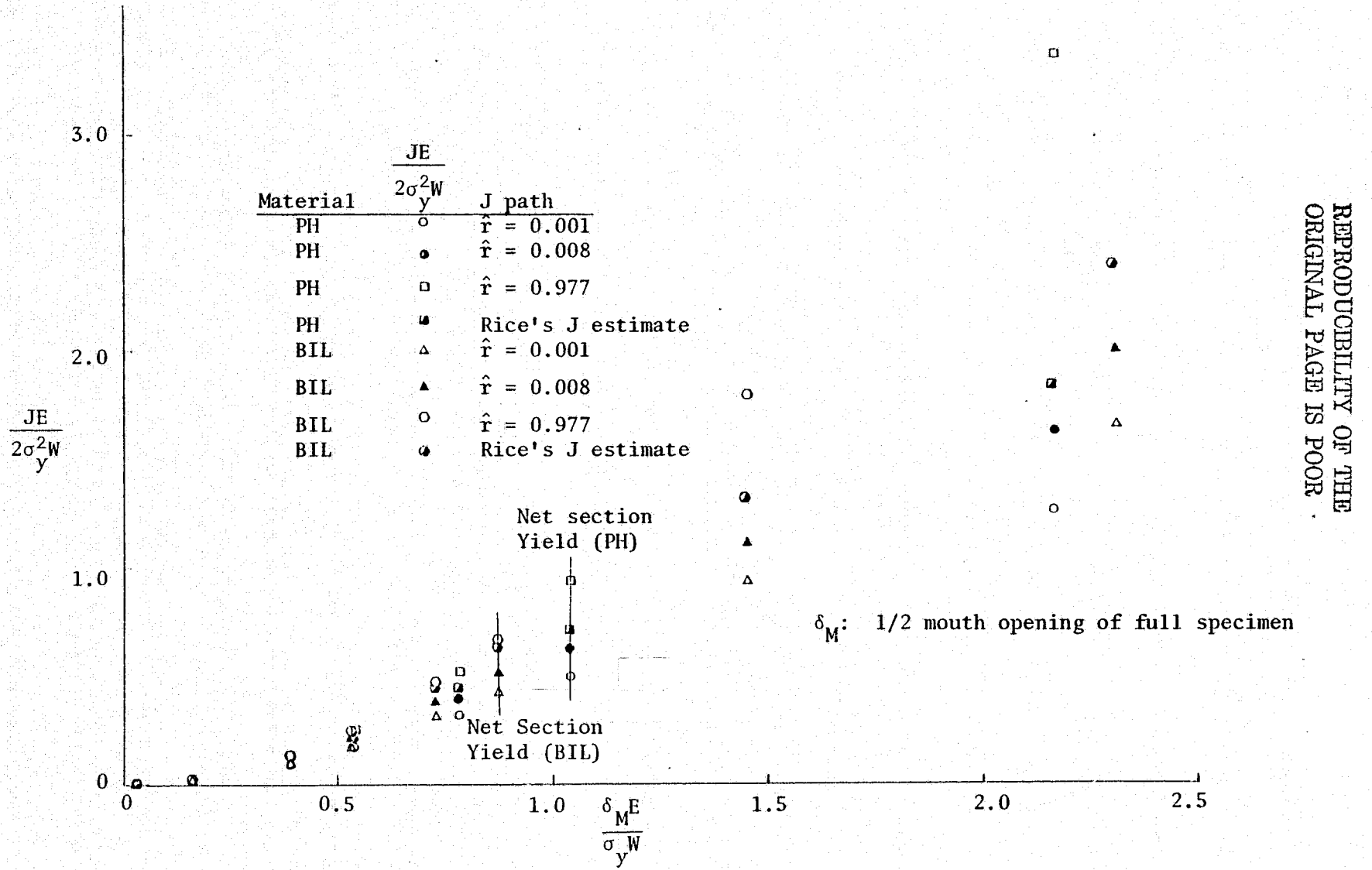

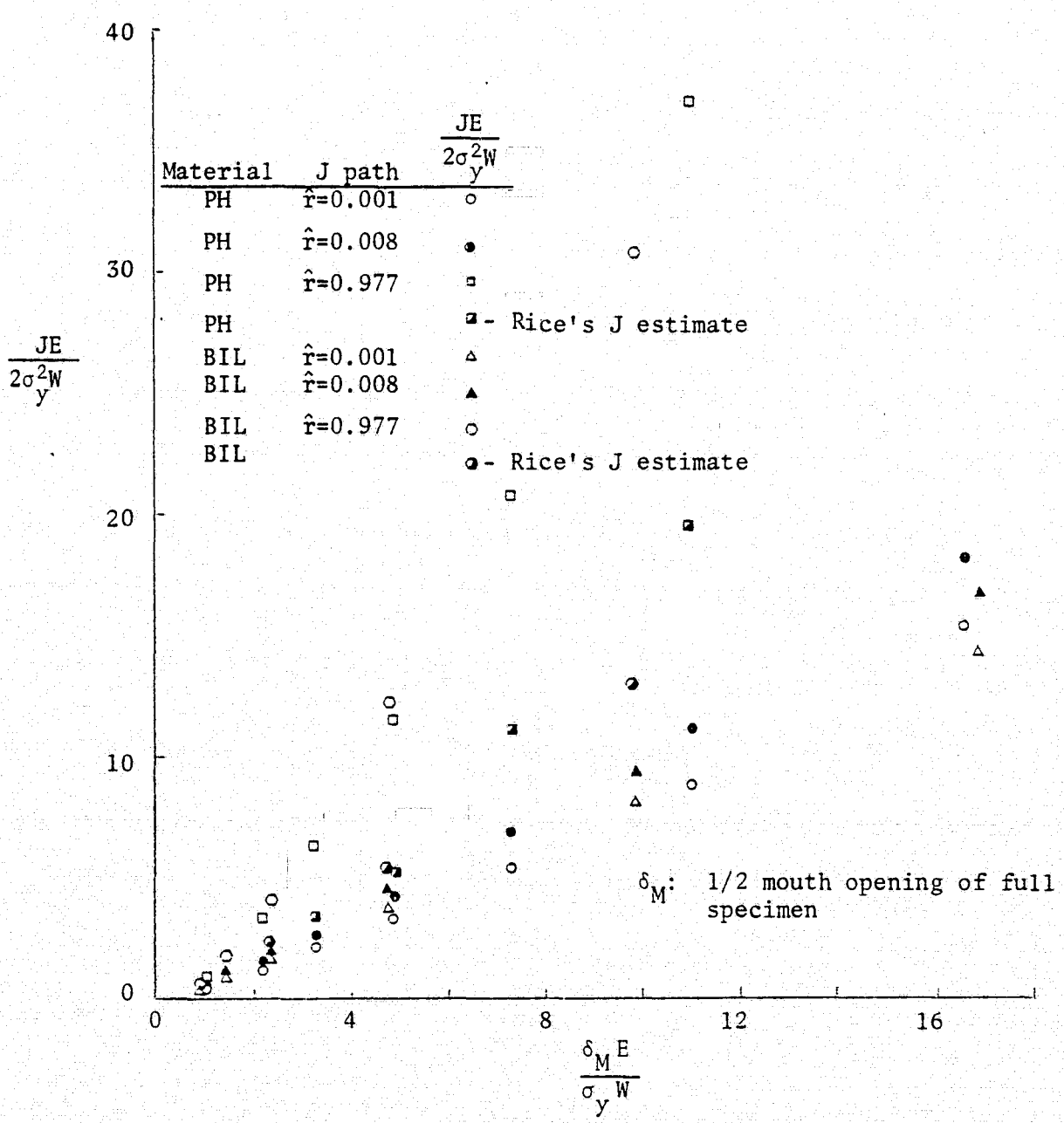

FIG. 90: J VS. Crack Mouth Opening from the Point of Net Section Yield (PH and BIL)

FIG. 91: J and Applied Displacement VS. Crack Mouth Opening (RS)

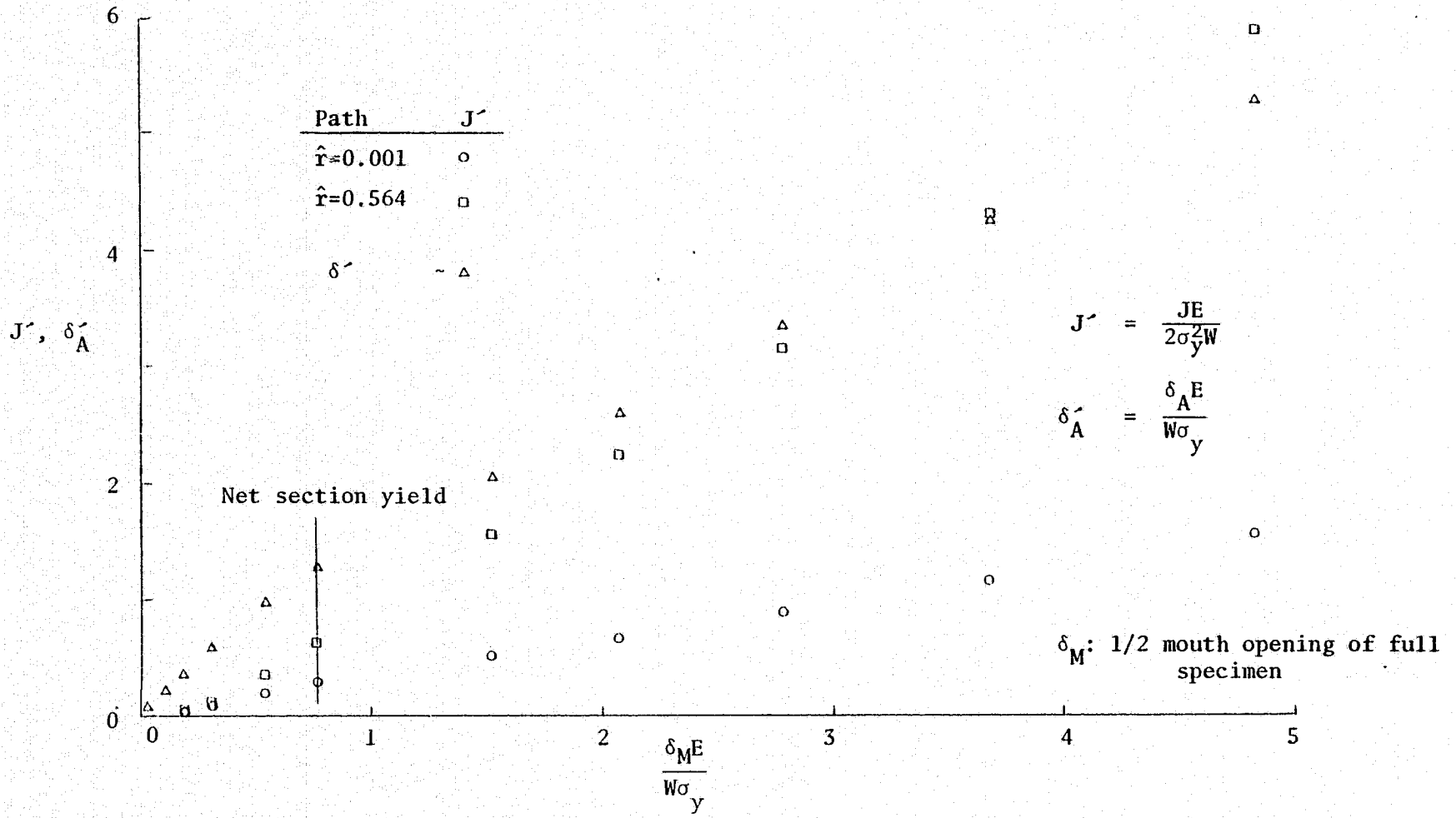

FIG. 92: J VS. Crack Mouth Opening (Bend)

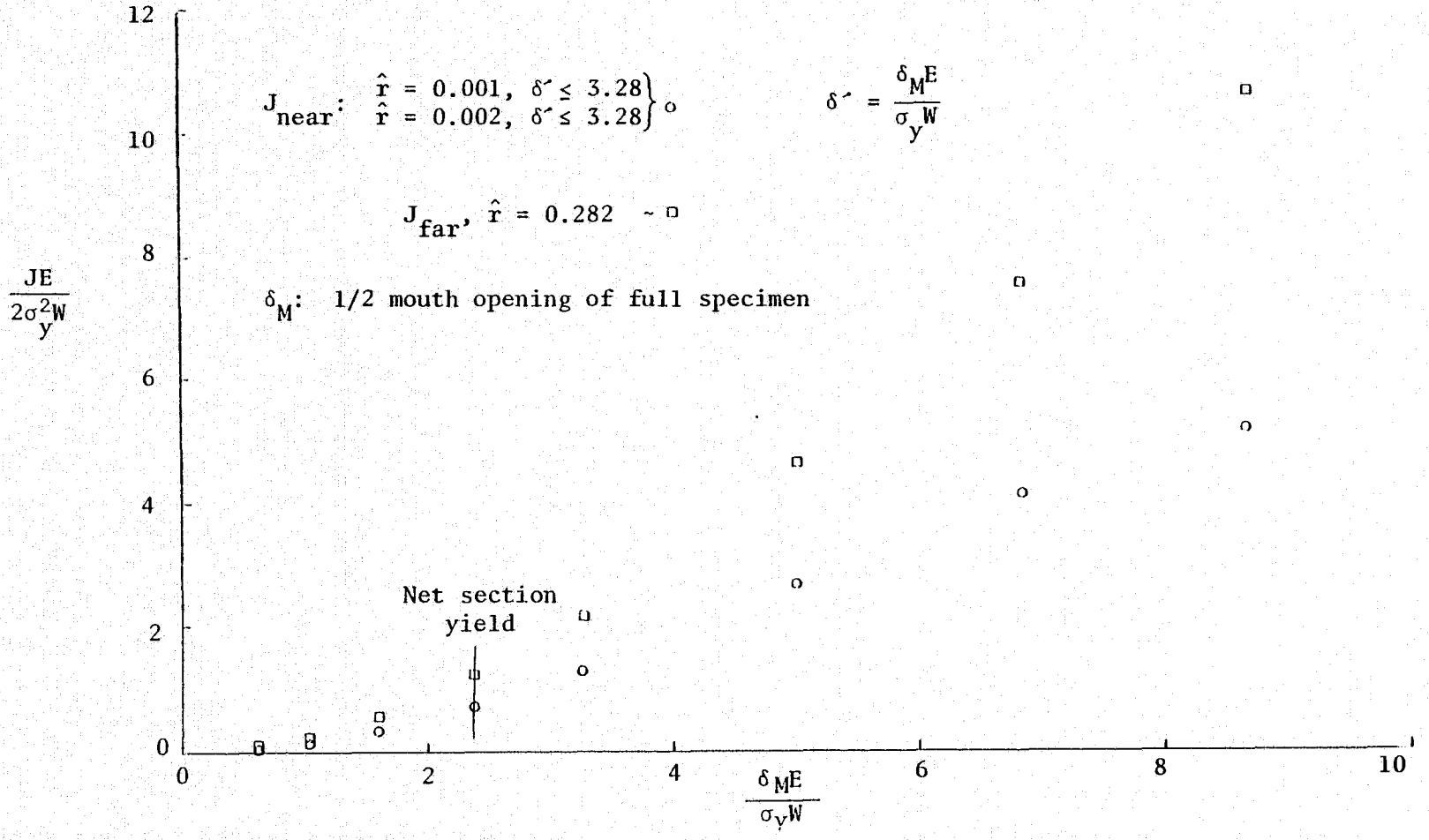

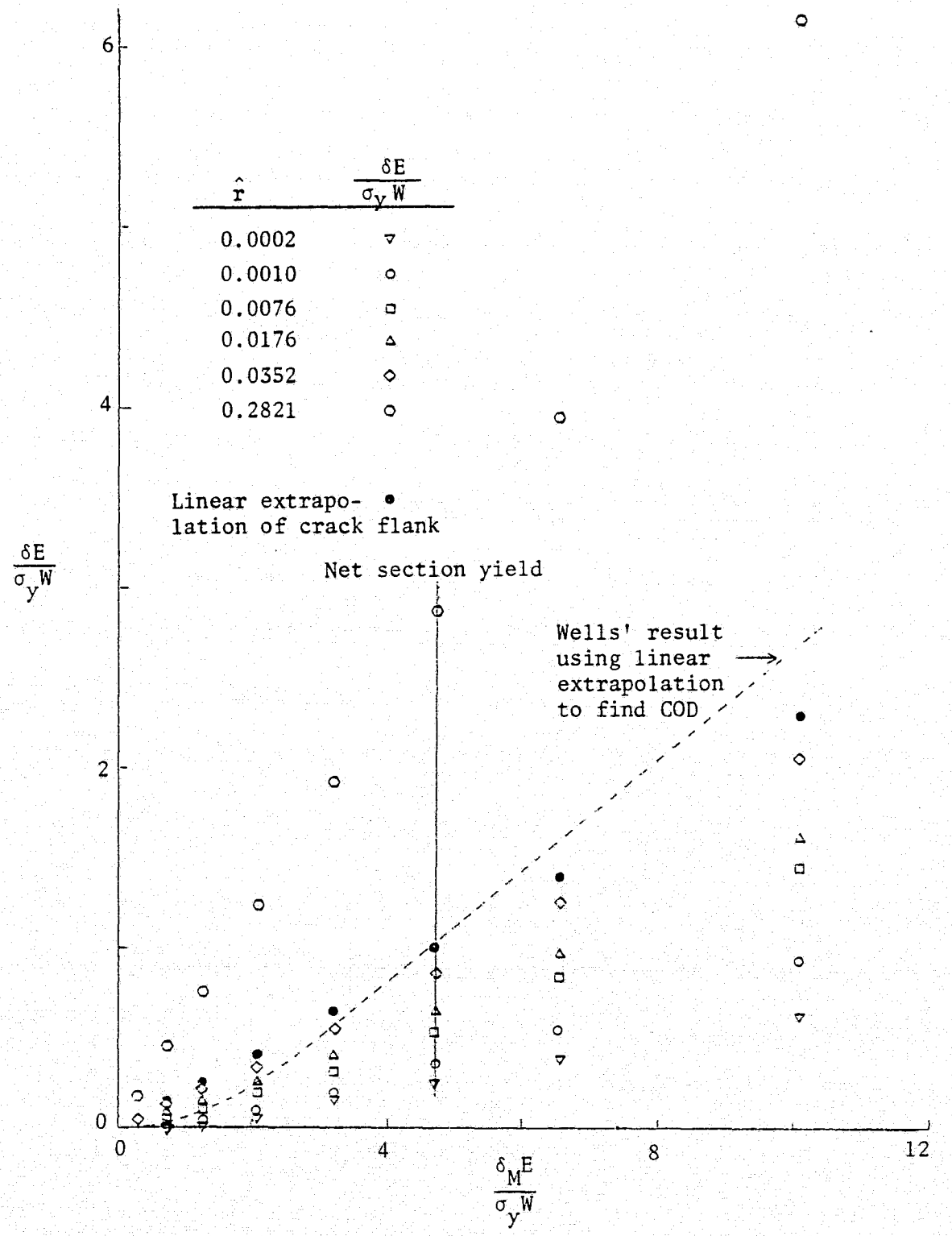

FIG. 93: Crack Flank Opening (δ) VS. Crack Mouth Opening (δ_M) (Bend)

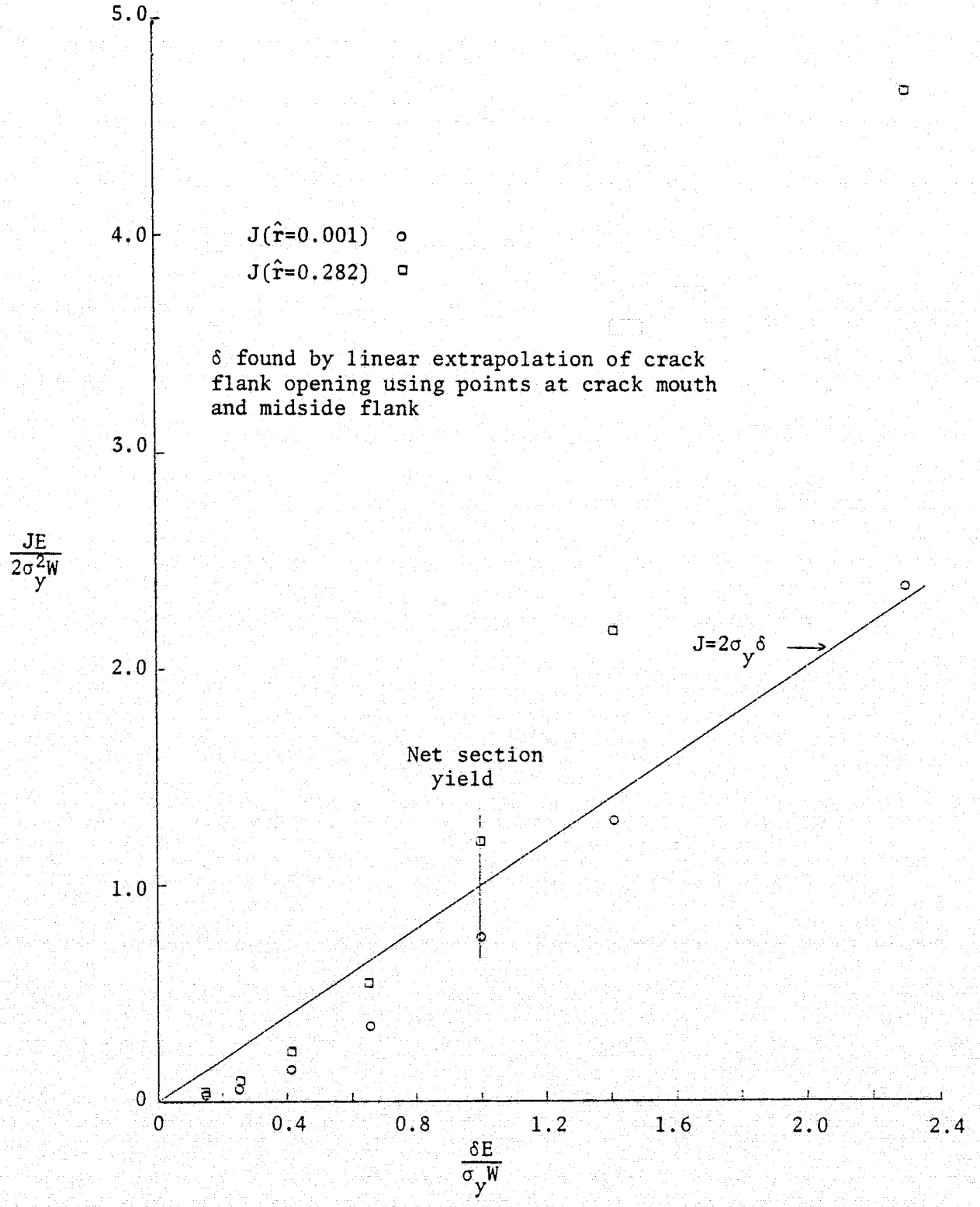

FIG. 94: J VS. COD (Bend)

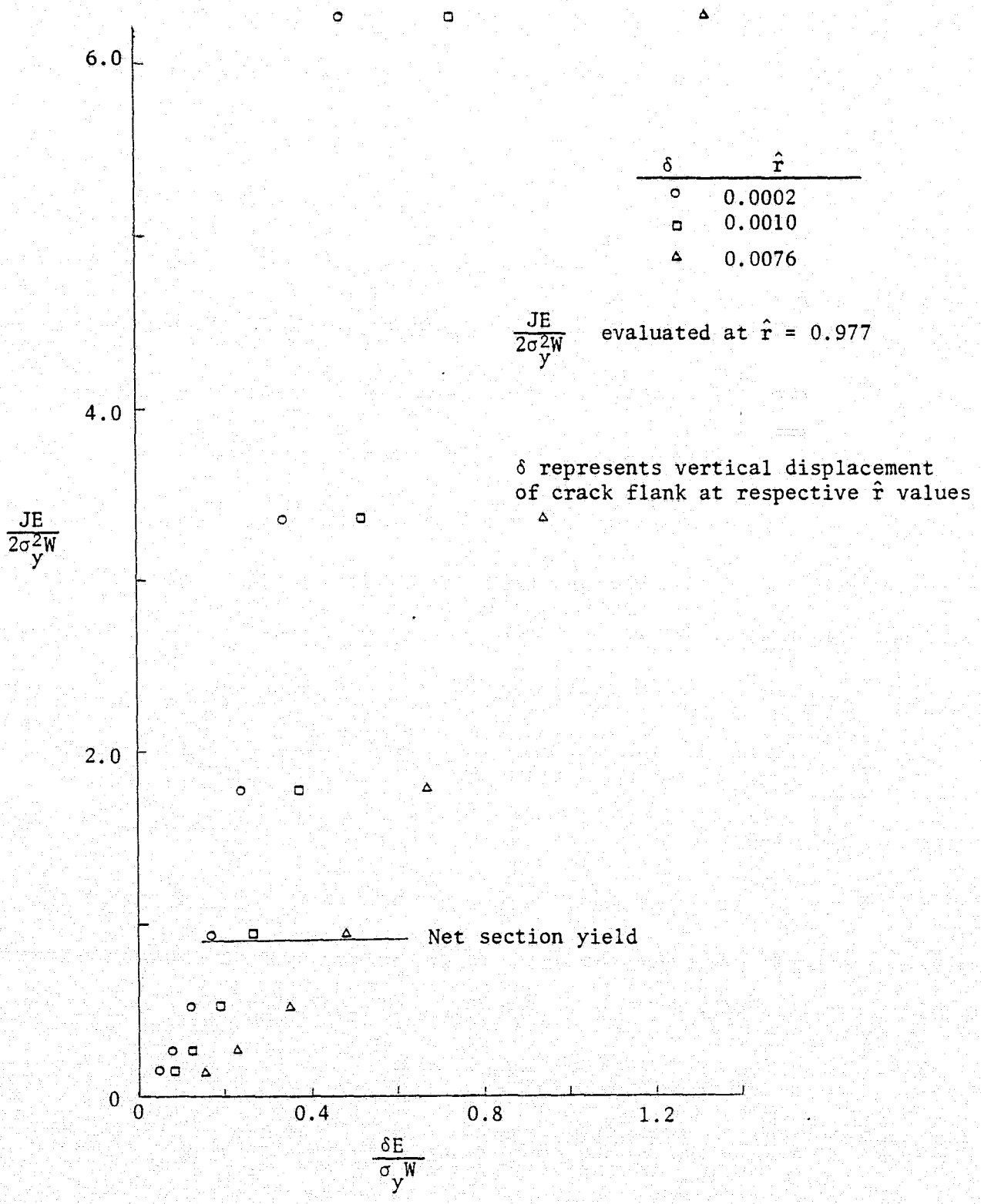

FIG. 95: Far Field J VS. Crack Tip Opening (PH)

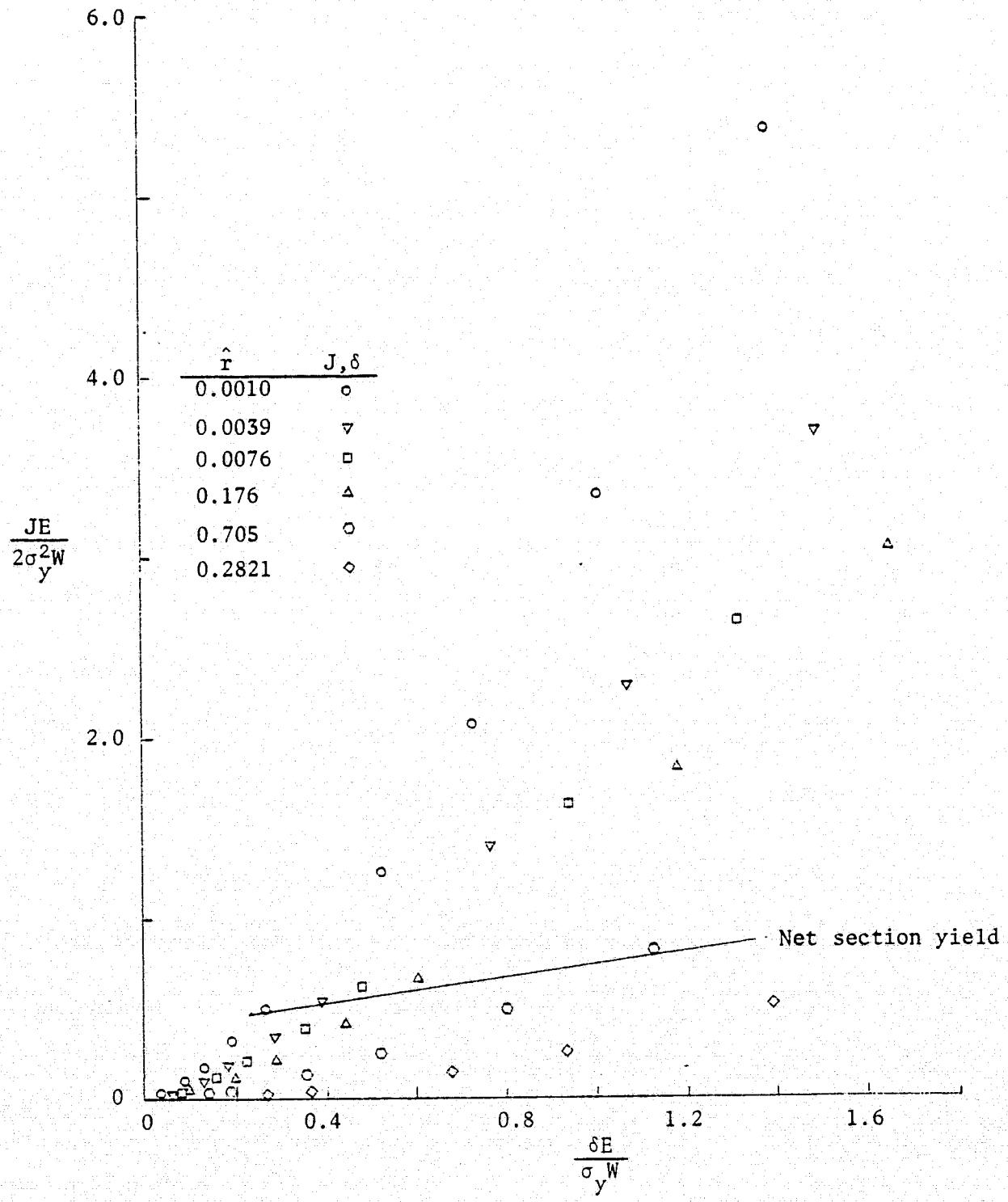

FIG. 96: J VS. Crack Flank Displacement at Respective Distances from the Crack Tip (PH)

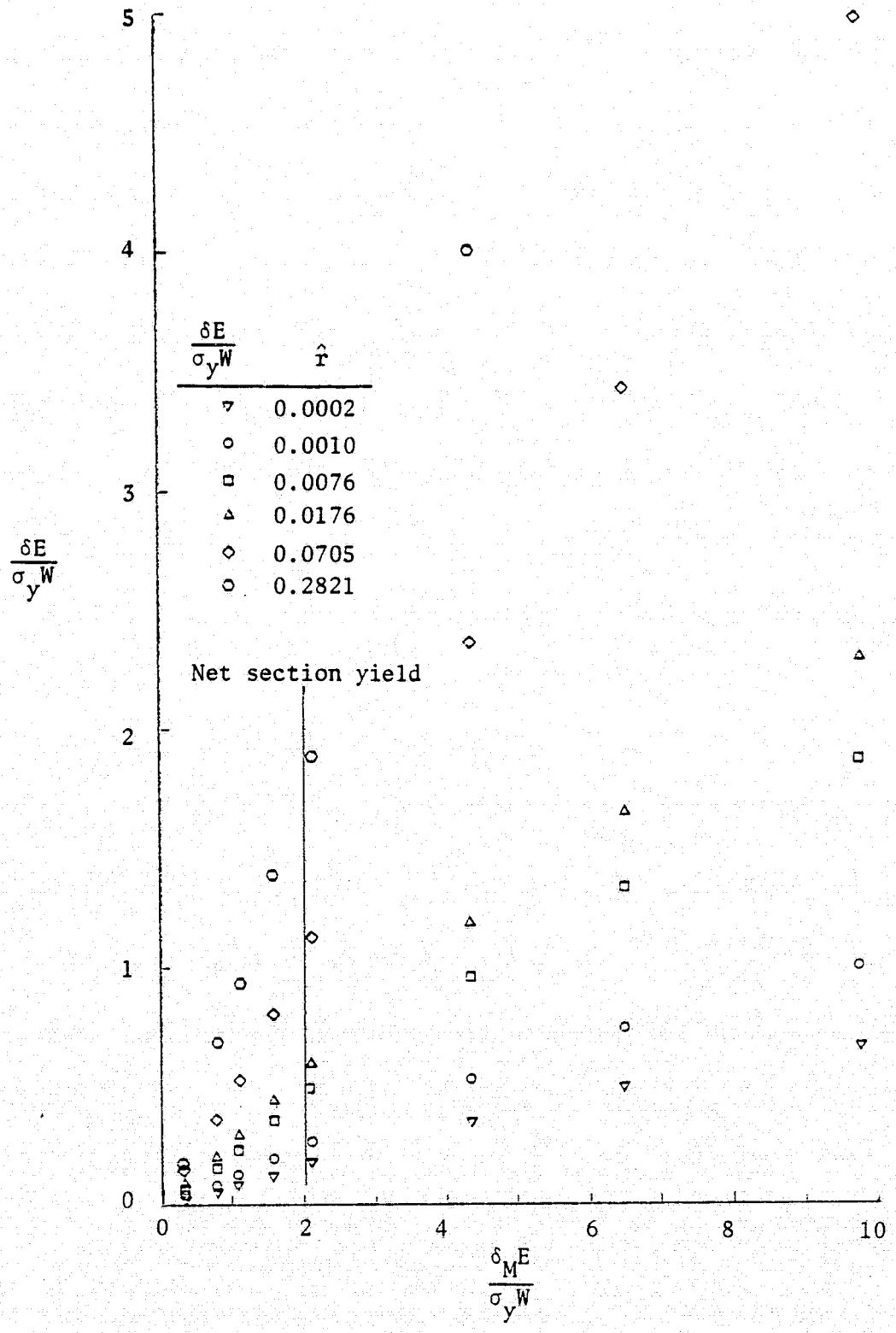

FIG. 97: Crack Flank Opening (δ) VS. Crack Mouth Opening (δ_M) (PH)

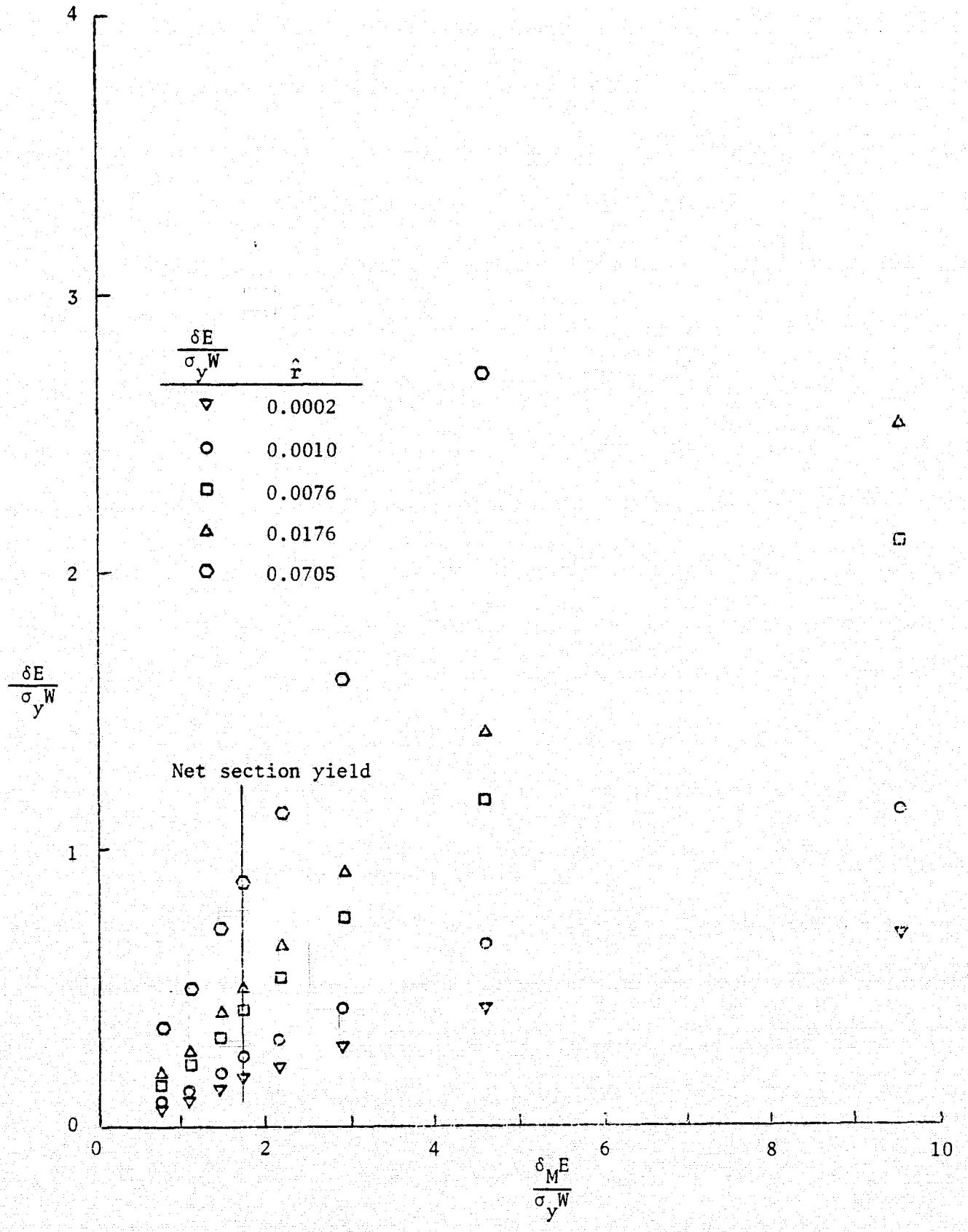

FIG. 98: Crack Flank Opening (δ) VS. Crack Mouth Opening (δ_M) (BIL)

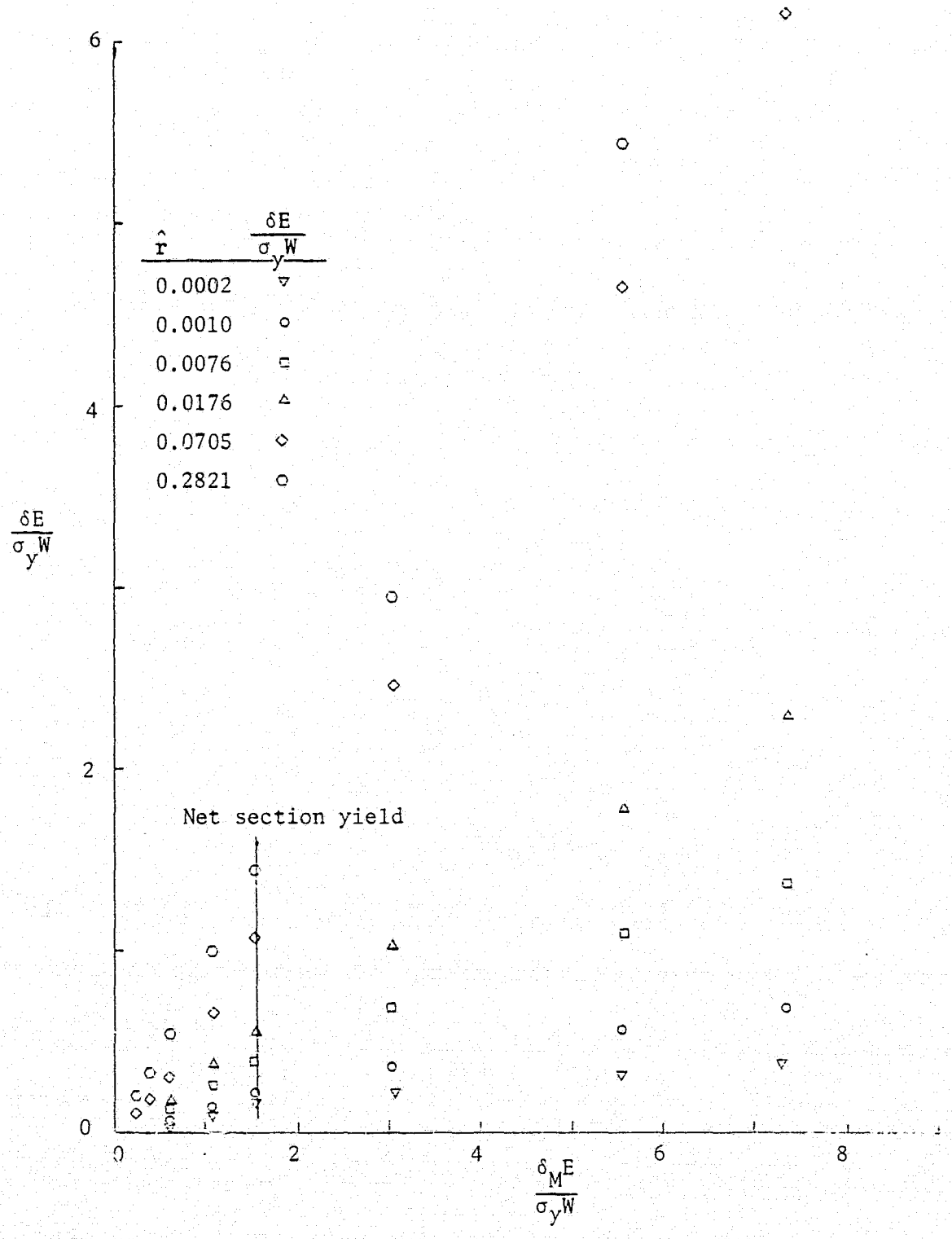

FIG. 99: Crack Flank Opening (δ) VS. Crack Mouth Opening (δ_M) (RS)

FIG. 100: Flow Chart for Proposed Experiment

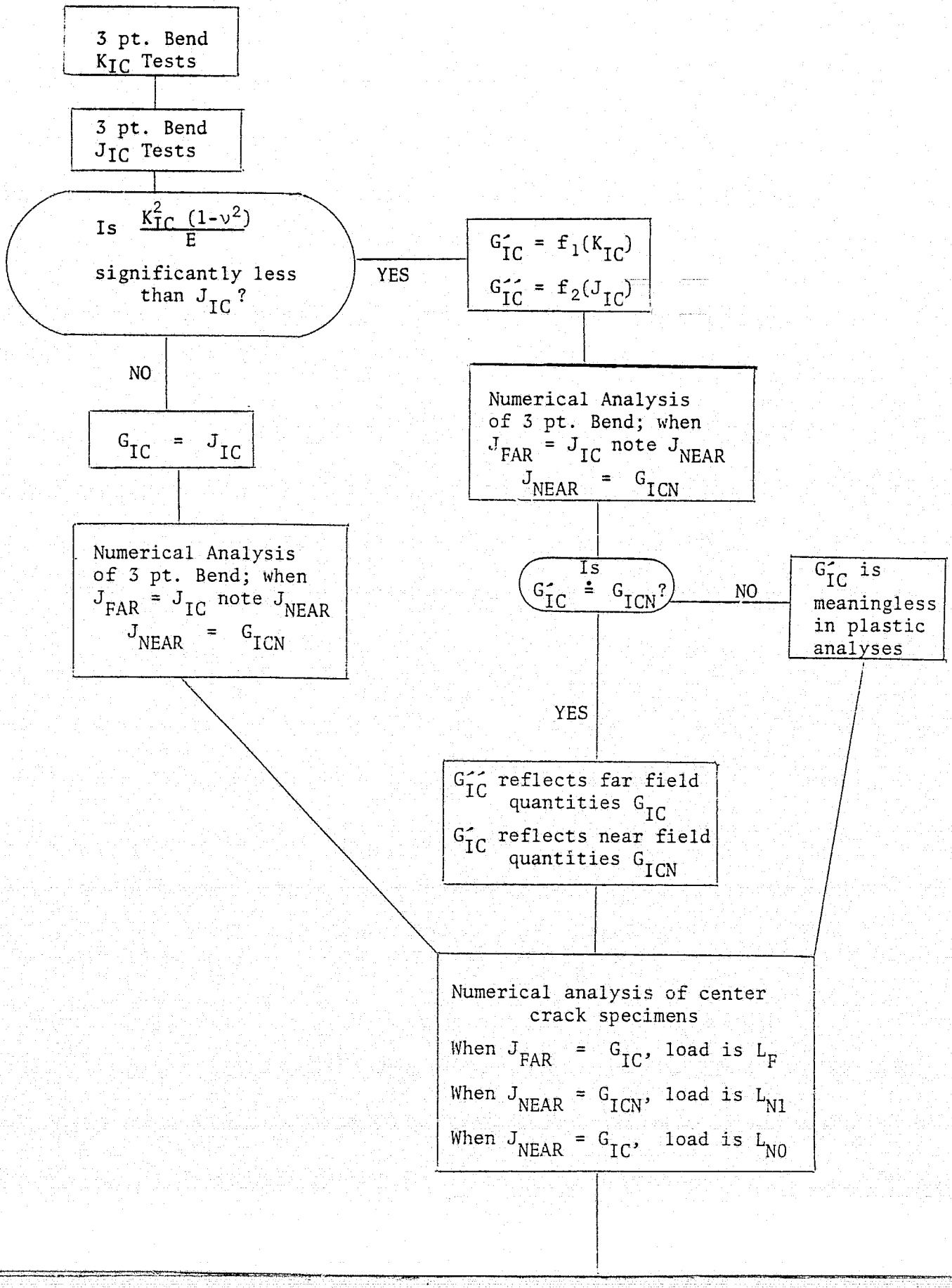

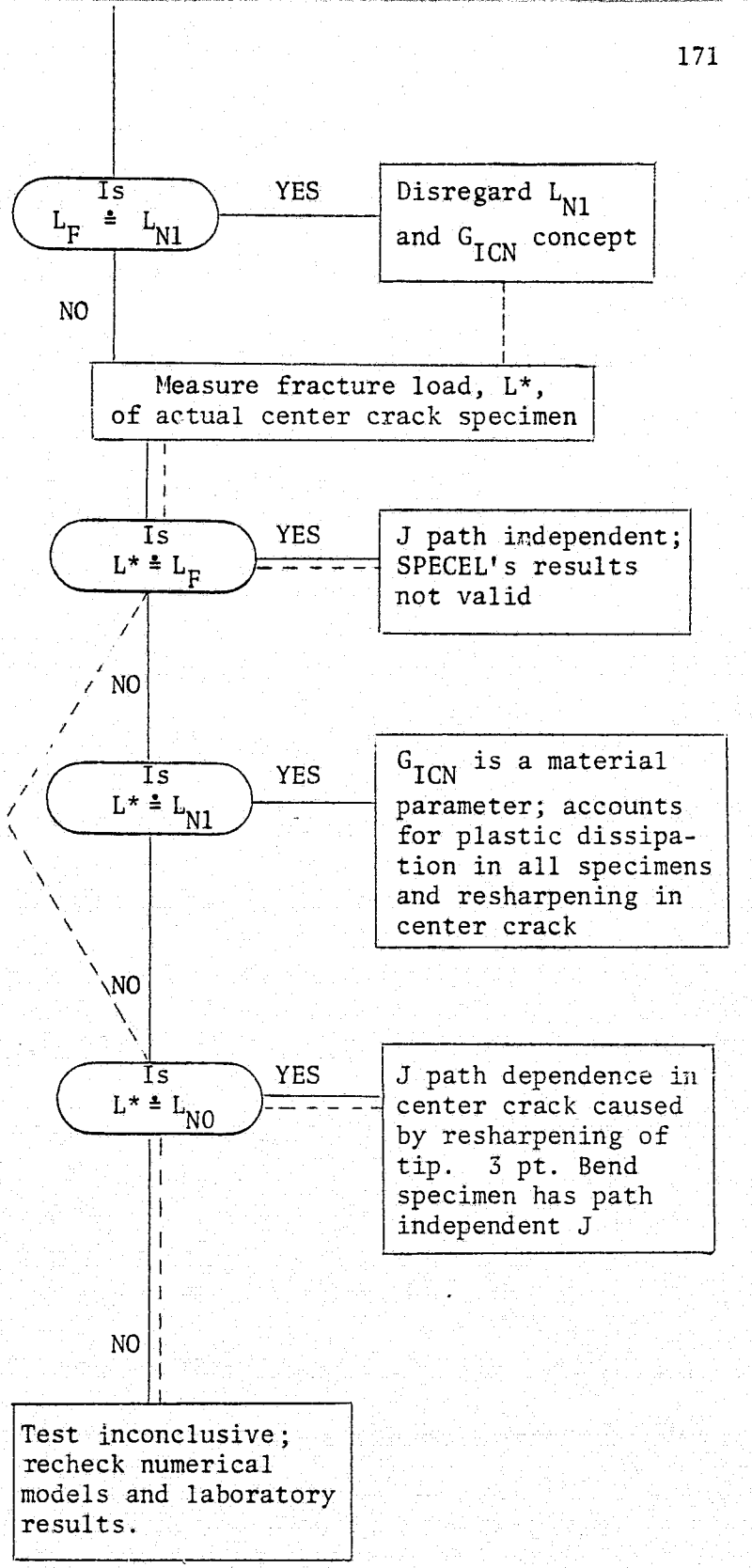

Fig. 100 (continued from page 170)

REFERENCES

American Society for Testing and Materials (1974), "Plane-Strain Fracture Toughness of Metallic Materials", E399-74.

Atluri, S. N., Nakagaki, M. and Chen, W. (1977a), Flaw Growth and Fracture, STP631, American Society for Testing and Materials, to be published.

Atluri, S. N. and Nakagaki, M. (1977b), Proceedings of the Fourth International Conference on Fracture 3, Waterloo, Canada, 457-462.

Brown, W. F., Jr. and Srawley, J. E. (1966), Plane Strain Crack Toughness Testing of High Strength Metallic Materials, STP410, American Society for Testing and Materials.

Clarke, G. A., Andrews, W. R., Paris, P. C. and Schmidt, D. W. (1976), Mechanics of Crack Growth, STP590, American Society for Testing and Materials, 27-42.

Goldman, N. L. and Hutchinson, J. W. (1975), International Journal of Solids and Structures 11, 575-591.

Hayes, D. J. and Turner, C. E. (1974), International Journal of Fracture 10, 17-32.

Hilton, P. D. and Hutchinson, J. W. (1971), Engineering Fracture Mechanics 3, 435-451.

Hutchinson, J. W. (1968a), Journal of the Mechanics and Physics of Solids 16, 13-31.

Hutchinson, J. W. (1968b), Journal of the Mechanics and Physics of Solids 16, 337-347.

Ilyushin, A. A. (1946), Prikladania Matematika i Mekhanika 10, 347-356.

Jones, D. P. (1972), "Elasto-Plastic Bending of Cracked Plates, Including the Effects of Crack Closure", Ph.D. Dissertation, Carnegie-Mellon University.

Knowles, J. K. and Sternberg, E. (1973), Technical Report 27, Division of Engineering and Applied Science, California Institute of Technology.

Landes, J. D. and Begley, J. A. (1974), Fracture Analysis, STP560, American Society for Testing and Materials, 170-186.

Larsson, S. G. and Carlsson, A. J. (1973), Journal of the Mechanics and Physics of Solids 21, 263-277.

Marino, C. (1978), Untitled Ph.D. Dissertation, Carnegie-Mellon University.

McMeeking, R. M. and Rice, J. R. (1975), International Journal of Solids and Structures 11, 601-616.

Riccardella, P. C. and Swedlow, J. L. (1974), Fracture Analysis, STP560, American Society for Testing and Materials, 134-154.

Rice, J. R. (1968), Journal of Applied Mechanics 35, 379-386.

Rice, J. R., Paris, P. C. and Merkle, J. G. (1973), Progress in Flaw Growth and Fracture Toughness Testing, STP536, American Society for Testing and Materials, 231-245.

Rice, J. R. and Rosengren, G. F. (1968), Journal of the Mechanics and Physics of Solids 16, 1-12.

Shih, C. F. (1974), Fracture Analysis, STP560, American Society for Testing and Materials, 187-210.

Swedlow, J. L. (1968), International Journal of Non-Linear Mechanics 3, 325-336.

Swedlow, J. L. (1973), Computers and Structures 3, 879-898.

Swedlow, J. L. (1974), Report SM 74-10, Department of Mechanical Engineering, Carnegie-Mellon University.

Swedlow, J. L. and Karabin, M. E., Jr. (1977), Proceedings of the Fourth International Conference on Fracture 1, Waterloo, Canada, 117-131.

Tada, H., Paris, P. C. and Irwin, G. C. (1973), The Stress Analysis of Cracks Handbook, Del Research Corporation, Hellertown, Pennsylvania.

Tracey, D. M. (1973), "On the Fracture Mechanics Analysis of Elasto-Plastic Materials Using the Finite Element Method", Ph.D. Dissertation, Brown University.

Tracey, D. M. and Cook, T. S. (1977), International Journal for Numerical Methods in Engineering 11, 1225-1233.

Wells, H. H. (1971), Proceedings of Third Canadian Congress of Applied Mechanics, Calgary, Canada, 59-77.

Williams, M. L. (1952), Journal of Applied Mechanics 19, 526-528.

Williams, M. L. (1951), Journal of Applied Mechanics 24, 109-114.

Wilson, W. K. (1977), Private communication, Progress Report of E-24 Task Group on Round Robin, Westinghouse Electric Corp., Pittsburgh, Pa.

Zienkiewicz, O. C. (1967), The Finite Element Method in Structural Continuum Mechanics, McGraw-Hill, London.

APPENDIX

The problem is to determine the accumulated exponent, p*, from the accumulated displacements, u. After N increments of load u is assumed to have the form

$$u = \sum_{i=1}^{N} \delta u_i = \sum_{i=1}^{N} \left(A_{1i}+A_{2i}r+A_{3i}r^{p_i}\right) = C_1'+C_2'r+C_3'r^{p^*} \qquad (A1)$$

where δu_i, p_i are the incremental displacements and exponents respectively; $A_{1i}\ldots$, $C_1',\ldots$, are constants, and r is the distance from the crack tip. This procedure is done at a fixed angular position using known values of displacement at seven Gaussian integration points within the special element. In cases where data near the tip are not credible these points may be omitted from the scheme but it is recommended at least five points be used. In order to find p* through linear regression analysis the functional expression of u must have the following form:

$$Y = a_1 + a_2 X \qquad (A2)$$

where Y represents a known value, X is the variable, and a_1,a_2 are constants to be determined.

In order to achieve the desired form the fact that C_1' is known is utilized. C_1' represents rigid translation which is found from displacements at the crack tip. If u_0 is the horizontal displacement at the tip (the vertical component is fixed at zero) then

$$\begin{aligned} C_1' &= u_0 \cos\theta && \text{for } u = u_r \\ C_1' &= -u_0 \sin\theta && \text{for } u = u_\theta \end{aligned} \qquad (A3)$$

A nonessential, but simplifying, step is to normalize the r variable on the radius of the special element, r_0.

$$u - C_1 = C_2 Z + C_3 Z^{p^*} \tag{A4}$$

where $Z = r/r_0$, $C_1 = C_1'$, $C_2 = C_2' r_0$, $C_3 = C_3' r_0^{p^*}$. Dividing by Z yields

$$\frac{u-C_1}{Z} = C_2 + C_3 Z^{p^*-1} \tag{A5}$$

where the left side of the expression is known at the Gauss points. This is almost in the form of (A2). Next, let

$$X = Z^{p^*-1} \tag{A6}$$

by selecting some value of p*. Then

$$Y = \frac{u-C_1}{r/r_0} = C_2 + C_3 X \tag{A7}$$

and the desired form is achieved. For a particular Gauss point, r_j (j = 1,...,7)

$$Y_j = \frac{u_j - C_1}{r_j / r_0} = C_2 + C_3 X_j \tag{A8}$$

C_2 and C_3 are found by linear regression techniques and are expressed by the following equations:

$$C_3 = \frac{\sum_{j=1}^{n} X_j Y_j - \frac{\sum_{j=1}^{n} X_j \sum_{j=1}^{n} Y_j}{n}}{\sum_{j=1}^{n} X_j^2 - \left(\sum_{j=1}^{n} X_j\right)^2 /n}$$

$$C_2 = \frac{\sum_{j=1}^{n} Y_j}{n} - C_3 \frac{\sum_{j=1}^{n} X_j}{n} \qquad \text{(A9)}$$

where n is the number of points used in the process. The closeness of the fit of the actual data to the functional form determined by selecting a p* is expressed by the coefficient of determination, t:

$$t = C_3^2 \frac{\sum_{j=1}^{n} X_j^2 - \left(\sum_{j=1}^{n} X_j\right)^2 /n}{\sum_{j=1}^{n} Y_j^2 - \left(\sum_{j=1}^{n} Y_j\right)^2 /n} \qquad \text{(A10)}$$

t ranges from 0 to 1; the closer t is to 1, the better the fit. Actually,

$$t = t(p^*) \qquad \text{(A11)}$$

and the best fit of the data is found by maximizing t(p*). The process is done by searching the range of p* until the maximum value of t(p*) is found between two values of p* which differ by less than 0.000002. The search procedure is actually done four times with a new starting value of p* each time. Usual starting values are 0.5, 0.4, 0.3, 0.2, and only in rare cases do the four final p* values differ by more than

0.002. The reliability of the method may be judged by the coefficients of determination which are reported in Chapter IV.

ADDENDUM

$$\delta u_r = (u_0 \cos\theta + v_0 \sin\theta) + r(C_1 \cos^2\theta + C_2 \sin^2\theta + (C_3 + C_4) \sin\theta \cos\theta) + r^p(C_5 + C_6 \theta)$$

$$\delta v_\theta = (-u_0 \sin\theta + v_0 \sin\theta) + r\big((-C_1 + C_2) \sin\theta \cos\theta - C_3 \sin^2\theta + C_4 \cos^2\theta\big) + r^p(C_6 + C_7\theta)$$

where $C_1,\ldots,C_8$, u_0, v_0 are coefficients to be determined; u_0, v_0 are the cartesian rigid translations of the element; p is the variable incremental exponent.